ORNL/HTSPC-15

ORNL Superconducting Technology Program for Electric Power Systems

Annual Report for FY 2003

SUPERCONDUCTIVITY FOR ELECTRIC SYSTEMS

ORNL/HTSPC-15

ORNL SUPERCONDUCTING TECHNOLOGY PROGRAM FOR ELECTRIC POWER SYSTEMS

ANNUAL REPORT FOR FY 2003

Compiled by
R. A. Hawsey
A. W. Murphy

Edited by
W. S. Koncinski

Manuscript Completed: March 2004
Date Published: June 2004

Prepared for the
Superconductivity Program for Electric Systems
Office of Electric Transmission and Distribution
U.S. DEPARTMENT OF ENERGY

Prepared by the
OAK RIDGE NATIONAL LABORATORY
P. O. Box 2008
Oak Ridge, Tennessee 37831-6285
Managed by
UT-Battelle, LLC
for the
U. S. DEPARTMENT OF ENERGY
Under contract DE-AC05-00OR22725

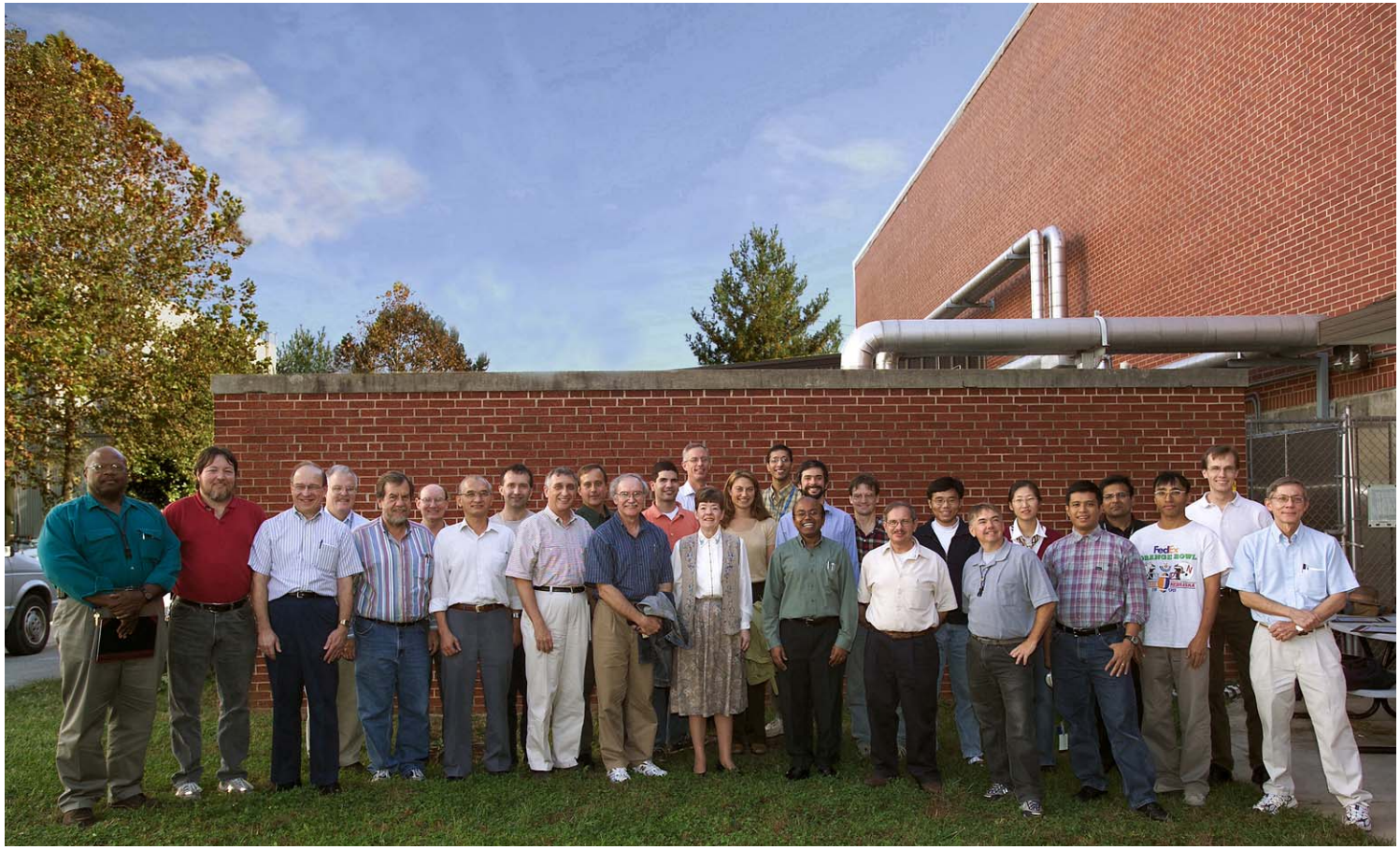

Front row (left to right): S. W. Cook, A. R. Ellis, H. R. Kerchner, L. Heatherly, Jr., J. W. Lue, B. W. McConnell, D. K. Christen, A. W. Murphy, M. P. Paranthaman, I. Sauers, P. M. Martin, A. A. Gapud, S. Kang, and J. R. Thompson.

Back row: M. J. Gouge, D. R. James, R. Grabovickic, J. A. Demko, T. Aytug, R. A. Hawsey, C. Cantoni, S. Sathyamurthy, E. D. Specht, F. A. List, H. Y. Zhai, J. Yoo, A. Goyal, and H. M. Christen.

Not present: D. F. Lee, K. J. Leonard, S. W. Schwenterly, P. W. Fisher, and R. Feenstra.

Contents

List of Figures

List of Tables

NOMENCLATURE

$\Delta\phi$	in-plane texture
$\Delta\omega$	out-of-plane texture
ρ	normal-state resistivity
σ	standard deviation
B_{irr}	irreversibility field
$c\ (2 \times 2)$	centered (2×2) superstructure
I_c	critical current
I_p	peak current
I_{mp}	propagation current
I_{rms}	root mean square cable current
J_c	critical current density
J_E	engineering critical current density
K_c	critical current per unit width of conductor
langmuir	10^{-6} Torr/s
ML	surface adsorbate atoms per surface substrate atoms
M_{sat}	saturation magnetization
P_{base}	base pressure
$P(H_2O)$	water vapor partial pressure
$P(O_2)$	oxygen partial pressure
T	tesla
T_c	critical temperature/transition temperature
t	thickness

ACRONYMS AND INITIALISMS

2G	second generation
ac	alternating current
ACCI	Accelerated Coated Conductor Initiative
ACCL	Accelerated Coated Conductor Laboratory
AEP	American Electric Power
AES	Auger electron spectroscopy
AFM	atomic force microscopy
AMSC	American Superconductor Corporation
ANL	Argonne National Laboratory
BIL	basic impulse level
BSCCO	Bi-Sr-Ca-Cu-O
CCC	coated conductor composite
CCVD	combustion chemical vapor deposition
CEIDP	Conference on Electrical Insulation and Dielectric Phenomena
CRADA	cooperative research and development agreement

dc	direct current
DEIS	Dielectric and Electrical Insulation Society
DOE	U.S. Department of Energy
DOE-HQ	DOE Headquarters
e-beam	electron beam
EDS	energy-dispersive spectroscopy
EDX	energy-dispersive X-ray diffraction
EELS	electron energy-loss spectroscopy
fcc	face-centered cubic lattice
FM	ferromagnetism
FWHM	full width at half maximum
GB	grain boundary
GBMD	grain-boundary misorientation distribution
GE	General Electric
GR	grain ring
GZO	gadolinium zirconium oxide
HRSEM	high-resolution scanning electron microscope
HTS	high-temperature superconductivity/superconductor/superconducting
HV	high vacuum
IBAD	ion-beam-assisted deposition
ICP-MS	inductively coupled plasma mass spectroscopy
IEEE	Institute of Electrical and Electronics Engineers, Inc.
IGC	Intermagnetics General Corporation
ISD	inclined substrate deposition
ISTEC	International Superconductivity Technology Center
LANL	Los Alamos National Laboratory
LMO	$LaMnO_3$
LN_2	liquid nitrogen
LSMO	$La_{0.7}Sr_{0.3}MnO_3$
LV	low voltage
LZO	lanthanum zirconium oxide ($La_2Zr_2O_7$)
MBCO	$MBa_2Cu_3O_{(7-x)}$
MBE	molecular beam epitaxy
MCT	MicroCoating Technology, Inc.
MFCL	matrix fault current limiter
MLI	multiple-layer insulation
MOCVD	metal-organic chemical vapor deposition
MOD	metal organic decomposition
MRS	Materials Research Society
ORNL	Oak Ridge National Laboratory
PD	partial discharge
PED	pulsed-electron deposition
PLD	pulsed-laser deposition
PPLP	polypropylene laminated paper
PSD	position-sensitive detector
PVD	physical vapor deposition
R&D	research and development
RABiTS™	Rolling-Assisted Biaxially Textured Substrate

RBS	Rutherford backscattering spectroscopy/spectrum
rf	radio frequency
RFP	request for proposal
RHEED	reflection high-energy electron diffraction
rms	root mean square
RTD	resistance temperature detector
SAD	selected area diffraction
SAIC	Science Applications International Corporation
SD	standard deviation
SEM	scanning electron microscopy
SF	self-field
SIMS	secondary ion mass spectrometer
SPI	Superconductivity Partnerships with Industry
SQUID	superconductivity quantum interference device
STC	Stirling Technology Company
STEM	scanning transmission electron micoscope
STO	$SrTiO_3$
TAB	Technical Advisory Board
TEM	transmission electron microscopy
TFA	trifluoroacetate
TGP	time gradient processed
TRC	Technical Review Committee
UHV	ultrahigh vacuum
WES	Waukesha Electric Systems
XPS	X-ray photoelectron spectroscopy
XRD	X-ray diffraction
YBCO	yttrium barium copper oxide ($YBa_2Cu_3O_{7-d}$)
YSZ	yttria-stabilized zirconia

Executive Summary

The Oak Ridge National Laboratory (ORNL) Superconductivity Program for Electric Power Systems is funded by the U.S. Department of Energy's (DOE's) Office of Electric Transmission and Distribution. Progress is reported this year in superconducting wire research and in electric power applications research. The projects conducted at ORNL are industry-driven, collaborative efforts that are leading to high-performance second-generation (2G) high-temperature superconducting (HTS) wires. U.S. industry succeeded in taking ORNL's "RABiTS™" technology out of the laboratory, improving upon it, and producing precommercial lengths of these 2G wires that are "best in class." In the meantime, significant progress is also reported this year in developing an improved understanding of the deposition and conversion of YBCO precursors as well as developing alternatives to the standard Y_2O_3-YSZ-CeO_2 buffer stack on Ni-3%W and alternatives to the Ni-3%W alloys.

Substantial progress is also reported in industry-led projects in which first-generation "BSCCO" HTS wires are used for power devices. Projects under way include the Southwire superconducting cable, the Waukesha/SuperPower superconducting transformer, and the General Electric 100-MVA HTS generator. A new initiative to test the performance limits of BSCCO and YBCO composite conductors under high fault current yielded insights into protection requirements for wires made from them. In addition, three companies were selected for negotiation of awards in the new cryogenics initiative, which will lead to higher-efficiency, higher-performance cryogenic systems for these applications.

The technical progress reported here was summarized from open-literature publications, presentations, and information prepared for the FY 2003 Annual DOE Peer Review held during July 2003. At that meeting, ORNL projects were consistently rated "good" to "outstanding," with two projects rated "world class" by a group of international expert reviewers. Aspects of ORNL's work that were presented at the 2003 ICMC/CEC meeting in Anchorage, Alaska, in September 2003, are also included in this report.

1. Technical Progress in Wire Development

1.1 REEL-TO-REEL EX SITU CONVERSION OF HIGH CRITICAL CURRENT DENSITY ELECTRON BEAM CO-EVAPORATED BaF_2 PRECURSOR ON RABiTS™

D. F. Lee, K. J. Leonard, L. Heatherly, Jr., N. Rutter, S. W. Cook, S. Sathyamurthy, M. Paranthaman, P. M. Martin, A. Goyal, and D. M. Kroeger (ORNL)

1.1.1 Introduction

During the past several years, a significant amount of effort in the high temperature superconductor community has been focused on the development of $YBa_2Cu_3O_{7-x}$ (YBCO) coated conductors. Very high critical current densities in excess of 1 MA/cm^2 at 77 K and self-field have been reported on YBCO films grown on biaxially textured metallic substrates. While the initial excellent results were obtained on short samples of a few centimeters long under stationary conditions, reports on the performance of longer length YBCO coated conductors, where YBCO films were grown in a moving mode, are slowly emerging. High end-to-end critical current densities exceeding 1 MA/cm^2 have been reported on meter-lengths of ion-beam-assisted deposition (IBAD) substrates where YBCO films were deposited in situ by the well-proven pulsed-laser deposition (PLD) technique [1–3] as well as by metal-organic chemical-vapor deposition (MOCVD) [4]. An alternate approach to YBCO deposition is the ex situ conversion of precursors. This approach of YBCO formation separates the precursor deposition step (i.e., compositional control) from the YBCO epitaxial growth process. Advantages of this approach include the usage of a reactor furnace where temperature control during YBCO formation is simplified, the possibility of a large conversion volume for enhanced production throughput, and non-vacuum deposition of precursor films [i.e., metal-organic decomposition (MOD)]. In fact, roughly 1 μm-thick YBCO with critical current densities greater than 1 MA/cm^2 have been converted in lengths of one meter or more using MOD and BaF_2 precursors on the Rolling-Assisted Biaxially Textured Substrate (RABiTS™) [5–6].

While the solution-based MOD precursor is a low-cost deposition method, development of thick YBCO precursor films in excess of ~1 μm (for very high critical current applications) that can be consistently produced without cracking is still not known. On the other hand, very thick (>5 μm), dense, and crack-free precursor films can be deposited by physical vapor deposition (PVD) techniques such as electron-beam co-evaporation (the so-called BaF_2 precursor). It is therefore important to investigate the processing characteristics and properties of BaF_2 precursor-derived YBCO concomitant to the development of various MOD methods. In this contribution, we report on the ongoing effort at ORNL in the reel-to-reel conversion of ex situ YBCO from BaF_2 precursors. This FY 2003 effort included (1) the study of process improvement for 0.9-μm and thicker precursors for enhanced critical current, (2) the initial attempt at experimentally determining the long-length percolation limit of RABiTS™ using BaF_2 precursor as a tool, and (3) a first evaluation of double-sided YBCO as a way to increase critical current.

1.1.2 Experimental

1.1.2.1 Sample Preparation

Samples used in the ex situ conversion were prepared by co-evaporating Y, Cu, and BaF_2 onto Ni-3 at. % W-based RABiTS™. Long-length RABiTS™ samples were prepared as follows [7–8]. As-rolled Ni-W tapes, 1 cm wide and 50 μm thick, were recrystallized by inductive heating in a reel-to-reel chamber under 3×10^{-7} Torr of H_2S and a resident time of 20 min at 1250°C. Various buffer layers were then deposited onto the cube-textured metallic substrates using a combination of reactive e-beam evaporation and magnetron sputtering. For the Ni-W-based RABiTS™, a CeO_2/YSZ/Y_2O_3/Ni/Ni-W substrate architecture was used. This architecture differs from that of the Ni-based RABiTS™ in that a Ni protective layer is added between the seed layer and textured metal tape. Presence of the Ni protective layer serves to circumvent the issue of weak W-oxide formation during the YBCO conversion stage,

which can lead to delamination at the buffer-metal interface. In the fabrication of Ni-W-based RABiTS™, the 1- to 2-μm-thick Ni protective layer was deposited onto annealed cube-textured Ni-W tapes in a reel-to-reel dc magnetron sputtering unit at an Ar-4%H_2 pressure of 10 Torr, a temperature of 500°C, and a deposition rate of ~18 Å/s. Once the cubed-textured Ni protective layer was deposited, the tape was transferred to the reel-to-reel e-beam evaporation chamber, where a 20-nm-thick Y_2O_3 seed layer was deposited onto the Ni protective layer using a Y-metal source. This epitaxial layer was deposited at 5×10^{-5} Torr H_2O, 650°C and a rate of ~2.7 Å/s. Following seed layer deposition, the tape was transferred to a reel-to-reel radio-frequency (rf) magnetron sputtering chamber for deposition of a yttria-stabilized zirconia (YSZ) barrier layer and CeO_2 cap layer. The 200-nm-thick YSZ and 20-nm-thick CeO_2 layers were deposited at an Ar-4%H_2 pressure of 5 Torr, P(H_2O) of 3×10^{-5} Torr, a temperature of 600°C, and deposition rates of ~0.4 Å/s and ~0.1 Å/s, respectively. The resulting Ni-W-based RABiTS™ possesses superior texture as compared to that of the Ni RABiTS™, with $\Delta\omega$ full width at half maximum (FWHM) of Ni-W, Y_2O_3 ,YSZ, and CeO_2 of ~6.5°± 0.5° and $\Delta\phi$ FWHM of ~7.5°± 0.5°.

Depending on the targeted YBCO thickness, RABiTS™ of 1 to 3 m long were loaded into a three-gun reel-to-reel e-beam co-evaporation system for precursor deposition. Details of the system and deposition procedure were described elsewhere [9]. Briefly, the deposition unit consists of three e-beam guns operating at a voltage of 8 kV with source materials in the form of Y metal, Cu metal, and BaF_2 crystal situated in three separate pockets. Precursor deposition was performed at room temperature under a P(H_2O) of 1×10^{-5} Torr with a total chamber pressure of less than 6×10^{-5} Torr. The film disposition rate was set at ~10 Å/s, where the rates for Y, BaF_2, and Cu were individually controlled by quartz crystal monitors. For each continuous pass through the deposition zone, the resultant thickness of the converted YBCO film is approximately 0.3 μm. Standard deviation of precursor thickness has been determined by Rutherford backscattering spectroscopy (RBS) to be ± 2.5% over a meter length. In addition, the typical film Y/Ba/Cu composition is roughly 1.05/2.1/3.0 with a standard deviation of less than ± 2%.

1.1.2.2 Reel-to-Reel YBCO Conversion

In the ex situ YBCO conversion approach, the precursor film is typically heated to an elevated temperature in a humidified reduced-oxygen atmosphere. Under these conditions, the precursor material decomposes in the presence of H_2O and forms YBCO, giving off HF as a reaction product [10]. In order to achieve complete conversion and to form epitaxial YBCO, it is necessary for the precursor to decompose totally and efficiently. While it is straightforward to process small-area, short-length high-critical-current-density samples in traditional atmospheric reaction chambers with a low rate of longitudinal gas flow, it is difficult to achieve a uniform high quality over longer lengths (i.e., more than a few centimeters) in this way. This is believed to be due to HF buildup both along the downstream sample surface and within the chamber itself, which slows the conversion process [11–13].

In order to minimize the problem of a nonuniform conversion rate, we have been engaging in the study of a two-pronged approach for the past few years [11–14]. This approach utilizes an extended transverse-flow geometry. By employing a transverse-flow geometry, where the direction of gas flow is parallel to the width of the sample, the effective conversion distance is reduced significantly. Furthermore, the presence of an extended reaction zone along the sample length will enable the simultaneous conversion of a larger area of precursor, thereby reducing the total amount of processing time.

A special reel-to-reel conversion chamber and a 22-zone furnace were constructed to study the continuous conversion of long-length samples [6]. Inconel 601 was selected as the chamber building material based, primarily on its mechanical integrity as well as its resistance to oxidation and HF corrosion. The 2.5-m-long chamber consists of seven transverse flow modules. These modules are stacked in an end-to-end fashion, and are separated by blocks with narrow slits to allow tape passage while minimizing crosstalk. Each 30-cm-long flow module is incorporated into the 5-cm-wide by 1-cm-high housing. Two 1-cm-diam Inconel 601 tubes with 125-μm holes are used as gas inlet and outlet ports. These tubes are welded in place such that the holes are opposite their counterparts and in line with the

sample suspended between them. Standard components, including gas supply, water bubblers, and oxygen sensors, are connected to the reaction chamber where necessary. In addition, multiple pressure sensors are strategically located such that pressures at gas inlets and gas outlets of different modules as well as the pressure of the reaction chamber can be continuously monitored. For this reaction chamber, flow modules 1 to 5 can be set to provide either a wet or dry gas environment, whereas modules 6 and 7 (downstream) remain dry at all times.

Reels are connected to the ends of the reaction chamber, which sits within the cradle of a custom-built 2-m-long, 22-zone tube furnace. Temperature of the hot zones of this furnace can be individually controlled such that a wide variety of thermal profiles as well as a sizable range of ramp-up temperature gradients (~14 to 32.5 ºC/cm) may be obtained. By continuously moving the sample at a chosen speed through a selected thermal profile, a prescribed conversion schedule can be performed.

1.1.2.3 Sample Characterization

Once continuous conversion had been completed, the sample was transferred to a reel-to-reel dc magnetron sputtering system where a 1-μm-thick Ag overlayer was deposited onto the superconductor. The sample was then transferred back and pulled through the reel-to-reel furnace such that every location of the sample was annealed for 1 h and cooled at a rate of 1.5 ºC/min in flowing oxygen. Transport measurements of samples up to 1 m long were performed in an apparatus where end-to-end as well as 1-cm sectional critical currents can be determined. For short samples, an apparatus with voltage separation distance of 4 mm was used. These transport critical current measurements were performed under standard four-probe configuration at 77 K and self-field according to the 1-μV/cm criterion. YBCO film thickness was confirmed by cross-sectional scanning electron microscopy (SEM) at various sample locations. In addition, X-ray diffraction (XRD) and SEM were used to examine film texture and microstructure of selected samples.

1.1.3 Results and Discussion

1.1.3.1 0.9-μm YBCO on Ni-W RABiTS™

We have previously reported on the initial success in the conversion of long-length 0.9-μm YBCO on Ni-W RABiTS™ [15]. Unlike thinner precursors (e.g., 0.3 μm thick), which can be processed under a uniformly high $P(H_2O)$ of ~ 40 Torr, a low initial $P(H_2O)$ appears to be more suitable. For the thicker precursors, a high initial $P(H_2O)$ resulted in phase segregation within the precursor as well as random nucleation of YBCO grains. In contrast, low initial $P(H_2O)$ provided well-textured epitaxial YBCO, possibly due to the reduction in the tendency of random YBCO nucleation and growth during the early period of epitaxial YBCO incubation. Using this approach, we have previously reported on a 1.1-m-long tape converted at a temperature of 740°C, $P(O_2)$ of 140 mTorr, flow rate at 5.5 L/min/module, ramp-up rate of 22.7°C/min, and a wet conversion time of 200 min. In addition, the $P(H_2O)$ of individual modules were progressively increased, ranging from a low initial $P(H_2O)$ of ~5 Torr to a final $P(H_2O)$ of 36 Torr. XRD analyses on a short section of the converted tape revealed a YBCO $\Delta\omega$ FWHM of 6.1°, $\Delta\phi$ FWHM of 7.9°, and a cube component of 97%, which agree well with the Ni-W RABiTS™ texture. End-to-end transport measurement performed with a voltage-tab separation distance of 103 cm revealed a critical current of 92 A (1.02 MA/cm^2) according to the 1-μV/cm criterion. Tape uniformity was examined by measuring 1-cm sectional critical currents along the entire sample and was found to be very uniform, with a maximum critical current of 102.2 A (1.14 MA/cm^2), a minimum critical current of 81.5 A (0.91 MA/cm^2), and a mean critical current of 94.4 A (1.05 MA/cm^2) with a standard deviation (SD) of only 4.3%.

Although we have succeeded in processing a YBCO coated conductor with a critical current near 100 A/cm and a critical current density greater than 1 MA/cm^2 in a length slightly greater than 1 m, further enhancement should still be possible. During FY 2003, we have concentrated on optimizing the conversion parameters and improving the buffer crystallinity and morphology. For example, we have

determined that the $P(H_2O)$ range has some effect on YBCO development and properties. Based on this observation, we have converted another 0.9-μm-thick YBCO on 1-cm-wide by 45-cm-long Ni-W RABiTS™ using essentially the same processing conditions as those of the 1.1-m-long conductor. The only variations were as follows: the conversion time was reduced slightly to 180 min, and the final $P(H_2O)$ was reduced to 30 Torr. XRD analyses revealed that the converted YBCO has identical texture to that of the 1.1-m conductor. However, end-to-end critical current of this tape is 111.8 A (1.24 MA/cm^2), an increase of 22%. The 1-cm sectional critical current measurements showed high sample uniformity with a maximum critical current of 123.3 A (1.37 MA/cm^2), a minimum critical current of 102.1 A (1.13 MA/cm^2), and mean critical current of 114.8 A (1.28 MA/cm^2) with a 4.8% SD (Fig. 1.1).

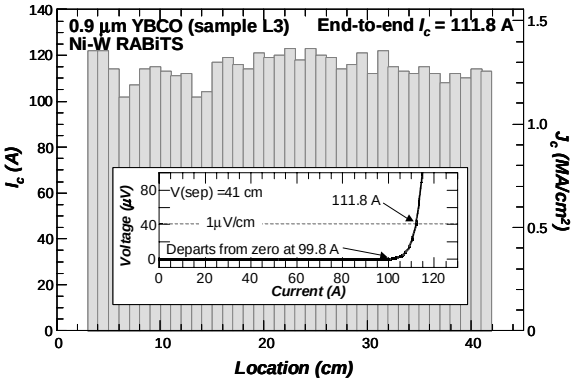

Fig. 1.1. Transport critical current and critical current density of a 0.9-μm YBCO layer on 45-cm-long, 1-cm-wide Ni-W RABiTS™. The 1-cm sectional properties are shown as columns and the end-to-end I-V curve is shown in the inset.

Further critical current enhancement has also been seen through the improvement of the buffer layer. For instance, a 1-cm-wide, 10-cm-long, and 0.9-μm thick YBCO sample was converted on a Ni-W RABiTS™ that had been subjected to post-buffer deposition annealing to improve the buffer crystallinity and morphology. A similar type of post-buffer deposition annealing treatment has been reported to increase the population of (001)-type surface termination planes, which can enhance the critical current density of the conductor [16]. Using the identical processing condition as that of the 45-cm-long sample, this short sample exhibited a critical current of 138 A, which is equivalent to a critical current density of 1.53 MA/cm^2, an improvement of 50% over the best FY 2002 result.

1.1.3.2 1.5-μm YBCO on Ni-W RABiTS™

In the continuing efforts to increase the critical current per centimeter and to study the conversion of even thicker BaF_2 precursors, a precursor film was deposited on 0.5-m-long Ni-W RABiTS™ in five successive passes that provide a 1.5-μm thickness of YBCO after conversion. An immediate issue arose when one considered the conversion parameters for films of such thickness in the present reel-to-reel furnace. Assuming a linear conversion rate of ~0.8 Å/s based on the 0.9-μm film results, a 1.5-μm-thick precursor would require more than 300 min of conversion time in this chamber. Since the length of the conversion zone was fixed to ~135 cm, a pull-through speed of ~ 0.43 cm/min would have to be employed. This would result in a ramp-up rate of less than 13°C/min. Previous observations have revealed that ramp-up rates at such a level or lower frequently led to YBCO films with a significant fraction of random components. Consequently, the study of the conversion of 1.5-μm-thick films was limited to short samples only (1 cm wide by 5 cm long). These films were initially pulled into the conversion zone at a speed that provided a ramp-up rate of 22.7°C/min (the same as that of the 0.9-μm films), at which point the pull-through speed was slowed to satisfy the selected total conversion times.

Several 1.5-μm-thick precursor tapes were converted using a nearly identical set of processing parameters (except conversion time) as those that provided the best 0.9-μm film result. After about 275 min of processing, the precursor was found to be fully converted (i.e., no BaF_2 signal was detected by XRD scans). Pole figure analysis revealed that the cube component of the YBCO was 96%, indicating good epitaxy for the YBCO phase present in the film. However, the YBCO(00*l*) peak intensities were considerably lower than those of the 0.9-μm films, suggesting that the content of YBCO in the converted film was significantly smaller. By adjusting parameters such as conversion temperature, $P(H_2O)$, and conversion time, the best critical current results ranged from 48 to 62 A, representing low critical current density values of 0.3 to 0.4 MA/cm^2. However, another parameter, $P(O_2)$, was found to be more effective

in improving the conversion and superconducting properties. By adjusting the $P(O_2)$, a critical current of 160.2 A (J_c = 1.07 MA/cm^2) was obtained. Even with this good result, the work revealed that it will be challenging to process thick PVD BaF_2 precursors with high critical currents and critical current densities at these conversion rates within the available processing window offered by the present "atmospheric" chamber. Work is under way to increase the conversion rate while maintaining high critical current densities.

1.1.3.3 4-mm-Wide, 0.3-μm-Thick YBCO on Ni-W RABiTS™

BaF_2 precursor has been used as a tool to experimentally study the long-length percolation limit of Ni-W RABiTS™. In FY 2002, we reported on the successful processing of 0.3-μm-thick YBCO on Ni-W RABiTS™. A meter-long tape was processed using a "partial conversion" technique to create graded YBCO along the length of a single tape, the procedure of which was described elsewhere [17]. The processing parameters used were a temperature of 740°C, $P(O_2)$ of 140 mTorr, flow rate at 5.5 L/min/module, ramp-up rate of 22.5°C/min, and a uniform $P(H_2O)$ of 40 Torr. As shown in Fig. 1.2, 1-cm sectional critical current measurements revealed that ~78 min of conversion was sufficient to fully process the precursor. Based on this information, a 1.5-m-long, 0.3-μm YBCO on Ni-W RABiTS™ was processed using these conversion parameters for 120 min (to guarantee the full conversion of the entire tape). The end-to-end critical current of the sample was determined to be 44.2 A (1.47 MA/cm^2) at a voltage-tab separation distance of 138 cm. A 1-m-long section of the tape was examined under a finer (1-cm) length scale; the examination revealed maximum, minimum, and mean critical currents of 52.7 A (1.76 MA/cm^2), 38.2 A (1.27 MA/cm^2), and 46.1 A (1.54 MA/cm^2), respectively, with a 6.2% SD. In this sample, most of the low local values could be traced directly to blemishes on the buffer surface, which occurred during sample handling and transfer.

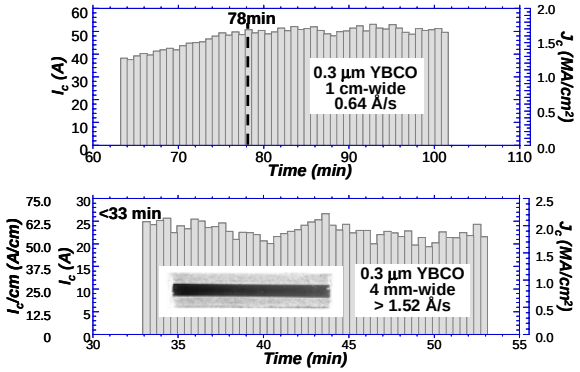

Fig. 1.2. The 1-cm sectional critical current measurements of partially converted 0.3-μm-thick YBCO films of 1 cm wide (upper) and 4 mm wide (lower).

To investigate the percolative behavior of Ni-W RABiTS™, we began by depositing a 0.3-μm precursor on a 1-cm-wide RABiTS™ through a 4-mm-wide mask. The result was a ~1.5-m-long sample with 4-mm-wide precursor film (see Fig. 1.2). Once the sample was obtained, a ~0.5-m-long section was cut and processed in the reel-to-reel system using the partial conversion technique so as to provide information on the necessary conversion time. As previous observations have indicated, BaF_2 conversion in this "atmospheric" chamber is dependent on sample volume, presumably due to HF buildup within the chamber and along the sample surface. As seen in Fig. 1.2, the 4-mm-wide sample had fully attained its maximum critical current density in less than 33 min, which represents at least a 138% increase in the effective conversion rate when compared with its 1-cm-wide counterpart.

Once the minimum processing time was known, the remaining 1 m of 4-mm-wide tape was loaded into the reel-to-reel converter and was processed using the identical conditions as those of the 1-cm-wide sample, except that the conversion time was set at 50 min to ensure the complete conversion of the entire tape. End-to-end critical current density of this tape is found to be 2.12 MA/cm^2, a substantial increase over that of the 1 cm-wide tape. This improvement is believed to be due to the better homogeneity afforded by the narrower tape such that under- and over-conversions were not factors along the sample width. The 1-cm sectional measurements along the entire sample length are shown in Fig. 1.3, which shows that the sample is extremely uniform, with maximum critical current density of 2.33 MA/cm^2, minimum of 1.84 MA/cm^2, and mean of 2.14 MA/cm^2 with a 4.1% SD The extremely uniform critical current density with no drop offs in this long-length sample indicates that the 4-mm-wide current path,

which encompasses more than 100 grains, is well within the percolative threshold as predicted theoretically. Work is under way to study narrower current paths.

1.1.3.4 Pseudo Double-Sided 1.8-μm YBCO on Ni-W RABiTS™

In yet another effort to increase the critical current per centimeter of coated conductors we have begun to study the possibility of a double-sided conductor geometry. Owing to the textured nature of the metallic substrate, RABiTS™ is ideally suited for the double-sided coating approach. The advantage of this conductor geometry is not merely the increase in critical current and the engineering critical current density, but also an increase in time savings in YBCO processing. Given the well-known exponential decrease in critical current density with YBCO thickness [see Fig. 1.4(a)], this improvement will translate to the critical current per centimeter vs thickness shown in Fig. 1.4(b). To obtain the desired value of 150 A/cm will require a YBCO film of 1.5 μm thickness for the single-sided geometry (J_c = 1 MA/cm^2 at this film thickness, marked by diamonds in Fig. 1.4). If we assume a relatively fast linear conversion rate of 2 Å/s, this outcome will require a conversion time of 125 min. However, if we now require a single-sided tape to carry twice the current (i.e., 300 A), the YBCO thickness will have to be increased to 4.1 μm (J_c = 0.73 MA/cm^2 at this film thickness, marked by stars in Fig. 1.4). This increase will require a conversion time of 342 min, nearly tripling the processing time. Therefore, a double-sided tape geometry should be able to take advantage of the higher critical current densities offered by thinner YBCO (per side). The question then is whether the processing time will increase due to the added precursor volume.

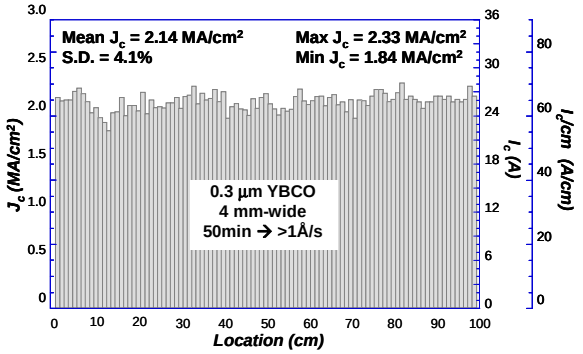

Fig. 1.3. Transport critical current and critical current density of a 1-m-long, 4-mm-wide, and 0.3 μm-thick YBCO on Ni-W RABiTS™. The conductor is highly uniform with no current drop-offs along its entire length.

To explore these issues, we have performed a simple experiment, in which a pseudo double-sided sample was produced. This was accomplished by selecting a 15-cm-long, 0.9-μm-thick precursor on Ni-W RABiTS™. A 5-cm-long section was cut from this tape, flipped, and spot-welded to the underside at the trailing end of the remaining 10-cm-long tape as shown schematically in Fig. 1.5. Thus, a 10-cm-long sample was produced that had a 5-cm single-sided section at the leading end and a 5-cm pseudo double-sided section at the trailing end. The sample was loaded into the reel-to-reel furnace and was processed using the conditions for a 0.9-μm precursor. That is, a conversion temperature of 740°C, P(O_2) of 140 mTorr, flow rate at 5.5 L/min/module, and a ramp-up rate of 22.7°C/min were used. The water vapor partial pressures of individual modules were progressively increased from an initial P(H_2O) of ~5 Torr to a final P(H_2O) of 30 Torr during a wet conversion time of 180 min.

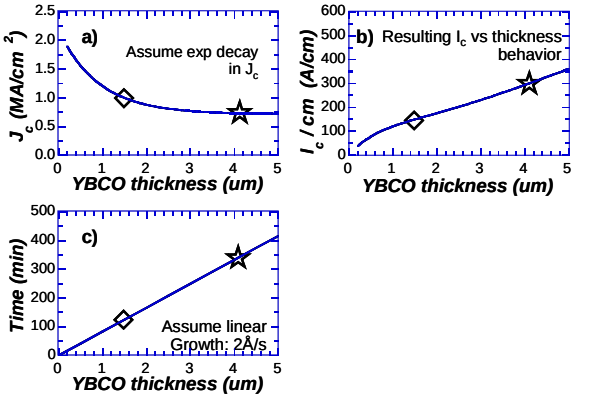

Fig. 1.4. Various characteristics of YBCO film. (a) Critical current density vs thickness, assuming an exponential decrease. (b) Critical current vs thickness based on exponential decrease in critical current density. (c) Conversion time of ex situ YBCO vs thickness, assuming a relatively fast linear conversion rate of 2 Å/s. (*Key:* diamonds: I_c/cm = 150 A; stars: I_c/cm = 300 A.)

The "atmospheric" reel-to-reel furnace was selected for this experiment because it is known to suffer from HF buildup and would be expected to best reveal any problem associated with the increased precursor volume at the double-sided section. XRD analyses of the processed samples showed that the single-sided sample and both sides of the double-sided sample were fully converted (i.e., no BaF_2 signal was detected). In addition, the YBCO intensities were virtually identical for both samples. Transport measurements showed that for the single-sided sample, I_c = 124 A (1.37 MA/cm^2). For the top side of the pseudo double-sided sample, I_c = 117 A (1.30 MA/cm^2), whereas for the bottom side, I_c = 121 A (1.34 MA/cm^2). Therefore, this is effectively a 238-A/cm conductor without the need to increase the YBCO conversion time. Work is currently under way to pursue this highly encouraging result in the form of true double-sided conductors.

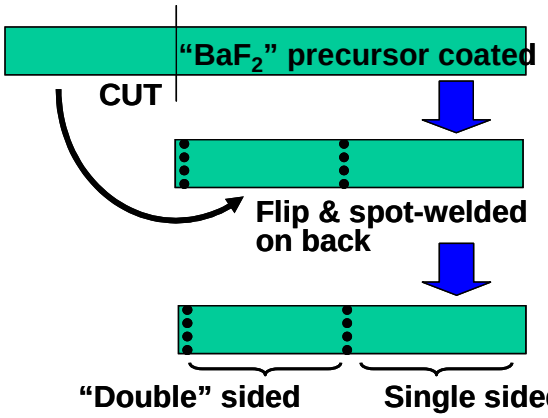

Fig. 1.5. Schematics of the preparation of a pseudo double-sided sample with 0.9-µm-thick YBCO on either side. The leading end of the final sample consisted of a single-sided tape; the trailing end consisted of a pseudo double-sided sample.

1.1.4. Summary

A variety of experiments were performed using the "atmospheric" reel-to-reel furnace available at ORNL. Based on FY 2002 results, further enhancement in performance on 0.9-µm-thick YBCO has been obtained by adjusting the P(H_2O) range. Using this approach, a 45-cm-long by 1-cm-wide film on Ni-W RABiTS™ was produced with an end-to-end critical current of 111.8 A (1.24 MA/cm^2), and 1-cm sectional critical current characteristics with maximum of 123.3 A (1.37 MA/cm^2), a minimum of 102.1 A (1.13 MA/cm^2), a mean of 114.8 A (1.28 MA/cm^2), and a 4.8% SD. Further enhancement in critical current density has also been obtained through improvement in buffer crystallinity and morphology. Initial results for a 10-cm-long, 0.9-µm YBCO on Ni-W provided a critical current of 138 A, which represents a high critical current density of 1.53 MA/cm^2.

For 1.5-µm-thick precursors, very low critical currents were obtained using the processing parameters of the 0.9-µm material. Even when various parameters were adjusted, the current characteristics remained low, with the critical current ranging from 48 to 62 A (0.3 to 0.4 MA/cm^2). One parameter, namely P(O_2), was found to be effective in improving the conversion and current capacity. By adjusting the P(O_2), a critical current of 160.2 A (J_c = 1.07 MA/cm^2) was obtained. Work is under way to further optimize the processing parameters and RABiTS™ quality to obtain higher critical current densities on thicker ex situ YBCO films.

Conductors that are 4 mm wide and up to 1 m long have been fabricated for the experimental study of the percolative threshold of Ni-W RABiTS™. Compared with that of its 0.3-µm, 1-cm-wide counterpart, the conversion rate of the narrower 4 mm-wide precursor was greatly increased, presumably due to a lower level of HF buildup. In addition, the critical current density value of the 4-mm-wide sample is higher. 1-cm sectional measurements along the entire sample length shows that the sample is extremely uniform, with a maximum critical current density of 2.33 MA/cm^2, a minimum of 1.84 MA/cm^2, and a mean of 2.14 MA/cm^2 with a 4.1% SD. The extremely uniform critical current density with no dropoffs in this long-length sample indicate that the 4-mm-wide current path is well within the percolative threshold. Work is under way to study narrower current paths.

Possible advantages of a double-sided conductor geometry have also been explored. A single-sided 0.9-µm YBCO tape and a pseudo double-sided tape with 0.9 µm YBCO per side were processed at the same time. The single-sided sample was found to possess critical current of 124 A (1.37 MA/cm^2). The

top side of the pseudo double-sided sample was found to possess a critical current of 117 A (1.30 MA/cm^2), whereas the critical current of the bottom side was found to be 121 A (1.34 MA/cm^2). Therefore, this is effectively a 238-A/cm conductor that was fabricated without the need to increase the YBCO conversion time. Work is under way to investigate true double-sided conductors.

1.1.5 References

1. S. R. Foltyn et al., *IEEE Tran. Appl. Supercond.* **9**, 1519 (1999).
2. A. Usoskin et al., *IEEE Tran. Appl. Supercond.* **13**, 2452 (2003).
3. Y. Iijima, K. Kakimoto, and T. Saitoh, *IEEE Tran. Appl. Supercond.* **13** 2466 (2003).
4. V. Selvamanickam et al., *IEEE Tran. Appl. Supercond.* **13** 2492 (2003); V. Selmanickam, J. Reeves, and D. E. Peterson, presented at the Superconductivity for Electric Systems 2003 Annual Peer Review July 23–25, 2003, Washington, D.C.
5. M. W. Rupich et al., *IEEE Tran. Appl. Supercond.* **13**, 2458 (2003).
6. D. F. Lee et al., *Supercond. Sci. Technol*. (2003) (to be published).
7. X. Cui et al., *Physica C* **316**, 27 (1999).
8. F. A. List et al., *ORNL Superconducting Technology Program for Electric Power Systems Annual Report*, ORNL/HTSPC 12, 27 (2000) (www.ornl.gov/HTSC/publication.htm).
9. S. W. Lu et al., *Supercond. Sci. Technol.* **14**, 218 (2001).
10 V. F. Solovyov et al., *Appl. Phys. Lett*. **76**, 1911, (2000).
11. D. F. Lee et al., *ORNL Superconducting Technology Program for Electric Power Systems Annual Report* ORNL/HTSPC 12, 30, (2000) (www.ornl.gov/HTSC/publication.htm).
12. V. F. Solovyov, H. J. Wiesmann, and M. Suenaga, *Physica C* **353**, 14 (2001).
13. T. Izumi et al., *IEEE Tran. Appl. Supercond.* **13**, 2500 (2003).
14. D. F. Lee et al., *Next Generation HTS Conductors*, ed. A. Goyal, Plenum Publishing Corp., N.Y. (in press).
15. D. F. Lee et al., *ORNL Superconducting Technology Program for Electric Power Systems Annual Report*, ORNL/HTSPC 14 (2002) (www.ornl.gov/HTSC/publication.htm).
16. U. D. Schoop et al., U.S. Patent No. 6,537,689, 2003.
17. K. Venkataraman et al., *Supercond. Sci. Technol.* (2003) (submitted).

1.2 UNIFORM PERFORMANCE OF CONTINUOUSLY PROCESSED MOD-YBCO COATED CONDUCTORS ON A TEXTURED Ni-W SUBSTRATE

D. T. Verebelyi, U. Schoop, C. Thieme, X. Li, W. Zhang, T. Kodenkandath, A. P. Malozemoff, N. Nguyen, E. Siegal, D. Buczek, J. Lynch, J. Scudiere, and M. Rupich (American Superconductor); A. Goyal, E. D. Specht, P. Martin, and M. Paranthaman (ORNL)

1.2.1 Introduction

HTS films, such as YBCO, can support critical current densities exceeding 1 MA/cm^2 (77 K, self field) on biaxially aligned substrates with an appropriate lattice match [1, 2]. Two methods to provide such templates for the epitaxial growth of the superconductor have dominated research in the field of second-generation HTS wires. The first method uses an untextured metal substrate combined with a technique to induce texture in a buffer layer such as ion-beam-assisted deposition [2] (IBAD) or inclined substrate deposition [3] (ISD). The second method begins with a textured metal substrate that is buffered with an epitaxial film for diffusion resistance and chemical compatibility with the superconductor. The rolling method used to achieve a biaxially textured substrate is called RABiTS^{TM} [1]. Numerous methods are available for epitaxial deposition of the superconductor, including in situ formation of YBCO by pulsed-laser deposition (PLD) [4] and an ex situ reaction of a BaF_2-based precursor deposited either by electron-beam evaporation [5] or web-coating of a metal-organic-based solution [6]. Results using the combination of the yttria stabilized zirconia (YSZ) IBAD and PLD-YBCO have shown previously that

critical currents greater than 100 A/cm-width can be obtained at 75 to 77 K on 1-m-long wires [7]. However, without significant improvements in the slow texture evolution in YSZ-IBAD and the cost of laser deposition, the IBAD-PLD approach remains costly and difficult for large volume manufacturing. High critical current performance has also been shown with a lower-cost approach [8], which combines the RABiTS™ architecture with a solution-derived (metal-organic deposition: MOD) YBCO. To show the potential of this process for commercial production of second-generation coated conductor composite wires, we report on the excellent critical current uniformity possible on wires up to 8 m in length. Results on 10-m lengths have been reported elsewhere [9].

1.2.2 Experimental Details

The coated conductor composite architecture presented in this paper consists of a textured Ni alloy substrate that is buffered with cubic oxide buffer layers and coated with an MOD YBCO superconductor. In this case, Ni is alloyed with 5 atm % W to produce a substrate with increased strength and reduced magnetism [10] compared with the standard Ni substrate widely used for RABiTS™ in the past. At room temperature, the tensile yield strength of the NiW (145 MPa) is four times that of pure Ni (34 MPa).

The NiW alloy was rolled to a thickness of 75 µm and slit to 1 cm wide before it was recrystallized in a reel-to-reel furnace to form the cube-textured template. Epitaxial buffer layers with the structure $Ni/Y2O_3/YSZ/CeO_2$ were also deposited in a reel-to-reel format with continuous processing that is scalable to longer length. The substrate was reel-to-reel coated with a 2-µm Ni layer prior to buffer deposition. Following the deposition of the Ni, a surface sulfurization process enhances the proper [100] nucleation of the yttria seed layer on the metal surface [11]. A 50-nm-thick Y_2O_3 seed layer was deposited on the Ni surface by reel-to-reel electron-beam evaporation. Both the 300-nm-thick YSZ barrier layer and a 30-nm CeO_2 cap layer were subsequently deposited by rf-sputtering.

Fully buffered wires were coated with a single layer of YBCO precursor by a commercial web-coating process with MOD using a trifluoroacetate (TFA)-based precursor [12]. The organic components were decomposed in a humid, oxygen atmosphere up to a temperature of 400ºC, to form a BaF_2-based precursor film with stoichiometric Cu and Y oxide for YBCO. This precursor was continuously converted to the epitaxial superconducting phase in a tube furnace in a humid, low-oxygen partial pressure environment [13, 14].

The resulting film thickness was 1.2 µm measured by SEM cross-section analysis, but Rutherford backscattering spectrum (RBS) data indicate the film contains the mass for a fully dense, stoichiometric 1.0-µm film. Although RBS has an accuracy of only ± 10%, we consider it more reliable than the SEM result because of the rough surface of the YBCO. The typical RMS roughness is 70 nm for a 25 μm^2 surface area of the YBCO. The structure was completed with a 3-µm Ag cap layer deposited by dc sputtering and an oxidation step to provide environmental protection, mechanical and electrical stability, optimum oxygen stoichiometry for YBCO, and a low resistivity contact to the superconductor.

1.2.3. Results

Second-generation HTS wires 7.5 and 8.0 meters in length were produced in a continuous process under nominally the same conditions with the above-described methods and architecture. Figure 1.6 shows I_c at 77 K, self field, for both wires, A (7.5 m) and B (8.0 m), measured at 50-cm intervals using the standard 1-µV/cm criterion. End-to-end I_c performance, also determined at a 1-µV/cm criterion was 132 and 127 A/cm-width for A and B, respectively. The inset in Fig. 1.6 provides I_c

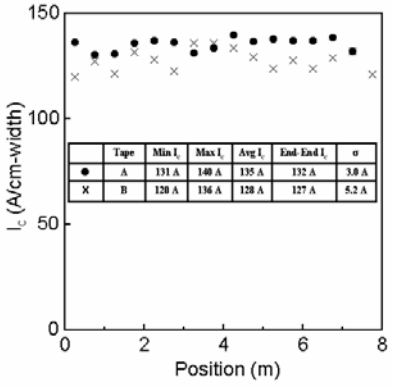

Fig. 1.6 Critical current as a function of length, measured at 50-cm intervals, for the 7.5- and 8.0-m-long YBCO superconducting wires measured at 77 K, self field.

statistical data for both wires. The 3.0 A/cm-width standard deviation (σ) of I_c, measured for wire A, is the highest uniformity yet reported on any second-generation wire of this length [15, 16]. Wire B is a replicate of A with nearly the same I_c and only slightly higher variability. The higher variability translates to a smaller "*n* value," where *n* is the exponent of a power law fit to the end-to-end IV curve near I_c, with wire B giving an exponent of 16, compared to 23 for wire A.

Texture of the substrates, deposited buffer layers and onYBCO is compiled in Table 1.1 as derived from pole figures. The in-plane YBCO texture of the two wires differ by 0.5°, but due to its global nature, pole figure analysis does not reveal the local texture, which is the important metric in determining J_c. To predict the macroscopic J_c explicitly, it would be necessary to map grain boundary misorientations of the entire wire, specify the dependence of the grain boundary J_c on misorientation angle (θ), and calculate the network solution. Statistical approaches to this have been reported that assume a random grain distribution related to a particular in-plane FWHM. Limiting path calculations of long-range current percolation by Specht et al. [17] model a conductor with a FWHM of 6º, with a simple cutoff in the grain boundary J_c above a critical angle θ_c = 5º, which corresponds to experimental results for high J_c films on bicrystal substrates. They find the maximum reduction in macroscopic J_c over 1000 m is only about 10% for a conductor that is at least 100 grains wide. These conclusions are supported in the recent work of Nakamura et al. [18]. In the case of a 0.4-cm-wide commercial size conductor the wire will be about 100 grains wide for a typical Ni-5%W substrate with a grain size of 40 μm. Hence, current modeling based on a random grain distribution predicts no significant reduction in J_c for the RABiTS™-based approach when scaled to commercial width and length.

Table 1.1. In-plane ($\Delta\phi$) and out-of-plane (ΔX) texture of buffer layers derived from pole figures[a]

	Wire A (7.5 m)		Wire B (8.0 m)	
	$\Delta\phi$ (degrees)	ΔX (degrees)	$\Delta\phi$ (degrees)	ΔX (degrees)
Ni-5 atm % W	6.6	6.3	6.8	6.8
YSZ	6.2	5.5	5.8	4.6
Y_2O_3/CeO_2	6.0	6.0	5.5	5.6
YBCO	6.1	4.8	5.6	4.6

[a]Full-width half maximum values are in degrees. The Y_2O_3 and CeO_2 peaks overlap enough to be indistinguishable.

Next we compare the measured dependence of I_c on the voltage tap distance to a simple extension of the statistical calculations of Specht et al. Since the IV response curve is nonlinear for HTS films, a small region anywhere between the voltage taps can be a dominant source of the voltage. This results in a situation in which the variation of I_c on any length of wire will increase with measurements at shorter voltage taps. Here, the full IV-curve of a 1-m length of wire A was measured at 1-cm intervals. Voltage data were then summed together to produce full IV curves at different length scales, for which the I_c was determined. Statistical results, including the maximum, minimum, algebraic average, and standard deviation are presented in Table 1.2, for 1-, 5-, and 10-cm intervals; the 1-μV/cm criterion was used for all data (see Fig. 1.6). Measurements taken at 1-cm intervals over 1 m, give a standard deviation (σ) of 4.4 A/cm-width which translates to a 3σ variation of 13.2 A/cm-width or ±9.2% of the mean I_c. As expected, data for 5- and 10-cm segments show a decreasing σ, 3.6 and 3.1 A/cm-width, respectively.

We compare these results to calculations extending the model of Specht et al. by the variation in I_c expected from percolation at different length scales. As described in the model, a YBCO film with FWHM $\Delta\Phi$ = 6.5° can be modeled by a hexagonal array of grains, in which a random 80% of the grain boundaries are conducting with the simple approximation that grains are either strongly linked and carry the full intragranular J_c or are completely nonconducting (80% corresponds to the expected fraction of strongly linked grains when the grain boundary angle cutoff is 5°). A 1 × 5 cm segment with a 50-μm grain size would consist of an array 200 grains wide and 1000 grains long. In the case of a 250-m wire with 5000 such segments, I_c is found to be 48% of the intragranular value, with σ = 3.6% of the mean.

Now we consider the scaling of σ with wire length. The statistical variation in I_c for *n*-cm segments is simulated by choosing I_c for each 5-cm segment from a Gaussian distribution with the calculated σ = 3.6 %; overall I_c for the longer wire is that of its worst segment assuming an infinitely sharp IV-curve (infinite index value *n*). The procedure was repeated 10^6 times. Figure 1.7 shows the calculated dependence of variation with segment length for the range of 1 to 1000 cm. Also plotted in Fig. 1.7 are the measured data compiled in Table 1.2. The measured data clearly fall below the calculated curve. Interestingly, the results are better than the calculations.

There are multiple possible reasons for this discrepancy. An important assumption in the model is the infinitely sharp IV curve, ignoring the more forgiving voltage criterion with finite index value characteristic of HTS materials. Further refinements are required to the models to include more complete J_c vs angle dependence and the measured grain boundary misorientation distribution from Kikuchi mapping, which could be non-Gaussian, showing short-range texture correlations. A benefit of a refined model would be the ability to look at deviation from expected behavior for use in identifying defects or variations corresponding to a particular length scale, and in turn to reveal valuable process control issues. A more fundamental understanding may be found by plotting the I_c distribution over shorter length segments to study the possibility of clustering coming from a non-Gaussian grain boundary distribution.

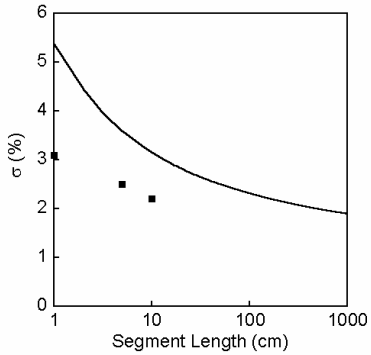

Fig. 1.7. Solid line shows percent standard deviation vs segment length, calculated assuming a random distribution of grain boundary misorientations for a wire 1 cm wide with 50-μm grains. Standard deviations determined from different measurement segment lengths from one meter of measurements taken on wire A are plotted for comparison. *Source:* E. D. Specht et al., *Physica C* **382**, 342 (2002).

Table 1.2. Comparison of critical current data for different segment lengths of wire A from position 4.8 to 5.8 m[a]

	Wire segment (cm)		
	1	**5**	**10**
Minimum I_c (A)	130	135	135
Maximum I_c (A)	155	148	146
Average I_c (A)	144	143	143
Std deviation (A)	4.4	3.6	3.1
Std deviation (%)	3.1	2.5	2.2

[a]The standard criterion of 1 μV/cm was used.

1.2.4. Conclusion

In this work, second-generation coated conductors fabricated with a low-cost RABiTS™ approach, in conjunction with a solution-based MOD YBCO process, produced very uniform, high-performance wires up to 8.0 m long. This work extends the processing length while maintaining the uniformity seen previously on 1-m wires. These results and statistical calculations indicate that the present processing methodology can be extended to commercial 1-km lengths with adequate uniformity and without significant loss of overall I_c.

1.2.5 References

1. A. Goyal et al., *J. Mater. Res.* **12,** 2924 (1997).
2. X. D. Wu et al., *Appl. Phys. Lett.* **67**, 2397 (1995).
3. K. Hasegawa et al., p. 745 in *Proc. 9th Int. Sym. on Super, Nakijama S Japan*, North-Holland (1996).
4. D. Norton et al., *Science* **274**, 755 (1996).
5. R. Feenstra et al., *J. Appl. Phys.* **69**, 6569 (1991).
6. A. P. Malozemoff et al., *Supercond. Sci. Technol.* **13**, 473 (2000).

7. S. R. Foltyn et al., *Physica C* **341–48**, 2305 (2000).
8. M. W. Rupich et al., *Appl. Super. Conf. Proc.* (2002) (accepted for publication).
9. L. Masur et al., *ISS2002 Conference Proceedings*, Yokohama, Japan, Nov. 11–14, 2002 (submitted).
10. B. deBoer et al., *Acta Materialia* **49,** 1035 (2001).
11. C. Cantoni et al., *Appl. Phys. Lett.* **79**, 3077 (2001).
12. P. C. McIntyre, M. J. Cima, and A. J. Roshko, *J. Appl. Phys.* **77,** 5263 (1995).
13. R. Teranishi et al., *Physica C* **378-81,** 1033 (2002).
14. T. Kato et al., *Physica C* **378-81,** 1028 (2002).
15. E. D. Specht et al., *Physica C* **382,** 342 (2002).
16. P. Arendt, *Next Generation HTS Wires*, ed. A. Goyal (2003) (to be published by Plenum Publishing Corporation).
17. E. D. Specht, A. Goyal, and D. M. Kroeger, *Super. Sci. Tech.* **13**, 592 (2000).
18. Y. Nakamura, T. Izumi, and Y. Shiohara, *Physica C* **371**, 275 (2000).

1.3. MICROSTRUCTURAL CHARACTERIZATION OF THICK $YBa_2Cu_3O_{7-\delta}$ FILMS ON IMPROVED ROLLING-ASSISTED BIAXIALLY TEXTURED SUBSTRATES

K. J. Leonard, S. Kang, A. Goyal, K. A. Yarborough, and D. M. Kroeger (ORNL)

1.3.1 Introduction

The deposition of $YBa_2Cu_3O_{7-\delta}$ (YBCO) films greater than 1 micron in thickness for achieving high critical current (I_c) while maintaining adequate critical current densities (J_c)[5] has been an elusive goal in producing commercially viable superconducting films. This is due in part to the difficulties in depositing and growing high-quality *c*-axis-oriented microstructures whose properties do not degrade with increasing film thickness. Typical problems in producing thick YBCO films can include the development of misoriented YBCO grains or porosity [1–5], formation of nonsuperconducting phases [6–9], oxygen deficiencies [10], and changes in stoichiometry [11]. In addition, due to the mismatch between the YBCO and substrate used, the development of strain within the film can produce different microstructural defects for a given choice of substrate [12]. While investigation of YBCO films through X-ray diffraction (XRD) techniques allows for a broad nondestructive overview of the materials' structural properties, XRD lacks the ability to provide information about the changes in microstructure with film depth and smaller-scale reactions that can have an effect on the film properties. In this investigation, transmission electron microscopy (TEM) was used to examine the microstructural changes associated with the reduced dependence of J_c with film thickness for pulsed laser deposition (PLD) YBCO films on RABiTS™ having a Ni-3%W/Y_2O_3/YSZ/CeO_2/YBCO architecture.

YBCO deposition on RABiTS™ has been well established [13, 14]. RABiTS™ consists of layers of metal oxide buffers epitaxially deposited with either a cube-on-cube or rotated cube-on-cube orientation on the {100}<100> textured Ni or Ni-alloy substrates. These ceramic buffer layers act as a barrier for Ni diffusion from the base metal substrate into the YBCO layer while providing a template of reduced lattice mismatch between YBCO and Ni for epitaxial growth. Although different deposition methods exist for the epitaxial growth of YBCO on substrates, all have significant barriers in developing thick YBCO films. In this investigation, YBCO layers of varying thicknesses deposited by PLD on RABiTS™ were examined.

The use of Ni-3at.%W (Ni-W), as the roll-textured substrate has been a recent improvement in the development of RABiTS™ materials [15]. These substrates possess a sharper texture over earlier pure Ni tapes, with in-plane and out-of-plane textures of $\Delta\phi = 7^o$ and $\Delta\omega = 5–6^o$ as compared with $\Delta\phi = 9–10^o$ and $\Delta\omega = 7–8^o$ of the Ni substrates used in a previous thickness dependence study of J_c vs thickness [9]. The tighter texture of the Ni-W substrates translating to fewer mismatched boundaries within the YBCO and thus a decrease in the number of barriers for superconductive current flow. The use of a seed layer composed of Y_2O_3 instead of CeO_2 as in earlier RABiTS™ is the result of another upgrade of the

substrates. Recent questions have arisen as to the stability of the CeO_2 seed layer during the subsequent processing of the other layers within the coated conductor stack. Cracking of the seed layer due to volumetric changes between the CeO_2 and Ce_2O_3 forms can result in the formation and uncontrolled growth of NiO into the upper layers of the stack. On the other hand, Y_2O_3 does not seem to crack as easily as CeO_2, even in relatively thick layers. The microstructures developed from using these new RABiTS™ substrates based on Ni-W and an Y_2O_3 seed layers will be shown as capable of producing *c*-axis-oriented films with minimal misorientations and reactions at the YBCO buffer interface.

1.3.2 Experimental

The initial fabrication of the powder formed metal substrates is described in detail elsewhere [15]. The {100} <100> biaxial texture of the Ni-W tape was developed through repeated cold rolling of a starting coil to a 50-μm thickness, followed by annealing in vacuum at 1300ºC for one hour. As shown previously [15], this was sufficient to form a fully developed c(2×2) superstructure on the surface of the tape. A 150-nm Y_2O_3 seed layer was deposited by electron beam evaporation of yttrium metal under 1×10^{-5} torr water vapor, with a 650ºC substrate temperature. Subsequent layers of 150-nm-thick YSZ oxide and 20-nm-thick CeO_2 were deposited by rf magnetron sputtering.

YBCO films ranging in thicknesses from 1.0 to 6.4 μm were deposited by PLD using a XeCl excimer laser (λ = 308 nm) on 2.5×0.5 cm samples. Substrates were secured with Ag paste to a heater placed a distance of 10 cm from the rotating YBCO target. During deposition the heater temperature was 790ºC and oxygen partial pressure in the chamber was 120 mTorr. Laser energy density was 4 J/cm^2 with a film growth rate between 5 and 13 Å/s. Following deposition, the films were cooled to room temperature at a rate of 5ºC/min, under an oxygen partial pressure of 550 Torr. Thicknesses of the films were verified using cross-sectional SEM and TEM examinations.

An additional 1.0-μm-thick Ag layer was deposited by rf magnetron sputtering on top of the YBCO film prior to preparing cross-sectional samples for TEM. The Ag layer is essential to preserve the integrity of the YBCO layer from damage incurred through sample preparation. An annealing treatment in O_2 was required in order to adhere the Ag layer to the sample: 10ºC/min ramp to 500ºC, 1-h hold, 5ºC/min cool to 350ºC, then furnace cooled. The samples were cleaned, cut in two, and glued silver-sides-together with M-bond 610. Additional pieces of YSZ single crystals were glued onto the sides of the sample stack in order to thicken the cross section for support. The sample stack was cured at 115ºC for 1-h while held under pressure in Teflon-jawed vise at 2 lb-in of torque to ensure a uniformly thin glue line. Samples were then cut with a diamond-wafering blade into approximately 1.0×1.0 mm square samples of 0.5 mm thickness.

The samples were set within the centers of 3-mm-diam graphite rings. A drop of two-part epoxy, Gatan 601-07-001, was placed onto the sample rings and was allowed to sit overnight. Final hardening of the epoxy was done the following day through heating the samples to 115ºC for 1 h. Overhanging epoxy could be removed by careful trimming of the samples with a flat razor. The 3-mm-diam samples were mechanically ground to a 90-μm thickness and 3-μm surface polish prior to milling in a Gatan Model 691 precision ion polisher. Milling was done using a 5-keV beam at an angle of incidence of 8º, with the dual guns impinging from both top and bottom of the sample at a direction perpendicular to the glue line and sample stacking sequence. Beam energies and angles of incidence were reduced in the later stages of sample polishing to prevent ion damage within the YBCO layer. At no time were the samples exposed to water.

The cross-sectioned samples were investigated using Philips Tecnai 20 (LaB_6, 200 kV) and CM200 (FEG, 200 kV) TEMs, equipped with energy-dispersive spectrometry (EDS) units. The CM200 microscope was used in both conventional and high-resolution scanning modes.

1.3.3 Results and Discussion

1.3.3.1 Properties of the thick YBCO films

The *J*c's of the thick YBCO films along with the film textures determined through XRD from previous work [16] are listed in Table 1.3. The values of J_c were calculated from the four-point probe measurements of I_c conducted at 77 K in self-field without micro-bridge patterning. Limitations in characterizing the I_c to 120 A prevented the full determination of I_c in films thicker than 1.0 μm under self-field. For these films a zero-field J_c was calculated from in-field measurements at 0.5 Tesla, assuming that a factor of 4 to 5 drop in J_c occurs from self-field to that of 0.5 Tesla [16]. Therefore, ranges of calculated values presented for the 2.9- and 4.3-μm-thick films. No J_c is presented for the 6.4-μm-thick film because a crack was generated across the sample upon reaching 60 A, which is believed to have been the result of sample heating. From Table 1.3 it can be seen that only a modest drop in J_c occurs with increasing YBCO thickness.

Table 1.3. Measured electrical and texture properties of thick YBCO films examined for electron microscopy[a]

Sample I.D.	YBCO thickness (μm)	J_c (MA/cm^2)	$\Delta\phi$ [b]	$\Delta\omega$ [c]	*a*-axis fraction (I_a/I_c)	Cube (%)
SK78	1.0	1.18	0.90	0.79	0.0	92.5
SK87	2.9	0.9–1.1	1.03	0.78	0.1	93.5
SK99	4.3	0.65–0.81	1.09	0.89	0.2	87.9
SK101	6.4		0.96	0.91	0.1	95.8

[a] *Source:* S. Kang et al., *Appl. Phys. Lett.*, in review (2002).
[b] Ratio of YBCO(113)/Ni-W(111).
[c] Ratio of YBCO(005)/Ni-W(200).

Despite difficulties in characterizing the electrical properties, the exceptional quality in texture of these films supports the high J_c values. The change of in-plane texture, $\Delta\phi$, taken as the ratio of the full-width-half-maximums of the X-ray intensities of the YBCO (113) peak vs that of the (111) Ni-W, was near 1.0 for all the samples, indicating that little change in the in-plane texture occurs from the Ni-W substrate through to the YBCO, even as film thickness increases. A slight increase in the out-of-plane texture, $\Delta\omega$, was observed as the YBCO film thickness is increased. Measured as the ratio of full-width-half-maximum of the YBCO (005) and Ni-W (200) rocking curves, a broadening of $\Delta\omega$ suggests increased dispersion of *c*-axis orientation within the YBCO grain columns, possibly increasing gradually from the bottom to the top of the YBCO film.

The fraction of *a*-axis-oriented (a⊥) to *c*-axis-oriented (c⊥) grains within the YBCO films, calculated from the ratio of $I_a\perp(200)/I$c⊥(002) X-ray intensities determined from θ–2θ scans, also shows an increase with film thickness. In comparison, the *a*-axis fraction for this RABiTS™ architecture is significantly higher than that for YBCO films grown on Ni/CeO_2/YSZ/CeO_2 substrates deposited under the same PLD conditions [17]. Although a larger a⊥ concentration was observed in these samples being investigated, the amount is substantially less than that occurring in YBCO films deposited on single crystal substrates [17].

While the *a*-axis fraction of these samples showed a higher value than that of previously investigated RABiTS™ materials with the Ni/CeO_2/YSZ/CeO_2 architecture [17], the percent cube texture was significantly better despite the random variation in results measured for the films being investigated. The Ni/CeO_2/YSZ/CeO_2 substrates had shown a drop in cube texture from 98.8 to 79.9% for YBCO films increasing in thickness from 0.19 to 3.0 μm. Random grain orientations began to form at a YBCO thickness of 0.45 μm and progressively dominated the upper portion of the thicker films [9]. By comparison, the samples with the new Ni-W/Y_2O_3/YSZ/CeO_2 RABiTS™ architecture still retain over ninety percent cube texture for the 2.9-μm-thick YBCO film.

The microstructures of YBCO films of increasing thickness deposited on improved RABiTS™ substrates of Ni-W/Y_2O_3/YSZ/CeO_2 architecture are presented in the following sections.

1.3.3.2 The 1.0-μm-thick YBCO film

A composite image of the thinned cross-sectional area of the 1.0-μm-thick sample is shown in Fig. 1.8(a). The YBCO layer, when viewed along the g=001 vector tilted away from the [100] zone axis, shows the $c_{\perp}$ grain columns outlined by the anti-phase boundaries separating them. These boundaries are produced from mismatch in crystallographic stacking across the interface, resulting either from changes in the initial sequence of YBCO nucleation occurring at the buffer interface [18] or through the presence of steps along the surface of the buffer. These $c_{\perp}$ grain columns extended from the buffer layer interface to the top surface of the YBCO film. Throughout the viewable cross section, neither random nor $a_{\perp}$-oriented grains were observed. The grains along the top of the YBCO film are from the protective Ag layer.

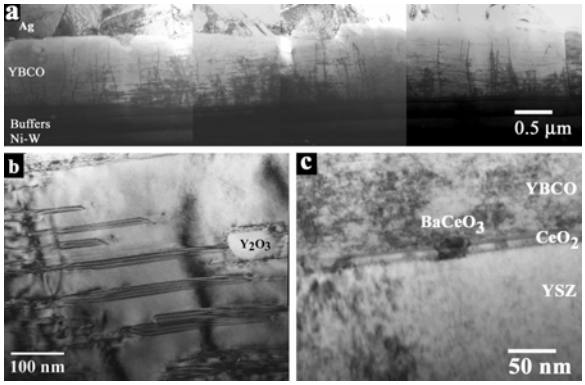

Fig. 1.8. (a) Composite bright field image of the 1.0-μm-thick YBCO film, with higher magnification images of (b) stacking faults and a Y_2O_3 particle within the film and (c) a $BaCeO_3$ particle at YBCO/CeO_2 interface.

In addition to the anti-phase boundaries separating the $c_{\perp}$ grain columns, contrast from stacking faults is visible within the cross section. These faults extended from the anti-phase boundaries into the $c_{\perp}$ grains. A closer view of the faults is shown in Figure 1.8(b), along with a particle of Y_2O_3. The Y_2O_3 particle held a Y_2O_3[110]//YBCO[010], Y_2O_3(110)//YBCO(100) orientation relationship to the $c_{\perp}$ grain, consistent with orientations previously reported by Verbist et al. [19] and Catana et al. [20] as Type A particles. The Y_2O_3 particle was located at roughly the center of the film and was not associated with any defects extending up from the buffer layers. Smaller Y_2O_3 particles noted as Type B, which have the Y_2O_3(110)//YBCO(001) relationship and generally appear near the top of the YBCO film surface [19–21], were not observed in this study. In earlier work on thick YBCO films on RABiTS™ [9], the stacking faults were shown to contain excess Cu-O and were identified to be Y248 intercalates based on the expanded *c*-axis lattice constant to 13.3 Å.

Along the YBCO/CeO_2 interface, particles of $BaCeO_3$ were observed [Fig. 1.8(c)], a by-product of the reaction between the two layers. Typically, these particles were 30 to 40 nm in size and were dispersed randomly along the interface. The reaction yielding theses particles can be written as follows:

$$2YBa_2Cu_3O_7 + 4CeO_2 \rightarrow 4BaCeO_3 + 2YCuO_2 + 4CuO + O_2 \quad (1)$$

The excess Y and Cu released have been shown to diffuse upward through the anti-phase boundaries and intercalate as single layers of Y and Cu oxide within the $c_{\perp}$ grain columns, producing the stacking faults observed within the film [8].

1.3.3.3 YBCO films thicker than 1.0 μm

The YBCO films greater than 1.0 μm in thickness were found to be similar to one another. For comparison they are shown together in Fig. 1.9. All of the thicker films showed *c*-axis-oriented grains that have grown the full thickness of the film. No dead layers consisting of misoriented grains were observed in any of the samples examined. However, some *a*-axis grains were observed. The most remarkable of the microstructures was found in the thickest YBCO film, in which the *c*-axis columns can be clearly seen as growing the full 6.4 μm thickness [Fig. 1.9(c)]. From the bright-field images of the thick samples, the anti-phase boundaries separating the $c_{\perp}$ columns are visible along with contrast from other defect structures. The mismatch across the anti-phase boundaries was found to be negligible through electron microdiffraction, with changes across the boundary comprising a displacement in the atomic planes of a fraction of the *c*-axis unit cell dimension. Numerous anti-phase boundaries originate and terminate within

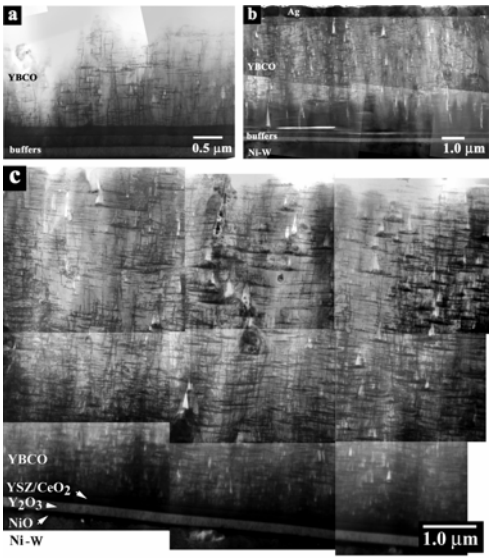

Fig. 1.9. Composite cross-section images of (a) the 2.9-, (b) 4.3-, and (c) 6.4-μm-thick YBCO films showing *c*-axis-oriented growth throughout the full thickness. The dark thick band above the buffers in (a) is an effect of shadowing during ion-milling, producing a thickened YBCO layer. The white horizontal line in the YBCO near the buffer layers in (b) is a crack produced during sample preparation.

the buildup of strain within the growing YBCO film. A state of strain still exists between YBCO and CeO_2, as it has been shown that an extended period of aging at deposition temperature can produce the formation of subgrains with mismatches of up to 8º within films that are devoid of subgrains in the as-deposited condition [9].

The thicker YBCO samples also showed porosity within the film, which had not been observed in the 1.0-μm-thick film. Figure 1.10(a) shows a higher magnification image of the 2.9-μm-thick YBCO film, from which the porosity is seen as being somewhat tubular or elongated. The triangular shape of the porosity imaged within the 4.3- and 6.40-μm-thick films [Figs. 1.9(b) and (c), respectively] is the result of the cross sections having been cut at an angle relative to the normal of the film, or specifically cut at an angle to the [001] direction of the YBCO. The porosity is observed at all depths in the YBCO layer and does not appear to be either interconnected or long enough to reach the free surface of the YBCO film. Analysis by EDS of these features showed no sign of Ag diffusion down into these voids from the protective overlayer.

the thickness of the YBCO layers, unlike in thinner YBCO films that have been examined, in which the boundaries typically run the full thickness of the layer [9].

Interestingly, the development of subgrains within the YBCO films was missing within all of the samples examined. Subgrains, between 0.2 to 1.2 μm in size with a boundary mismatch of up to 5º have been previously reported in PLD-deposited YBCO on $Ni/CeO_2/YSZ$ substrates [22]. While the PLD conditions used were similar to those in this study, the lack of a CeO_2 cap layer between the YBCO and YSZ films completing the fully buffered RABiTS™ structure is believed to have been the likely cause for subgrain growth. Despite no correlation in size between the YBCO subgrains and underlying grains of YSZ, the larger lattice mismatch between YBCO and YSZ (5.03%) than that of CeO_2 (0.12%) would produce a higher state of strain at the interface, thus favoring the introduction of subgrains within the YBCO to alleviate

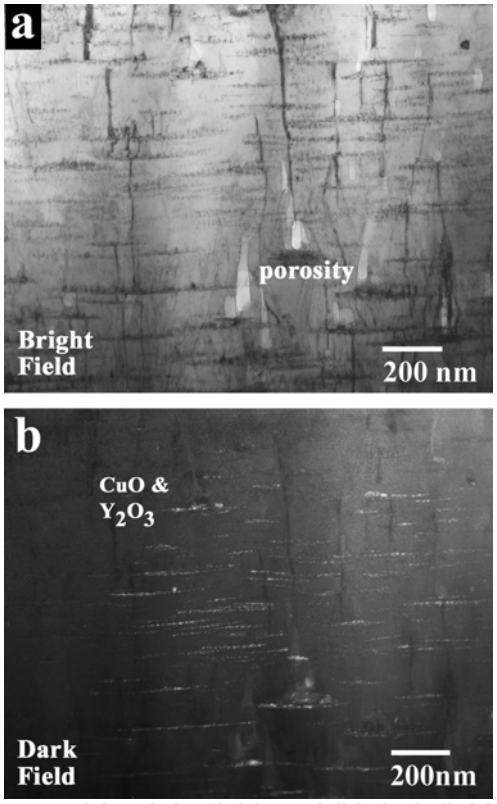

Fig. 1.10. (a) Bright-field, and (b) dark-field images of the 2.9-μm-thick YBCO film showing porosity and the formation of CuO and Y_2O_3 particles along former stacking faults within the film. Note the start and termination of anti-phase boundaries throughout the film.

Further revealed in higher magnification images was the presence of secondary phase particles within the YBCO layer. These particles can be seen in the dark-field image accompanying the bright field image of Fig. 1.10 and were identified as CuO and Y_2O_3 through electron diffraction as shown in Figs. 1.11(a) and 1.11(c), respectively. The monoclinic CuO particles were indexed as having a CuO[010]//YBCO[100] orientation relationship and were typically much larger in size than the Y_2O_3 particles [Fig. 1.11(b)]. The CuO particles also tended to grow as long continuous particles or groupings of particles. The Y_2O_3 particles that held the Y_2O_3[110]//YBCO[100] relationship were smaller and discontinuous in the film [Fig. 1.11(d)] and typically formed separate from other Y_2O_3 or CuO particles. As shown in Figs. 1.9 and 1.10, the CuO and Y_2O_3 particles formed along (001) planes within the YBCO film and grew in the [100] and [010] YBCO directions. This is thought to be the result of the coalescence of excess Y and Cu oxide along the former stacking faults. Fault structures were no longer observed around the CuO and Y_2O_3 particles. The formation of CuO and Y_2O_3 from the intercalated layers of the stacking faults may have resulted in the volumetric changes resulting in the development of porosity in films thicker than 1.0 μm. Both particles and porosity were observed at all depths within the films. Further work is required in understanding this relationship. In addition, it is also uncertain whether the elimination of the stacking faults within the films caused a removal of portions of the anti-phase boundaries, as they were found to both terminate and initiate throughout the film.

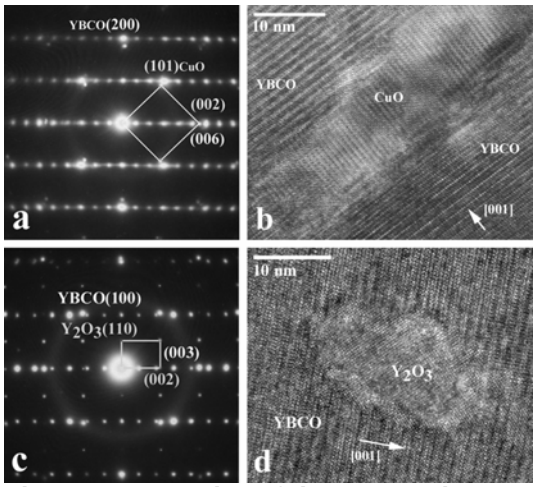

Fig. 1.11. Examples of the CuO and Y_2O_3 particles within the YBCO films thicker than 1.0 μm. (a) Selected area diffraction pattern of the CuO[010]//YBCO[010] orientation relationship, with (b) the corresponding high-resolution image of CuO within the YBCO film. (c) The Y_2O_3[110]// YBCO[010] relationship with (d) a Y_2O_3 particle imaged within the YBCO film. Both CuO and Y_2O_3 particles developed on former stacking fault structures.

The contrast that is produced from the CuO and Y_2O_3 particles shown in Fig. 1.9 can be used to illustrate the slight variation in orientation of the $c_\perp$ grains that occurs in the YBCO film near the upper surface. The observed waviness is the result of small variations in orientation of the (001) planes of the YBCO film, which produced the change of $\Delta\omega$ measured through XRD.

Reactions at the YBCO/CeO_2 interface were also observed to progress with the increasing time of deposition. While nearly tripling the deposition time, the 2.9-μm-thick film still showed only $BaCeO_3$ particles at the interface similar to that of the 1.0-μm-thick film [Fig. 1.12(a)]. Although the particles remained widely scattered, a modest increase in size did occur. Not until the film thickness was increased to 6.4 μm was the presence of Y_2BaCuO_5 (Y211) at the interface observed in addition to $BaCeO_3$ [Fig. 1.12 (b)]. However, in the 6.4-μm film, the CeO_2 is still intact in most places.

The formation of Y211 has been previously reported [9, 21] and is related to the excess Y released from the formation of $BaCeO_3$. As reported by Scotti di Uccio and coworkers [23], for a 50% excess in Y within YBCO, its decomposition can be written as two competing reactions:

$$(1.5Y + 2Ba + 3Cu + xO) \rightarrow YBa_2Cu_3O_7 + 1/4Y_2O_3 \quad (2)$$

$$(1.5Y + 2Ba + 3Cu + xO) \rightarrow 5/6YBa_2Cu_3O_7 + 1/3Y_2BaCuO_5 + 1/6CuO \quad (3)$$

Based on these equations, a greater amount of the Y211 phase over Y_2O_3 is expected, despite the fact that many studies characterizing YBCO films have typically reported Y_2O_3 particle formations near the interface [19–21].

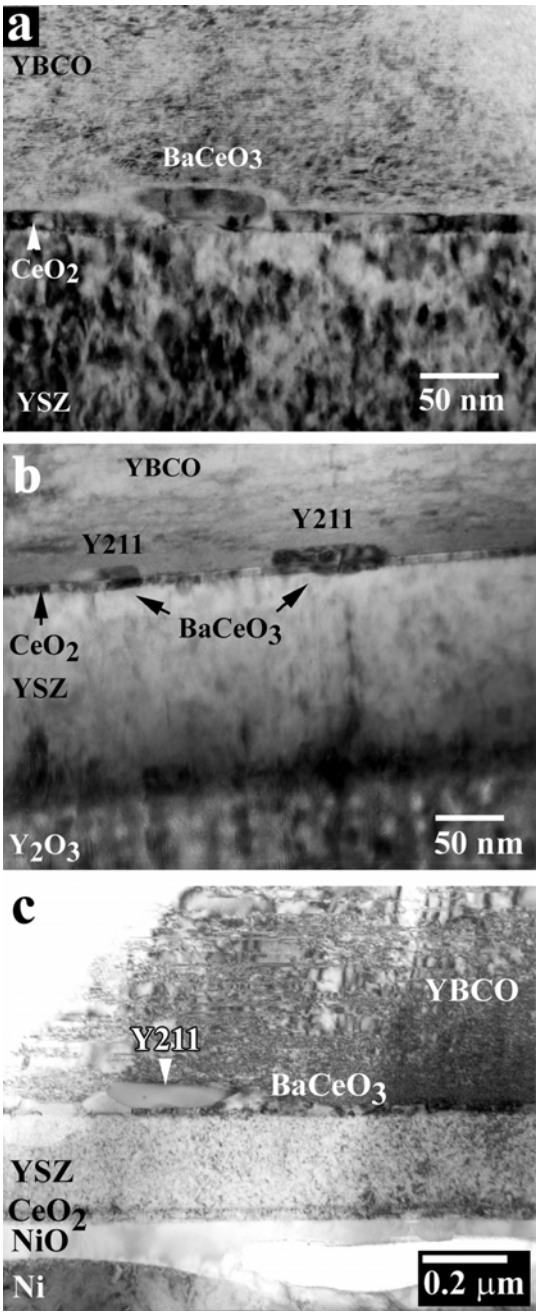

Fig. 1.12. Images of the reaction phases produced at the YBCO/CeO_2 interface producing (a) $BaCeO_3$ particles within the 2.9-μm-thick YBCO film and (b) $BaCeO_3$ and Y211 phases within the 6.4-μm-thick film. (c) Image of the highly reacted interface within a 3.0-μm-thick YBCO film deposited on RABiTS™ with substrate architecture of Ni/CeO_2/YSZ/CeO_2 under the same PLD conditions as in (a) and (b).

The reason for this is the higher nucleation energy of Y211 than Y_2O_3 [23], even though Y211 is more thermodynamically stable than Y_2O_3 under conditions experienced during YBCO deposition [24]. While the formation of $BaCeO_3$ and Y211 have been observed in YBCO films deposited on Ni/CeO_2/YSZ/CeO_2 type substrates [9], the amount of these phases within the thick films deposited on the Ni-W substrates using a Y_2O_3 seed layer is significantly less. As Fig. 1.12(c) shows, the formation of $BaCeO_3$ at the interface of a 3.0-μm-thick YBCO film deposited on the old RABiTS™ substrate is extensive and has completely consumed the CeO_2 cap layer, producing a reaction layer that has removed approximately 0.1 μm in thickness of YBCO from contributing to the superconducting property of the film. In contrast, the 6.4-μm-thick YBCO film on the new RABiTS™ structure deposited under the same PLD conditions showed much less interface reaction than that of the 3.0-μm-thick film on the old substrates, even though the sample had seen twice the deposition time at elevated temperatures.

The reaction between Ni-W and oxygen from the buffer layers has produced NiO growing into the Ni-W substrate, as shown in the bright-field image of the 1.0-μm-thick YBCO in Fig. 1.13(a). Electron diffraction analysis of the NiO layer reveals it to be nonepitaxial relative to the buffer layers. While the NiO {111} reflections are observed when viewed along the Ni-W[010]//Y_2O_3[110] zone axis [Fig. 1.13(d)], the grains are rotated off-zone relative to the substrate and buffer layers. On closer inspection of the NiO layer, the presence of an additional phase was found at the interface between the growing NiO layer and the Ni-W substrate. Reflections from this phase were identified within the electron diffraction patterns taken at the interface in Fig. 1.13(d) with intensities appearing at a d-spacing of 4.59 ± 0.03Å, which is slightly smaller than that of the Y_2O_3 (002) plane. Dark-field imaging using this reflection [Fig. 1.13(b)] shows a discontinuous layer within the 1.0-μm-thick YBCO sample, with complete or continuous layers forming in the thicker films.

An EDS line scan across the boundary between the Y_2O_3 buffer and Ni-W substrate [Figure 1.14(a)], using an electron probe of approximately 1.5 nm in diameter, determined that the interface layer consists of the Ni, W, and O species. The line scan, displayed for the 1.0-

μm-thick YBCO sample, shows the NiO layer as being approximately 20 to 25 nm thick and having an 8-nm nickel-tungsten oxide layer. Similar to NiO, the nickel-tungsten oxide layer was oriented off-axis when viewed down the Ni-W[010]//Y_2O_3[110] zone axis [Fig. 1.14(b)]. Tilting the sample along the <111> NiO direction away from the Ni-W [010] zone axis, the NiO [110] zone was reached. Examination of the electron diffraction pattern from the selected area of the NiO layer revealed the $NiWO_4$ [010] pattern [Fig. 7(c)]. The $NiWO_4$ intensities observed within Fig. 1.13(d) and common to the $NiWO_4$ [010] pattern were the $NiWO_4$ {100}. The $NiWO_4$ [100] direction is therefore normal to the tape or parallel to the out-of-plane normal of the Ni-W substrate. It is possible that multiple orientations of the $NiWO_4$ phase exist in the reaction layer based on the fixed [100] direction. As seen in the high-resolution image in Fig. 1.14(b), both an off-axis orientation image and an on-axis $NiWO_4$ [001] lattice image are observed relative to the Ni-W[010] condition at which the overall image was taken.

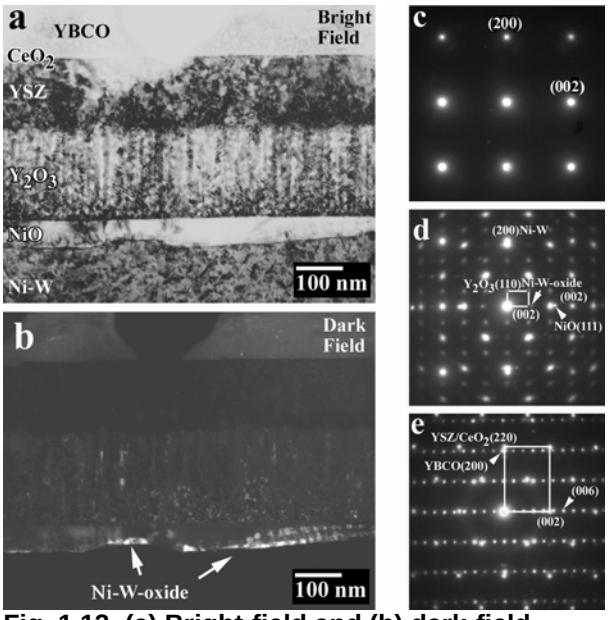

Fig. 1.13. (a) Bright-field and (b) dark-field images of the buffer layer structure within the 1.0-μm-thick YBCO film, showing the presence of a Ni-W-O phase between Ni-W and NiO. Diffraction patterns showing the epitaxial stacking of YBCO and buffer layers on top of the Ni-W substrate. (c) The Ni-W[010] pattern of the biaxially cube textured substrate. (d) The rotated cube-on-cube orientation of the Y_2O_3 layer-, showing the Y_2O_3[110] //Ni[010] relationship. NiO(111) and Ni-W-oxide reflections are identified. (e) The YSZ[110]// CeO_2[110] // YBCO[010] orientation.

Although the formation of NiO is not unique, having been observed in different RABiTS™ materials using Ni substrates, the apparent effect of the $NiWO_4$ layer on NiO growth was not previously observed. In examining the thickness of the NiO layer within the four samples of increasing YBCO thickness, no significant change in thickness of the NiO layer was measured. Bright-field and dark-field images along with a high-magnification image of the NiO/Ni-W interface for the 6.4-μm-thick sample is shown in Fig. 1.15 for comparison with the images taken of the 1.0-μm-thick YBCO film of Figs. 1.13 and 1.14. For all the samples, the NiO layer was approximately 20 to 25 nm in thickness with a 5- to 8-nm-thick $NiWO_4$ layer, despite the thickest of the YBCO samples having been at the deposition temperature for over six times as long as that of the thinnest. By comparison, for YBCO deposition on Ni-substrate RABiTS™ under the same PLD conditions, the thickness of the NiO layer was found to increase from 10 nm to over 150 nm in samples for YBCO layers of 0.2 and 3.0 μm, respectively [9] [see Fig. 1.12(c)]. Therefore, once continuously formed along the NiO/substrate interface, the barrier that $NiWO_4$ forms may prevent catastrophic damage to the upper layers of the conductor stack by the diffusion of Ni.

1.3.4 Conclusions

In conclusion, thick YBCO films have been successfully prepared on RABiTS™ substrates the samples demonstrated exceptional electrical properties, which were reflected within the examined cross-section microstructures. While the critical currents measured for these materials were high, they did demonstrate a slight decrease in J_c with increasing film thickness. Unlike those in previous studies, the YBCO films showed no apparent dead zone of material composed of misoriented grains and porosity. Very little grain misorientation was observed in the film and was limited to *a*-axis-oriented grains. In general, the films were observed to be very uniform with *c*-axis grain columns extending the full length of the film thickness.

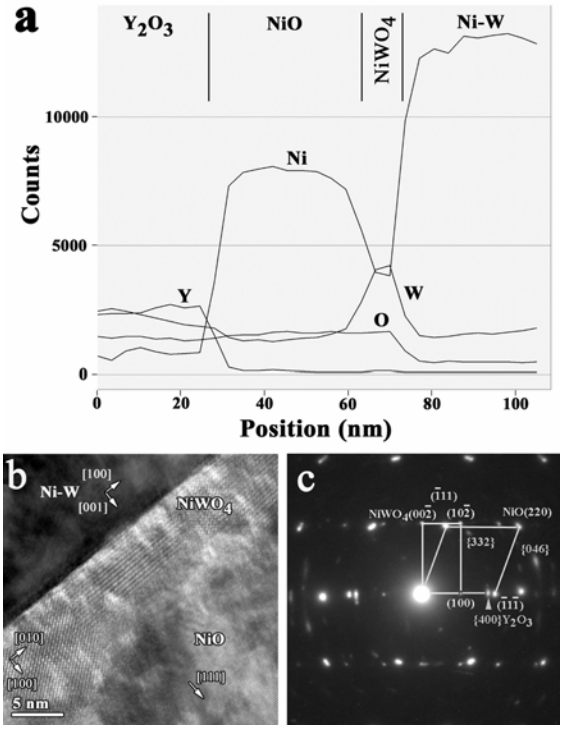

Fig. 1.14. High-resolution EDS line scan across the Y_2O_3/Ni-O interface within the 1.0-μm-thick film, revealing the presence of a 37-nm-thick NiO and 8-nm-thick $NiWO_4$ layers. (b) High-resolution image of the $NiWO_4$ layer between Ni-W and NiO. (c) Selected area diffraction pattern of the NiO[110] pattern with the $NiWO_4$[010] pattern revealed.

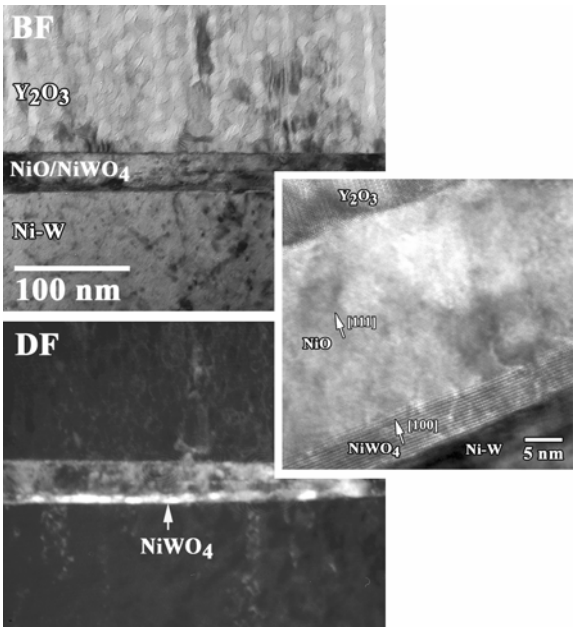

Fig. 1.15. Bright-field, dark-field, and high-resolution images of the NiO reaction layer containing the $NiWO_4$ phase within the 6.4-μm-thick YBCO sample.

As a result of the extended times for deposition, the formation of small particles of CuO and Y_2O_3 along the stacking fault structures was observed in films greater than 1.0 μm in thickness. The formation of these phases and the resulting volumetric changes produced a uniform distribution of pores through the microstructure. The pores were found elongated to the normal of the film but remained unconnected to each other and to the free surface of the film. Due to their size and lack of interconnectivity, the pores and secondary phases are not believed to have significantly reduced the properties of the conductor.

While previous investigations of thick YBCO films have shown substantial interfacial reactions between the YBCO and cap layer of the buffers [5, 8], even under the same deposition conditions as this study [9], very little reaction was found to occur for the improved RABiTS™ architecture. Therefore, less degradation of the YBCO film occurred near the buffer that would reduce the effective film thickness capable of carrying current.

The nickel-tungsten oxide layer formed within the growing NiO reaction layer appears to have acted as a passivating layer, preventing the uncontrolled growth of the nickel oxide on these Ni-3at.%W substrates. While it is not clear whether any cracking in the buffer layers occurred, the prevention of NiO from reaching into the upper layers during processing by $NiWO_4$ would have significantly contributed to the exceptional I_c of the films.

1.3.5 References

1. S. R. Foltyn et al., *Appl. Phys. Lett.* **75** (23), 3692 (1999).
2. S. Sievers et al., *J. Appl. Phys.* **78** (9), 5545 (1995).
3. X. F. Zhang et al., *J. Mater. Res.* **14** (4), 1204 (1999).
4. J. H. Park and S. Y. Lee, *Physica C* **314**, 112 (1999).
5. T. G. Holesinger et al., *IEEE Trans. On Appl. Superconductivity*, **11** (1), 3359 (2001).
6. K. D. Develos et al., *Physica C* **361**, 121 (2001).

7. K. D. Develos et al., *Physica C* **357**, 1353 (2001).
8. T. G. Holesinger et al., *J. Mater. Res.* **15** (5), 1110 (2000).
9. K. J. Leonard et al., *J. Mater. Res.*, in print (2003).
10. O. Eibl and B. Roas, *J. Mater. Res.* **15** (11), 2620 (1990).
11. S. R. Foltyn et al., *J. Mater. Res.* **12** (11), 2941 (1997).
12. H. Y. Zhai et al., *Phil. Mag. Lett.* **81** (10), 683 (2001).
13. A. Goyal et al., *Appl. Phys. Lett.* **69** (12), 1795 (1996).
14. A. Goyal et al., U.S. Patents 5,739,086; 5,741,377; 5,846,912; 5,898,020; 5,964,966; 5,958,599; and 5,968,877.
15. A. Goyal et al., *Physica C* **382**, 251 (2002).
16. S. Kang et al., *Appl. Phys. Lett.*, in review (2002).
17. B. W. Kang et al., *J. Mater. Res.* **17** (7), 1750 (2002).
18. S. Bals et al., *Physica C* **372**, 711 (2002).
19. K. Verbist, A. L. Vasiliev, and G. Van Tendeloo, *Appl. Phys. Lett.* **66** (11), 1424 (1995).
20. A. Catana et al., *Appl. Phys. Lett.* **60** (8), 1016 (1992).
21. A. Catana et al., *Appl. Phys. Lett.* **63** (4), 553 (1993).
22. C-Y. Yang et al., *Physica C* **377**, 333 (2002).
23. U. Scotti di Uccio et al., *Physica C* **321**, 162 (1999).
24. P. R. Broussard et al., *J. Appl. Phys.* **74** (1), 446 (1993).

1.4 REEL-TO-REEL X-RAY DIFFRACTION AND RAMAN MICROSCOPY ANALYSIS OF DIFFERENTIALLY HEAT TREATED Y-BaF_2-Cu (YBCO) PRECURSOR FILMS ON METER-LENGTH RABiTS™

K. Venkataraman, M. Mika, and V. A. Maroni (ANL); D. F. Lee, K. J. Leonard, L. Heatherly, Jr., S. W. Cook, and M. Paranthaman (ORNL)

1.4.1 Introduction

Rapid progress is being made in the development of the $MBa_2Cu_3O_{7-x}$ (MBCO) coated conductor on long-length textured substrates. It is well within reasonable expectation that functional, reliable MBCO-based conductor (M = Y or a rare earth element) in lengths of 100 m or more will be available in another three to five years [1–9]. The coated conductor manufacturing process consists of a series of film deposition steps that will have to be monitored to ensure compositional and structural uniformity together with product quality control. The utility of reel-to-reel X-ray diffraction (XRD) for coated conductor characterization has already been described and demonstrated [10]. In the past several years, we have also found Raman microscopy to be easily implemented and extremely informative for the examination of chemical composition and microstructure evolution during and after MBCO phase formation. This is due in part to the exhaustive data base covering the molecular spectroscopy of all forms of MBCO (see, for example, Refs. 11–17 and references therein). This data base particularly emphasizes YBCO but generally applies to the entire MBCO family. The work of Iliev and coworkers [12–14] is a good starting point for those interested in the interpretation of Raman spectra of quasi-epitaxial YBCO films.

One of the routes to long-length YBCO coated conductors involves the electron beam deposition of a Y-BaF_2-Cu precursor [18, 19]. YBCO films formed from this precursor on single crystal substrates and on rolling-assisted biaxially-textured substrates (RABiTS™) have yielded critical current densities (J_Cs) in excess of 1.0 MA/cm^2 [18]. This paper describes experiments performed on differentially heat treated Y–BaF_2-Cu precursors deposited on meter-long buffered RABiTS™. These experiments were designed to investigate the evolution of the YBCO phase as a function of time at a fixed processing temperature and in a fixed processing atmosphere. The thermal processing and the subsequent examination of the meter-long tapes were conducted in a reel-to-reel mode that permitted the creation of a time-synchronized phase

composition gradient (in the reeling direction) and the detailed examination of that composition gradient by Raman microscopy and XRD.

1.4.2 Experimental

Y-BaF_2-Cu precursors were deposited on meter-length buffered Ni-3%W RABiTS™ using methods developed and facilities in place at the Oak Ridge National Laboratory [20, 21]. The specific buffered RABiTS™ architecture used in this study was CeO_2 (15 nm)/YSZ (ca. 200 nm)/Y_2O_3 (15 nm)/Ni (1.0 μm)/Ni-3%W (50 μm). Details pertaining to the fabrication of this substrate architecture and the electron-beam deposition of the Y-BaF_2-Cu precursor have been reported elsewhere [20–22]. Results for two tapes will be reported on in this paper—one with a ca. 300-nm-thick YBCO precursor film on a 1.24-m tape segment, and another with a ca. 1000-nm-thick precursor on a 1.14-m tape segment. Half-meter lengths of nickel leader tape were spot welded to both ends of each coated substrate to facilitate heat treatment and subsequent examination in a reel-to-reel mode.

To provide a means of studying the effect of time at processing conditions for the Y-BaF_2-Cu precursor conversion to YBCO, the precursor-coated substrate tapes were reeled into a 2-m-long, 22-zone furnace housing a specially designed long-length coated conductor treatment chamber, the basic features of which are illustrated in Fig. 1.16. The 2.5-m-long chamber consists of seven transverse flow modules. These modules are stacked end-to-end and are separated by blocks with narrow slits to allow tape passage while minimizing crosstalk. Each 30-cm-long flow module is incorporated into the 5-cm-wide by 1-cm-high housing, and two 1-cm-diam Inconel 601 tubes with 125-μm holes are used as gas inlet and outlet ports. These tubes are welded in place such that the holes are opposite their counterparts and in line with the sample suspended in between. Standard components (including gas supply, water bubblers, and oxygen sensor) are connected to the reaction chamber where necessary. In addition, multiple sure sensors are strategically located such that pressures at gas inlets and gas outlets of different modules as well as that of the reaction chamber can be continuously monitored. Temperature of the hot zones of this furnace can be individually controlled such that a wide variety of thermal profiles and a sizable range of ramp-up temperature gradients may be obtained.

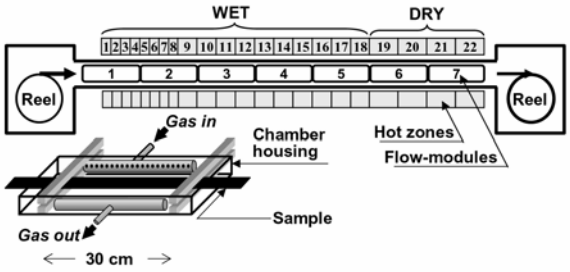

Fig. 1.16. Schematic of the reel-to-reel conversion system consisting of a seven-flow-module chamber in a 22-zone furnace. Also shown is the gas delivery configuration of an individual flow module.

During typical processing runs, the sample is continuously moved through the chamber at a chosen speed through a selected thermal profile pressuch that a prescribed conversion schedule can be performed. To create differentially heat-treated Y-BaF_2-Cu precursors with time-synchronized phase composition gradient, however, a procedure of partial conversion with fast cooling was developed. By interrupting the conversion process in such a fashion, the precursor would be subjected to a continuously varying amount of conversion time along the entire sample. In the present work the tape specimens were fed into the treatment chamber at rates of 46 cm/h for the 300-nm-thick precursor and 25 cm/h for the 1000-nm-thick precursor. In the case of the 300-nm precursor, the chamber was preheated to 740°C, and the tape was drawn into the chamber until the back end of the precursor-coated segment reached a temperature of 600°C. Then the tape was rapidly backed out of the chamber (at 2 m/min) to effect a quench condition. The 1000-nm precursor tape was handled in the same way, except that the trailing end of the tape was at 640°C when the tape was backed out of the chamber. The partial pressure of oxygen (pO_2) was held at 180 mTorr throughout the chamber, while the partial pressure of water vapor (pH_2O) ranged from 27 Torr at the entry end to 3.5 Torr at the exit end.

The Raman measurements were made using a Renishaw System 2000 Imaging Raman Microprobe equipped with a He-Ne (633-nm) laser. The laser power on the specimen surface was ca. 5 mW. Spectra were recorded with the laser fully focused and at varying degrees of defocusing (see Sect. 1.4.3). The coiled meter-length tapes (width = 1.0 cm) were manipulated with the specially designed reel-to-reel device shown in Fig. 1.17. The reel-to-reel XRD measurement methodology has been described and diagrammed elsewhere [10]. Briefly, XRD measurements were performed using a specially designed unit consisting of a large 4-circle diffractometer, a modular reel-to-reel insert for tape positioning, an X-ray source and a detector, and standard computerized controls. XRD intensities of specific phases as a function of tape position were obtained by driving the source-detector to the appropriate θ-2θ angles, and data were collected along the sample length using the reel-to-reel drive.

Fig. 1.17. Reel-to-reel device used to feed and control long-length coated conductor tape specimens during Raman microscopy examinations. The device is shown in position on the microscope stage of the Raman microprobe.

1.4.3 Results and Discussion

A sketch of the time/temperature/position relationship for the 300-nm YBCO tape is shown in Fig. 1.18. The precursor transformation temperature used for this sample was 740°C. The consecutive increments of the precursor spent times ranging from zero to 150 min at that temperature. In addition, there were increments of the precursor near the trailing end of the coated section (the ramp section) that experienced peak temperatures ranging from 600 up to 740°C prior to the quench. In the increment-by-increment Raman microscopy examination of this tape, we used a partially defocused excitation laser (633-nm wavelength) to probe two ca. 6-μm-diam spots at each increment along the tape. The two spots were chosen to be one quarter of the way in and three quarters of the way in from the top edge (as depicted in Fig. 1.18). This was done to search for evidence of transverse variations in the direction of gas flow in the phase composition along the length of the precursor coating. However, because there were very few instances where a discernable difference in the two spectra was seen, we will focus most of the attention in this paper on the end-to-end variations using the averaged value of the two Raman spectra recorded at each lengthwise location probed. In the following subsections, we present a segment-by-segment synopsis of the XRD and Raman microscopy results for the 300-nm film-on-tape specimen that starts at the trailing end of the precursor zone, highlights the key findings and implications of the Raman results, and points out the instances where these results complement, reinforce, and augment the findings of reel-to-reel XRD analyses performed on the same tape.

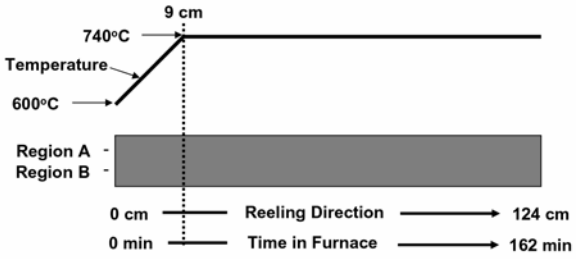

Fig. 1.18. Schematic diagram illustrating the time and temperature profiles used to produce the 300-nm-thick TGP YBCO film on a 1.25-m metal substrate.

1.4.3.1 The Ramp Zone (650 to 740°C)

The Raman spectra of increments of the precursor in this zone (see Fig. 1.19) exhibit two broad diffuse band envelopes, one between 100 and 200 cm^{-1} and another between 500 and 700 cm^{-1}, indicating the precursor-dominant presence of an amorphous phase mix from which CuO (ca. 300 cm^{-1} [23]) appears as the first crystalline phase. BaF_2, the cubic form of which exhibits a characteristic phonon at 242 cm^{-1} [24], is not detected in this region (3 to 8 cm) by Raman microscopy, and the time-synchronized XRD results (Fig. 1.20) likewise show little evidence of cubic BaF_2 in this region. The results in Fig. 1.21 present a comparison of the 3-cm increment (650°C maximum temperature) and the 9-cm increment (initial minute at 740°C) to provide a beginning-to-end perspective of the aggregate phase transformation that takes place in the ramp segment. From the two spectra in Fig. 1.21, we observe that by the time the precursor has reached 740°C, the CuO phonon dominates the spectrum, but other sharp modes begin to appear as well.

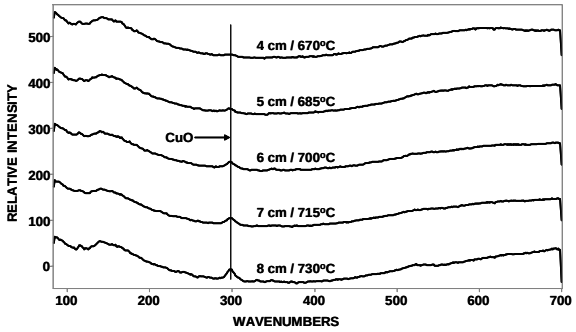

Fig. 1.19. Raman spectra of the Y-BaF_2-Cu precursor at five increments in the ramp zone of the 1.25-m time-gradient-processed tape. The indicated temperature is the maximum reached prior to quench at that location.

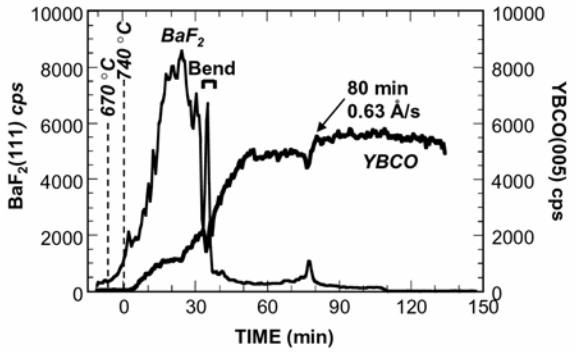

Fig. 1.20. XRD intensities of the BaF_2(111) and the YBCO(005) lines as functions of conversion time in the 300-nm-thick time-gradient-processed precursor tape. As indicated in the figure, YBCO(005) intensity first reaches its maximum at roughly 80 min. Also indicated is the location where the sample was "bent" during tape handling resulting in distortion of the XRD data.

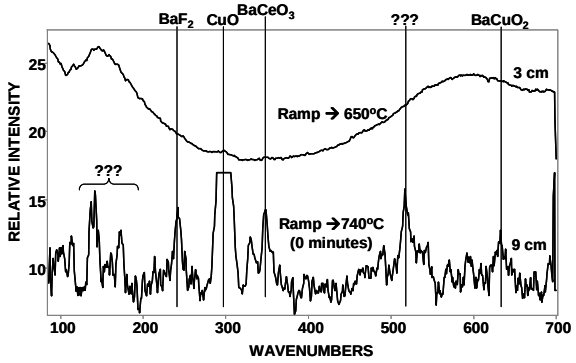

Fig. 1.21. Raman spectra recorded at the 650°C ramp increment and at the increment where the precursor just reached the transformation temperature (740°C) prior to quench. Note the onset of crystallization in the latter case (lower spectrum).

1.4.3.2 Synopsis of Phase Evolution on the 740°C Plateau

Figure 1.22 contains selected Raman spectra that comprise an overview of phase transformation along the 740°C plateau. On the right-hand side of this figure, we correlate each spectrum with the elapsed time at 740°C to provide a summary visualization of the overall reaction kinetics. In just a few minutes at 740°C, the broad bands associated with the amorphous phase mix are completely gone and evidence of several new crystalline phases (in addition to CuO) is clearly present. In just a little over ten minutes, phonons attributable to BaF_2 and $BaCeO_3$ (ca. 350 cm^{-1} [25]) are apparent, YBCO is starting to form, and there are other bands in the spectra that we will subsequently discuss and assign. In a little over

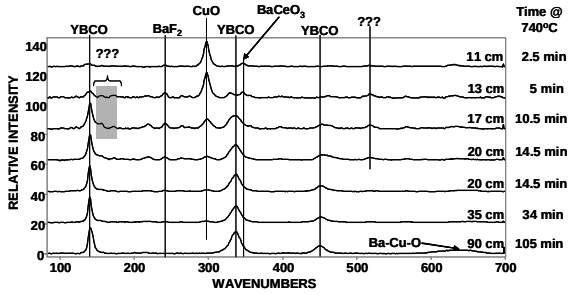

Fig. 1.22. Raman spectra of increments along the portion of the 1.25-m time-gradient-processed YBCO tape that reached the treatment temperature of 740°C. The time each increment spent at 740°C prior to the quench is indicated along the right side of the plot.

1.4.3.3 New Phases in the first 20 min at 740°C

A series of bands that begin to emerge in the initial few minutes at 740°C and persist through the first 20 min were found to exhibit a compelling correlation with the phonon pattern of the phase $Y_2Cu_2O_5$ [26] (referred to hereinafter as 202). This correlation can be seen in Fig. 1.23, where we plot the precursor spectra at ca. 0 min and ca. 16 min of 740°C treatment together with the spectrum of pure 202 in powder form recorded under the same instrument conditions used to examine the 1.25-m tape. The correlation at 0 min is clearer than the one at 16 min, where YBCO and BaF_2 modes tend to mask some of the 202 modes. In addition, we recognize modes in the 590 to 650 cm^{-1} range as being due to barium cuprates (Ba-Cu-O) [26, 27]. These results imply that 202 and Ba-Cu-O phases (along with CuO) are intermediates to YBCO formation. Furthermore, we note that none of these phases were conclusively identified during the XRD examinations. Figure 1.24 is included to show that these phases persist through the early stages of YBCO formation.

1.4.3.4 The Heartland of YBCO Formation and the "Sweet Spot"

30 min, the spectra are dominated by phonons of tetragonal YBCO (YBCO/T); in fact, the last vestiges of CuO are seen at the 34-min point. It is noteworthy that the reel-to-reel XRD intensity vs time data for this region (as projected in Fig. 1.20) reveal the in-growth of BaF_2 and the formation of YBCO on much the same temporal basis as the Raman results. Other reel-to-reel XRD/time data recorded for the 300-nm YBCO tape evidence the formation of $BaCeO_3$ in the same time domain as the Raman data. Unlike Raman, however, XRD could not unambiguously distinguish other intermediate phases because those minor intensities tend to be masked by YBCO and the buffer materials.

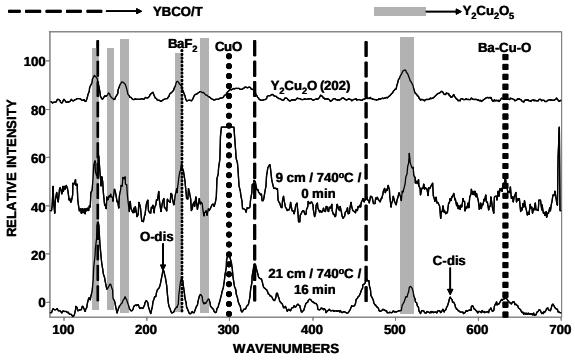

Fig. 1.23. Plot showing the correlation of Raman bands for a pure $Y_2Cu_2O_5$ powder specimen (top spectrum) with bands seen in the early stages of YBCO precursor transformation during time-gradient-processing of the 1.25-m YBCO tape specimen. The middle spectrum is for the 9-cm increment, which just reached 740°C prior to quench; the lower spectrum is for the 21-cm increment, which spent ca. 16 min at 740°C prior to quench. "O-dis" and "C-dis" are bands attributed to the oxygen-disorder and cation-disorder induced phonons of YBCO Source: M. N. Iliev, *American Chemical Society Symposium Series* 730, 107 (1999); M. N. Iliev et al., *J. Alloys and Compounds* 251 99 (1997); G. Gibson et al., *Physica C* 333, 139 (2000).

Figure 1.25 presents a series of Raman spectra covering the time range at 740°C that extends from the final appearance of modes due to intermediates (i.e., CuO, 202, and Ba-Cu-O), through the region of optimum YBCO/T presence, to the onset of the overprocessed state, where Ba-Cu-O modes reappear. We believe these results define a "sweet spot" in the time-at-740°C progression, where the film is composed

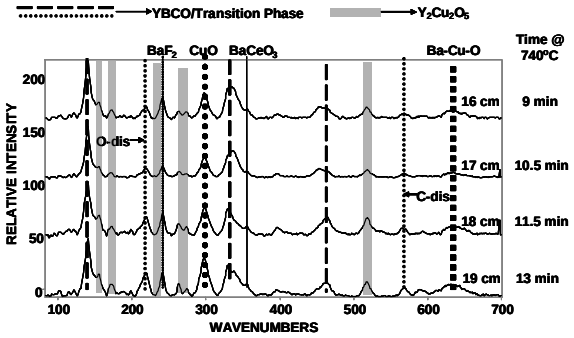

Fig. 1.24. Raman spectra of increments in the mid-portion of the phase transition region, showing the persistence of the $Y_2Cu_2O_5$ and CuO phonons in the early stages of YBCO formation along the 1.25-m YBCO time-gradient-processed tape.

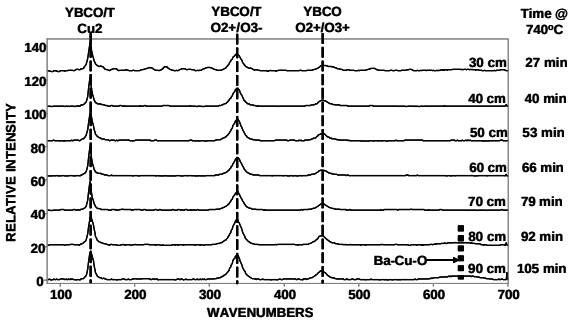

Fig. 1.25. Raman spectra of increments ranging from the end of the transformation region to the beginning of the over-processed region along the 1.25-m YBCO time-gradient-processed tape. The "sweet spot" appears to occur in the range of 50 to 70 min at 740°C for the 300-nm-thick YBCO film.

of nearly phase pure YBCO/T. This "sweet spot" occurs in the range from 50 to 80 min at 740°C. In the blowup of the 40- through 79-min region, shown in Fig. 1.26, we see little evidence of any phonons other than the three characteristic ones due to YBCO/T [12] but do note the onset of the well-studied YBCO cation disorder mode near 585 cm^{-1} [28] in the 79-min spectrum. This result is in excellent correlation with the reel-to-reel XRD data shown in Fig. 1.20 for the (005) diffraction line of YBCO. The intensity of this line first reaches its maximum value near the 80-min point at 740°C. Interestingly, the Raman-measured "sweet spot" observed for the 1000-nm YBCO tape specimen corresponds to approximately 220 to 230 min at 740°C (roughly three times that for the 300-nm YBCO tape specimen), illustrating the same approximately linear relationship between processing time and YBCO film thickness deduced from the XRD measurements on this thicker YBCO film (Fig. 1.27).

1.4.3.5 Broad Overview of the Phase Evolution Process

To provide a broader view of the Y-BaF_2-Cu to YBCO conversion process, we consolidated the dozens of individual Raman spectra recorded along the length of each of the time-gradient-processed (TGP) tapes into three-dimensional histograms. These histograms portray the phase evolution process in a graphical format that reveals many of the salient features of the precursor conversion process already alluded to above. A typical histogram that portrays the Raman band frequency (wavenumbers) and the relative band intensity as a function of distance (and concomitantly, time) with respect to the tape origin is shown in Fig. 1.28.

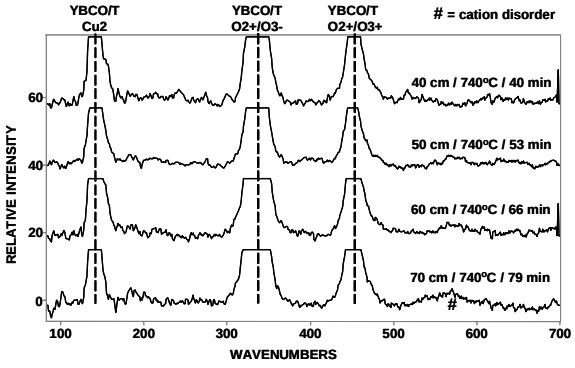

Fig. 1.26. Intensity-scale-expanded Raman spectra at four increments in the region of the "sweet spot" along the 1.25-m YBCO time-gradient-processed tape. There is no discernable evidence of residual second phases and only minimal evidence of cation disorder.

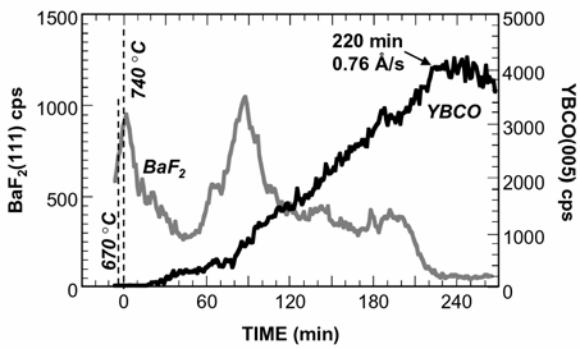

Fig. 1.27. XRD intensities of the BaF_2(111) and the YBCO(005) lines as functions of conversion time in the 1000-nm-thick time-gradient-processed precursor tape. YBCO(005) intensity first reaches its maximum at roughly 220 min.

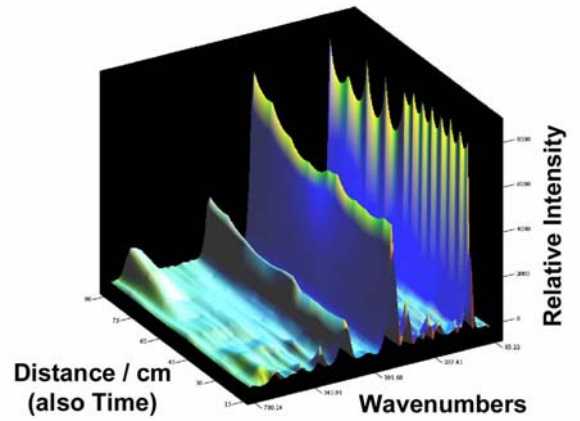

Fig. 1.28. Three-dimensional plot of Raman spectral frequency (wavenumbers) and relative intensity vs position (cm) along the ca. 300-nm ORNL TGP tape. The set of results portrayed in this figure cover most of the segment of the tape that experienced the soak temperature (740°C) for some period of time.

This histogram covers the major portion of the ca. 300-nm precursor tape that experienced the soak temperature (740°C) for some period of time (i.e., the ca. 15- to ca. 90-cm segment). The histogram is dominated by three of the YBCO/T phonons (at ca. 450 cm^{-1}, 330 cm^{-1}, and 145 cm^{-1}), but other Raman bands associated with BaF_2, CuO, $Y_2Cu_2O_5$, and barium cuprates are also clearly present. After forming the families of 3-D histograms for each of the two TGP tapes, it became clear that the most informative view was the one looking down from above on the distance (or time) vs wavenumber plane, using gray scale or color to portray intensity. Two such plots for the ca. 300-nm YBCO tape specimen are presented in Figs. 1.29 and 1.30.

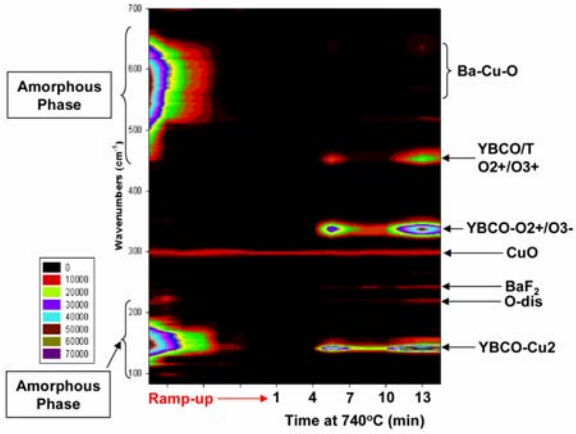

Fig. 1.29. Top view of the Raman frequency-reaction time plane (with intensities in color scale format) for the ca. 300-nm TGP tape. The time domain covered is the ramp up and early soak period at 740°C. All Raman band intensities are normalized to the intensity of the CuO mode at ca. 300 cm^{-1}.

Figure 1.29 shows the early stages of the reaction process that encompass the ramp-up segment and the first 15 min at 740°C. In this plot, all the intensities are normalized to the intensity of the CuO phonon at ca. 300 cm^{-1} because that particular mode is present at some detectable level across the entire time span of the plot. The two broad band envelopes at the left edge of the plot are the Raman scattering from the amorphous phase mix identified in Figs. 1.19 and 1.21. This phase mix dissipates before the soak temperature is reached, leaving only CuO as a Raman-detectable phase. Quite possibly, this dissipation occurs as a result of the formation of a liquid phase from which the three characteristic YBCO/T phonons begin to emerge after about 4 min at 740°C.

Figure 1.30 shows the time vs wavenumber plot for the remainder of the 300-nm precursor tape (from 10 min at 740°C to the overprocessed domains at the end of the precursor-coated segment). In this plot, all the Raman band intensities are normalized to the Cu2 (145 cm^{-1}) mode of YBCO/T because the Cu2 mode is persistently present over this entire segment of the tape. In Fig. 1.30, (1) Raman bands associated with $BaCeO_3$, BaF_2, CuO, $Y_2Cu_2O_5$, and barium cuprates vanish after approximately 30 min at

740°C, (2) there is an intermediate time domain from 30 to 90 min at 740°C wherein the three YBCO/T phonons sharpen up to eventually form the indicated "sweet spot", and (3) beyond the 90-min point at 740°C, the three YBCO/T phonons exhibit broadening along with the reappearance of barium cuprate (Ba-Cu-O) phonons, indicating the onset of YBCO decomposition, presumably due to overprocessing. Two other weak Raman bands that appear during the early stages of YBCO formation, indicated as C-dis and O-dis in Figs. 1.29 and 1.30, are ascribed to cation disorder and oxygen atom disorder, respectively, in the YBCO lattice [12, 14, 28]. Their presence in the early (formative) stages of YBCO evolution is both understandable and expected.

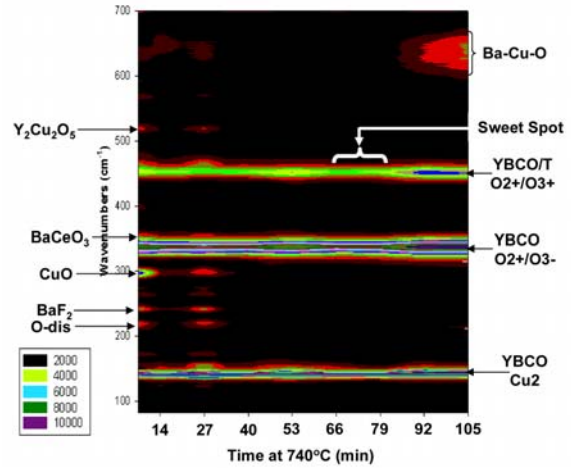

Fig. 1.30. Top view of the Raman frequency-reaction time plane (with intensities in color scale format) for the ca. 300-nm TGP tape. The time domain covered is the early through late soak period at 740°C. All Raman band intensities are normalized to the intensity of the Cu_2 mode of YBCO/T at ca. 145 cm^{-1}

Plots comparable to Figs. 1.29 and 1.30 were also constructed from reel-to-reel Raman data for the ca. 1000-nm precursor tape specimen. The results and corresponding conclusions are tacitly the same as for the ca. 300-nm precursor, with the expected exception that the thrice-thicker precursor took approximately three times longer at 740°C to reach the "sweet spot" condition. Figure 1.31 shows the plot for the ca. 1000-nm precursor specimen that generally corresponds to the conditions/results in Fig. 1.30 for the 300-nm specimen. The non-YBCO spectral features seen in Fig. 1.30 are present in Fig. 1.31 as well and appear with greater vividness in several cases.

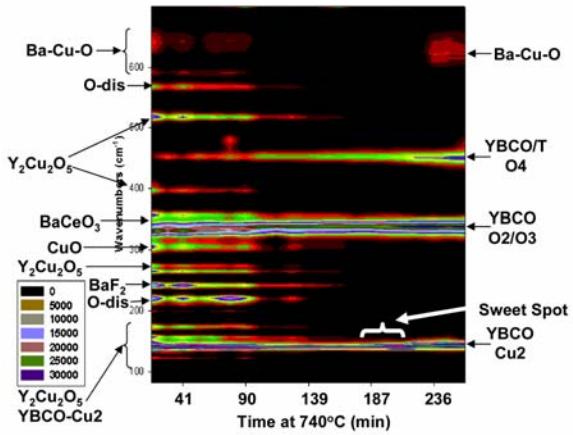

Fig. 1.31. Top view of the Raman frequency-reaction time plane (with intensities in color scale format) for the ca. 1000-nm TGP tape. The time domain covered is the early through late soak period at 740°C. All Raman band intensities are normalized to the intensity of the Cu_2 mode of YBCO/T at ca. 145 cm^{-1}.

1.4.3.6 Relationship of the "Sweet Spot" to the Optimum Performance Point

In a paralleling series of measurements, two tapes that were processed so as to exactly duplicate the 300- and 1000-nm specimens were subsequently silver coated and oxygenated to produce the orthorhombic (superconducting) form of YBCO. These two replicate tapes were then subjected to critical current measurements in 1-cm increments along the length of each tape. The results of these measurements for the replicate 300- and 1000-nm tapes are shown in Fig. 1.32. It can be seen from this figure that the sectional critical current densitiess of both tapes increase with processing time until the respective optimum time has been reached. One major question is then whether the diagnostic techniques that are presented here can be used to monitor the J_c development. It has previously been shown that nonuniformity of coated conductor tapes can be determined by XRD (i.e., relative changes in

J_c are closely mirrored by changes in the YBCO(00*l*) intensity) [10]. Therefore, it is not surprising that in the case of both replicate tapes, the onset of the maximum critical current value occurs in a time window at 740°C that corresponds very closely with those indicated by the XRD data shown in Figs. 1.20 and 1.27. What is a novel finding is that we have shown that Raman data may be used to determine the optimum processing window for MBCO superconductors, as evident from the close correlation between J_c development and the "sweet spot" temperature windows shown in Figs. 1.30 and 1.31.

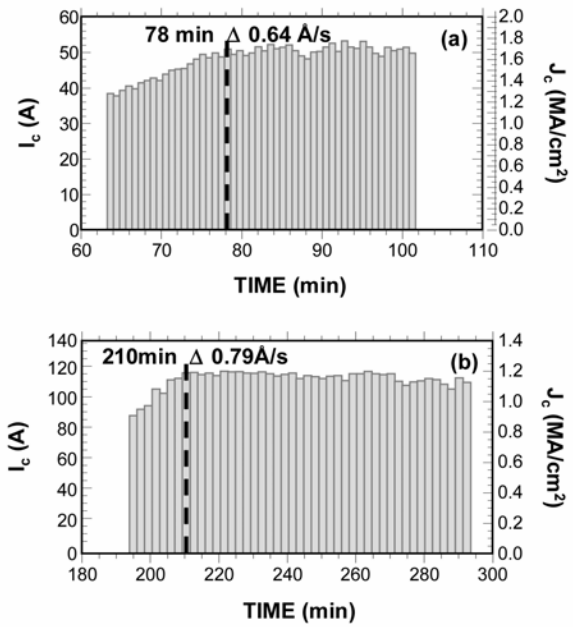

Fig. 1.32. Variation in sectional J_cs with processing time for the (a) 300-nm and (b) 1000-nm replicate tapes.

1.4.4. Conclusions

Great advances were made in the recent year where coated conductors with J_cs in excess of 1 MA/cm^2 have been fabricated in 1- to 10-m lengths. In anticipation of much longer tapes being produced within a few years, the need for online diagnostic tools becomes more urgent. We have investigated the applicability of XRD and Raman microspectroscopy, and found that these complementary techniques can pinpoint the optimum processing time and conditions for ex situ YBCO films, as well as provide rapid feedback for process development and valuable insights into the reaction pathway of ex situ YBCO.

To reach these conclusions, we have developed a procedure where differentially heat treated Y-BaF_2-Cu precursors with a time-synchronized phase composition gradient can be obtained in a single long-length sample. By using this procedure of partial conversion with fast cooling, the sample preparation time is greatly reduced, and unintended sample-to-sample variation is eliminated. Two TGP YBCO tapes, a 300-nm-thick and a 1000-nm-thick film on RABiTS™, were fabricated using this procedure. Reel-to-reel Raman data on these films revealed that an amorphous phase mix was present during the ramp-up stage of conversion. This phase mix dissipates before the conversion temperature is reached, leaving only CuO as the Raman-detectable phase. After a short period of conversion at soak temperature, the three characteristic YBCO/T phonons begin to emerge. Also present as intermediate phases in the Raman spectra are BaF_2, CuO, $Y_2Cu_2O_5$, and barium cuprates. These intermediate phases vanish after a certain amount of time, depending on the precursor thickness, leading to an intermediate time domain wherein the three YBCO/T phonons sharpen up to eventually form an optimum "sweet spot." As processing continues beyond this "sweet spot," the three YBCO/T phonons exhibit broadening along with the reappearance of barium cuprate (Ba-Cu-O) phonons, indicating the onset of YBCO decomposition.

Reel-to-reel XRD scans performed on these two tapes revealed the reduction in BaF_2 content and development of epitaxial YBCO on much the same temporal basis as the Raman results. Most striking is the excellent agreement between the optimum processing time windows offered by the two diagnostic techniques. Just as important, these deduced optimum times closely matched those for the onset of maximum J_c directly measured on replicate samples. Thus, we have shown that these techniques may be used as on-line process indicators without the need to directly measure the conductor transport characteristics at cryogenic temperatures.

1.4.5 References

1. D. Larbalestier et al., *Nature* **414**, 368 (2001).
2. M. W. Rupich et al., *IEEE Trans. Appl. Supercond.* **13**, 2458 (2003).
3. D. T. Verebelyi et al., *Supercond. Sci. Technol.* **16**, L19 (2003).
4. B. Ma et al., *Supercond. Sci. Technol.* **16**, 464 (2003).
5. V. Selvamanickam et al., *IEEE Trans. Appl. Supercond.* **13**, 2492 (2003).
6. T. Watanabe, Y. Shihara, and T. Izumi, *IEEE Trans. Appl. Supercond.* **13**, 2445 (2003).
7. V. Matias et al., *IEEE Trans. Appl. Supercond.* **13**, 2488 (2003).
8. A. Usoskin et al., *IEEE Trans. Appl. Supercond.* **13**, 2452 (2003).
9. R. Nemetschek et al., *IEEE Trans. Appl. Supercond.* **13**, 2477 (2003).
10. E. D. Specht et al., *Physica C* **382**, 342 (2002).
11. J. R. Ferraro and V. A. Maroni, *Applied Spectroscopy* **44**, 351 (1990).
12. M. N. Iliev, *American Chemical Society Symposium Series* **730**, 107 (1999).
13. M. N. Iliev, V. G. Hadjiev, and V. G. Ivanov, *J. Raman Spectrosc.* **27**, 333 (1996).
14. M. N. Iliev et al., *J. Alloys and Compounds* **251**, 99 (1997).
15. E. Liarokapis, *Physica C* **317–18**, 270 (1999).
16. M. Kakihana, M. Osada, and V. Petrykin, *Physica C* **338**, 144 (2000).
17. C. Camerlingo, I. Delfino, and M. Lepore, *Supercond. Sci. Technol.* **15**, 1606 (2002).
18. A. Goyal et al., *Physica C* **382**, 251 (2002).
19. L. Wu et al., *Supercond. Sci. Technol.* **16**, 1127 (2003).
20. X. Cui et al., 1999 *Physica C* **316**, 27 (1999).
21. F. A. List et al., *ORNL Superconducting Technology Program for Electric Power Systems Annual Report* ORNL/HTSPC 12, 27 (2000). (www.ornl.gov/HTSC/publication.htm).
22. S. W. Lu et al., *Supercond. Sci. Technol.* **14**, 218 (2001).
23. J. C. Irwin et al., *Physica C* **166**, 456 (1990).
24. O. Castano et al., *Physica C* **372–376**, 806 (2002).
25. S. Loridant et al., *Solid State Ionics* **78**, 249 (1995).
26. R. Bhadra et al., *Phys. Rev. B* **37,** 5142 (1988).
27. H. Chang et al., *Physica C* **252**, 333 (1995).
28. G. Gibson et al., *Physica C* **333**, 139 (2000).

1.5 MOD APPROACH FOR THE GROWTH OF EPITAXIAL CeO_2 BUFFER LAYERS ON BIAXIALLY TEXTURED Ni-W SUBSTRATES FOR YBCO COATED CONDUCTORS

M. S. Bhuiyan (ORNL & University of Houston); M. Paranthaman, S. Sathyamurthy, T. Aytug, S. Kang, D. F. Lee, A. Goyal, and E. A. Payzant (ORNL); and K. Salama (University of Houston)

1.5.1 Introduction

Chemical solution processing techniques have emerged as viable low-cost nonvacuum methods for producing ceramic oxide powders and films. The most commonly used solution techniques are (1) sol-gel processes that use 2-methoxyethanol as a reactant and solvent; (2) hybrid processes that use chelating agents such as acetylacetonate or diethanolamine to reduce alkoxide reactivity; and (3) metal-organic decomposition (MOD) techniques that use high-molecular-weight precursors and water-insensitive reactants such as carboxylates and 2-ethylhexanoyates. These processes offer many desirable aspects, such as precise control of metal oxide precursor stoichiometry and composition, ease of formation of epitaxial oxides, relatively easy scale-up of the film, and low cost. In recent years various rare-earth oxides (RE_2O_3) and rare-earth zirconium oxide ($RE_2Zr_2O_7$) films have been grown epitaxially on biaxially textured Ni and Ni-W substrates by solution-based methods.

In the RABiTS™ approach, a four-layer architecture of $CeO_2/YSZ/Y_2O_3/Ni/Ni\text{-}W$ is used to fabricate long lengths of buffered tapes. The purpose of the buffer layers is to retard oxidation of Ni, to reduce the lattice mismatch between Ni and YBCO, and to prevent diffusion of Ni into YBCO. We have chosen cerium oxide (CeO_2) as a potential buffer layer for this study. CeO_2 has a fluorite CaF_2 structure with a lattice parameter of 5.41 Å; it gives better chemical compatibility with Ni-W substrates and good lattice matching with YBCO. Thin films of CeO_2 have been grown by various vacuum- and nonvacuum-based deposition techniques on rolled-Ni substrates.

In this report, we describe our successful development of the growth of a CeO_2 seed layer on rolled Ni-W substrates by the MOD technique, which is different from reported chemical solution deposition techniques, where sol-gel CeO_2 solution buffers were grown on biaxially textured Ni substrates. By using CeO_2 seed layers, we have eliminated the need for Ni overlayers. The three-layer architecture of $CeO_2/YSZ/CeO_2/Ni\text{-}W$ is utilized to produce short prototype samples of YBCO coated conductor in the present study. The CeO_2 seed layer helps to grow cube-textured yttria-stabilized zirconia (YSZ) buffers on Ni-W substrates; otherwise it is difficult to grow YSZ directly on Ni or Ni-W substrates using our experimental conditions. Here, the CeO_2 seed layer was grown by a solution process. Both the YSZ barrier and the CeO_2 cap layers were grown by rf-magnetron sputtering, and the YBCO films were grown by the pulsed laser deposition (PLD) technique.

The MOD precursor solution was prepared in ambient atmosphere. The reagents cerium (III) acetylacetonate ($Ce(acac)_3.xH_2O$), acetic acid and methanol were used as received from Alfa Aesar. $Ce(acac)_3.xH_2O$ (2.1872 g, 5 mmol) was dissolved in acetic acid (15 mL) by heating on a hot plate at 60°C for 10 min with continuous stirring. Then 5 ml of methanol (25% in volume of the solution) was added, which helps to stabilize the solution. The final volume of the solution was adjusted to 20 mL by adding methanol to obtain a 0.25 M CeO_2 precursor solution. This solution was then spin-coated onto short (2×1 cm) cube-textured Ni-W substrates at 5000 rpm for 30 s; heat treatment followed at 1100°C for 15 min in a reducing forming gas atmosphere of Ar-4% H_2. The samples were introduced into a preheated furnace and kept at 1100°C after a 5-min purge with an Ar-4% H_2 gas mixture at room temperature. After 15 min of heat treatment at 1100°C, the samples were quenched to room temperature with the same atmosphere. The heating and cooling rates were in the range of 350 to 400°C/min.

The CeO_2 films were characterized by using X-ray diffraction (XRD) for phase purity and texture, high-temperature XRD for nucleation and growth, scanning electron microscopy (SEM) for homogeneity and microstructure, and atomic force microscopy (AFM) for surface roughness analysis. A Philips model XRG3100 diffractometer with Cu Kα radiation was used to record the θ-2θ XRD patterns. The texture analysis was performed using a Picker 4-circle diffractometer. High-temperature in situ XRD experiments were carried out in a flowing atmosphere of He-4%H_2 and heating ramp of 400°C/min on a Scintag PAD X diffractometer with an mBraun linear position-sensitive detector (PSD) covering an 8° range centered at $2\theta = 31°$. The microstructure analyses of these samples were performed by using a Hitachi S-4100 field-emission SEM and Digital Instruments nanoscope AFM in contact mode.

The superconducting quality of the CeO_2 seed layer was tested with a layer sequence of $YBCO/CeO_2/YSZ/CeO_2/Ni\text{-}W$. A 200-nm-thick YSZ layer and a 10-nm-thick CeO_2 cap layers were deposited by rf magnetron sputtering on the CeO_2 seeded Ni-W substrates at 780°C in 10 mtorr of forming gas and 2×10^{-6} torr pressure of water vapor. The YBCO deposition was done by PLD at 790°C in 120 mtorr oxygen with an average laser energy of 400 to 410 mJ using a stoichiometric YBCO target, followed by annealing under 550 torr oxygen during cooldown. The samples were prepared for electrical property measurements by depositing silver for current and voltage contacts, followed by oxygen annealing at 500°C for 1 h. The transport critical current density, J_c, was measured by using a standard four-point probe technique with an electric-field criterion of 1 μV/cm. The J_c measurements were also performed with the applied magnetic field parallel to the substrate (H // c).

1.5.2 Nucleation and Growth Analysis by in situ HTXRD

The sample was heated from room temperature to 1200°C at a heating rate of 400°C/min in a reducing atmosphere of He-4% H_2, and the θ-2θ XRD patterns were recorded at 400, 600, 800, 900, 1000, 1100, 1150 and 1200°C. For the growth test, a sample was heated to 1100°C with the same heating ramp and atmosphere, and then XRD patterns were recorded for every 30 s for 1 h. Plots for nucleation and growth characteristics of CeO_2 film on textured Ni-W substrates are shown in Fig. 1.33 (a) and (b). The nucleation of CeO_2 starts at 600°C, and the growth of the film was completed within 5 min when heat-treated at 1100°C.

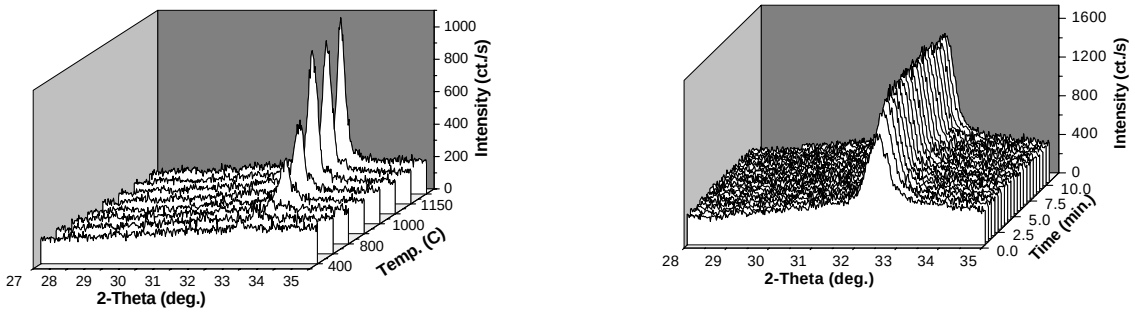

(a) (b)

Fig. 1.33. A typical θ-2θ scan obtained for a 20-nm-thick CeO_2 buffered Ni-W substrate in a high-temperature in situ XRD heat-treated at (a) various temperatures and (b) at a constant temperature of 1100°C for various times. The CeO_2 film has a preferred *c*-axis orientation, and the crystallization starts around 600°C (a) and is completed in 5 min (b).

1.5.3 Structure and Texture Analysis by XRD

A typical θ-2θ XRD scan for a spin-coated CeO_2 film on Ni-W substrate is shown in Fig. 1.34. The intense CeO_2 (200) peak reveals the presence of a *c*-axis-aligned film. The ω (out-of-plane) and ϕ (in-plane) scans of these films on the Ni-W substrates are shown in Fig. 1.35. The CeO_2 film has a good out-of-plane and in-plane texture with full-width-at-half-maximum (FWHM) of 5.86° and 7.55°, respectively. These values are well comparable to those of Ni-W substrates ($\Delta\omega = 5.95°$, $\Delta\phi = 7.47°$). The typical (111) pole figure for a CeO_2 film grown on the Ni-W substrate is shown in Fig. 1.36, which indicates the presence of a single cube-on-cube texture.

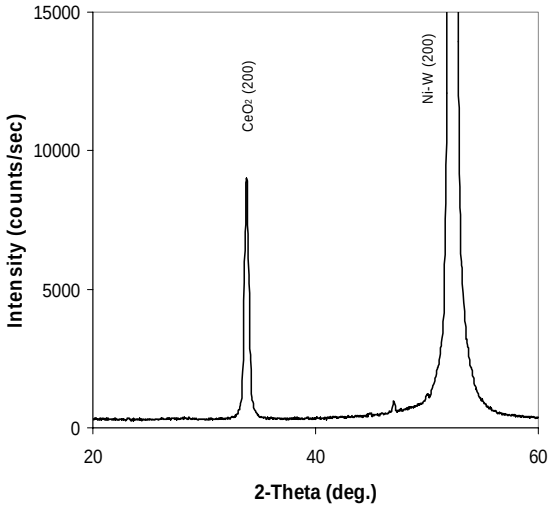

Fig. 1.34. A typical room-temperature θ-2θ scan obtained for a 20-nm-thick CeO_2 buffered Ni-W substrate. The CeO_2 film has a preferred *c*-axis orientation.

1.5.4 Microstructure Analysis by SEM and AFM

SEM studies of the CeO_2 films exhibit a uniform, smooth, and crack-free surface morphology, as can be observed from Fig. 1.37(a). An AFM image of the same sample is shown in Fig. 1.37(b). It

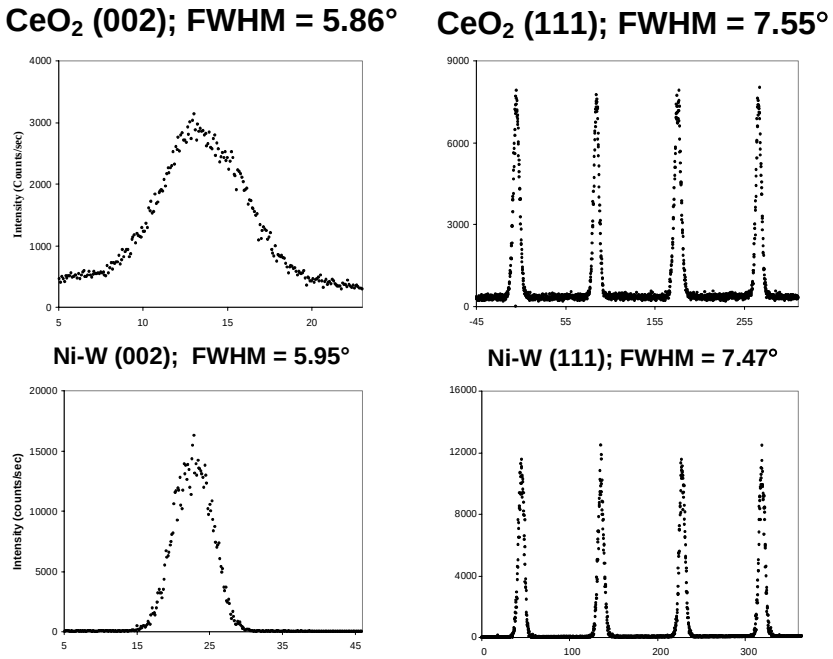

Fig. 1.35. The ω and ϕ scans obtained for a 20-nm-thick MOD CeO_2 film grown on textured Ni-W substrate. The FWHM values for each scan are shown inside the patterns.

reveals a root-mean-square roughness (Ra) of the CeO_2 films as 3 nm, which is comparable to that of the underlying alloy substrate (Ra = 1 nm). For lower concentrations of CeO_2 solution (i.e., a thinner film) there was a partial coverage of the substrate surface; for thicker CeO_2 films (i.e., higher concentrations), crack formation was detected due to lattice mismatch and/or the thermal expansion coefficient difference between the CeO_2 and Ni-W substrate. Details of this observation need further investigation.

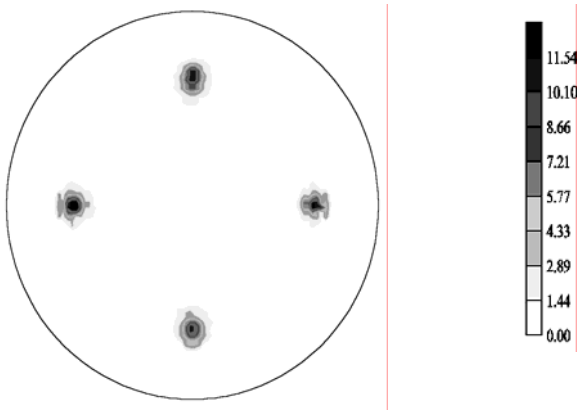

Fig. 1.36. The typical CeO_2 (111) pole figure obtained for a 20-nm-thick MOD CeO_2 film grown on a textured Ni-W substrate.

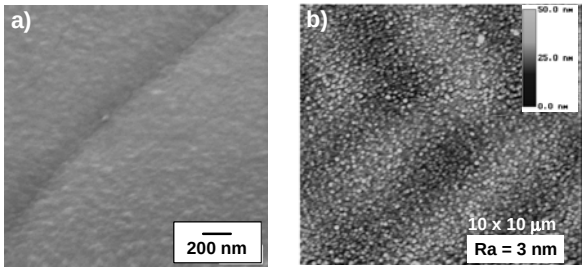

Fig. 1.37. SEM micrograph (a) and AFM images (b) obtained on a 20-nm-thick CeO_2 surface.

1.5.5 Superconducting Performance

The XRD pattern obtained from the YBCO/CeO_2/YSZ/CeO_2/Ni-W multilayer structure shown in Fig. 1.38 indicates that YBCO film has a strong *c*-axis texture. It also reveals the presence of a small amount of NiO and $NiWO_4$ at the buffer-substrate interface. The magnetic field dependence of J_c (77 K)for a 0.2-µm-thick YBCO film grown epitaxially on CeO_2/YSZ/ CeO_2/Ni-W is shown in Fig. 1.39, where the magnetic field is applied parallel to *c*-axis. The highest J_c obtained is about 1.5 MA/cm^2

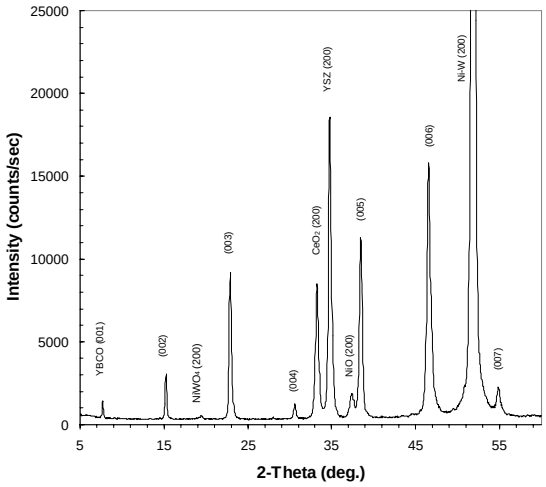

Fig. 1.38. A typical room-temperature θ-2θ scan obtained for a 200-nm-thick PLD YBCO film on a CeO_2 (sputtered)/YSZ (sputtered) /CeO_2 (MOD)/Ni-W substrate. The YBCO film has a preferred *c*-axis orientation.

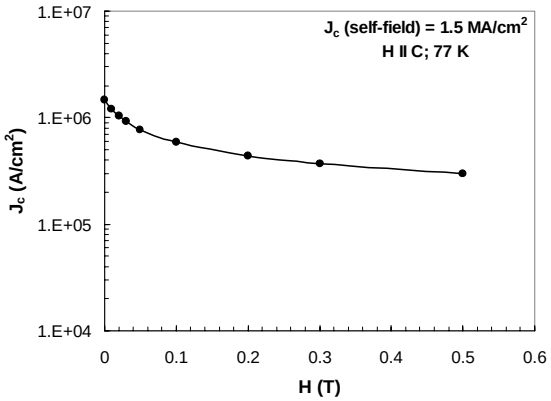

Fig. 1.39. Field dependence of critical current density, J_c, for a 200-nm-thick PLD YBCO film on a CeO_2 (sputtered)/YSZ (sputtered /CeO_2 (MOD)/Ni-W substrate.

for a 0.2-μm-thick YBCO film in self-field. The J_c at 0.5 T was about 20% of the zero-field J_c, which resembles the field dependency of a typical YBCO coated conductor. Efforts are being made to optimize the growth of CeO_2 as a cap layer on suitable barrier layers.

1.5.6 Summary

We have successfully developed a new MOD process to grow epitaxial CeO_2 buffer layers on Ni-W (100) substrates. The spin-coated buffers on Ni-W substrates were smooth, crack-free, and dense. On spin-coated CeO_2 seed layers, having a total buffer layer sequence of CeO_2 (sputtered)/YSZ (sputtered)/CeO_2 (spin-coated)/Ni-W, high-quality YBCO films with J_c values around 1.5 MA/cm^2 at 77 K and self-field were obtained. By this demonstration, we have eliminated the need for Ni overlayers.

1.6 DEVELOPMENT OF LOW-COST ALTERNATIVE BUFFER LAYER ARCHITECTURES FOR YBCO COATED CONDUCTORS

M. Parans Paranthaman, T. Aytug, H. Y. Zhai, H. M. Christen, D. K. Christen, A. Goyal, L. Heatherly, and D. M. Kroeger

1.6.1 Introduction

The Rolling-Assisted Biaxially Textured Substrate (RABiTS™) and ion-beam-assisted deposition (IBAD) approaches have been identified recently as the leading techniques to fabricate long lengths of high-performance YBCO coated conductors [1–4]. In the standard RABiTS™ approach, a four-layer architecture of CeO_2/YSZ/Y_2O_3/Ni/Ni-W is used to fabricate long lengths of buffered tapes by the epitaxial deposition on the thermomechanically textured Ni alloy substrates. In an effort to develop a low-cost alternative buffer layer architecture, we focused our studies on investigating both oxygen and metal diffusion layers. For development of a robust oxygen diffusion barrier layer, MgO has been chosen as the potential candidate since the oxygen diffusivity in MgO at 800°C is 8×10^{-22} cm^2/s. The oxygen diffusion into the metal/buffer interface could oxidize the substrate surface to oxides such as NiO or WO_3, based on the substrate composition and thermodynamical considerations. This may lead to delamination of both buffers and superconductors. It could also adversely affect the mechanical properties of the conductors. To overcome these issues, MgO has been grown directly on textured Ni or Ni-W3% substrates for the first time. In the past, we have demonstrated the epitaxial growth of MgO layers on both Ag/Pd-buffered

Ni substrates and Pd-buffered Ni substrates [5]. In addition, $LaMnO_3$ (LMO) has also been identified as a good diffusion barrier to nickel contamination [6, 7]. The pseudo-cubic lattice parameter of LMO (3.88 Å) is closely matched to YBCO; the lattice mismatch is less than 0.8%. We have also shown recently that LMO is compatible with MgO surfaces [8]. Based on these studies, we have also grown LMO on MgO-buffered Ni substrates. Here we report our recent results obtained on MgO-RABiTS™ architecture.

1.6.2 Experimental Procedure

The MgO seed layers were grown directly on biaxially textured Ni or Ni-W3% substrates using electron beam evaporation. As-rolled Ni or Ni-W tapes were cleaned by ultrasonification in isopropanol. The tapes were then annealed in a high-vacuum system at 1200 to 1300°C in the presence Ar/H_2(4%) and H_2S gas atmospheres to obtain the desired cube texture with a complete surface coverage of sulfur c(2×2) superstructures. The substrates used were 1 cm wide and 50 μm thick. Biaxially textured Ni substrates were mounted on a heater in the e-beam system. After the vacuum in the chamber had reached a background pressure of 1×10^{-6} Torr at room temperature, the substrates were heated to various temperatures, ranging from 300 to 600°C. The MgO layers were deposited on the Ni substrates at an optimum temperature of 400°C. The crucibles used were graphite. Magnesium oxide crystals were used as the source material. The deposition rate for MgO was 0.5 nm/s with the operating pressure of 10^{-5} Torr, and the final thickness was varied from 30 to 300 nm. We have deposited 60-nm-thick LMO buffer layers on MgO-buffered Ni substrates by rf-magnetron sputtering. The oxide sputter targets were made from single-phase LMO powders, prepared by solid-state reaction, which were loosely packed in a 4-in. copper tray. Typical sputter conditions consisted of 2 to 5×10^{-5} Torr of H_2O with a total pressure of 3 mTorr forming gas (Ar/H_2 4%). The water pressure is sufficient to oxidize the film to form stoichiometric $LaMnO_3$, when grown at a substrate temperature of 650 to 750°C. The deposition rate was ~0.06 nm/s. CeO_2 cap layers (~ 20-nm-thick) were also deposited on the LMO-buffered MgO/Ni substrates by using rf magnetron sputtering at 780°C in 10 mTorr of Ar/H_2 (4%) gas and a water pressure of 2×10^{-5} torr. The plasma power was 75 W. YBCO was deposited by pulsed laser deposition at 790°C in 120 m torr oxygen with an average laser energy of 400 to 410 mJ using a stoichiometric YBCO target, followed by annealing under 550 Torr oxygen during cooldown. Typical YBCO thickness was 200 nm.

The crystalline structure of the films was analyzed by X-ray diffraction (XRD) techniques. SEM micrographs were taken using a Hitachi S-4100 field emission microscope. The thicknesses of both buffer layers and YBCO were determined by Rutherford backscattering spectroscopy. The films were then prepared for current density measurements by depositing silver for current and voltage leads, followed by oxygen annealing at 500°C for 1 h. The transport critical current density, J_c, was measured using a standard four-point probe technique with a voltage criterion of 1 μV/cm.

1.6.3 Results and Discussion

Typical θ-2θ scan for a 30-nm-thick MgO film grown on textured Ni substrate is shown in Fig. 1.40. These scans indicate the presence of *c*-axis-aligned films. No NiO is present in the film. Detailed XRD results from ω and ϕ scans revealed good epitaxial texturing (see Fig. 1.41). The FWHM values for Ni (002) and MgO (002) are 9.6° and 4.7°, and those of Ni (111) and MgO (220) are 8.0° and 7.4°, respectively. There was a significant improvement in the out-of-plane texture. This could be due to the smoothness of the MgO layers. As shown in Fig. 1.42, the MgO (220) pole figure revealed the presence of a single four-fold cube texture. Similarly, highly aligned MgO layers were grown on both Ni-W3% and Ni/Ni-W3% substrates. SEM micrographs for both 30- and 300-nm-thick MgO seeds are shown in Figs. 1.43(a) and (b). Sample morphology of 30-nm-thick MgO layer is smooth, uniform, crack-free, and dense. MgO has also excellent coverage at grain boundaries. However, 300-nm-thick MgO layers were cracked in orthogonal regions. This could be due to either thermal expansion or lattice mismatch between Ni and MgO, causing the release of strain in MgO at higher thicknesses. Hence, it is essential to grow thin, crack-free MgO. The AFM images obtained on both 60- and 300-nm-thick MgO surfaces are shown

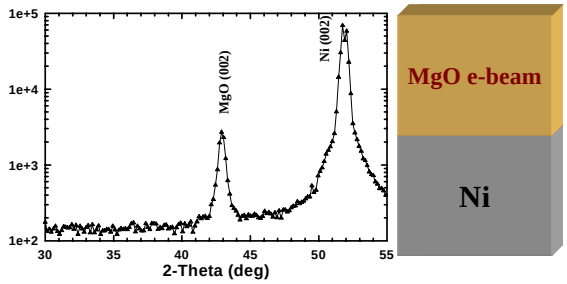

Fig. 1.40. A typical θ-2θ scan for a 30-nm-thick MgO film on textured Ni substrate. The MgO film has a preferred *c*-axis orientation.

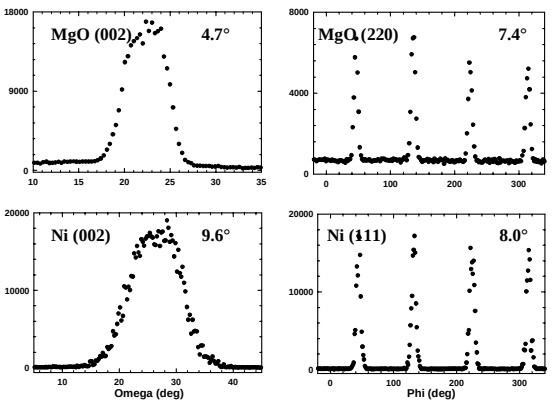

Fig. 1.41. The ω and ϕ scans obtained for a 30-nm-thick e-beam MgO film grown on textured Ni substrate. The FWHM values for each scan are shown inside the scans.

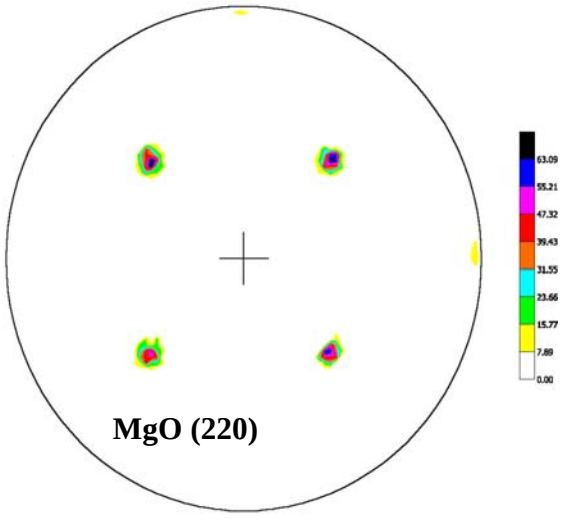

Fig. 1.42. The typical MgO (220) pole figure obtained on a 30-nm-thick e-beam MgO film grown on a textured Ni substrate.

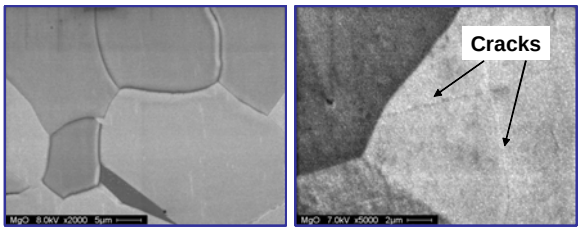

Fig. 1.43. SEM micrograph obtained on (a) crack-free 30-nm-thick and (b) cracked 300-nm-thick MgO surfaces.

in Fig. 1.44. The surface roughness, Ra, obtained on the 60-nm-thick MgO surface is 7 nm; that on the 300-nm-thick MgO surface is 5.8 nm.

A typical θ-2θ scan for a 60-nm-thick sputtered $LaMnO_3$ film grown on an e-beam MgO-buffered Ni substrate is shown in Fig. 1.45. These scans indicate the presence of a highly *c*-axis-aligned $LaMnO_3$ film. Figure 1.46 shows detailed X-ray results obtained from ω and ϕ scans on $LaMnO_3$ layers. It revealed very good epitaxial texturing. The FWHM values for Ni (002), MgO (002), and LMO (004) are 8.2°, 4.8°, and 5.2°, and those of Ni (111), MgO (220), and LMO (222) are 8.4°, 7.5°, and 7.2°, respectively. A typical θ-2θ scan for a 20-nm-thick PLD-YBCO film grown on sputtered CeO_2-capped LMO/MgO/Ni substrate is shown in Fig. 1.47. These scans indicate the presence of highly *c*-axis-aligned CeO_2 and YBCO films. The total thicknesses of the buffer layers were ~ 100 nm. A J_c of 500,000 A/cm^2 at 77 K and self-field was obtained on these films. Some of the buffers delaminated during the YBCO growth. The main cause

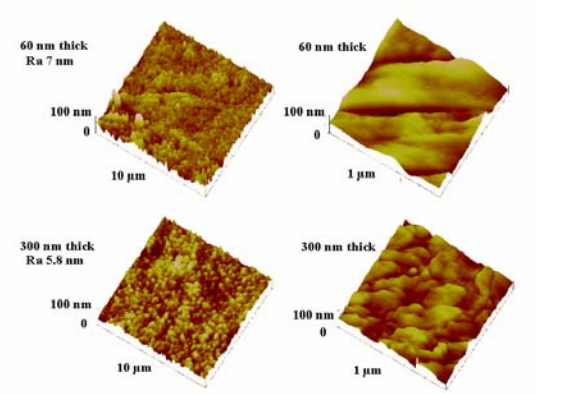

Fig. 1.44. AFM images obtained on both 60- and 300-nm-thick MgO surfaces.

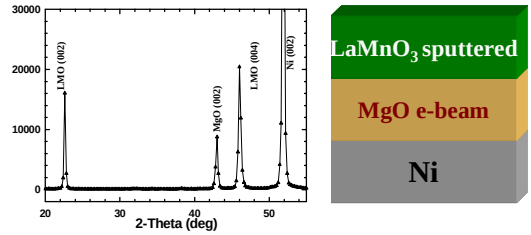

Fig. 1.45. A typical θ-2θ scan for a 60-nm-thick sputtered $LaMnO_3$ film on an e-beam MgO-buffered Ni substrate. The $LaMnO_3$ film has a preferred *c*-axis orientation.

for the delamination is unknown at this time. Since there is no oxygen transport through MgO layers to the substrates during the YBCO growth, the formation of self-passivating layer of $NiWO_4$ may be limited. Recent cross-sectional TEM studies on high-I_c thick YBCO film based RABiTS™ have shown that the presence of the $NiWO_4$ layer may be beneficial [9, 10]. Efforts are being made to optimize the YBCO growth conditions and also to understand the role of MgO seeds in detail.

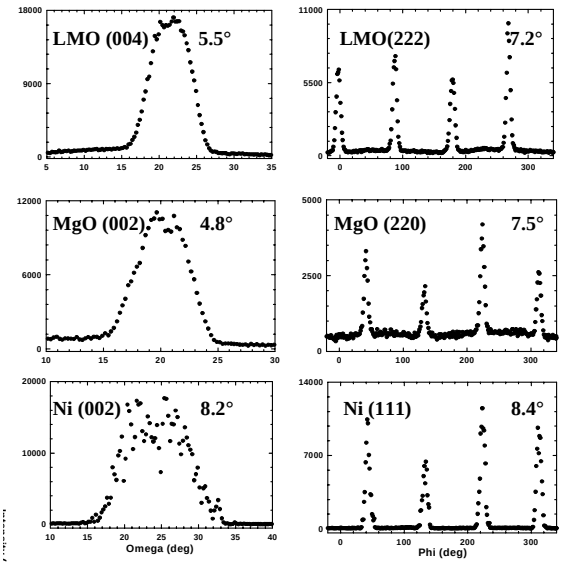

Fig. 1.46. The ω and ϕ scans obtained for a sputtered 60-nm-thick $LaMnO_3$ film on e-beam MgO-buffered Ni substrate. The FWHM values for each scan are shown inside the scans.

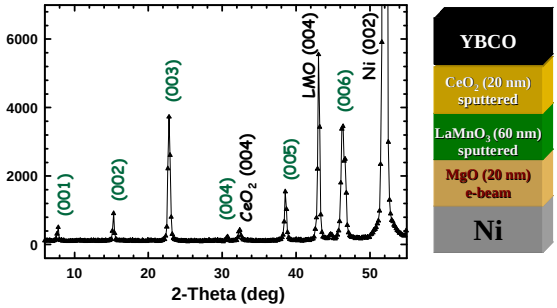

Fig. 1.47. A typical θ-2θ scan for a 200-nm-thick PLD-YBCO film on sputtered $LaMnO_3$-buffered MgO/Ni substrate. The YBCO film has a preferred *c*-axis orientation.

1.6.4 Summary

We have demonstrated that MgO films can be grown epitaxially with a single cube-on-cube orientation on textured Ni substrates. The microstructure of the 30-nm-thick e-beam grown MgO films was dense, crack-free, and continuous. Highly aligned $LaMnO_3$ layers were grown on MgO-buffered Ni substrates. Sputtered CeO_2 cap layers were also developed for these architectures for compatibility with ex situ YBCO process. Our preliminary results indicate that PLD-YBCO films with a J_c of 500,000 A/cm^2 can be obtained on CeO_2/LMO/MgO/Ni substrates.

1.6.5 References

1. A. Usoskin et al., "Large area YBCO-coated stainless steel tapes with high critical currents," *IEEE Trans on Appl. Supercond*. **13**, 2452 (2003).
2. Y. Iijima, K. Kakimoto, and T. Saitoh, "Fabrication and transport characteristics of long length Y-123 coated conductors processed by IBAD and PLD," *IEEE Trans. on Appl. Supercond.* **13**, 2466 (2003).
3. D. T. Verebelyi et al., "Uniform performance of continuously processed MOD-YBCO-coated conductors using a textured Ni-W substrate," *Supercond. Sci. and Technol*. **16**, L19 (2003).
4. J. R. Groves et al., "Improvement of IBAD MgO template layers on metallic substrates for YBCO HTS deposition," *IEEE Trans. on Appl. Supercond*. **13**, 2651 (2003).
5. M. Paranthaman et al., "MgO buffer layers on rolled nickel or copper as superconductor substrates," U.S. Patent No. 6,261,704 (Issue date: July 17, 2001); M. Paranthaman et al.,"Method of making MgO buffer layers on rolled nickel or copper as superconductor substrates," U.S. Patent No. 6,468,591 (Issue date: October 22, 2002).
6. M. P. Paranthaman et al., "Single buffer layer technology for YBCO coated conductors," *Mater. Res. Soc. Symp. Proc*. **689**, 323 (2002).
7. T. Aytug et al., "Single buffer layers of $LaMnO_3$ or $La_{0.7}Sr_{0.3}MnO_3$ for the development of $YBa_2Cu_3O_{7-\delta}$-coated conductors: A comparative study," *J. Mater. Res*. **17**, 2193 (2002).
8. M. Paranthaman et al., "Growth of thick $YBa_2Cu_3O_{7-\delta}$ films carrying a critical current of over 230 A/cm on single $LaMnO_3$-buffered ion-beam assisted deposition MgO substrates," *J. Mater. Res*. **18**, 2055 (2003).
9. S. Kang et al., "High critical current $YBa_2Cu_3O_{7-\delta}$ thick films on rolling-assisted biaxially textured substrates (RABiTS)," *J. Mater. Res.* (in press).
10. K. J. Leonard et al., "Microstructural characterization of thick $YBa_2Cu_3O_{7-\delta}$ films on improved rolling-assisted biaxially textured substrates," *J. Mater. Res.* **18**, 1723 (2003).

1.7 CHEMICAL SOLUTION DEPOSITION OF LANTHANUM ZIRCONATE BARRIER LAYERS APPLIED TO LOW-COST COATED CONDUCTOR FABRICATION

S. Sathyamurthy, M. Paranthaman, H. Y. Zhai, S. Kang, T. Aytug, C. Cantoni, K. J. Leonard, E. A Payzant, H. M. Christen, and A. Goyal (ORNL); X. Li, U. Schoop, T. Kodenkandath, and M. W. Rupich (American Superconductor Corp.)

1.7.1 Introduction

Fabrication of high-temperature superconductors in wire form based on epitaxial deposition on biaxially textured substrates has been a major worldwide research thrust for the past few years. Currently, three technologies are being explored to fabricate conductors by epitaxial deposition of YBCO and other superconducting materials on biaxially textured substrates – ion beam assisted deposition (IBAD) [1–4]), inclined substrate deposition (ISD) [5–7]), and rolling-assisted biaxially textured substrates (RABiTS™) [8–12]. In the RABiTS™ approach, a biaxial texture is first produced in the metal substrate by using thermomechanical processing, and various epitaxial layers are deposited on the metal substrate by using industrially scalable processing techniques

Currently, a common RABiTS™ architecture employs a Ni – 3at.% W (Ni-W) alloy substrate with a nickel overlayer, followed by a buffer layer sequence of Y_2O_3/YSZ/CeO_2 [13]. The superconductor is then deposited on the CeO_2 cap layer. A variety of deposition techniques are used for the deposition of the various layers. The Ni overlayer is deposited by dc-sputtering [13], the Y_2O_3 seed layer is deposited by electron beam evaporation [14], and the YSZ barrier layer and the CeO_2 cap layer are deposited by rf-sputtering [15]. Due to the use of several layers deposited using a variety of vacuum deposition techniques, the scale-up of this architecture becomes complex and expensive. We have previously

reported our results on the deposition of lanthanum zirconium oxide (LZO) seed layers directly on Ni-W substrates with consistent and reproducible properties, and a critical current density (J_c) up to 2 MA/cm^2, using a scalable nonvacuum solution-based deposition technique [16]. We found that LZO seed layers can be consistently deposited on the Ni-W surface by sol-gel process and that they show optimal adhesion to the substrate. This eliminates the need for the Ni overlayer.

Recently, using solution-processed LZO as a single buffer layer we demonstrated a J_c of 2 MA/cm^2 for a 0.2-μm YBCO layer deposited using pulsed laser deposition (PLD) [17]. In this paper, we explore in depth the use of solution-processed LZO films as seed and barrier layers, thus simplifying the coated conductor architecture from YBCO/CeO_2/YSZ/Y_2O_3/Ni/Ni-W to YBCO/LZO/Ni-W or YBCO/CeO_2/LZO/Ni-W. Such a simplified architecture will render the conductor fabrication route more scalable and cheaper. We report on the epitaxial growth and characterization of sol-gel processed LZO buffers on Ni-W substrates, including onset of the nucleation and growth of these layers, the properties of the interface between the Ni-W substrate and the LZO layer, and the crystallinity of the surface of the LZO film. We also report on the performance of these LZO films as barrier layers during deposition of YBCO films of various thicknesses using PLD. Lastly, we demonstrate high J_c on YBCO processed by a trifluoroacetate (TFA)-based metal organic decomposition (MOD) process on CeO_2-capped LZO barrier layers on Ni-W substrates.

1.7.2 Experimental

1.7.2.1 Processing

The coating solution was prepared from alkoxides of lanthanum and zirconium. Lanthanum isopropoxide (Alfa, La 40% assay), zirconium n-propoxide in n-propanol (Alfa, 70%) and 2-methoxyethanol (Alfa, spectrophotometric grade) were used as received. The alkoxides were handled in an argon-filled glove box, and the solution preparation was carried out by using a Schlenck-type apparatus under an argon atmosphere. Stoichiometric quantities of lanthanum isopropoxide and zirconium n-propoxide were dissolved in 50 mL of 2-methoxyethanol in a 250-mL round-bottom flask. The solution was refluxed in excess 2-methoxyethanol. Based on the studies reported in the literature [18, 19], we believe that lanthanum and zirconium methoxyethoxides are formed. The isopropanol formed during the exchange reaction was distilled out along with the excess 2-methoxyethanol. Solutions with a total cation concentration of 0.25 M and 1 M were used, respectively, to coat thin (20-nm) and thicker (100-nm) films of LZO.

The Ni-W tapes were fabricated by cold-rolling to total deformations greater than 98%. The details of this process have been reported earlier [20]. The Ni-W substrates, 1 cm wide and 50 μm thick, were then cleaned by using reel-to-reel ultrasonication in isopropanol at a rate of 1m/h. Cleaning was followed by a recrystallization anneal by inductive heating in a reel-to-reel vacuum chamber under 3×10^{-7} Torr of H_2S and a residence time of 20 min at 1250°C to obtain the desired cube texture. The substrates, about 3 cm long and 1 cm wide, were coated with LZO films by spin-coating at a spin speed of 2000 rpm for 30 s. The samples were then annealed at 1100°C for 15 min to 1 h.

1.7.2.2 Characterization

The LZO layers were characterized by X-ray diffraction (XRD) for phase purity and texture, scanning electron microscopy (SEM) for homogeneity and microstructure, and Rutherford backscattering spectroscopy (RBS) for composition and thickness analysis. A Philips XRG3100 diffractometer with Cu-K_α radiation was used to record θ–2θ XRD patterns. The texture analysis was performed using a Picker 4-circle diffractometer. The microstructural analysis of these samples was performed using a Hitachi S-4100 SEM with a field emission gun. The measurement of thickness and analysis of composition were performed by RBS, using 5-MeV He^{2+} ions at near normal incidence detected at a 160° scattering angle. Using RBS, the thickness could be measured to within 0.5 to 1 nm, and the composition to within 5%. The nucleation and growth of LZO from the amorphous film were observed by using high-temperature in situ XRD in a He-4%H_2 atmosphere on a Scintag PAD X diffractometer with an mBraun linear position

sensitive detector (PSD) covering a 8° range centered at a 2θ of 31°. The surface quality of the LZO films was analyzed by using atomic force microscopy (AFM) and reflection high-energy electron diffraction (RHEED). The interface between the substrate and the LZO films was characterized by using a Philips CM200 transmission electron microscope (TEM) with a field emission gun.

The performance of the LZO films as a barrier layer was evaluated by depositing YBCO films. YBCO films deposited by two approaches were used in this study. YBCO films were deposited by PLD directly on LZO-buffered Ni-W substrates (YBCO/LZO/Ni-W). Additionally, YBCO films were deposited by using a trifluoroacetate-based solution approach on LZO buffer layers with a sputtered CeO_2 cap layer (YBCO/CeO_2/LZO/Ni-W). The details of the PLD process [10] and the trifluoroacetate process [21] have been published elsewhere. The samples were then prepared for current density measurements by depositing silver for current and voltage leads, followed by oxygen annealing at 500°C for 1h. The transport critical current density, J_c, was measured by using a standard four-point probe technique; a 1 μV/cm criterion was used.

1.7.3 Results and Discussion

1.7.3.1 LZO Film Growth

The initial thin LZO films were coated on annealed Ni-W substrates by spin-coating the 0.25 M LZO solution with a spin speed of 2000 rpm for 30 s, followed by annealing in Ar-4%H_2 atmosphere at 1100°C for 1 h. The thickness of the films was determined by RBS analysis to be 20 nm. For a single LZO layer to perform as a good single barrier layer, a film thickness of 80 to 100 nm is required [17]. To achieve this, the coating and annealing steps were repeated several times. The XRD patterns obtained from one, three, and five coats of LZO with intermediate annealing steps are shown in Fig. 1.48, where it is evident that there is a proportional increase in the intensity of the (400) peak with the number of coats while the intensity of the (222) peak remains at background levels. The in-plane and out-of-plane textures of the various layers were measured by using a Picker 4-circle goniometer. The LZO films were found to have an out-of-plane texture (Δω) of 6.25° and an in-plane texture (Δϕ) of 8.4°.

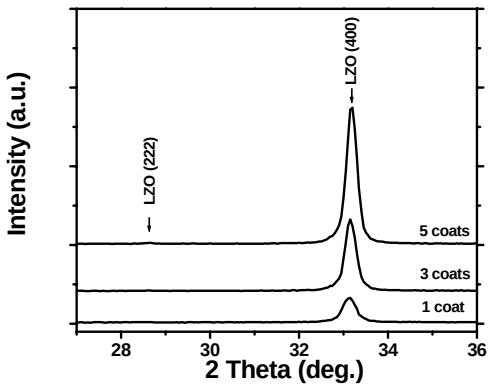

Fig. 1.48. XRD patterns of multiple coats of LZO showing proportional increase in the (004) peak intensity with the number of coats with no detectable amount of the (222) peak.

For epitaxial films used in multilayers, however, measuring the bulk crystallinity and texture by XRD is not sufficient. It is necessary to monitor the surface texture and crystallinity. For this purpose, RHEED analysis was performed on the LZO multiple coats. The RHEED patterns, shown in Fig. 1.49, indicate that the one, three, and five coats of the LZO films have both good surface crystallinity and texture.

HTXRD was used to study the nucleation and growth of the 20-nm-thick LZO films. The nucleation of LZO was studied by heating the sample from room temperature to 1200°C at a heating rate of 600°C/min in a reducing He-4% H_2 atmosphere and monitoring the θ–2θ XRD patterns at 400, 600, 700, 750, 800, 850, 900, 1000, and 1100°C. The growth of the LZO film was studied by heating a sample up to 1100°C and collecting θ–2θ XRD data every 16 s. The nucleation and growth characteristics of the LZO film obtained from this experiment are shown in Fig. 1.50 (a) and (b), respectively. It is evident from this figure that the LZO nucleates at around 750°C and that the film growth is complete in less than 10 min. From this result, it is clear that the processing of the LZO films does not require a 1-h hold at 1100°C, which has been the usual hold time to fabricate LZO films. Consequently, the hold time for processing these 20-nm LZO films was reduced to 15 min. By

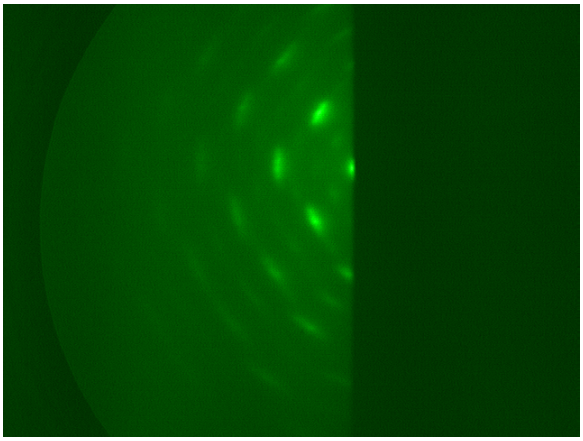

One coat

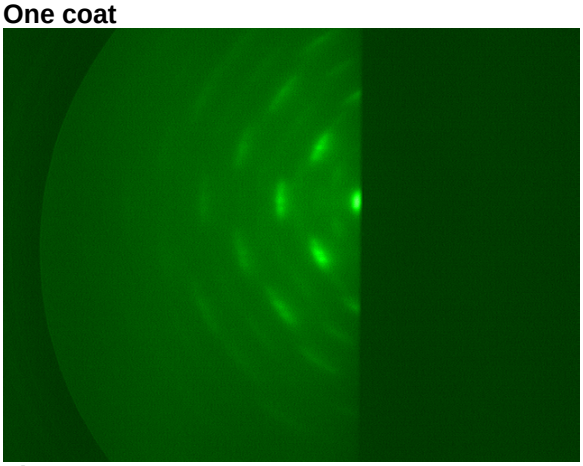

Three coats

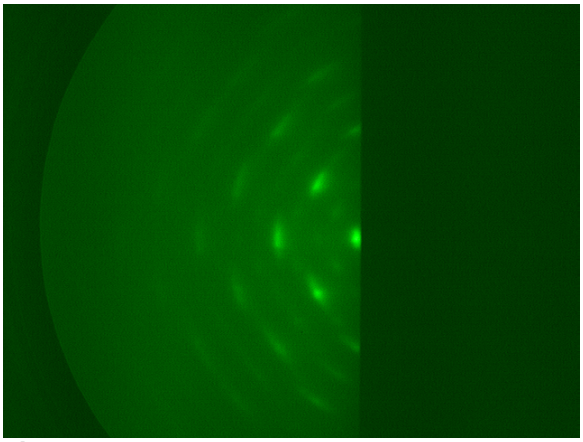

Five coats

Fig. 1.49. RHEED patterns of multiple coats of LZO showing good surface crystallinity of the sol-gel derived films.

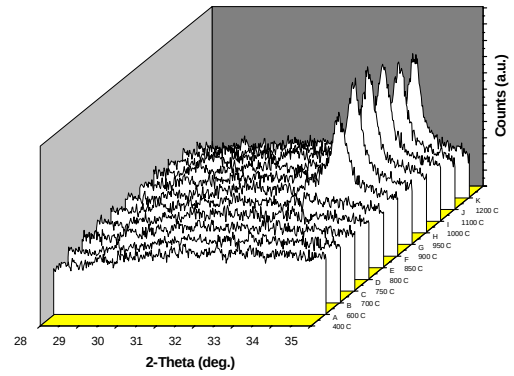

(a)

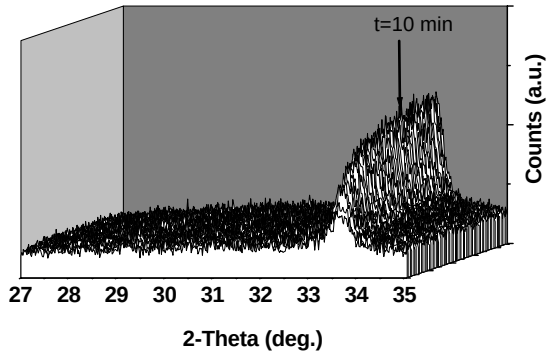

(b)

Fig. 1.50. A typical θ–2θ scan obtained for a 20-nm-thick LZO film on Ni-W substrates in a high-temperature in situ XRD showing (a) nucleation of LZO during the heat-up to the process temperature and (b) growth of LZO as a function of the hold time at a temperature of 1100°C.

using multiple coatings, it was observed that the proportional increase in the (004) peak intensity with the number of coats obtained for the heat treatment with a 1-h hold time was also obtained for the heat treatment with a 15-min hold time.

Cross-sectional TEM was used to study the interface between the Ni-W substrate and the multiple-coat LZO barrier layer. The high-resolution TEM image shown in Fig. 1.51 shows that the LZO film grows with a rotated cube-on-cube epitaxy of LZO[110](1$\tilde{0}$)Ni-W [001](020) in-plane and LZO(004)//Ni-W(200) out-of-plane alignments. This is illustrated within the selected area diffraction (SAD) pattern shown in Fig. 1.51(b). By using a high-resolution energy-dispersive spectroscopy (EDS) line scan [Fig. 1.51(c)], it was determined that the interface between the LZO and the Ni-W substrates was clean. The surface roughness of the LZO film was characterized by AFM. The film was found

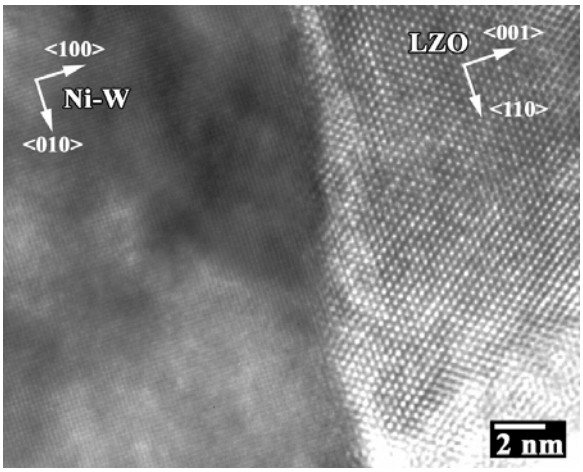

(a)

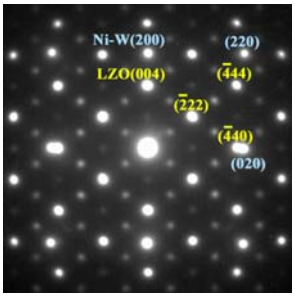

(b)

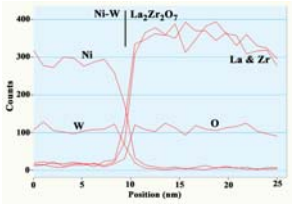

(c)

Fig. 1.51. (a) High-resolution cross-section TEM of LZO film on Ni-W substrate. (b) SAD pattern obtained from cross-section TEM showing Ni-Ws001]//LZO[110], Ni-W(010//LZO(110) orientation in the in-plane direction and Ni-W(100)//LZO(001) in the out-of-plane orientation. (c) EDS line scan showing a clean interface between LZO film and Ni-W substrate.

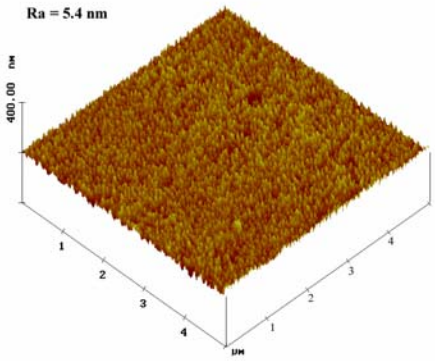

Fig. 1.52. AFM image of a 20-nm-thick LZO film on Ni-W substrate.

to have an average roughness of about 5.4 nm on a 5×5 μm scale as shown in Fig.1.52.

Attempts are currently under way to replace the multiple-coating annealing step of LZO with a single-step process. Figure 1.53 shows XRD of a thin LZO film (20-nm) and a thick (100-nm) film, both processed in a single step. The 1 M coat shows an increase in (400) peak consistent with larger thickness, but the (222) is at background levels. This finding suggests that it may be possible to process LZO in a single step. The RHEED pattern of the 100-nm LZO film (shown in the figure as an inset) shows that the thick LZO film processed in a single step has good surface crystallinity.

1.7.3.2 Performance of LZO Barrier Layers

The performance of the LZO buffer layers was evaluated by depositing YBCO by PLD directly on the LZO films and by deposition of YBCO by a TFA-based MOD process on a sputtered CeO_2 cap on the LZO films. The CeO_2 cap layer was used in the latter case to prevent reaction between the LZO layer and the TFA precursors used for YBCO deposition.

The performance of a single LZO buffer layer is compared with that of the $CeO_2/YSZ/Y_2O_3$ buffer architecture in Fig. 1.54. This figure shows a comparison of the field-dependent critical current density (J_c) for 0.2-μm-thick YBCO films deposited by PLD on Ni-W substrates with: (1) a single solution buffer, (2) a three layer buffer with a solution seed layer, and (3) all-vacuum standard three-layer buffer architecture. It is clear from this figure that the performance of the single LZO buffer layer is comparable to that of the three-layer buffer architecture. The thickness of the LZO buffer layers in this case was only about 70 nm compared to a buffer layer thickness of about 300 nm for the three-layer buffer architecture. To further evaluate the performance of these thin LZO buffer layers, thick YBCO films were deposited by PLD and the properties of the samples were monitored as a function of the YBCO thickness. Figure 1.55

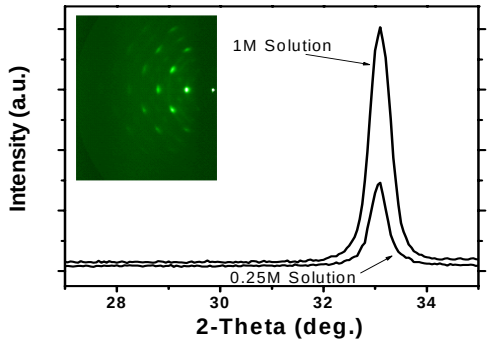

Fig. 1.53. Comparative θ–2θ patterns of thin (20-nm) and thick (100-nm) LZO films on Ni-W substrates processed in a single step. Inset: RHEED pattern obtained from the thick LZO film showing good surface crystallinity.

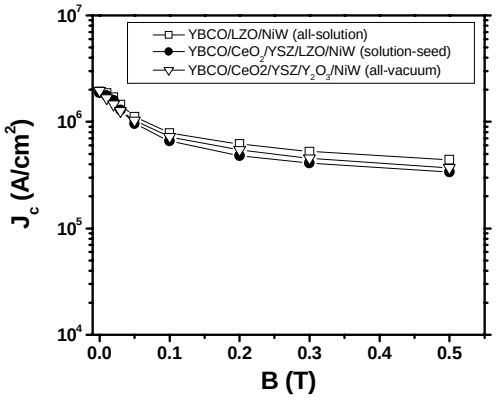

Fig. 1.54. Comparison of J_c-B performance of solution-deposited LZO as seed layer and as barrier layer with a traditional all-vacuum buffered Ni-W substrate using PLD-YBCO.

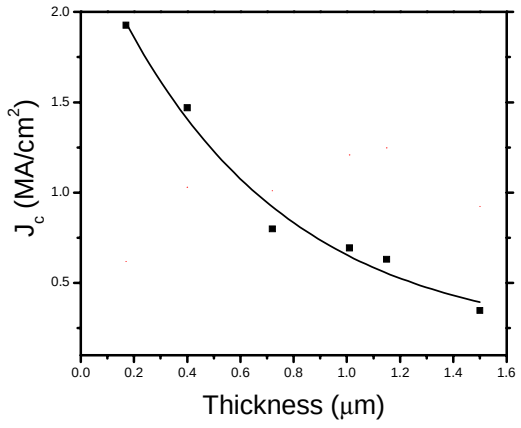

Fig. 1.55. Performance of a 60-nm-thick LZO barrier layer during thick PLD-YBCO film deposition. Variation of J_c has been plotted as a function of YBCO thickness.

illustrates that the J_c of the samples drops as the thickness of the YBCO increases. While this trend has been reported by many researchers, the extent of drop in J_c with thickness in this case is more severe. To understand the reason for this behavior, the samples were studied closely by using XRD and RBS. Figure 1.56 (a) and (b) shows the XRD pattern across the NiO peaks and the YBCO (005) peak for the thin (0.2-μm) and thick (1.5-μm) YBCO samples. For both samples the extent of NiO observed in the XRD is minimal, suggesting that the LZO buffer layers are acting as good oxygen barrier layers, preventing extensive oxidation of the metal substrate. Figure 1.56 (c) and (d) shows the RBS patterns obtained for the same samples along with simulated patterns for the layer architecture, for which ideal flat interfaces were assumed. It is clear from this comparison that while the thin YBCO sample shows close agreement with the simulation, the thick YBCO sample shows significant deviation at the interfaces between the various layers. This suggests that there could by some roughening of the interfaces induced during the YBCO PLD, which could be due to some reaction at the interface between the LZO and the YBCO. Further optimization of the YBCO deposition conditions and an addition of a CeO_2 cap layer to the LZO film may be needed to improve properties of thicker YBCO films.

The current-voltage (I-V) characteristics of TFA-based MOD YBCO on CeO_2 capped LZO barrier layers on Ni-W substrates are shown in Fig. 1.57. The figure shows that for a 0.8-μm YBCO deposited on about 150 nm of buffer layers (80 to 100 nm of LZO with about 50 nm of CeO_2), a J_c of 1.7 MA/cm^2 and an I_c of 135 A/cm has been measured. Although this is lower than the *J*c obtained on comparable TFA-based YBCO films deposited on typical vacuum-deposited buffer layers, it demonstrates that both the e-beam Y_2O_3 seed layer and the sputtered YSZ barrier layer can be replaced by a solution-processed LZO layer.

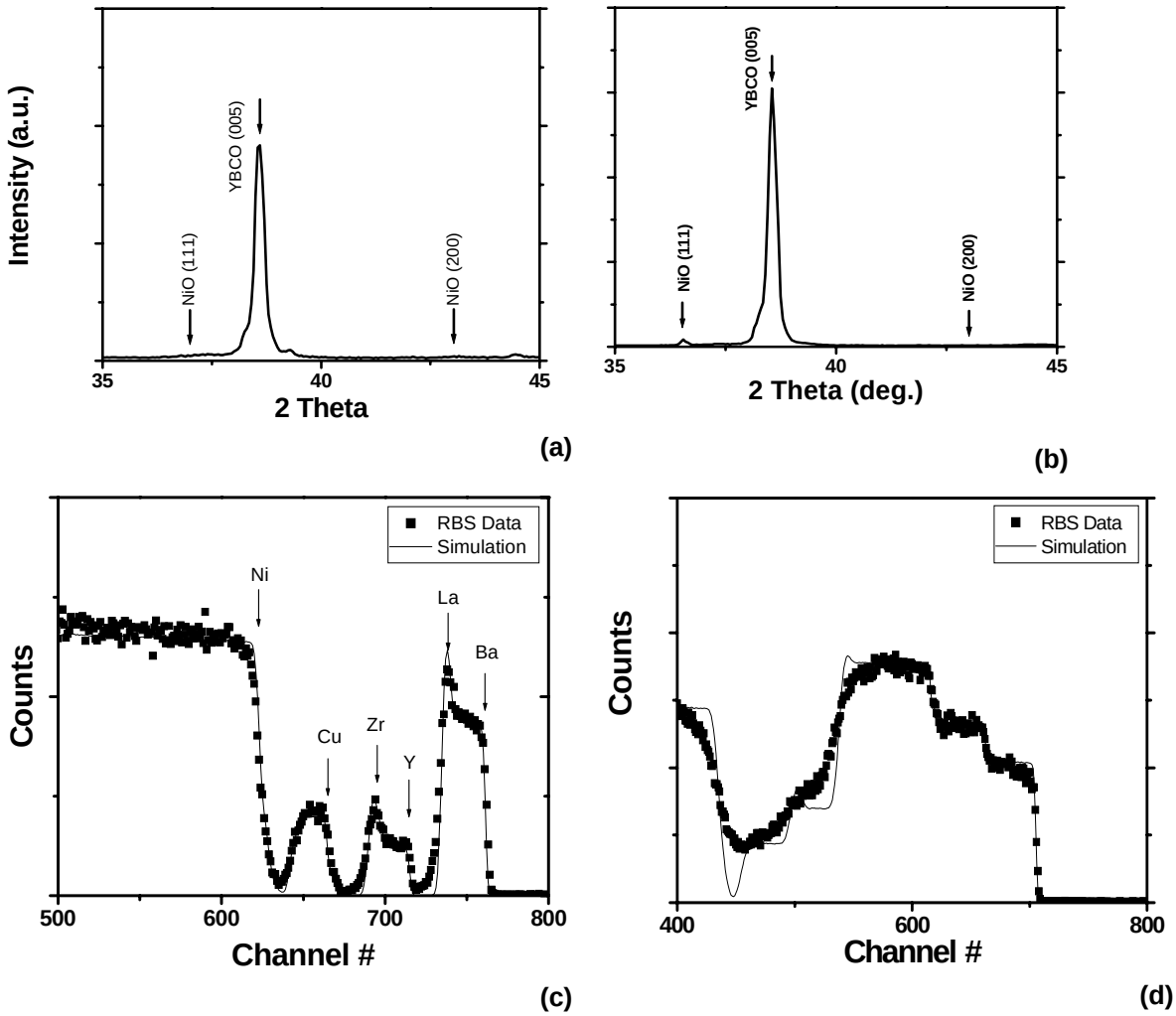

Fig. 1.56. Performance of a 70-nm LZO buffer layer for thin (0.2-μm) and thick (1.5-μm) PLD-YBCO. XRD data of LZO-buffered Ni-W substrates with 0.2-μm PLD-YBCO. XRD data of LZO-buffered Ni-W substrates with 1.5-μm PLD-YBCO. RBS data with simulation for 0.2-μm PLD-YBCO on LZO-buffered Ni-W. RBS data with simulation for 1.5-μm PLD-YBCO on LZO buffered Ni-W.

1.7.4 Conclusions

We have successfully demonstrated the use of solution-processed LZO films as barrier layers for coated-conductor fabrication. Epitaxial LZO films with a thickness of 80 to 100 nm have been deposited on Ni-W substrates by spin-coating and annealing.

These films were found to have a smooth, crack-free

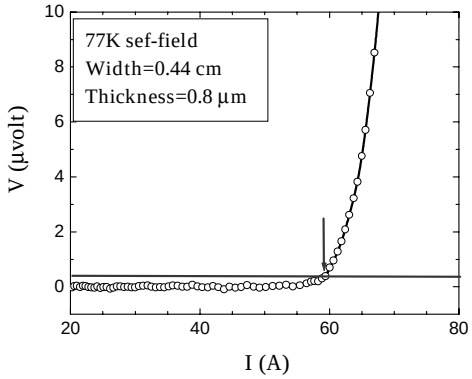

Fig. 1.57. I-V characteristics of 0.8-μm YBCO deposited by the TFA-MOD process on 80-nm-thick LZO-buffered Ni-W substrate with a CeO_2 cap layer.

microstructure with very high surface crystallinity. The performance of the LZO barrier layers was evaluated by depositing YBCO on these samples by PLD or by a TFA-based MOD process. The PLD-YBCO films, deposited directly on the LZO-buffered Ni-W substrates (YBCO/LZO/Ni-W), showed J_cs up to 2 MA/cm^2. For the MOD-YBCO, a CeO_2 cap layer was sputtered on the LZO barrier layer to avoid reaction between the LZO film and the YBCO film. Thus, using a layer sequence of YBCO/CeO_2 /LZO/ Ni-W, for the MOD-YBCO, J_c of 1.7 A/cm^2 and an I_c of 135 A/cm were measured. These results show that the buffer layer architecture in a typical coated conductor may be simplified by using solution-processed LZO films.

1.7.5 References

1. Y. Iijima et al., *Appl. Phys. Lett*. **60**, 769 (1992).
2. R. P. Reade et al., *Appl. Phys. Lett*. **61**, 2231 (1992).
3. W. D. Wu et al., *Appl. Phys. Lett*. **67**, 2397 (1995).
4. M. Bauer et al., *IEEE Trans. Appl. Supercond*. **9**, 2244 (1999).
5. K. Matsumoto et al., *IEEE Trans. Appl. Supercond*. **13**, 2535 (2003).
6. M. Fukutomi et al., *Physica C* **219**, 233 (1994).
7. M. Bauer, R. Semerkand, and H. Kinder, *IEEE Trans. Appl. Supercond*. **9**, 1502 (1999).
8. A. Goyal et al., *Appl. Phys. Lett*. **69**, 1795 (1996).
9. D. P. Norton et al., *Science* **274**, 755 (1996).
10. J. E. Mathis et al., *Jap. J. Appl. Phys*. **37**, L1379 (1998).
11. R. I. Tomov et al., *Physica C* **383**, 323 (2003).
12. S. Kreiskott et al., *Physica C* **383**, 306 (2003).
13. D.F. Lee et al., *Supercond. Sci. Tech.* (submitted).
14. M. Paranthaman et al., *Supercond. Sci. Tech*. **12**, 319 (1999).
15. F. A. List et al., *Physica C* **302**, 87 (1998).
16. S. Sathyamurthy, *J. Mater. Res*. **17**, 1543 (2002).
17. S. Sathyamurthy et al., *J. Mater. Res.* **17**, 2181 (2002).
18. L. F. Francis, D. A. Payne, and S. R. Wilson, *Chem. Mater*. **2**, 645 (1990).
19. S. D. Ramamurthy and D. A. Payne, *J. Am. Cer. Soc*. **73**, 2547 (1990).
20. A. Goyal et al., *Physica C* **382**, 251 (2002).
21. M. W. Rupich et al., *IEEE Trans. Appl. Supercond*. **11**, 2927 (2001).

1.8 ELECTRICAL AND MAGNETIC PROPERTIES OF CONDUCTIVE Cu-BASED COATED CONDUCTORS

T. Aytug, M. Paranthaman, A. Goyal, N. Rutter, H. Y. Zhai, A. A. Gapud, and D. K Christen (ORNL); J. R. Thompson and A. O. Ijaduola (University of Tennessee)

For the effective implementation of coated conductors at cryogenic temperatures (~30–77 K), stabilization against thermal runaway will be required in the event of an overcurrent situation (exceeding critical current, I_c, of the HTS coating). In general, a coated conductor architecture involves epitaxial fabrication of a thin layer (1–2 μm) of HTS film, usually $YBa_2Cu_3O_{7-\delta}$ (YBCO), on biaxially textured buffer layers deposited on a thick (50-μm) flexible metal substrate (Ni or dilute Ni-alloys). Thus, additional stabilization by electrical connection to a good conductor is required for insulating buffer layers and resistive Ni-alloy substrates (> 10 μΩ-cm at 77 K). A solution is to electrically shunt the HTS layer, either by an intermediate conductive buffer layer to a low-resistive metal substrate (i.e., Ni or Cu) or by depositing a stabilizing metallic cap layer (i.e., Cu or Ag) onto the HTS coating. While a conductive buffer provides an effective solution only when the substrate material is highly conductive, it is the most desirable approach from an applications perspective since it would yield the optimum engineering current density, J_E, (I_c per unit total cross sectional area). Coupling the HTS layer adequately to a pure Ni or Cu tape through a conductive buffer layer also provides an overall less complicated structure with reduced

resistance and an increased thermal conductivity, providing more efficient heat transfer to either a coolant bath or through the thermal diffusivity of the system.

To date, many reports on coated conductor fabrication using the rolling-assisted biaxially textured substrates (RABiTS™) technique have utilized high-purity (99.99%) Ni and strengthened Ni-alloy as the textured base material. However, the ferromagnetism (FM) of pure Ni and Ni-alloy hinders their use in applications requiring time-varying (ac) currents due to hysteretic energy losses. On the other hand, Cu is a lower-cost, lower-resistivity and nonmagnetic alternative for the production of long-length RABiTS™-based coated conductor tapes. Recently, we have demonstrated the growth of electrically well-coupled YBCO films on conductive $SrRuO_3/LaNiO_3$ bilayer and $La_{0.7}Sr_{0.3}MnO_3$ (LSMO) single-layer buffer structures deposited on biaxially textured Ni tapes. Although there has been recent progress in the development of nonconductive, protective buffer architecture, there have been no reports on the development of conductive buffer layers on pure Cu substrates for coated conductor applications. Because of its electrical conductivity, thermal stability, and structural compatibility with YBCO; we have investigated the viability of LSMO as a conductive buffer interface on biaxially textured Cu substrates. Here, we demonstrate the fabrication of electrically connected high-critical-current ($> 2 \times 10^6$ A/cm^2 at 77 K) YBCO coatings on Cu tapes. The electrical, superconducting, and magnetic (hysteretic loss) properties of these short prototype conductors are reported.

Cube-textured [{100}(100)] Cu substrates of 50 μm thickness were obtained from randomly oriented high-purity (99.99%) Cu bars by cold-rolling, followed by an anneal in vacuum at 800°C for 1 h. To minimize Cu diffusion and to reduce the oxidation rate of the substrate, first a protective Ni overlayer (1.6 μm) was deposited by dc-magnetron sputtering at a temperature of 600°C in a reducing atmosphere of forming gas (96%Ar + 4%H_2). Subsequent growth of the LSMO buffer was conducted by rf-magnetron sputtering in a mixture of forming gas and 2×10^{-5} Torr of H_2O, with the substrate temperature at 550 to 625°C. These conditions have solved the slight Sr contamination that we have observed in earlier work of LSMO on Ni. The YBCO films were grown at 780°C in 120 mTorr of O_2 by pulsed laser deposition (PLD), using a KrF excimer laser system operated at an energy density of ≈2 J/cm^2. For these research samples, typical thicknesses of the LSMO and the YBCO films were 300 and 200 nm, respectively. The crystallographic orientation and texture of the films were characterized by X-ray diffraction (XRD). A standard four-probe technique was used to evaluate the electrical properties, including the temperature-dependent resistivity of the conductive buffer layers, superconducting transition temperature (T_c), J_c, and current-voltage (I-V) characteristics of the composite structure. Values of J_c were assigned at a 1-μV/cm criterion. The magnetic properties of the samples were measured in a superconducting quantum interference device (SQUID)-based magnetometer at a temperature of 95 K, in fields, H, up to 800 Oe applied parallel to the tape plane.

Figure 1.58 shows the J_c performance of a YBCO film deposited on LSMO/Ni/Cu substrate as a function of magnetic field measured at the boiling point and near-triple-point temperatures of liquid nitrogen, with the field applied parallel to the *c*-axis. The sample has a $T_c > 90$ K, indicating that it is cation-contamination-free YBCO. At 77 K, the zero-field transport J_c is 2.3×10^6 A/cm^2 and the irreversibility field (H_{irr}) is high, near 7 T. At 65 K, J_c is 4.8×10^6 A/cm^2 and remains around 1×10^6 A/cm^2 at 3 T, which is highly desirable for applications such

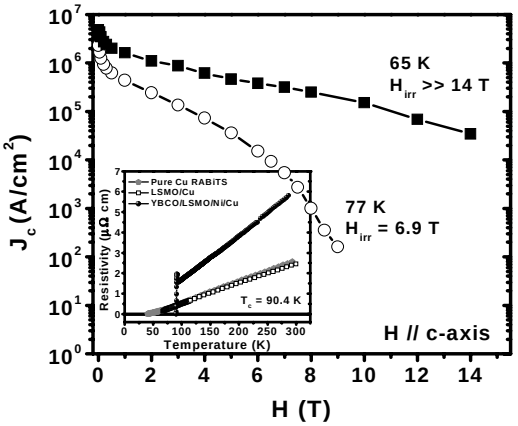

Fig. 1.58. Magnetic field dependence of J_c curves measured at 65 and 77 K, for a YBCO film on the conducting buffer structure of LSMO/Ni/Cu. Inset: Temperature-dependent net resistivity of the same YBCO sample, as well as the data for LSMO/Cu and for a pure biaxially textured Cu substrate.

as motors, generators, and energy storage requiring field strengths of several Tesla. These high J_c values could be obtained primarily due to the excellent texture, with low-angle grain-to-grain correlations dominating the entire sample and an overall high degree of in-plane ($\Delta\phi$) and out-of-plane ($\Delta\omega$) alignment. In fact, the measured XRD FWHM widths $\Delta\phi$ and $\Delta\omega$ of the average total ensemble of grains are sharp; 7° and 6.5° for YBCO, 6° and 5° for underlying Cu substrate, respectively. It is clear from the inset of Fig. 1.59, showing the temperature-dependent four-point resistivity measurements, that there is excellent electrical coupling between the Cu substrate and the LSMO layer, as evidenced by the similar ρ_{net}-T behaviors. However, after the YBCO deposition, ρ_{net}-T characteristics of the sample deviates from the ideal behavior, indicating somewhat degraded metallic connectivity, most likely resulting from the presence of discontinuous NiO regions (detected from the XRD analysis) at the LSMO-Ni interface. In fact, our model calculations showed that the observed increase in ρ_{net} at the superconducting transition can be associated with a significant interfacial contact resistance between the YBCO film and the Cu substrate. On the other hand, complete isolation of YBCO from the substrate would yield a ρ_{net} (calculated for the entire structure) that is 2×10^4 times higher than the present value of ρ (2 μΩ-cm) at the transition regime. The observed value is low enough to provide significant stabilization for the current levels of the present structure. Next we compare in Fig. 1.59 the I-V characteristics at 77 K of a model, ideally coupled conductor architecture (HTS + conductive buffer + substrate) with experimental results from the actual sample in Fig. 1.60. Figure 1.59 (model) plots I vs electric field (V/distance between voltage taps) curves for the Cu tape only, for the isolated HTS coating with an I_c of 150 A/cm-width (practical level of operating current), and for the combined ideal case, where the HTS layer and Cu are electrically connected through an intermediate conductive buffer layer.

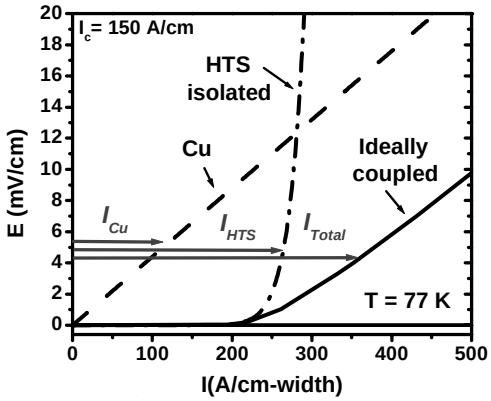

Fig. 1.59. Ideal current vs electric field characteristics for a model conductor architecture. Data for Cu, electrically isolated high-temperature superconductor (HTS), and the same HTS layer electrically connected to the underlying Cu substrate are compared. Arrows indicate the current sharing among layers for a specific electric field criterion.

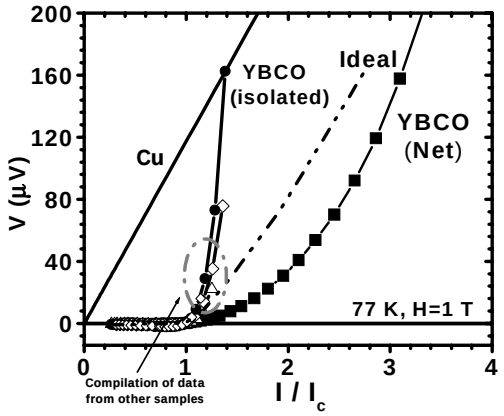

Fig. 1.60. The I-V curves obtained from the actual sample in a field of 1 Tesla. The figure includes curves for Cu, isolated YBCO films, and data from the YBCO/LSMO/Ni/Cu sample. The dashed line displays the response if there were a complete electrical coupling.

The interfacial contact resistance is assumed to be negligible (i.e., $< 10^{-8}$ Ω-cm^2). The nonlinear I-E behavior is typical for the isolated HTS layer, having the power law relation $E \propto (I/I_c)^n$. For $I > I_c$. The ideal case exhibits a near-linear differential ohmic behavior, with slope determined by the metal tape resistivity. Then, for an envisioned transient with $I > I_c$, the total current through the conductor partitions between the HTS layer and the metal tape, greatly reducing the power excursion in the entire structure. The I-V curves obtained from our actual sample are displayed in Fig. 1.60. While the scales are quantitatively different, qualitatively we observe similar I-V characteristic compared to the model conductor, although the interfacial resistivity is not negligible.

To check the stabilization provided by the metal tape and to push the current to levels greater than I_c, we recorded the data at 1 Tesla and compared that

with the data compiled from three other isolated YBCO films having similar power law behaviors. While the results exhibit similar I-V characteristics for bare Cu and isolated HTS film (compared with Fig. 1.59), data obtained from the actual sample do not agree quantitatively with the ideal behavior (dashed curve). This may be explained by the inhomogeneous electrical coupling and current transfer between the YBCO and the Cu substrate, possibly due to the formation of a discontinuous NiO layer at the interface. Nevertheless, were there a complete isolation, the superconductor would have been destroyed at current levels of $I = 3 \times I_c$ (see Fig. 1.60). Currently, we are trying to improve the electrical coupling and implement a detection mechanism that will monitor voltage across the metal tape.

To determine the potential FM ac loss due to the Ni diffusion barrier, we measured the hysteretic magnetic properties of a fully formed coated conductor at T = 95 K, just above the superconductive T_c. For these Ni materials, the loss properties change little below 95 K. The quasi-static studies were performed on a sample of mass 9.6 g, with the dc magnetic field oriented parallel to the plane of the tape. This configuration approximates the self-field on the substrate due to current flow in a tape and minimizes demagnetization effects. After cooling to 95 K in zero applied field, the hysteretic magnetization loop M(H) was measured by sweeping the field from $+H_{max}$ to $-H_{max}$ to $+H_{max}$ in small steps. A numerical integration of the area inside the loop M(H) provides $W = \oint M(H)d(H)$, the FM energy loss per cycle, with maximum magnetic field H_{max}. The measurements were repeated as a function of H_{max} up to 800 Oe, since the FM loss increases with ac field amplitude, which is proportional to the peak ac current. The resulting FM loss, W, per cycle per gram of tape is shown in Fig. 1.61 as a function of H_{max}. The inset of this figure shows the magnetization of the sample for several field excursions. At H_{max} = ±800 Oe, the loss has nearly saturated at approximately 180 erg/g of tape per cycle. The calculated maximum FM hysteretic ac loss at 60 Hz for a 1-m-long, 1-cm-wide tape of thickness 50 μm would be 5.5 mW, compared with 43 mW for the biaxially textured all-Ni RABiTS™ and 8.4 mW for a magnetically reduced Ni–5 at.%W tape. These FM losses of 5 to 9 mW correspond to modest additions (10–20 %) to the energy losses expected in HTS coating of achievable YBCO-based conductors. As an example, for an envisioned coated conductor architecture operating at $I_0 = I_c$ of 200 A/cm-width, applying the Norris theory, which is shown to provide a good estimate of ac loss for YBCO-based conductors, the power loss per meter per cycle is, $L_c = (\mu_o / 2\pi)I_o^2$ = 480 mW at 60 Hz. For more realistic operation at $I_o = I_c/2$, in which case the loss is smaller by a factor of 17, the superconductive hysteretic loss component yields a value of $L_c \sim 28$ mW. Obviously, further reducing the total energy loss would be possible either by reducing the thickness of Ni or by completely replacing the Ni film by a functional nonmagnetic metal layer. Similarly, the hysteretic loss in HTS can also be decreased by producing conductors with higher I_c that can operate at smaller I_o/I_c, or possibly by geometrical optimization such as subdividing the tape into noninteracting conductors.

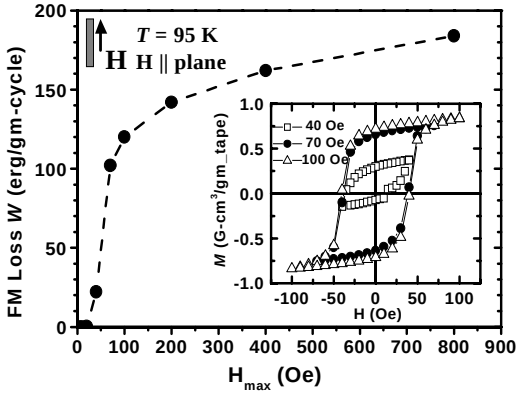

Fig. 1.61. Ferromagnetic hysteretic loss, *W*, due to the Ni layer in YBCO/LSMO/Ni/Cu. *W* first increases rapidly with H_{max}, then saturates. The inset shows the magnetization loops for the same sample at T = 95 K, for various H_{max} excursions, where the field is applied parallel to the plane of the tape.

This work shows the development of a conductive coated conductor architecture on biaxially textured Cu tapes having a layer sequence of YBCO/LSMO/Ni/Cu. A self-field J_c (77 K) value exceeding 2×10^6 A/cm^2 was achieved, and electrical characterization suggests good electrical coupling between the YBCO and the Cu substrate. Assessment of the magnetic loss associated with the Ni overlayer shows that it should be small compared with the hysteretic loss in an operational superconductive coating. Although these initial studies were conducted on pure copper, the ultimate implementation will require strengthened

tape. In principle, this can be achieved by appropriate alloying and precipitation hardening, which will also retain high electrical conductivity of the tape.

1.9 HIGH-J_c $YBa_2Cu_3O_{7-\delta}$ COATINGS ON $LaMnO_3$ BUFFERED BIAXIALLY TEXTURED Cu TAPES FOR COATED CONDUCTOR APPLICATIONS

T. Aytug, A. Goyal, N. Rutter, M. Paranthaman, J. R. Thompson, H. Y. Zhai, and D. K Christen

Copper-based tapes could offer an appealing alternative to textured Ni alloys for use in the production of long-length RABiTS™-based coated conductors. These materials would offer several advantages over Ni: absence of ferromagnetism, substantially lower material cost, and potentially lower electrical resistivity. The attainment of sharp cube texture in Cu by thermomechanical treatment has already been reported. The main drawback to utilizing Cu is its poor oxidation resistance. Since the epitaxial growth of oxide films generally requires elevated temperatures and oxidizing environments, prevention of unfavorably oriented CuO/Cu_2O on the Cu surface presents a major challenge. So far there have been limited reports on the development of buffer layers and HTS coatings on Cu or Cu-alloys for coated conductor applications. Previous results indicated either poor buffer-layer texture, with no attempts to grow HTS films, or with YBCO coatings exhibiting low J_c values.

Here we present an alternative route for buffer layer fabrication on Cu. First, thin Ni overlayers have been developed on Cu-RABiTS™ to obtain reproducible epitaxial growth of subsequent oxide films. For the oxide buffer layer, we have chosen $LaMnO_3$ since our previous research has demonstrated the viability of $LaMnO_3$ as a buffer layer for the fabrication of high-J_c YBCO films on Ni-based and on single crystal Cu templates. In that work, YBCO films deposited on highly textured LMO buffer layers on Ni and Ni-alloy tapes showed high superconducting transition temperatures (T_c = 90–92 K) and high J_c (77 K, self-field) values $\approx 1.3 \times 10^6$ A/cm^2. Here, we report the achievement of high-J_c ($> 1 \times 10^6$ A/cm^2 at 77 K) YBCO coatings on biaxially textured Cu substrates. The structural, magnetic (hysteretic loss), electrical, and superconducting properties of these short prototype conductors are reported.

Biaxially textured, 50-μm-thick Cu tapes were prepared by consecutive cold rolling of copper bars to greater than 95% deformation. After the final rolling, the substrates were annealed in vacuum at 800°C for 1 h in a vacuum furnace with a base pressure of 2×10^{-6} Torr, to obtain the desired {100}(100) cube texture. Deposition of the Ni overlayers was performed by dc-magnetron sputtering in a reducing forming-gas (96%Ar + 4% H_2) environment at a substrate temperature of 500°C. The Ni film thickness was ~1.7 μm. Conditions for deposition of Ni were optimized by examining the quality of epitaxy and surface roughness of the Ni films by atomic force microscopy. Subsequent growth of LMO layers was accomplished by rf-magnetron sputtering at temperatures ranging from 570 to 670°C. Typical sputtering conditions consisted of a sputter-gas mixture of forming gas and 2×10^{-5} Torr of H_2O at a total pressure of 4 mTorr. Water vapor provided low-level oxygen for the stability of the oxides, and forming gas helped suppress the oxidation of the Ni film surface as well as the Cu tape. The LMO thickness was controlled at about 300 nm.

The YBCO films were grown by pulsed laser deposition (PLD), using a KrF excimer laser system operated at an energy density of ≈ 2 J/cm^2 and a repetition rate of 15 Hz. During YBCO deposition, the substrates were maintained at 780°C in 120 mTorr of O_2. After deposition, the samples were first cooled to 500°C at a rate of 5°C/min; then the O_2 pressure was increased to 550 Torr, and the samples were cooled to room temperature at the same rate. Typical YBCO film thicknesses were 200 nm. Film crystal structures were characterized with a Huber high-resolution X-ray diffractometer (XRD), and microstructural analyses were conducted using a JOEL model JSM-840 scanning electron microscope (SEM). Magnetization measurements were conducted in a superconducting quantum interference device (SQUID)-based magnetometer at temperatures between 5 and 100 K, in fields, H, up to 60 kOe. A standard four-probe technique was used to evaluate the electrical transport properties, including T_c and J_c of the YBCO films. For those measurements, electrical contacts of silver were deposited onto the samples

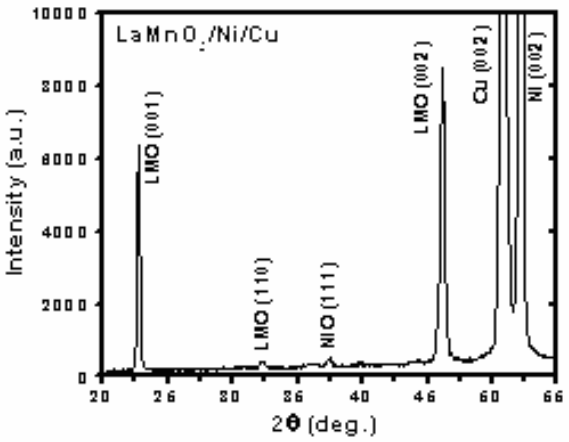

Fig. 1.62. XRD θ-2θ pattern of LMO film grown on a Ni-capped biaxially textured Cu substrate.

with dimensions of 20 mm in length and 3 mm in width using dc-magnetron sputtering followed by O_2 annealing in 1 atm for 30 min at 500°C. Values of J_c were defined at a 1-μV/cm criterion.

Figure 1.62 shows the XRD θ-2θ spectrum of a buffered Ni/Cu substrate with the LMO deposited at 570°C. It is clear from the figure that both the Ni and LMO layers exhibit a good *c*-axis-oriented growth on Cu, as evidenced by the strong (00*l*) reflections. The ratio of integrated intensities for the LMO (110) to (002) rocking curve peaks is less that 4%, indicating that an insignificant volume of the LMO is (110) textured. The presence of this component may be attributed to the presence of a small amount of (111) oriented NiO at the interface after LMO deposition. Epitaxial orientation of the LMO buffer layers was characterized by XRD pole figure analysis.

Typical background-corrected logarithmic (111) pole figures of a 300-nm-thick LMO film, along with that of the underlying Cu substrate, are illustrated in Figs. 1.63 (a) and (b), respectively. Both reveal sharp cube texture and cube-on-cube epitaxy with the in-plane LMO[110]//substrate[110]. Quantitative analyses of the pole figure intensities indicate cube volume percentages of 95% and 96%, for the LMO layer and Cu substrate (along with the Ni overlayer), respectively. The ω-scan rocking curve on the (002) and ϕ-scan on the (111) peak reflections for LMO, Ni, and Cu yielded out-of-plane and in-plane peak-width FWHM of $\Delta\omega = 9.2^o$, 7.7^o, 6.6^o and $\Delta\phi = 8.9^o$, 6.8^o, 6.3^o, respectively. Clearly, a good epitaxial relationship was obtained among the layers in the multilayer stack. The slight increase in both out-of-plane and in-plane texture from the Ni/Cu substrate to the LMO layer probably arises from the relatively low deposition temperature for the growth of LMO layers. Optimization of processing conditions for LMO is under way to develop nearly complete (00*l*) texture with reduced FWHM values.

The YBCO films deposited on this LMO/Ni/Cu substrate were epitaxial with out-of-plane and in-plane FWHM of $\Delta\omega = 9.3^o$ and $\Delta\phi = 8.5^o$, respectively, and exhibited a smooth, uniform, and dense surface morphology, as illustrated by the SEM micrograph in Fig. 1.64. This surface microstructure is similar to that observed for the YBCO films on LMO buffered Ni-based substrates. Electrical transport and superconducting property characterization results are shown in Fig. 1.65, which

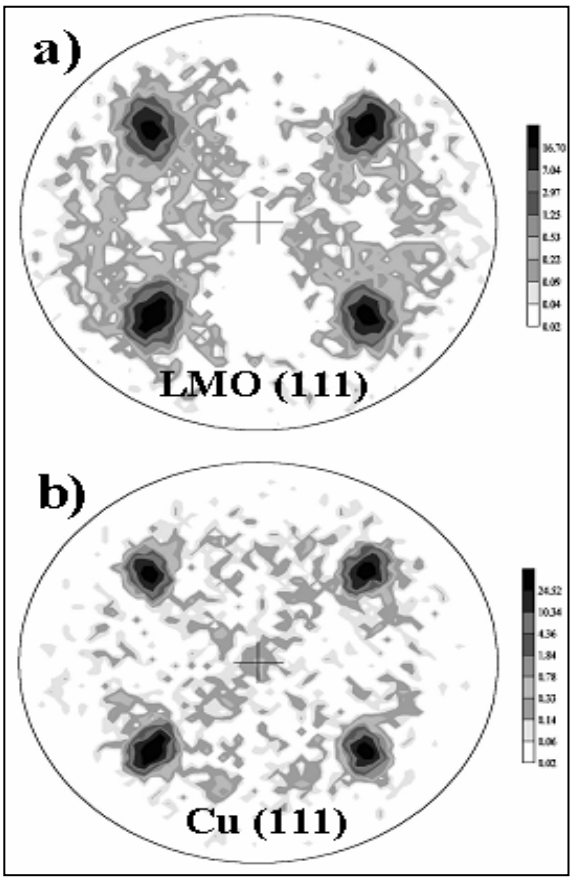

Fig. 1.63.The background-subtracted, logarithmic scale (111) pole figures of (a) a 300-nm-thick LMO film deposited on Ni/Cu and (b) the underlying biaxially textured Cu substrate.

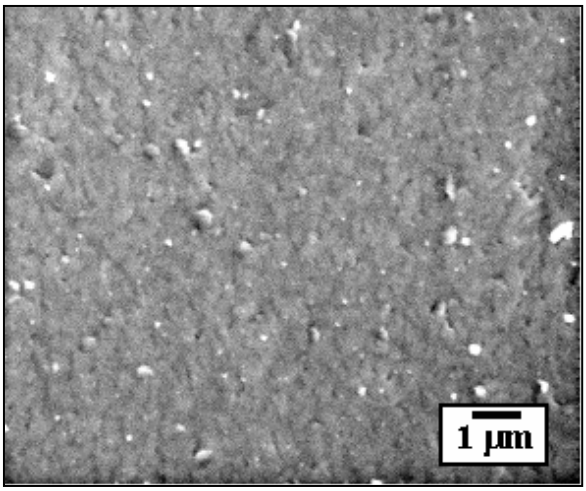

Fig. 1.64. SEM micrograph of the surface morphology for a YBCO film grown on LMO/Ni/Cu architecture.

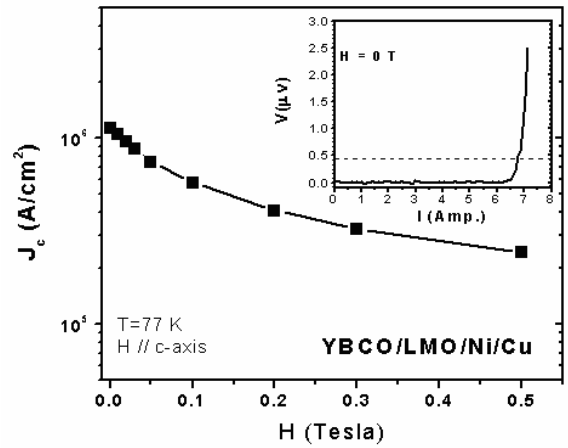

Fig. 1.65. Magnetic field dependence of the transport J_c, measured at 77 K, for a YBCO film grown on LMO/Ni buffered Cu substrates. The inset shows the I-V curve for the same sample measured in self-field. The dashed line designates the voltage criterion to extract J_c.

displays the magnetic field dependence of transport $J_{c,t}$ at 77 K, with the field applied parallel to the *c*-axis. The inset of Fig. 1.65 shows the self-field I-V curve of the YBCO/LMO/Ni/Cu, yielding an I_c value of 6.75 A (at 1-μV/cm criterion) with the corresponding $J_{c,t}$ of 1.1×10^6 A/cm^2. The high-T_c value ~90 K implies that LMO not only blocks Ni diffusion (as previously shown in our work on Ni-based substrates) but, in conjunction with the nickel layer, it also acts as a Cu diffusion barrier. Studies are being made to confirm the overall levels of interdiffusion. The present results represent the first reported achievement of high-J_c YBCO on Cu-based RABiTS™.

To examine the current-density–temperature characteristics of YBCO/LMO/Ni/Cu conductors, magnetic hysteresis measurements were carried out with a magnetic field applied normal to the tape. These measurements were conducted on another sample having a lower transport $J_{c,t} = 0.6 \times 10^6$ A/cm^2, where the processing parameters of both the Ni and LMO layer depositions were not yet optimized. Nevertheless, the measurements should adequately reflect the relative current density vs temperature behavior of YBCO films on Cu-RABiTS™. The magnetic field dependence of persistent current density, $J_{c,m}$, as estimated from the magnetic-hysteresis loops using the Bean critical state model, $J=10(M_+ - M_-)/R_{eff}$, is plotted in Fig. 1.66. Here, M_+ and M_- are the upper and lower branch magnetization values, respectively. These values were corrected for the small ferromagnetic hysteresis of the substrate measured at 100 K. The effective circulation radius, R_{eff}, of the current is estimated using $2R_{eff} = b\,(1\text{-}a/3b)$, where *a* and *b* are the short and long transverse dimensions of the sample, respectively. We assumed that the critical current in the *ab*-basal plane of the YBCO film is isotropic and the total area covered by the film is used as the relevant loop dimension rather than the grain size. Values in zero applied field range from $J_{c,m} = 3.5$

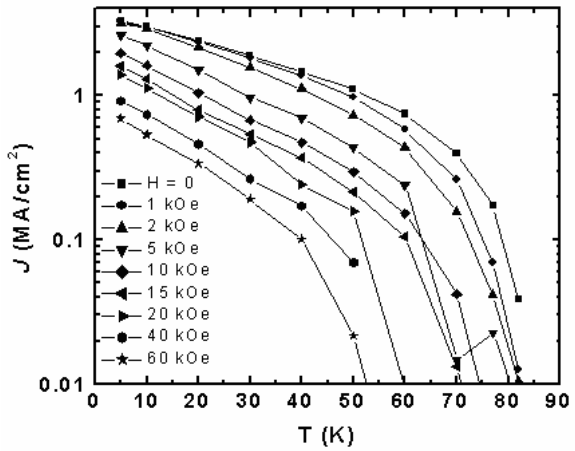

Fig. 1.66. The persistent current density *J* vs temperature *T*, with magnetic field *H* applied normal to the tape. Values were obtained from a critical state analysis of the magnetization, and were corrected for hysteresis from the Ni-layer.

MA/cm^2 at 5 K to 0.18 MA/cm^2 at 77 K. The latter value is about one-third that of $J_{c,t}$ obtained by the transport measurements (0.6×10^6 A/cm^2). The discrepancy is most likely due to the differences in electric field criteria in defining J_c. As the temperature increases, $J_{c,m}$ decreases approximately exponentially for a wide range of fields with $J_{c,m}(T) \cong J_{c,m}(0) \exp(-T/T_o)$, with $T_o \approx 23$ K. These results imply that thermally activated depinning of vortices produces the observed falloff of $J_{c,m}$.

Besides the J_c performance, another important consideration is the overall energy loss in alternating current applications. It is well known that ac gives rise to hysteretic loss in the superconducting material, even for currents below I_c. Moreover, additional losses can occur in a ferromagnetic (FM) substrate material due to hysteretic movement of magnetic domains. In the present case, salient features of the FM Ni layer on the Cu substrate need to be determined. While the Cu substrate is nonmagnetic, the Ni overlayer introduces an additional mechanism for potential energy loss in ac due to the FM hysteresis. Thus we measured the magnetic response of the substrate at 100 K, just above the superconductive T_c, but far below the 627 K Curie temperature of Ni. The results are shown in Fig. 1.67. With H || tape to reduce demagnetizing effects, the applied fields of ±800 G nearly saturate the Ni; the full saturation moment yields a value of 1.7 μm for the Ni thickness. The coercive field of the coating is about 20 Oe, somewhat larger than that of pure RABiTS™ nickel, apparently due to additional defects in the deposited film, and possibly arising from some level of copper interdiffusion. By integrating the area inside the hysteresis loop, we obtain an FM loss per cycle per unit area of tape = 11.4 erg/cm^2 per cycle. This is "worst case scenario" for applications because the material experiences its largest possible hysteretic loss. Referenced to a unit volume of Ni, this corresponds to 6.8×10^4 erg/cm^3 per cycle, compared with a loss (at 77 K) of 1.8×10^4 erg/cm^3 for fully processed, biaxially textured Ni-RABiTS™ and 0.2×10^4 erg/cm^3 for similarly processed Ni-7 at % Cr alloy with reduced ferromagnetism. However, the present materials contain little actual Ni, as the layer is thin. For example, for a 1-m length of tape with width of 1 cm and substrate metal thickness of 50 μm, operating at 60 Hz: for the present Cu-based substrate, the maximum FM power loss would be 7 mW, compared with 42 mW for the all-Ni case and 6 mW for the case with Ni–7 at. % Cr. These losses of 6 to 7 mW correspond to modest additions (10 to 20%) to the hysteretic losses expected in achievable YBCO-based conductors. Of course, in conductor configurations either with reduced Ni overlayer thickness or with lower ac magnetic fields, the FM losses would be smaller still.

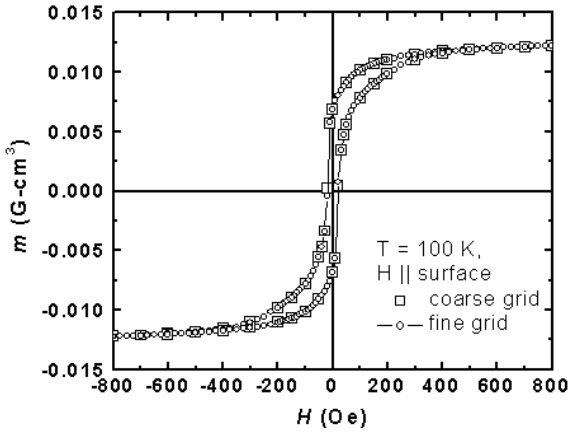

Fig. 1.67. The ferromagnetic moment hysteresis loop of a YBCO/LMO/Ni/Cu coated conductor at *T* = 100 K, with *H* in the plane of the tape.

In summary, we have demonstrated the successful fabrication of high-quality epitaxial YBCO coatings on nonmagnetic, biaxially textured Cu substrates, employing the layer sequence $LaMnO_3$/Ni/Cu. Property characterization revealed good-quality crystalline structure and surface characteristics for YBCO films on this architecture. For 200-nm-thick YBCO, self-field J_c values resulting from the Ni overlayer should be small compared to the hysteretic losses arising from the superconducting layer on an implemented coated conductor. These observations demonstrate a potentially promising route toward the fabrication of low-cost, nonmagnetic YBCO-based coated conductors for power applications of superconductivity. Further support requires additional studies that provide optimization of the nickel and LMO layer thicknesses and quality, especially with regard to their stability and function under conditions for the deposition of practical, thick YBCO coatings. Also of interest is the development of conductive buffer layers for a stabilized overall structure.

1.10 CHARACTERIZATION OF SUITABLE BUFFER LAYERS ON Cu AND Cu-ALLOY METAL SUBSTRATES FOR DEVELOPMENT OF COATED CONDUCTORS

C. Cantoni, D. K. Christen, E. D. Specht, M. Varela, A. Goyal, Y. Xu, and S. J. Pennycook (ORNL); J. R. Thompson (University of Tennessee)

We investigated several issues associated with the development of buffer and superconducting layers directly on Cu substrates, including poor Cu oxidation resistance, high Cu thermal expansion, and surface sulphur-mediated buffer layer epitaxy.

The fast Cu oxidation is due to the very high diffusivity of Cu ions through CuO/Cu_2O and the consequent inability of the native metal oxide to be self-protective (at YBCO processing conditions). This poses stringent requirements on the buffer layers to be used on Cu. Such layers need to block cation and oxygen diffusion more efficiently than the $Y_2O_3/YSZ/CeO_2$ buffer combination on Ni-W alloy, for which self-passivation of the native oxide at the buffer/substrate interface does occur.

Another concern related to the use of Cu-RABiTS™ is the large strain imposed by the substrate on the YBCO film during cool-down. In fact, the thermal expansion coefficient of Cu can be estimated as 18×10^{-6} K^{-1} in the temperature region of interest (the same quantity for Ni is 16×10^{-6} K^{-1}). On the sole basis of the difference between Cu and YBCO thermal expansion ($a_{YBCO} = 12 \times 10^{-6}$ K^{-1}), a residual strain of ~ 0.45% in the YBCO film can be calculated. This value is very close to the failure limit of 0.5% for compressive strain, as experimentally derived by bending tests in coated conductors.

Although an ordered sulphur superstructure is necessary on the Cu surface (just as for Ni) to nucleate and grow many cubic oxides, such superstructure cannot be formed on Cu by controlling sulphur adsorption as is done for Ni and Ni alloys. Therefore, the choice of possible buffer layers on Cu is limited to materials that can be grown on a clean fcc metal surface.

Among the possible oxides used today in coated conductor technologies, MgO is certainly a good candidate as a barrier layer for oxygen in buffer layer architectures intended for Cu. Previous O^{18} transport studies indicate that the oxygen diffusion coefficient of MgO at 800°C is roughly 10^{-20} cm^2/s, nearly 13 orders of magnitude smaller than that of YSZ at the same temperature. Although MgO is known to grow on clean fcc metal surfaces, this layer alone is not a suitable buffer layer due to rapid Cu diffusion. For that reason, a seed layer of TiN was introduced as a Cu diffusion barrier between MgO and the metal substrate. TiN is one of the most widely investigated barrier materials in Cu metallization for integrated circuit technology, and is also structurally compatible with MgO, having the same rock-salt crystal structure and a lattice mismatch of only 0.5%. Further, we found that TiN could be easily grown epitaxially on Cu without the need for a sulphur template. Finally, we deposited $LaMnO_3$ (LMO) as a cap layer on MgO for good lattice match and chemical compatibility with YBCO. LMO was selected from among other perovskites ($SrTiO_3$, $SrRuO_3$) because of the wide window of deposition conditions for single-oriented (100) films on MgO.

The Cu substrates used for this study include Cu (001) single crystals, Cu (001) epitaxial films deposited on (001) MgO or (001) $SrTiO_3$ (STO) single crystals, {100}<100> textured Cu tapes, and {100}<100> textured Cu-48%Ni-1%Al tapes. All the oxide buffer layers were grown in an ultrahigh vacuum (UHV) pulsed-laser deposition (PLD) chamber equipped with a load lock for loading samples and targets, a reflection high-energy electron diffraction (RHEED) system, a residual gas analyzer, and a Kaufman-type ion source for sputter-cleaning. The laser used for ablating target materials was a KrF excimer laser with a power of 150 W and a wavelength of 248 nm. The laser fluence varied between 4 and 5 J/cm^2, and the repetition rate between 10 and 20 Hz.

Fully (100)-oriented, epitaxial TiN films were grown using a TiN target in a nitrogen background pressure of 3.0 to 10×10^{-5} Torr and a substrate temperature of 580°C. The film nucleation and growth were monitored by RHEED, and a cube-on-cube epitaxial relationship was observed between the Cu substrate and TiN film. After a nearly 200-nm-thick TiN film was grown, the nitrogen was pumped out, the substrate temperature was increased to 600°C, and oxygen was introduced in the chamber with a partial pressure of 0.8 to 1.0×10^{-5} Torr for the growth of the MgO layer. At such oxygen pressure, the

TiN RHEED pattern exhibited spots in addition to those typical of a clean (001) surface. Figure 1.68 shows the RHEED pattern produced by a clean TiN surface and that of a TiN film when exposed to the oxygen pressure and temperature indicated above. The latter suggests the presence of a 6 × 6 superstructure, likely formed by oxygen adatoms bonded on film surface lattice sites. This superstructure was stable at the deposition condition employed for the MgO buffer layer, and fully (001) oriented MgO films could be grown on this surface. Thermodynamic data of free energy of formation for MgO and TiO indicate higher stability of the former oxide than the latter. The formation of MgO is thus favored over the formation of TiO, and the O adatoms initially present on the TiN surface at the time the MgO deposition starts are likely incorporated in the growing MgO film. Once a 100-nm-thick MgO film was grown, an additional LMO cap layer was deposited in situ at a temperature of 620°C and an H_2O partial pressure of 5 to 8 mTorr.

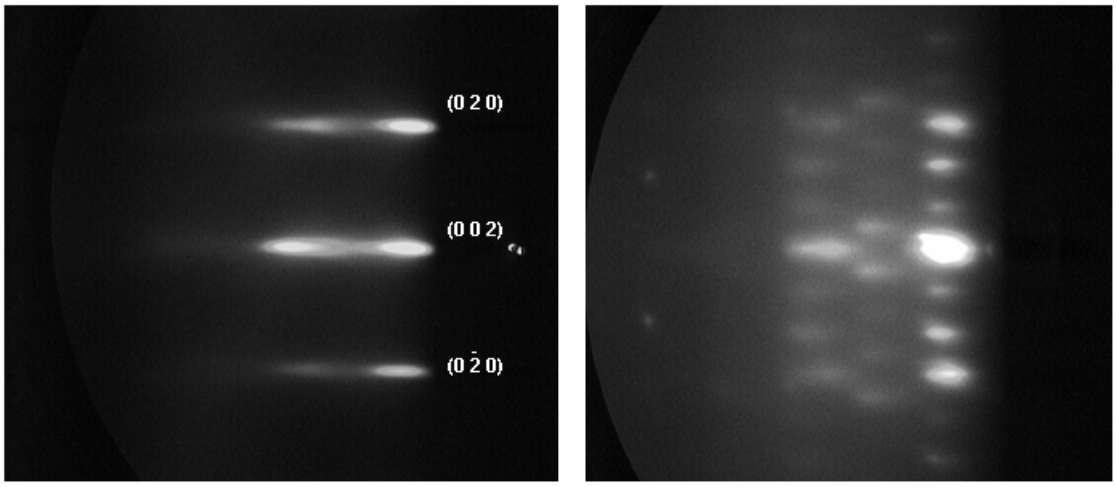

Fig. 1.68. RHEED patterns of an epitaxial TiN film on (001) Cu as deposited (a) in a vacuum background and (b) when exposed to an oxygen partial pressure of 8×10^{-6} Torr at a temperature of 600°C.

Figure 1.69 shows the critical current density of an YBCO film grown by PLD on a buffered Cu (001) epitaxial film on MgO single crystal. The critical current was measured by electrical transport as a function of the applied magnetic field at 77 K. The thickness of the laser-ablated YBCO film (180 nm) was measured by Rutherford back scattering (RBS) and the corresponding J_c in self-field was 3.5 MA/cm^2. Such a value is comparable with those obtained on YBCO films deposited directly on single-crystal STO substrates. The behavior of J_c in field and the value of irreversibility field (H_{irr} = 7 T) are also typical of YBCO films on STO or LAO single crystals.

Figure 1.70 shows a low-magnification Z-contrast STEM image of the multilayered structure LMO/MgO/TiN grown on the Cu film on MgO single crystal, after deposition of the YBCO top film. All the interfaces appear clean, and there is no evidence of reactions or interdiffusion between the different layers. Further, oxygen presence at the Cu/TiN interface was not detected from in situ electron energy loss spectroscopy (EELS) measurements.

To estimate the actual residual strain induced by the Cu substrate in the superconductor, we deposited the same buffer layer architecture and YBCO film described above on a 1.5-mm-thick Cu crystal. The Cu crystal was nearly a single crystal with a FWHM of 0.28° for the (001) rocking curve, and

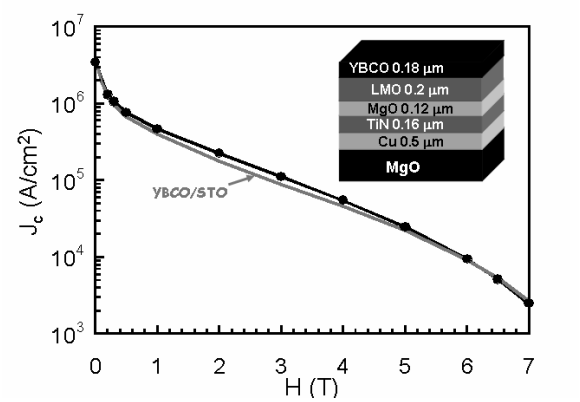

Fig. 1.69. Critical current density vs applied magnetic field for a YBCO film deposited on LMO/MgO/TiN/Cu/MgO (crystal) (black line and dots), and a typical YBCO film deposited on single crystal STO (gray line).

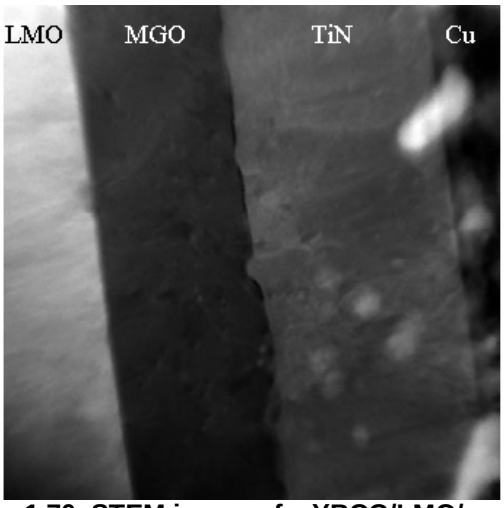

Fig. 1.70. STEM image of a YBCO/LMO/MgO/TiN/Cu multilayer structure on MgO single crystal acquired with high-angle annular dark field detector. This technique provides direct compositional contrast, and the heavier elements appear brighter.

a [001]-tilt of 1°. The critical current density was derived in this case by measuring the sample magnetic moment hysteresis in a SQUID magnetometer as a function of temperature and field. The observed sharp T_c transition and the high value of J_c at low temperature (J_c [5 K] = 1.42 × 10^7 A/cm^2) were indicative of an absence of weak-links. The value of J_c at 77 K and low magnetic field was 1 MA/cm^2. We used high-resolution X-ray diffraction (XRD) to measure the lattice parameters of the layers composing our heterostructure. By using (002) and (111) type reflections, we calculated a lattice distortion of (a-c) / a = -1.31% in the TiN film and 0.04% for MgO. The YBCO lattice constants were evaluated using (005), (006), and (113) reflections, and the residual strain was estimated to be ε_{zz} = 0.25%. This value is significantly lower than the 0.45% calculated on the basis of differences in thermal expansion, and closer to the residual strain measured on the 50-μm-thick Ni-3%W substrate (0.08%). This result indicates that strain is released by introduction of dislocations within the buffer layers or at their interfaces. An example of such mechanism is illustrated in Fig. 1.71, which shows a high-magnification Z-contrast STEM image of the interface between MgO and LMO. The large lattice mismatch between the two oxides (7.3%) is accommodated in the early stages of film nucleation with the introduction of disorder and misfit dislocations in the very first atomic planes of LMO, leading to virtually unstrained growth of the rest of the film. Another strain relief mechanism that can occur when stiff and brittle films are deposited on soft and ductile metals is the insertion (and motion) of dislocations in the underlying metal substrate rather than the film.

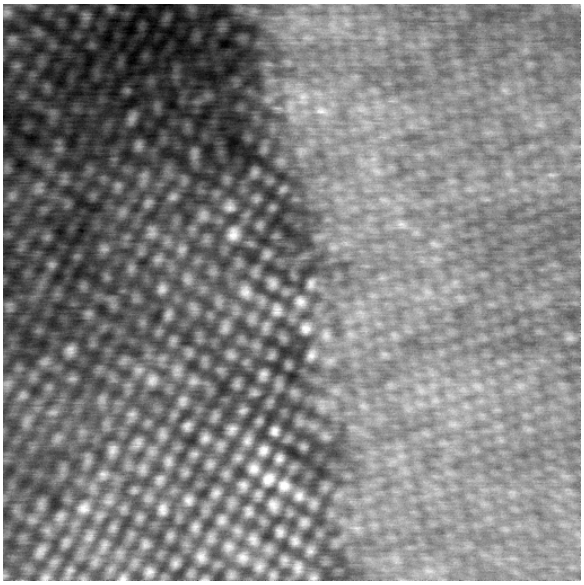

Fig. 1.71. High-resolution STEM micrograph of the LMO/MgO interface (LMO on the left, MgO on the right).

To complete our study, we grew the LMO/MgO/TiN buffer layer heterostructure and the YBCO film on 99.99% pure Cu tapes that were thermomechanically processed to obtain a biaxial texture with XRD FWHMs of 6° and 5° for the in-plane and out-of-plane alignment. In this case, the magnetically

determined J_c at 77 K and low magnetic field was 0.7 MA/cm^2, corresponding to a transport J_c value of nearly 1.5 MA/cm^2. Although this is a very encouraging value, it is not consistent with the optimal degree of texture of the buffered substrate, which, according to previous studies on the dependence of transport J_c on grain boundary distribution in coated conductors, should correspond to a J_c around 2.5 MA/cm^2. These samples also showed a lower T_c (T_c = 88.5 K) than typical YBCO films on coated conductors, which suggests the possibility of chemical contamination of the YBCO film by outward Cu diffusion. SEM measurements were consistent with this hypothesis and in particular showed sparse Cu_2O outgrowths in the form of big particles and, sometimes, straight lines aligned with the substrate rolling direction. We attributed the formation of these outgrowths to oxidation that occurs during the YBCO deposition on the unprotected back side and edges of the substrate and propagates toward the front. Outgrowths form preferentially in correspondence to defects, such as pinholes or scratches introduced on the substrate surface during the rolling process. Energy-dispersive X-ray diffraction (EDX) measurements performed before and after subsequent high-temperature vacuum anneals on TiN/Cu bi-layers deposited on 7° STO bi-crystals indicated no detectable Cu diffusion through the TiN grain boundary. This experiment suggests that the occurrence of the Cu_2O outgrowths is not related to the presence of low-angle grain boundary in the textured substrate. No such Cu_2O eruptions were in fact observed along the Cu substrate grain boundaries, whose traces are still visible through the YBCO film.

One of the possible ways to avoid oxidation from the back side is to alloy Cu with a more oxidation-resistant metal. We investigated the performance of nonmagnetic Cu-48%Ni with 1 to 1.5% Al using the same buffer layer architecture used on pure Cu and a 0.3-μm-thick YBCO film grown by PLD. The small percentage of Al in such a substrate is very effective in passivating the CuNi alloy, which otherwise can oxidize nearly as fast as pure Cu. Passivation occurs by formation of a thin surface Al_2O_3 layer at extremely low oxygen partial pressure. The alumina layer is very desirable for protecting the back side but is not a suitable template for well-oriented buffer or superconducting layers. Therefore, the Al_2O_3 layer that had formed on the substrate front surface during the texturing anneal was removed by ion sputtering prior to the deposition of the seed layer. Although the TiN deposition occurs without introduction of oxygen in the deposition chamber, the Al present in the substrate can readily diffuse up to the surface at temperatures greater than 400°C and can oxidize in the presence of residual background oxygen, thus corrupting the buffer layer epitaxy. To avoid this problem, we deposited an initial 100-Å-thick TiN layer at 400°C. The cube epitaxial growth, which does not normally occur at such low temperature, was achieved by locally increasing the energy of the impinging species with an Ar^+ ion beam of 400 to 500 eV in energy. The rest of the TiN film and the subsequent buffer layers were deposited at the conditions used for pure Cu substrates.

Figure 1.72 shows the XRD θ–2θ pattern acquired on a YBCO/LMO/MgO/TiN/CuNiAl sample that showed a transport J_c of 2 MA/cm^2. Only YBCO and substrate peaks are present, and there is no evidence of unwanted oxide peaks. Four-circle diffractometer measurements revealed optimal alignment of the YBCO film with a FWHM of 2.8° for the out-of-plane texture (in the rolling direction) and 6.5° for the in-plane texture.

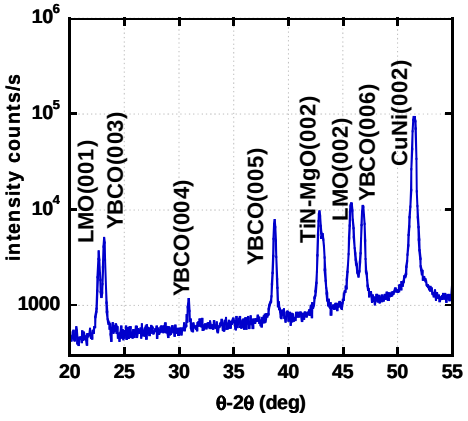

Fig. 1.72. θ–2θ XRD scan of a YBCO/LMO/MgO/TiN/CuNiAl sample.

In conclusion, we have shown that a multilayered structure consisting of LMO/MgO/TiN acts as a good diffusion barrier and structural template for the deposition of high-J_c YBCO film on pure Cu and Cu alloy substrates. Each of the three buffer layers has a unique property that is essential to

suppress Cu oxidation, keep the interfaces clean, and accommodate strain. TiN is a barrier to outward Cu diffusion; MgO is a barrier to inward oxygen diffusion and is stable enough thermodynamically to be grown on TiN. LMO provides structural compatibility with the YBCO lattice.

1.11 DIFFERENCES IN J_c HOMOGENEITY AND MAGNETIC FIELD DEPENDENCY IN EX SITU BaF_2 PRECURSORS ON Ni-W RABiTS™ PROCESSED IN OVERPRESSURE AND REDUCED-PRESSURE ENVIRONMENTS

D. F. Lee, J. Yoo, K. J. Leonard, L. Heatherly, A. A. Gapud, P. M. Martin, M. Paranthaman, A. Goyal, and D.M. Kroeger

1.11.1. Introduction

High-J_c YBCO films have been obtained at ORNL by converting e-beam–deposited BaF_2 precursors under vastly different environments. One "atmospheric" reel-to-reel conversion system employs an extended transverse-flow chamber with high gas flow rate [1]. Due to the high flow rate and small exhaust nozzles (125-μm holes in Inconel 601 tubes), pressure is found to build up within the chamber, leading to a typical conversion pressure of ~ 1.5 atm. Another reduced-pressure system [2] incorporates pumping on the exhaust such that a chamber pressure of < 0.1 atm can be maintained during conversion. Since HF buildup both within the conversion chamber and along the sample surface will influence precursor conversion rate, it is also expected to affect the sample homogeneity as well as superconducting properties. To examine these issues, we have produced YBCO films of 0.9- and 0.3-μm thicknesses in the two systems and are in the process of comparing their characteristics.

1.11.2. Experimental

The "atmospheric" overpressure conversion system used in this investigation consists of a long reel-to-reel reaction chamber with seven 30-cm-long transverse flow modules. Gas inlet and outlet tubes with small nozzle holes are situated on either side of the sample. Standard components, including gas supply, water bubblers, and oxygen sensors, are connected to the reaction chamber where necessary. In addition, multiple pressure sensors are strategically located such that pressures at gas inlets and gas outlets of different modules as well as that of the reaction chamber can be continuously monitored. Reels are connected to the ends of the reaction chamber, which sits within the cradle of a custom-built 2-m-long 22-zone tube furnace. Temperature of the hot zones of this furnace can be individually controlled such that a wide variety of thermal profiles, as well as a sizable range of ramp-up temperature gradients may be obtained. By continuously moving the sample at chosen speed through a selected thermal profile, a prescribed conversion schedule can be performed.

The reduced-pressure chamber used in this work contains a sample holder that is equipped with gas delivery and exhausted tubes with nozzles, and samples are mounted such that a transverse flow pattern similar to that of the "atmospheric" chamber was used. Necessary controls and monitoring devices such as mass flow controllers, pressure sensors, and oxygen sensors are strategically placed at various locations, and reduced chamber pressure is achieved by pumping the exhaust. Under typical processing conditions, a reduced chamber pressure $P(_{TOT})$ of < 0.1 atm can be attained.

1.11.3. Results

A 0.9-μm-thick precursor film designated for conversion in the "atmospheric" system was obtained by depositing BaF_2 precursor onto a 45-cm-long by 1-cm-wide Ni-W RABiTS™ in three passes. The tape was then loaded onto the payout reel and was converted for 200 min at 740°C, $P(O_2)$ of 140 mTorr, flow rate of 5.5 L/min/module, and $P(H_2O)$ ranging from an initial level of ~ 5 Torr to a final level of 30 Torr. This combination of conversion parameters resulted in a YBCO conversion rate of 0.75 Å/s in a P_{TOT} of ~ 1.5 atm. The converted conductor has been found to possess an end-to-end I_c of 114.8 A, with an equivalent J_c value of 1.28 MA/cm^2. A short (~ 3 cm-long) segment was cut from the long tape, and the

segmental I_c was measured to be 110 A across the full width of the sample. Edge-to-edge I_c variation was determined by cutting the full sample into three sections, as shown in Fig. 1.73. The section closest to the gas inlet is labeled "A," whereas the one furthest from the inlet is labeled "C." Critical currents of these sections were measured and are listed in Table 1.4. It can be seen from the table that J_cs of these sections vary from 1.24 MA/cm^2 for the section next to the gas inlet to 0.98 MA/cm^2 for the one furthest from the inlet. This represents a 27% change in J_c; the difference is believed to be the result of inhomogeneous conversion due to HF buildup at the downstream sample surface. Such nonuniformity in sample property across a 1-cm scale does not bode well for the strategy of increased production by fabricating wide tapes followed with slitting.

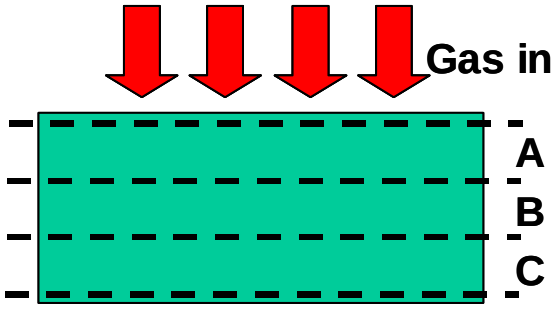

Fig. 1.73. Schematic of the 3-mm-wide sections cut from the full sample. Also shown is the sample location-gas flow relationship.

Another similarly prepared 0.9-μm-thick precursor film was processed in the reduced-pressure chamber. For the present investigation, a ~ 2.5-cm-long stationary sample was cut from the stock material and was mounted in an orientation such that a transverse flow geometry similar to that of the overpressure chamber was used. Processing conditions used in the experiment are as follows: conversion temperature of 740°C, P(O_2) of 150 mTorr, P(H_2O) that gradually increased from < 7 Torr to 11 Torr, conversion time of 60 min, and a chamber pressure of 0.07 atm. Due to enhanced HF removal, the YBCO conversion rate was more than three times that of the overpressure chamber. Full width I_c of the sample has been determined to be 110.5 A, which is virtually identical to that of its overpressure counterpart. The sample was again cut into three 3-mm-wide sections, and J_cs were determined for each sections (see Table 1.4). It can be seen from the table that the edge-to-edge property of this sample is much more uniform; J_c changes from 1.28 MA/cm^2 to 1.20 MA/cm^2. This variation of 6.7 % is similar in magnitude to the typical J_c variability along the sample length, and reflects the advantage of enhanced HF removal on YBCO conversion.

Table 1.4. Full 1-cm and 3-mm sectional J_cs of 0.9-μm-thick YBCO samples converted in overpressure and reduced-pressure conditions

Sample	Width (cm)	I_c (A)	I_c/cm (A/cm)	J_c (MA/cm^2)
Chamber pressure ~ 1.5 atm				
Full	1	110.00	110.0	1.22
A	0.301	33.53	111.4	1.24
B	0.305	29.02	95.1	1.06
C	0.301	26.68	88.6	0.98
Chamber pressure 0.07 atm				
Full	1	110.50	110.5	1.23
A	0.296	34.05	115.0	1.28
B	0.297	33.29	112.0	1.24
C	0.322	34.83	108.1	1.20

In addition to the difference in sample homogeneity, the magnetic field dependence of J_c has been found to differ for samples processed in the two reaction chambers. Variations in J_cs of the two 0.9-μm-thick YBCO samples with applied magnetic field (B//c) at 77 K and 65 K are shown in Fig. 1.74. It can be seen from this figure that at low to moderate fields (less than ~ 4 T at 77 K and less than ~ 8.5 T at 65 K), the sample processed in the overpressure condition exhibits a much stronger field dependency. At higher fields, there is a crossover such that the sample J_c is less dependent on field strength. This stronger field dependency of samples converted in the overpressure condition is not limited to 0.9-μm-thick films. The normalized field dependencies of a collection of representative samples, including 0.3- and 0.9-μm YBCO obtained from the two chambers are shown in Fig. 1.75. Also included in Fig. 1.75 is the behavior of a 0.3-μm YBCO on a non-ORNL substrate processed in the overpressure condition. It can be seen from Fig. 1.75 that regardless of YBCO thickness or substrate, the samples processed in the overpressure condition routinely exhibit a stronger field dependency; a ~ 6.5 to 1 drop at 0.5 T instead of the typical ~ 4 to 1 drop shown by the reduced-pressure samples. Whether this strong field dependency is the result of conversion in an

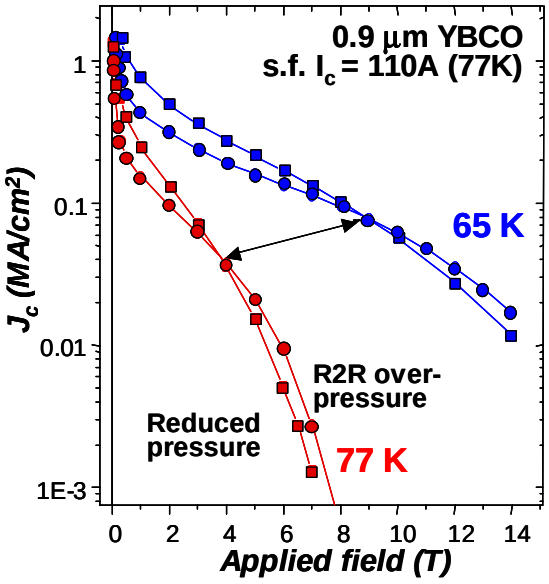

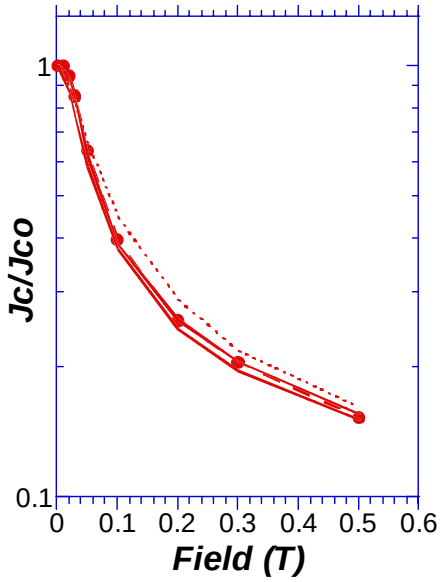

overpressure environment, the long residence time at elevated temperatures, or some other subtle parameters is not known; however, the consistently different field dependencies offered by the two systems afford a unique opportunity for probing an effective pinning mechanism that can be influenced by processing. Work is under way to identify the pinning centers responsible for the different field behaviors.

1.11.4. Summary

Ex situ YBCO films have been processed in both overpressure and reduced-pressure conditions. Even with a high gas flow rate, the edge-to-edge homogeneity of the 0.9-µm-thick YBCO sample processed in the overpressure environment is believed to be affected adversely by HF buildup. With an overall J_c of 1.22 MA/cm^2, the J_c varied from a value of 1.24 MA/cm^2 at the leading edge to 0.98 MA/cm^2 at the trailing edge, a change of 27%. In contrast, a similar precursor tape processed under a reduced-pressure environment resulted in an overall J_c of 1.23 MA/cm^2, which is virtually identical to that of the overpressure sample. However, the edge-to-edge sample homogeneity for the reduced-pressure tape has been found to be much superior; the J_c varied from a value of 1.28 MA/cm^2 at the leading edge to 1.20 MA/cm^2 at the trailing edge, a change of only 6.7%. In addition, the conversion rate for the reduced-pressure material was three times faster than that of the overpressure condition. Moreover, J_c dependency on magnetic field for the overpressure samples is found to be stronger than the reduced-pressure cases, regardless of YBCO film thickness or substrate fabrication method. Work is under way to identify the pinning centers responsible for the different field behaviors.

1.11.5 References

1. D. F. Lee et al., *Supercond. Sci. Technol*. (2003) (to be published).
2. J. Yoo et al., *J. Mater. Res.* (2003) (submitted).

1.12 PROCESSING OF ELECTRON BEAM CO-EVAPORATED BaF_2 PRECURSOR ON RABiTS™ IN A REDUCED-PRESSURE ENVIRONMENT

J. Yoo, K. J. Leonard, D. F. Lee, H. S. Hsu, L. Heatherly, F. A. List, N. A. Rutter, M. Paranthaman, and D. M. Kroeger

1.12.1 Introduction

As the texture quality of coated conductor substrates improves, increasing numbers of high-J_c YBCO films fabricated by a variety of methods are being reported. Ex situ processing of YBCO is an attractive alternative technique because it separates the compositional control step from epitaxial YBCO formation. Different precursors such as BaF_2 [1], MOD [2], and TFA [3] have been demonstrated successfully on these flexible substrates. Following these high-J_c demonstrations, other characteristics, such as high I_c/cm, fast YBCO conversion rate, large volumetric throughput, and cost-effectiveness in manufacturing, are becoming more important.

One of the rate-limiting factors in ex situ conversion of YBCO is believed to be HF buildup, both along the downstream sample surface and within the chamber itself, which slows the conversion process [3–5]. One approach to reduce the influence of HF is the use of an extended transverse-flow geometry. By employing a transverse-flow geometry, in which the direction of gas flow is parallel to the width of the sample, the effective conversion distance is reduced significantly. Furthermore, the presence of an extended reaction zone along the sample length enables the simultaneous conversion of a larger area of precursor, thereby reducing the total amount of processing time [4]. This approach, however, requires the use of a significant gas flow rate such that gas management may be a challenge. Another approach that is currently being investigated is the employment of a reduced-pressure processing atmosphere. It is generally believed that under such conversion environments, HF removal will be enhanced, thereby leading to the acceleration of the HTS conversion process. In addition, lower chamber pressures will result in much reduced gas use and thus will facilitate gas management.

1.12.2. Experimental

A reduced-pressure conversion chamber has been set up to process BaF_2 precursor on RABiTS™ (see Fig. 1.76). The material of this chamber is Inconel 601, which was selected based on its mechanical integrity as well as its resistance to oxidation and HF corrosion. The chamber contains a sample holder that is equipped with gas-delivery and exhaust tubes (Fig. 1.77). Short samples can be mounted such that either a longitudinal or transverse flow pattern may be used. Necessary controls and monitoring devices, such as mass flow controllers, a water bubbler, and pressure and oxygen sensors, are strategically placed at various locations. A chamber pressure range between 1.3 and < 0.1 atm can be achieved by a combination of pumping on the exhaust and adjustment of the gas flow rate.

Fig. 1.76. The reduced-pressure chamber that sits in the cradle of a tube furnace.

1.12.3. Results

To verify the ability of such a furnace in converting high-J_c precursor films, short samples were first processed without pumping. Briefly, BaF_2 precursor was co-evaporated onto a long-length Ni-W RABiTS™ in a single pass that results in a converted YBCO film thickness of 0.3 μm. Samples measuring 2.5×1 cm were cut from the stock and were converted at 740°C, $P(O_2)$ of 150 mTorr, $P(H_2O)$ of 20 Torr, and a no-pumping chamber pressure (P_{TOT}) of 1.3 atm. In this series of preliminary tests,

processing time was varied to determine the optimum conversion duration based on J_c. The results showed that the chamber configuration is capable of producing high-quality YBCO films; a maximum I_c of 42 A (J_c = 1.4 MA/cm^2) was obtained for a wet conversion time of 100 min.

With the suitability of chamber operation verified, the effect of chamber pressure was studied based on the no-pumping results. Short (2.5 × 1 cm) side samples were cut from the stock and were converted using identical parameters as those in the previous tests for 100 min (0.5 Å/s conversion rate). The only exception was that P_{TOT} was varied from 0.8 to 0.1 atm. Variation in I_c with P_{TOT} is shown in Fig. 1.78. Also included in the figure is the 1.3-atm result obtained without pumping. It can be seen in Fig. 1.78 that I_c increases with decreasing P_{TOT} until ~ 0.35 atm, where I_c becomes approximately constant with a further decrease in chamber pressure. By processing the YBCO films in a reduced atmosphere, an extremely high I_c of 64.7 A (2.16 MA/cm^2) has been obtained at 0.1 atm and 100 min of conversion.

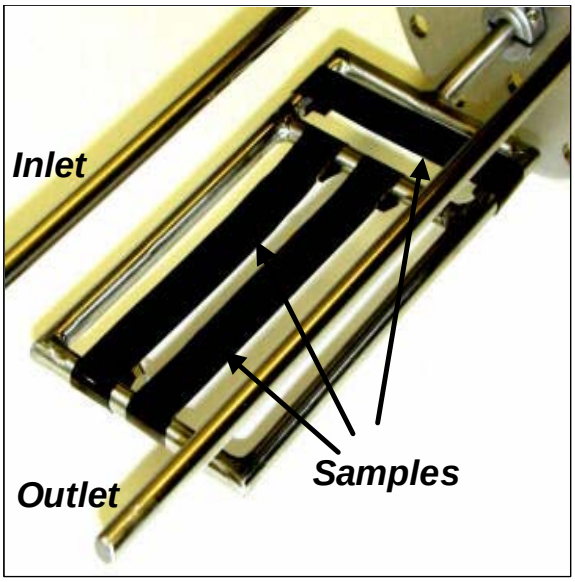

Fig. 1.77. The sample holder. Gas delivery and exhaust tubes equipped with nozzles are indicated. Samples can be oriented either parallel or transverse to the gas flow.

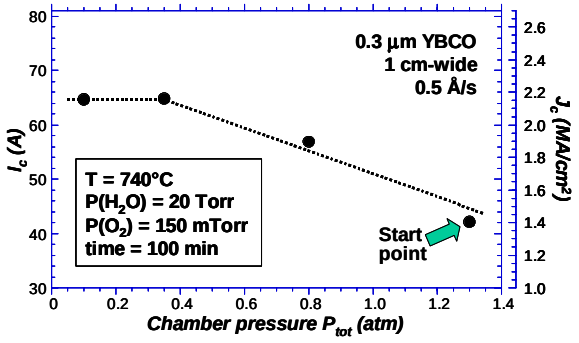

Fig. 1.78. Variation in I_c with P_{TOT} in 0.3-µm-thick YBCO on Ni-W RABiTS™.

Once the positive effect of reduced pressure was verified, the influence of P(H_2O) on sample I_c was examined. Short (2.5 × 1 cm) samples were again cut from the stock tape, and were processed at 0.1 atm for 100 min by varying the P(H_2O) from 70 to ~ 7 Torr. Variation in I_c with P(H_2O) for this series of samples is shown in Fig. 1.79. It can be seen in Fig. 1.79 that I_c increases with decreasing P(H_2O), reaching a high value of 66.2 A (2.21 MA/cm^2) at P(H_2O) of ~ 7 Torr. The beneficial effect of enhanced HF removal on conversion rate has also been confirmed in a similar set of samples that were converted for only 20 min. As seen in Fig. 1.79, the effect of P(H_2O) is similar to that of 100-min conversion. In addition, the I_cs of samples processed in P(H_2O) greater than 20 Torr are higher than those of 100 min. This is equivalent to a conversion rate of 2.5 Å/s, which is five times that of the 100-min samples. Moreover, differences in I_cs between the two sets of samples represent the detrimental effect of overconversion and highlight the advantage of a low P(H_2O).

In addition to P_{TOT} and P(H_2O), we have also studied the effect of conversion temperature on conversion rate and I_c. Short (2.5 × 1 cm) samples were cut from the long stock tape and were converted at temperatures ranging from 700 to 790°C for various amounts of time. Other processing parameters were set at P(O_2) of 150 mTorr, P_{TOT} of 0.1 atm and P(H_2O) of ~ 7 Torr. As seen in Fig. 1.80, the I_c of samples converted at 700°C increases gradually with time. Even though a J_c of almost 1 MA/cm^2 can be obtained, the general the J_c level is comparatively low. In addition, conversion has not gone to completion after 100 min of processing (i.e., a BaF_2 signal was detected in XRD) due to the slow YBCO formation rate under this low-temperature condition. For samples processed at 730 and 740°C, I_c increases rapidly with conversion time up to roughly 20 to 30 min, at which point the I_c increases slowly or remains

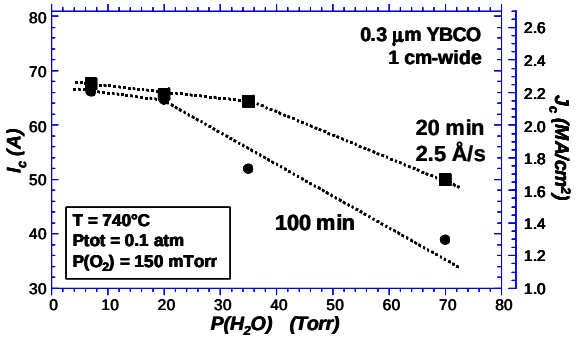

Fig. 1.79. Variations in I_c with $P(H_2O)$ for samples converted for 100 min and 20 min.

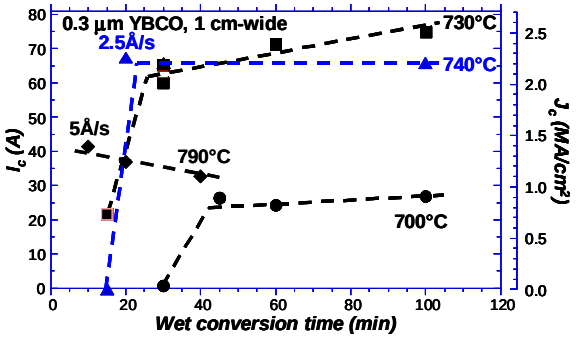

Fig. 1.80. Critical currents as functions of conversion time for samples processed from 700 to 790°C.

constant with further processing. The highest I_c of 75.2 A (2.5 MA/cm^2) was achieved on a sample converted at 730°C for 100 min. At a high processing temperature of 790°C, YBCO formation was very rapid; an I_c of 41.7 A (1.4 MA/cm^2) was attained after only 10 min (conversion rate of 5 Å/s). However, buffer integrity degrades at this high temperature, and I_c decreases with additional processing time. Variation in I_c with processing temperature for these and additional samples are summarized in Fig. 1.81. It can be seen in Fig. 1.81 that for the present set of conversion parameters, the optimal processing temperature ranges from roughly 725 to 745°C. Work is under way to examine the processing characteristics and properties of thicker films in reduced-pressure environments.

1.12.4. Summary

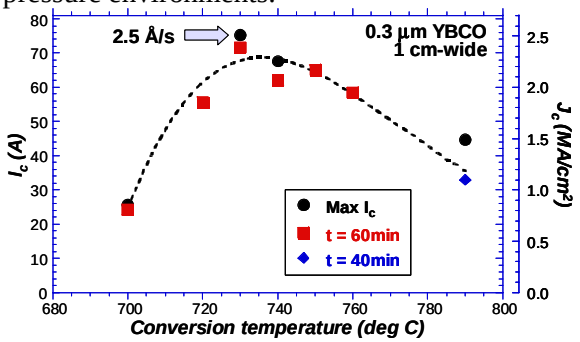

Fig. 1.81. Variation in I_c with conversion temperature for 0.3-µm-thick YBCO.

Reduced-pressure processing of an ex situ BaF_2 precursor has been found to be capable of increasing both conversion rate and J_c. By simply reducing the conversion pressure, the J_c was found to increase by 54%. By simultaneously reducing both the conversion pressure and water partial pressure, a J_c at 77 K and self-field of 2.21 MA/cm^2 was obtained in just 20 min. Compared with the sample converted in high $P(_{TOT})$ and $P(H_2O)$, this result represents a J_c improvement of 58% and a fivefold increase in conversion rate. Moreover, by decreasing the water partial pressure, the detrimental effect of overconversion was greatly reduced. In addition, an optimal processing temperature range of roughly 725 to 745°C has been found for the present set of reduced-pressure conversion parameters

1.12.5 References

1. D. F. Lee et al., *Supercond. Sci. Technol*. (2003) (to be published).
2. M. W. Rupich et al., *IEEE Tran. Appl. Supercond.* **13**, 2458 (2003).
3. T. Izumi et al., *IEEE Tran. Appl. Supercond.* **13**, 2500 (2003).
4. D. F. Lee et al., *ORNL Superconducting Technology Program for Electric Power Systems Annual Report*, ORNL/HTSPC-12, 30 (2000), www.ornl.gov/HTSC/publication.htm.
5. V. F. Solovyov, H. J. Wiesmann, and M. Suenaga, *Physica C* **353**, 14 (2001).

1.13 HIGH CRITICAL CURRENT DENSITY $YBa_2Cu_3O_{7-\delta}$ THIN FILMS FABRICATED BY EX SITU PROCESSING AT LOW PRESSURES

Y. Zhang and J. R. Thompson (University of Tennessee); R. Feenstra, A. A. Gapud, T. Aytug, P. M. Martin, and D. K. Christen (ORNL)

1.13.1 Introduction

The ex situ syntheses of YBCO coatings for coated conductors are being investigated using physical-vapor-deposited BaF_2 precursors or metal-organic deposition of (MOD) trifluoroacetate (TFA) precursors, annealed to form epitaxial YBCO films. The postdeposition annealing is usually conducted at atmospheric pressure in a tube furnace under a flowing gas mixture of oxygen, water vapor, and a carrier gas of nitrogen or argon. Recently, considerable effort has been devoted to better understanding the reaction mechanism and to optimize the conversion processing. For both vapor-deposited and TFA precursors, barium exists in a molecular state as BaF_2. The epitaxial nucleation and growth of YBCO during the processing anneal is directly related to the decomposition of BaF_2, for example, according to the following effective reaction:

$$1/2\ Y_2O_3 + 2\ BaF_2 + 3/2\ Cu_2O + 2\ H_2O + 1/2\ O_2 \rightarrow YBa_2Cu_3O_{6.0} + 4\ HF \quad (1)$$

Under typical atmospheric pressure processing conditions, the removal of the decomposition product HF is mainly determined by the detailed convection due to the gas flow conditions of the particular reaction furnace geometry. For large area samples, an HF partial pressure gradient establishes along the gas flow direction, leading to a stagnation boundary layer along the sample surface that may result in nonuniform reactions and inhomogeneous films with poor properties. Such problems may be solved by the combination of increased gas flow rate and careful design of the processing furnace configuration. For practical tape production, however, normal atmospheric pressure processing generally consumes large quantities of gases.

To obtain high critical current density films, the postannealing step has to be well controlled to produce epitaxial *c*-axis-oriented YBCO, with little nucleation and growth of *a*-axis and randomly oriented material. A rapid effective growth rate is also important for practical production by either batch or reel-to-reel processes, particularly when thicker (>1-μm) films are concerned. In principle, a faster growth rate can be achieved by increasing water partial pressure and/or reducing HF partial pressure according to the reaction kinetics. By substantially reducing the total pressure (P_{tot}), the removal of HF can be greatly enhanced through molecular diffusion instead of unduly relying on convection. Recently, it has been shown that, for TFA precursors, effective YBCO growth rates can be as rapid as 60 Å/s when the total pressure is reduced to about 1Torr. For coevaporated BaF_2 precursors, a growth rate increase has also been observed under low total pressure of about 200 mTorr to 10 Torr. However, in the latter case the average growth rate was limited to about 2 to 3Å /s due to the formation of non-*c*-axis components that degrade superconducting properties.

Here we report the possibility of fabricating YBCO thin films by ex situ processing under very low pressures and the influence of the basic annealing parameters on the properties of the films. For controlled studies, the precursor films were deposited on single-crystal (100) $SrTiO_3$ substrates by e-beam coevaporation of Y, BaF_2, and Cu at room temperature. The compositions of the precursor films were determined by Rutherford backscattering spectroscopy (RBS), and the final thickness was measured using a profilometer. Postdeposition anneals were carried out in an induction vacuum furnace in which P_{O2} and P_{H2O} were carefully controlled and varied to different levels. X-ray diffraction (XRD) and scanning electron microscopy (SEM) were used for characterizing the structure and morphology of the YBCO films obtained. The normal state electronic and superconducting properties were measured using a SQUID magnetometer as well as a standard four-probe electrical method.

1.13.2 Experimental

The configuration of the induction vacuum furnace system is schematically shown in Fig. 1.82. The sample is located at the center of a quartz tube in which the base pressure is 3 to 5×10^{-6} Torr. In operation, valve (1) is set to maintain a gas flow that is consistent with the controlled pressure in the quartz tube. The gas flow rate is about 0.3 sccm in this particular system during the annealing. Water vapor is introduced first by adjusting the variable leak valve (11), and the partial pressure (P_{H2O}) is monitored by the ionization vacuum gauge (9) and the Micropole™ model MPA6-7-2/65C RGA (residual gas analysis) detector (3). Values of P_{H2O} were set at different fixed levels from 5×10^{-5} to 8×10^{-3} Torr. After the stabilization of P_{H2O}, high-purity oxygen is introduced by adjusting the variable leak valve (12). The total pressure in the quartz tube (P_{tot}) is set as indicated by the convectron vacuum gauges (2,8), which are located upstream and downstream from the sample, respectively. Therefore, $P(O_2)$ is obtained as $P_{O2} \approx P_{tot}$ when $P_{H2O} << P_{O2}$, and $P_{O2} = P_{tot} - P_{H2O}$ when P_{H2O} is comparable to P_{O2}. For this study, all samples were annealed at a fixed temperature of 730°C. Sample temperature was monitored by a two-color optical pyrometer (17) that was previously calibrated against a type-K thermocouple introduced at the sample position. The increased-temperature ramp rates used for all anneals were about 60°C/min. Annealing times at 730°C varied from 45 to 180 min, depending on film thickness. About 10 min before starting the cooldown, the water vapor supply was shut off, and P_{O2} was raised to 300 mTorr. The cooling rate was about 30°C/min, and upon reaching 450°C, more oxygen was introduced until P_{O2} = 150 Torr, in order to fully oxygenate the YBCO film.

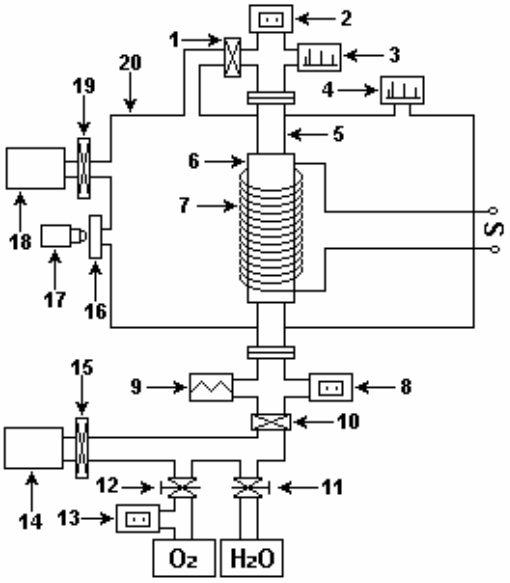

Fig.1.82. Schematic configuration of the postannealing induction vacuum furnace system.

1, 10, 15. valves
2, 8. convectron vacuum gauges
3, 4. residual gas analyzer detectors
5. quartz tube
6. susceptor
7. induction coil
9. ionization vacuum gauge
11, 12. variable leak valves
13. capacitance manometer
14. roughing pump
16. view port
17. pyrometer
18. cryopump
19. gate valve
20. ultrahigh-vacuum chamber

To reveal and analyze the phases developed in the films, a Philips model XRG3100 X-ray diffractometer with Cu K_α radiation was used to record powder θ-2θ diffraction patterns. Scanning electron microscopy (SEM) micrographs were taken using a JEOL JSM-840 SEM at a beam voltage of 7 kV. The electrical resistivity and critical current density (J_c) were measured using a standard four-probe method in which the J_c values were defined at a 1 μV/cm criterion. For films where the J_cs were measured by a Quantum Design MPMS 7 SQUID magnetometer, the magnetic fields were applied perpendicular to the film surfaces. In this case, J_c values were determined by the application of the Bean critical state model formula, $J_c = 30\Delta M/d$, where ΔM is the magnetization hysteresis (emu/cm^3) and d is the lateral size of the sample (cm).

1.13.3 Results and Discussion

YBCO films were obtained by postannealing of the e-beam co-evaporated precursor films at different fixed P_{O2} values of 10, 20, and 40 mTorr, and for film thicknesses ranging from 0.14 to 0.34 μm and from 0.34 to 1.04 μm. Figure 1.83 shows a typical XRD θ-2θ scan obtained from a 0.34-μm-thick

sample that was annealed under P_{O2} = 10 mTorr and P_{H2O} = 0.1 mTorr. Apparently, even at this low oxygen pressure, *c*-axis-oriented YBCO film can be formed. XRD examination of other samples indicated that there is no appreciable difference in the phase composition and YBCO orientation as P_{O2} is varied from 10 to 40 mTorr, with P_{H2O} fixed at 0.1 mTorr. However, when P_{O2} was lowered to 2 mTorr, very little YBCO formed after a 90-min anneal. This result is consistent with extrapolation of the measured thermodynamic stability of YBCO in terms of temperature and oxygen partial pressures. It can be seen from the equilibrium phase diagram (Fig. 1.84), that the processing conditions used in this study are marginally within the YBCO stability region. By extension, we may speculate that *c*-axis YBCO films can be formed at lower P_{O2}, provided that the annealing temperature is lowered to be consistent with sufficient cation diffusion for phase formation.

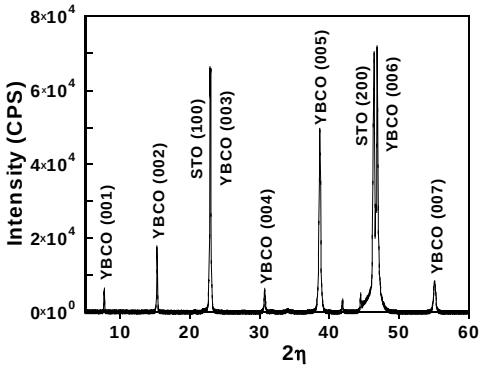

Fig.1.83. XRD θ-2θ scan for a 0.34-μm-thick sample annealed under P_{O2} = 10 mTorr and P_{H2O} = 0.1 mTorr.

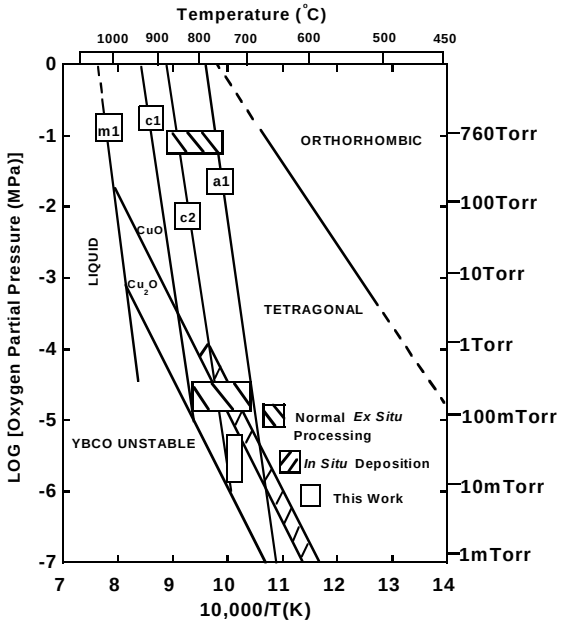

Fig. 1.84. YBCO equilibrium phase diagram showing the low-pressure processing condition as well as the commonly used ex situ and in situ condition for fabrication of YBCO films. Predominantly *c*-oriented films can be obtained between c1 and c2 and mixed *c*- and *a*-oriented films between c2 and a1. m1 is the melting line.

Shown in Fig. 1.85(a) is the resistive superconducting transition, where it can be seen that the transition is sharp and T_{c0} is near 90 K. Figure 1.85(b) compares the magnetic field dependence of the transport J_c at 77 K of two 0.34-μm-thick samples, one that was annealed at P_{O2} = 40 mTorr and the other under typical standard conditions (P_{O2} = 200 mTorr in a carrier gas at 1 atm). The properties are comparable to within usual variations among high-quality films. In this case, J_c at self-field for the sample annealed at P_{O2} = 40 mTorr is about 3.6 MA/cm^2, which is a little lower than the value of 4.1 MA/cm^2 measured for the sample annealed at atmospheric pressure. However, as the magnetic field increases, the decline in J_c is somewhat less than that of the normal-pressure annealed sample, and the irreversibility field, H_{irr}, is about 7.3 Tesla, which implies that the low-pressure annealed film may have stronger flux pinning. Measurement of a 1.04-μm-thick sample gave 77 K J_c values of 1.45 MA/cm^2 at self-field and 0.2 MA/cm^2 at 1 Tesla. Figure 1.86 shows the magnetic field dependence of J_c at several different temperatures, determined from SQUID magnetometry measurements of another 0.34-μm-thick sample.

In order to obtain totally *c*-axis-oriented YBCO, the growth rate was controlled to less than 2 Å/s by adjusting the water partial pressure to ~0.1 mTorr. The preliminary data indicate that, although this water partial pressure for low-pressure annealing is much lower than that used for atmospheric pressure processing, the YBCO growth rates are equivalent to those producing good *c*-axis films under

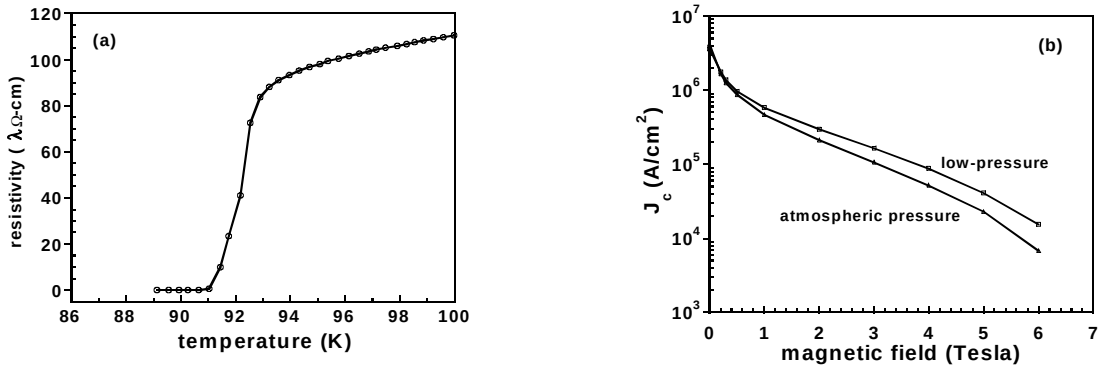

Fig.1.85. (a) Resistivity vs temperature for a 0.14-μm-thick film annealed at P_{O2} = 10 mTorr. (b) Magnetic field dependence of transport J_c values at 77 K for two 0.34-μm-thick films. One film was annealed at P_{O2} = 40 mTorr, and the other at P_{O2} = 200 mTorr in an atmospheric carrier gas.

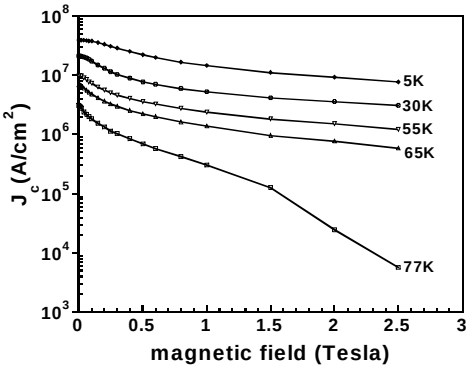

Fig. 1.86. Magnetic field dependence of J_c values determined by magnetic hysteresis for a 0.34-μm-thick sample measured at different temperatures. The agreement between transport and magnetization J_c measurements is good at low magnetic fields, whereas the magnetization measurements fall below those of transport at progressively higher fields and temperatures. This is due to the much lower effective voltage criterion of the magnetic measurement technique. In regimes of a shallow voltage-current relation, significant flux creep diminishes the magnetic hysteresis. At low fields, however, where the superconductor voltage-current relation is very sharp, large differences in voltage level have minimal effect on the deduced critical current.

atmospheric pressure. This result can be attributed to the much lower HF partial pressure at the sample surface under the low-pressure conditions, as we show with the following simple model.

The rate of the reaction [Eq. (1)], thus the YBCO film growth rate, strongly depends on the value of the ratio P_{HF}^2/P_{H2O}. The concentrations of HF and H_2O at the interface between the precursor and the reacting YBCO can be approximated by the partial pressures P_{HF} and P_{H2O} at the sample surface. Therefore, the removal of HF determines YBCO growth rate when the water partial pressure is maintained constant. The removal of HF at the surface is mainly implemented by gas flow (forced convection) when the total pressure is high (e.g., at 1 atmospheric pressure). At lower pressures, however, HF can diffuse from the surface more effectively, and the effect of HF outdiffusion on YBCO growth rate can be evaluated under conditions when the gas flow rate is assumed so slow that convection can be neglected.

For an assumed constant YBCO growth rate, r (cm/s), the steady-state HF molecular out-flux, Φ (molecules/cm^2-sec) is

$$\Phi = \frac{4r}{V_{cell}} \tag{2}$$

where $V_{cell} \cong 1.74 \times 10^{-22} cm^3$, is the volume of YBCO unit cell. For a planar geometry, the molecular flux of HF can be expressed as

$$\Phi = -D\frac{dC(z)}{dz}, \tag{3}$$

where D is the diffusivity of HF and $C(z)$ is the HF concentration, which can be related to P_{HF} as $C(0)=P_{HF}/kT$ at the sample surface.

From kinetic gas theory, the diffusivity D is inversely proportional to the total gas pressure, and for a binary gas system with HF as one component and the other gases (O_2 and H_2O) as the second component,

$$D \approx \frac{\sqrt{\frac{8kT}{\pi}(\frac{1}{M_{HF}}+\frac{1}{M_{O_2}})}kT}{3\pi\delta^2 P_{tot}} \tag{4}$$

where M_{HF} and M_{O2} are the molecular weight of HF and O_2, and $\delta=(\delta_{HF}+\delta_{O2})/2$ is the average molecular diameter. For simplicity, suppose that the HF is absorbed at the wall of the furnace tube a distance z_0 away from the sample surface, so that $C(z_0) \approx 0$. Then, from Eqs. (2) through (4), we obtain P_{HF} at the sample surface:

$$P_{HF} = \frac{12\pi r\delta^2 z_0 P_{tot}}{V_{cell}\sqrt{\frac{8kT}{\pi}(\frac{1}{M_{HF}}+\frac{1}{M_{O_2}})}} \tag{5}$$

Figure 1.87 gives the relationship between the ratio P_{HF}/P_{H2O} and the assumed YBCO growth rate r based on Eq. (5) for given total pressures and specific water partial pressures under typical atmospheric pressure processing and present low-pressure processing conditions. It can be seen that, even by assuming the absence of convection, the ratio P_{HF}/P_{H2O} for atmospheric pressure processing is lower than that for low-pressure processing at a given YBCO growth rate. However, the assumed growth rates r are only possible provided the ratio P_{HF}/P_{H2O} is far below that defined by the thermodynamic equilibrium condition (when the Gibbs free energy of the reaction approaches zero) from which P_{HF} is calculated as

$$P_{HF} = \{P_{H_2O}^2 P_{O_2}^{\frac{1}{2}} \exp[-\frac{\Delta H^o - T\Delta S^o}{RT}]\}^{\frac{1}{4}} \tag{6}$$

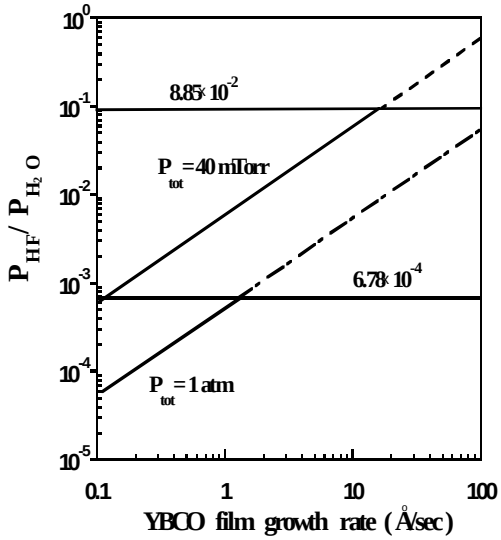

Fig. 1.87. Relationship between P_{HF}/P_{H2O} and assumed YBCO growth rate at the given conditions of P_{tot} = 1 atm with P_{H2O} = 20 Torr for atmospheric pressure processing, and P_{tot} = 40 mTorr with P_{H2O} = 0.1 mTorr for low-pressure processing. The temperature used in the calculation is 730°C. Equilibrium ratios of P_{HF}/P_{H2O} are 6.78×10^{-4} and 8.85×10^{-2} for P_{O2} = 1 atm and P_{O2} = 40 mTorr, respectively.

For the reaction (1), the standard enthalpy $\Delta H^\circ \cong$ 488.3 kJ/mole and standard entropy $\Delta S^\circ \cong$ 183.6 J/mole-K, based on the data from references [1] and [2]. At the temperature of 730°C, the equilibrium ratios of P_{HF}/P_{H2O}, which are also indicated in Fig. 1.87, are 6.78×10^{-4} and 8.85×10^{-2} for P_{O2} = 1 atm and P_{O2} = 40 mTorr, respectively. These ratios actually limit the validity of any assumed YBCO growth rates. It can be seen that without the forced gas flow, which should further decrease the ratio P_{HF}/P_{H2O}, YBCO film growth is limited below a slower rate under atmospheric-pressure processing conditions, while the low-pressure regime potentially may enable much faster growth.

To investigate the effect of P_{H2O} on YBCO formation, different P_{H2O} values, ranging from 0.02 to 8 mTorr, were used with P_{O2} fixed at 40 mTorr. The XRD results indicated that YBCO was formed with complete *c*-axis orientation only at P_{H2O} = 0.1 mTorr. For all anneals with P_{H2O} > 0.1 mTorr, some *a*-axis and randomly oriented YBCO appeared along with the predominant *c*-axis YBCO. As P_{H2O} increases, the intensities of *a*-axis (*h00*) peaks and random crystalline peaks in the XRD θ-2θ scan pattern increased while the intensities of *c*-axis YBCO (00l) peaks decreased. The qualitative relationship between the intensities of *c*-axis (005) peaks and the water partial pressures are shown in Fig. 1.88. Also shown are the J_c values at 77 K and self-field. The influence of water partial pressure on YBCO orientation can also be seen in the SEM surface morphology shown in Fig. 1.89(a) and (b). Typical *c*-axis YBCO morphology is shown in Fig. 1.89(a), where the sample was annealed at P_{H2O} = 0.1 mTorr. In contrast, *a*-axis YBCO is evident in Fig. 1.89(b), where P_{H2O} = 0.8 mTorr. On the other

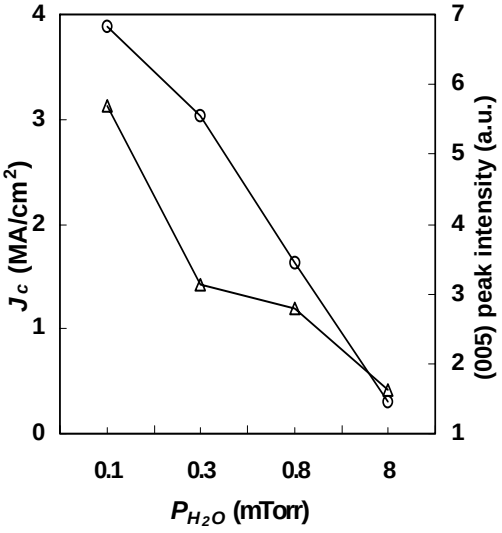

Fig.1.88. The dependence of J_c and the XRD θ-2θ YBCO (005) peak intensities on water vapor partial pressure for 0.34-μm-thick films processed at P_{O2} = 40 mTorr.

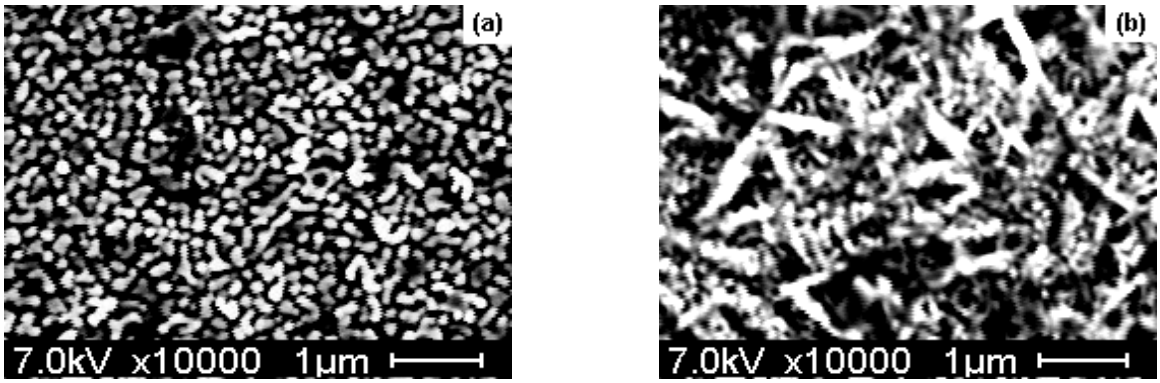

Fig.1.89. Surface SEM micrograph of films annealed at P_{O2} = 40 mTorr: (a) P_{H2O} = 0.1 mTorr and (b) P_{H2O} = 0.8 mTorr. The difference indicates that the YBCO growth morphology is sensitive to the water partial pressure.

hand, when the water partial pressure was lowered to about 0.02 mTorr, appreciable BaF_2 peaks appeared in the θ-2θ scan, indicative of incomplete conversion.

1.13.4 Conclusion

YBCO films were successfully prepared by postannealing of e-beam coevaporated precursors under a low-oxygen-pressure atmosphere. The highest J_c (77 K and self-field) obtained is 3.6MA/cm^2 for 0.34-μm-thick films. Water is indispensable for the conversion reaction to proceed, although the water partial pressure used can be as low as 0.1 mTorr. The YBCO growth morphology is very sensitive to water partial pressure under the low-pressure condition we used. With increasing water partial pressure, the non-*c*-axis YBCO component increases, which results in the decrease of J_c values. Optimization of the YBCO growth rate, coupled with the suppression of non-*c*-axis growth, needs to be addressed in the future studies of these low-vacuum processing protocols.

1.13.5 References

1. D. R. Lide, *CRC Handbook of Chemistry and Physics*, 83rd Edition, CRC Press LLC, 2002–2003.
2. T. B. Lindemer et al., *J. Am. Ceram. Soc.* **72**, 1775 (1989).

1.14 THROUGH-THICKNESS SUPERCONDUCTING AND NORMAL-STATE TRANSPORT PROPERTIES REVEALED BY THINNING OF THICK-FILM EX SITU $YBa_2Cu_3O_{7-X}$ COATED CONDUCTORS

D. M. Feldmann and D. C. Larbalestier (University of Wisconsin); R. Feenstra, A. A. Gapud, and J. D. Budai (ORNL); T. G. Holesinger and P. N. Arendt (LANL)

To meet the technical requirements of applications, coated conductors need to deliver large critical current (I_c) values, most readily achieved by increasing the thickness *t* of the superconductor layer. However, for several YBCO growth processes, there is a strong decrease in the critical current density (J_c) with increasing film thickness.

Most knowledge of the thickness dependence of the critical current density of YBCO films comes from studies of multiple films produced with different YBCO layer thicknesses. A complementary approach to investigate $J_c(t)$ uses ion milling to successively thin a YBCO coating, with J_c measured at multiple thickness on a single sample. This second approach also produces a variable thickness dataset; with enhanced emphasis on through-thickness homogeneity. Previous work by others on YBCO films by PLD has shown the existence of "dead" layers, but that these are not endemic of thick YBCO coated

conductors, but instead are dependent on the growth conditions. Here we report ion-milling studies on YBCO grown by the BaF_2 ex situ process on IBAD-YSZ buffered metal substrates.

Briefly, precursor layers of the desired thickness were prepared by vacuum deposition using three electron-beam sources onto a "cold" substrate; the layers were subsequently converted into epitaxial YBCO by annealing in a furnace under flowing gas conditions at atmospheric pressure. Maximum temperatures during anneal reached 780°C, and the growth rate was about 1 to 1.5 Å/s. The oxygen partial pressure was 200 mTorr; the water partial pressure (needed to decompose incorporated BaF_2 of the precursor layer) was kept below 5 Torr.

Two samples with YBCO layer thicknesses of 2.0 and 2.9 μm were prepared on substrates having similar but slightly different textures. The full-width-at-half-maximum (FWHM) values of the (205)/(025) YBCO reflections in X-ray diffraction (XRD) Φ-scans for the 2.0- and 2.9-μm films were 6.9° and 5.9°, respectively. Bridges 300 μm wide were cut with a laser to restrict I_c to < 10 A. The resistivity ρ(T) and J_c(H,77K) were measured using pulsed-current (50-ms pulse duration with 30-ms voltage read) with a standard four-point configuration and a 1-μV/cm J_c criterion. For ion milling, samples were cooled to ~230 K, and Ar ions having an energy of 500 eV impacted the samples at 45° with the film surface normal. The YBCO etch rate was ~12 nm/min. Thickness was measured using a Tencor profilometer.

Figure 1.90 shows ρ(T) for the 2.9-μm film as it was thinned to a thickness t. The curves exhibit a slight positive curvature, generally associated with O_2 overdoping. The inset to Fig. 1.90 shows T_c as a function of thickness. The fluctuations in T_c are believed to be greater than the measurement accuracy, but overall T_c remains relatively constant. The resistivity ρ(300K) as a function of film thickness (Fig. 1.91) is nearly constant at ~400 μΩ-cm down to ~0.4 μm, below which it starts to increase abruptly, suggestive of a reaction between the YBCO and the buffer layer. However, based on the constant T_c, ρ(300K), and

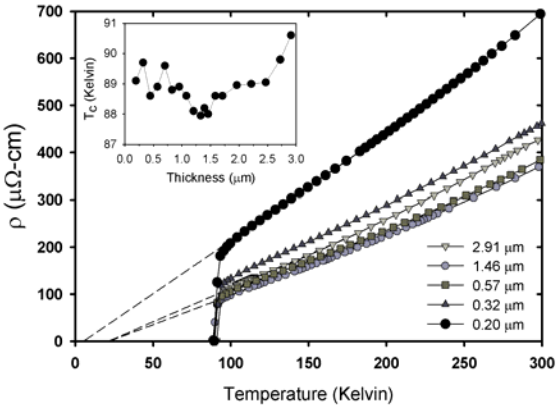

Fig. 1.90. Temperature dependence of the resistivity for the 2.9-μm film at full thickness and selected values of t after ion milling. Linear extrapolations to T = 0 K are shown for t = 2.91, 1.46, and 0.20 μm and have a slight negative intercept. Inset shows T_c(t) for the film, where T_c is defined as the highest temperature such that ρ = 0.

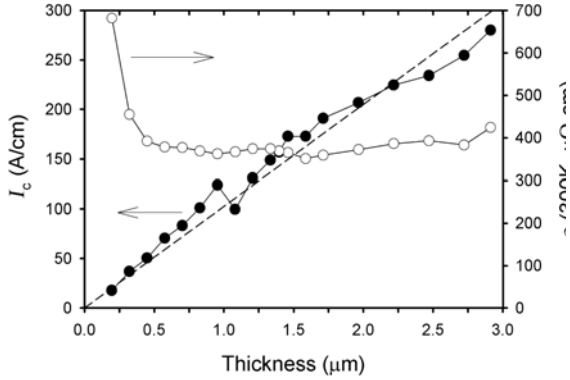

Fig. 1.91. Thickness dependence of I_c (filled circles) and ρ(300K) (open circles). The dashed line is a fit to the I_c data, through the origin, with a slope of 103 A/(cm·μm).

the curvature of the ρ(T) data we conclude that repeated ion milling did not significantly damage the film or affect the oxygenation state of the remaining layer.

Also shown in Fig. 1.91 is I_c(77K) as a function of thickness, where the critical current of the bridge has been normalized to a 1-cm width (units: A/cm). The data exhibit a high degree of linearity and provide no evidence of substantial dead layers in the film at either the substrate interface or the film surface.

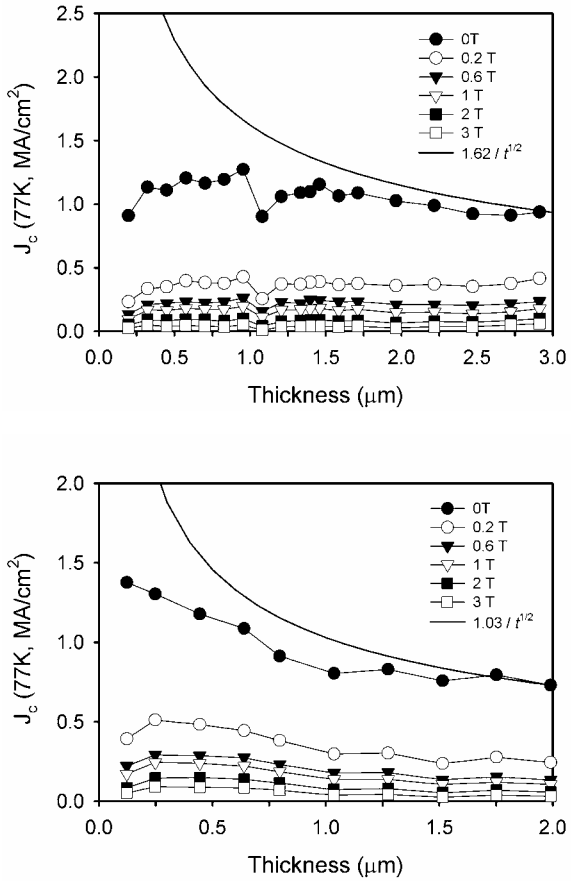

Fig. 1.92. Thickness dependence of J_c(77K) for (top) the 2.9-μm and (bottom) the 2.0-μm films. Solid lines are fits to J_c data from multiple films reacted from different precursor thicknesses. With the exception of the t = 0.19 μm data of the 2.0-μm film, the $J_c(t)$ curves maintain their qualitative shape in applied fields.

Figure 1.92(a) shows $J_c(t,77K)$ for self-field (SF) and several applied fields ($H||c$). J_c(SF) is nearly constant through thickness, tightly scattered around 1 MA/cm^2. Figure 1.92(b) shows data for the 2.0-μm-thick YBCO film. Due to a slightly worse substrate texture, this film had a lower full-thickness J_c(77K , SF) of 0.73 MA/cm^2. $J_c(t,SF)$ is not as flat as for the thicker-film sample, with J_c rising to almost twice the full-thickness value at 0.12 μm. Again, the $J_c(t)$ data of these samples give no evidence of dead layers or otherwise strong substrate reaction. This observation is consistent with the cross-sectional scanning electron microscope (SEM) image of the 2.9-μm sample shown in Fig. 1.93. While there is more porosity in the upper portion of the film, the

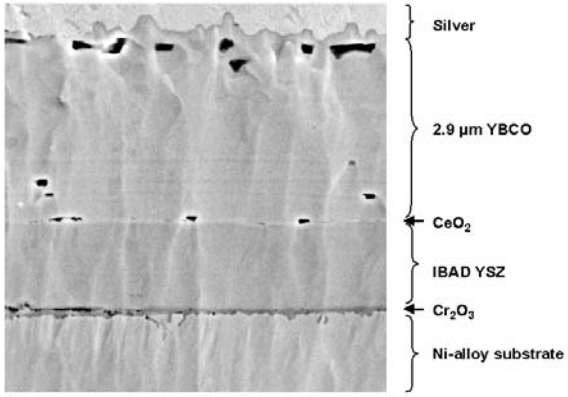

Fig. 1.93. Cross-sectional SEM image of the 2.9–μm-thick YBCO film.

microstructure is dense through its thickness with nothing to suggest a complete current-blocking layer. An interesting question arising from Figs. 1.92(a) and (b) is why higher J_c values were not recovered as the films were milled thinner. The solid line in the figures is a power law fit of the form $J_c \propto 1/t^{½}$, fit to $J_c(t,SF)$ data from multiple films reacted from different precursor thickness. At full thickness the J_c(SF) of the 2.0- and 2.9-μm samples are representative of the fit, but as they are milled thinner, J_c(SF) deviates significantly. For instance, at a thickness of 0.32 μm, the 2.9-μm sample had a J_c of 1.1 MA/cm^2 compared to 2.7 MA/cm^2 for a film reacted from a 0.35-μm precursor on a nominally identical substrate. For the previous in situ PLD YBCO films, the I_c degradation in the bottom portion of the films was attributed to a reaction with the buffer layer that took place in the time it took to grow the upper portion of the films. Likewise, it is possible that a time-dependent reaction has degraded the bottom part of the ex situ YBCO, although apparently to a lesser degree than in the PLD films. A second explanation, which is unique for the ex situ process, is that the YBCO that nucleated at the substrate interface had poorer properties from the start (relative to films reacted from thinner precursors). For conversion of increasingly thicker films, the H_2O required for the reaction and the HF produced must diffuse through increasingly more precursor material, and the thickness of the precursor itself becomes a growth parameter.

The flat $J_c(t)$ dependence observed for the 2.9-μm film would seem to be ideal and representative of a uniform microstructure. However, while the SEM shows a structure that is dense and relatively

homogeneous through the thickness (Fig. 1.93), the TEM presents a different picture. A representative image is shown in Fig. 1.94. The bottom portion (~1.6 μm) of the film consists of large, well-formed YBCO grains (> 10 μm) containing a high density of small, coherent Y_2O_3 particles. Some layers and discrete particles of Ba-Cu-O can also be found. The upper part of the film contains smaller, highly defective YBCO grains and an overall different morphology and chemistry of second phases. The top part of the film appears similar to films reacted from thin precursors (< 0.5 μm). Thus, the image provides evidence of a "bilayer" structure suggestive of different growth events through the thickness.

The absence of correlated behavior in the $I_c(t)$ (Fig. 1.91) and $J_c(t)$ [Fig. 1.92(a)] data for this film (near t = 1.6 μm) is highly surprising in view of this microstructure (Fig. 1.94). It suggests that either the different growth modes did not affect J_c and the underlying flux pinning mechanism, or the defects that are controlling J_c are not revealed by TEM at this magnification. The data clearly illustrate that it is possible to have a J_c that is nearly independent of t, despite an inhomogeneous microstructure.

A further remarkable observation is that the empirical behavior $J_c \propto 1/t^{½}$ agrees with predictions from collective pinning models, based on a homogeneous random pinning potential. If this fit were interpreted as intrinsic behavior then the $J_c(t)$ observed from thinning the 2.9-μm film should have followed more closely the $1/t^{½}$ fit. One explanation of this discrepancy, in the context of the collective pinning model, is that there is a reduced density of pins in the bottom part of the film. This interpretation is qualitatively consistent with the TEM image in Fig. 1.94 and would indicate that the primary difference between a high-J_c thin film and a thin remaining layer after ion milling results from a thickness-dependent growth mechanism. Further work is in progress to test this hypothesis and to probe the dependence on growth conditions. We conclude that for a proper interpretation of thickness-dependent effects, consideration should be given to the origin of flux pinning and the nature of defects in the superconductor.

In summary, we have directly observed of the absence of dead layers in thick (> 2 μm) YBCO films grown on buffered metal tapes by successive ion milling and J_c measurements. The lack of a surface dead layer is highly encouraging, and the linearity of the $I_c(t)$ curve of Fig. 1.91 suggests that growing thicker ex situ YBCO films should lead to further increases in I_c. The roles of intrinsic and microstructural effects on $J_c(t)$ are not fully understood at this time.

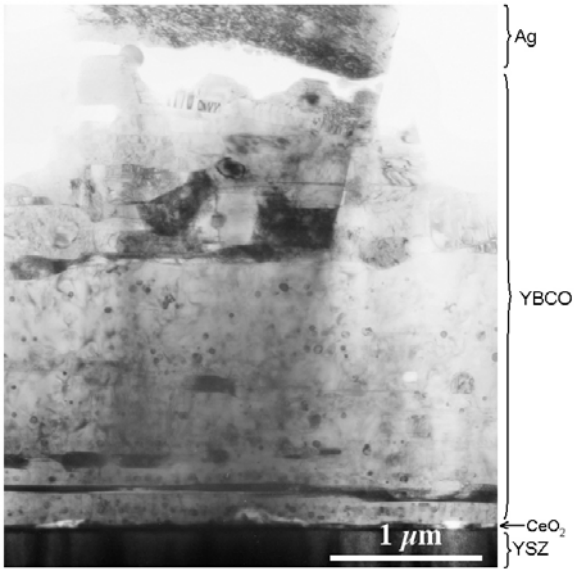

Fig. 1.94. Cross-sectional TEM image of the 2.9-μm sample, showing a distinct bilayer structure.

1.15 PULSED ELECTRON DEPOSITION OF YBCO: LIMITS TO IN SITU GROWTH AND APPLICATION TO PRECURSOR DEPOSITION

H. M. Christen, H. Y. Zhai, F. A. List, S. W. Cook, K. J. Leonard, R. Feenstra, D. K. Christen, P. M. Martin, and A. Goyal (ORNL); V. A. Maroni (ANL)

1.15.1 Introduction

The term "ablation" describes the rapid and energetic removal of material from a solid surface as consequence of the interaction with an intense energy source. In pulsed laser deposition (PLD), this mechanism is exploited to grow thin films from the plasma plume that is formed through the interaction of a focused excimer laser beam with a ceramic target. PLD has enjoyed great success in film growth of a multitude of oxide materials, including, in particular, $YBa_2Cu_3O_{7-\delta}$ (YBCO). In contrast, pulsed electron deposition (PED) employs an electron spark as the energy source, but the shape and nature of the plasma plume is similar to that encountered in PLD. However, PED has not (yet) enjoyed the great success of PLD, despite the significant cost advantages of PED over PLD.

PED has only recently gained interest as a promising alternative to PLD for thin-film growth. The technique was first developed by C. Schultheiss and co-workers at the Max Planck Institute in Karlsruhe, Germany, and had then been applied to the growth of $YBa_2Cu_3O_{7-x}$ [1]. Since then, the technique has been improved significantly, and Neocera, Inc. (of Beltsville, MD), introduced a commercial PED source to the market in 2000.

While PED is conceptually similar to PLD (with the excimer laser being replaced by a comparatively simple and cost-effective electron source), there are fundamental differences that cannot be overlooked. For the propagation of the electron beam in the deposition chamber, the background pressure has to be kept in the range of 5 to 30 mTorr, possibly the most stringent restriction on the approach. In that range, however, our results from FY 2002 clearly showed that the plume dynamics in PED are similar to those of PLD.

Based on some reliability issues with the original triggering mechanism (airgap trigger), an external trigger generator has been added to our system, as shown in Fig. 1.95.

This fiscal year (FY 2003), two projects have been pursued on the PED system. First, the in situ growth of YBCO on buffered RABiTS™ tapes has been pursued further, and our results show serious challenges to be overcome. Second, PED has been used to deposit precursors for ex situ conversion, and studies of conversion rates, resulting critical currents, and reproducibility of the approach, show great promise of this technique.

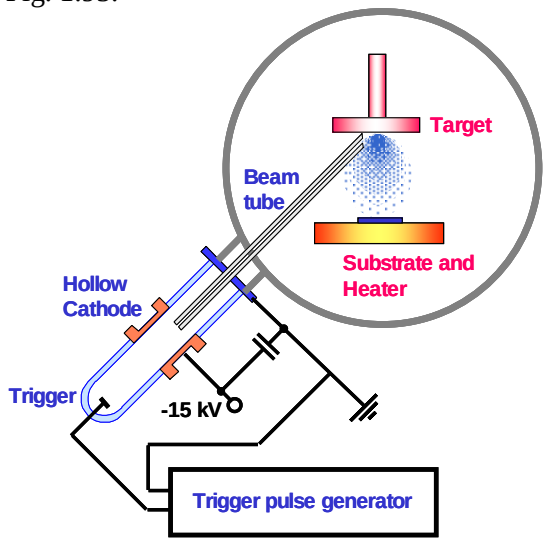

Fig. 1.95. Schematic representation of the pulsed-electron-deposition process using an external pulse generator.

1.15.2 In Situ Growth of YBCO

1.15.2.1 Growth from stoichiometric targets

Films were first grown onto single-crystalline substrates ($LaAlO_3$ and $SrTiO_3$). Typical deposition parameters are 15-kV pulses at 5 Hz, 20-mTorr O_2 background gas, and a substrate heater temperature of 820°C. X-ray diffraction (Fig. 1.96) shows the presence of numerous impurity phases, most of which also occur in PLD films grown under similar conditions. Critical current density values in excess of 2 MA/cm^2 were routinely achieved at these temperatures. However, for the deposition onto buffered RABiTS™ tapes, the temperature had to

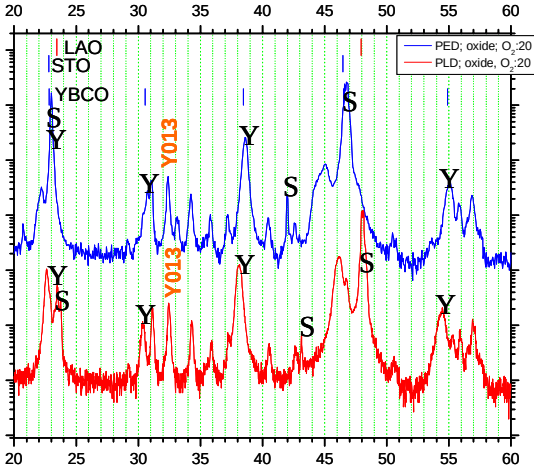

Fig. 1.96. X-ray θ-2θ scans for YBCO films grown by PED (top) and under similar conditions by PLD (bottom). Substrate peaks and satellites are labeled "S," YBCO reflections are indicated by "Y." Also visible is the YBCO(013) peak (labeled "Y013"), and several impurity phase lines.

Similar samples (grown in 15 mTorr O_2, 16 kV, 5 Hz, at 830°C) were analyzed both by Raman spectroscopy and transmission electron microscopy (TEM). Figure 1.98 shows Raman spectra taken at a number of positions on a single sample. The YBCO lines are weak compared with what is observed on comparable PLD (or other) films, but clearly distinguishable. The curve resolution of the copper-2 mode (near 150 cm^{-1}) indicates orthorhombic YBCO, but there is a second, unidentified mode at slightly higher frequencies within the same envelope.

Other Raman bands are also visible, likely due to Ba-Cu-O phases (there are several barium cuprates with phonons in the same region). In addition, lines possibly corresponding to Y_2O_3 are also observed.

To gain a better understanding of these films, TEM images were obtained (see Fig. 1.99). It is clearly observed that the YBCO film is uniform in thickness. However, large islands or outgrowths of $BaCuO_2$ protrude from the surface and penetrate into the film. Within the YBCO, a large number of small Y_2O_3 particles were observed, some of them positioned at the YBCO/LAO

be lowered by about 30°C to avoid oxidation of the Ni substrate. This lowered substrate temperature resulted in a decreased J_c for all of these samples, typically in the range of 0.4 to 0.5 MA/cm^2.

Figure 1.97 shows the field dependence of J_c for a PED-grown film on $LaAlO_3$ (14 mTorr O_2, 16 kV, 5 Hz, 820°C). While this sample did not exhibit the highest zero-field J_c, the data nevertheless indicate a drop by a factor of 4 in J_c between zero field and 0.5 T, as is often observed for samples of other origin as well.

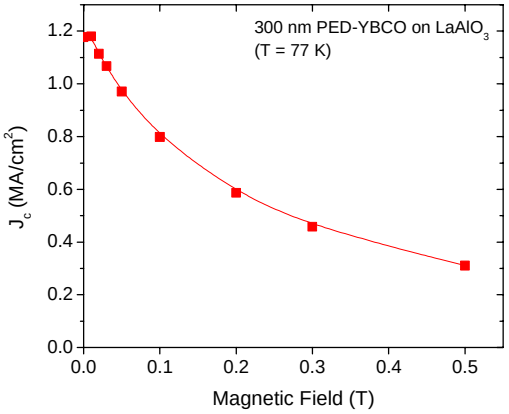

Figure 1.97. Magnetic field dependence of a PED-grown YBCO film on a $LaAlO_3$ substrate.

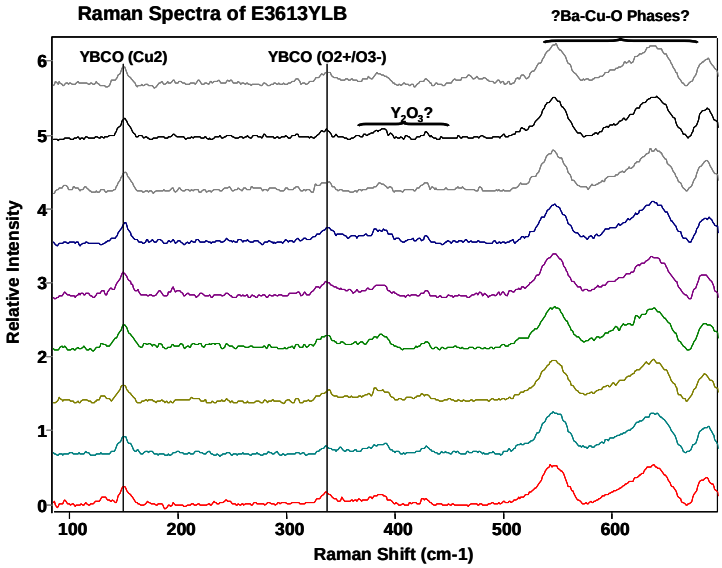

Fig. 1.98. Raman spectra of a PED-grown YBCO film on $LaAlO_3$.

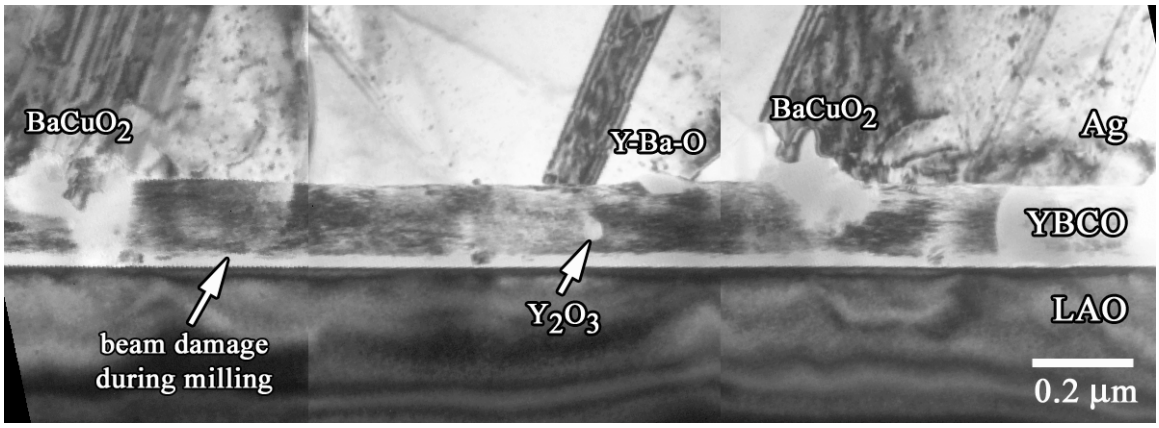

Fig. 1.99. Cross-sectional TEM image of a PED-grown YBCO film on $LaAlO_3$. Most of the material consists of crystalline YBCO with a rather smooth upper surface. However, large $BaCuO_2$ outgrowths are observed.

interface. However, no signs of reaction between the YBCO and the LAO are apparent. Due to the softness of the LAO substrate, tripod polishing to electron transparency was not possible. Therefore, ion milling was required to complete sample thinning. This produced milling damage within the YBCO at the LAO interface. However, energy-dispersive spectroscopy (EDS) shows that this region is still stoichiometric YBCO.

As we will show, pulsed-electron ablation from a stoichiometric target under the conditions used in this work yields Ba-rich material. This helps to explain, at least in part, the formation of the $BaCuO_2$ islands.

The results presented here are consistent with the following—albeit somewhat speculative—interpretation: The PED process introduces a large number of energetic electrons into the growth environment, in close proximity to the growing film. In fact, we have observed that a grounded copper aperture placed between the target and the substrate results in a significantly improved surface morphology of the films. Not all of the energetic electrons will be trapped by this grounded shield. It is therefore likely that these free electrons introduce near-surface damage to the growing material; however, at sufficiently elevated temperatures, this damage can be partially annealed out. Therefore, growth must occur at temperatures higher than that typically used in PLD. Due to the requirement of comparatively low oxygen pressure, however, YBCO is not stable at these deposition temperatures, and secondary phases are formed. These observations indicate a very serious limitation of the PED approach for in situ growth of YBCO. Approaches other than simple ablation from a stoichiometric target must therefore be explored to overcome these difficulties.

1.15.2.2 Growth from fluoride-based targets

The ex situ process of YBCO formation owes its success to the possibility to thermally convert BaF_2-based precursors into YBCO. It is thus a natural extension to investigate the in situ growth of YBCO from fluorine-based targets to determine whether good YBCO formation can be promoted by the addition of fluorine-based species.

Two targets were prepared by grinding and mixing powders of BaF_2, Y_2O_3, CuO (case I) and BaF_2, YF_3, CuO (case II), followed by sintering in air at 600ºC.

PLD experiments were used to determine the amount of fluorine transferred from the target to the substrate in a simple ablation process (assuming, to first order, that the gas dynamics differ only insignificantly between the two processes). Films were deposited onto vitreous carbon substrates at room temperature, and Rutherford backscattering spectroscopy (RBS) was used to determine the F content. Table 1.5 shows the results for the two targets.

Table 1.5. RBS composition analysis of PLD-grown fluoride-based layers

	Target composition	Deposition atmosphere	Fluorine:barium ratio
Type I	BaF_2, Y_2O_3, CuO	Vacuum	1.4
Type II	BaF_2, YF_3, CuO	Vacuum	2.1
Type II	BaF_2, YF_3, CuO	100 mTorr O_2	1.9

These measurements show that a fluorine: barium ratio comparable to that employed in the ex situ process using BaF_2 (i.e., F:Ba = 2) can be achieved by an enriched target.

Most importantly, initial PLD experiments showed that ablation from a stoichiometric oxide target at 20 mTorr of O_2 yields films that are not superconducting above 77 K (i.e., PLD does not produce superconducting films under the conditions used in PED). However, PLD at 20 mTorr of O_2 and using a fluoride-based target (Type II) led to YBCO films with a J_c of the order of 0.3 MA/cm^2.

The PED growth of films from the type II target at 780°C and 15 mTorr O_2 yielded an X-ray diffraction pattern clearly exhibiting BaF_2 lines (Fig. 1.100). At the same time, many of the impurity phase lines observed during the growth from an oxide target were strongly reduced in intensity. However, the films were not superconducting above 77 K.

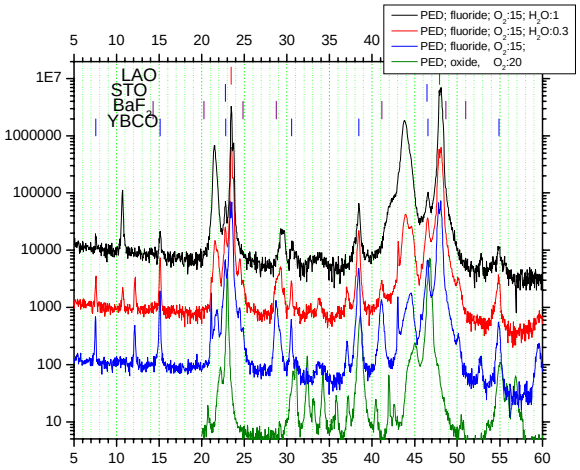

Fig. 1.100. X-ray θ-2θ scans for PED-grown films obtained from a fluoride-based target (type II) at different water vapor pressures (mTorr), and compared to results for a film grown from an oxide target.

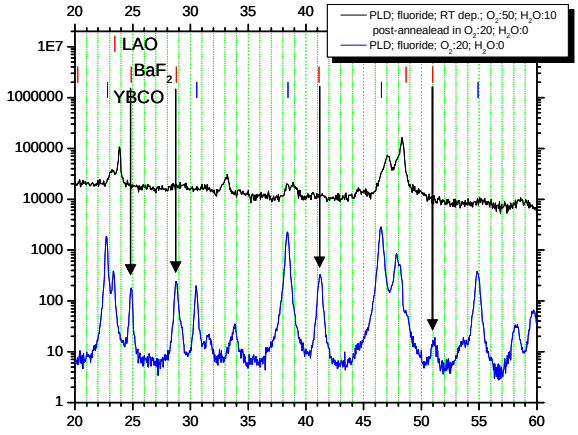

Fig. 1.101. X-ray θ-2θ scans for PLD-grown films obtained from a fluoride-based target (type II) in the absence of water vapor (bottom curve), compared with the diffraction pattern of a film formed by ex situ (vacuum) reaction of a precursor formed by deposition at room temperature in 10-mTorr H_2O. No indication of the presence of BaF_2 is found in the film obtained by ablation in water vapor.

In an attempt to convert the BaF_2 in situ, water vapor was introduced into the chamber during growth. As can clearly be seen from Fig. 1.100, this leads to a strong reduction of the BaF_2 line intensity, accompanied, however, with a decrease in the intensity of the YBCO lines, and the appearance of peaks corresponding to lattice parameters of 8.19, 4.11, and 2.07 (all ± 0.1) Å. Furthermore, none of these films was superconducting above 77 K.

Discontinuation of our RBS facilities made a direct observation of the F content in these films (as function of water-vapor pressure during growth) impossible. However, the following indirect experiment provides a convincing argument that introduction of water vapor does not lead to decomposition of BaF_2 in the growing film or at its surface, but rather reacts with the BaF_2 in the plume, effectively eliminating the fluoride before it reaches the substrate. To illustrate this, a film was deposited at room temperature in the presence of water vapor, using PLD (assuming that a similar behavior would be observed for PED). Here, we assume that all of the material impinging on the substrate will become incorporated into this amorphous layer. Thermal

treatment (750ºC) is sufficient to crystallize BaF_2 (as evidenced by the BaF_2 lines in the X-ray patterns of other samples deposited at similar temperatures). As shown in Fig. 1.101, no BaF_2 lines are observed, indicating indeed that the fluorine is not being incorporated into the film under these conditions. Our interpretation is that it is precisely this reaction in the plasma phase that ultimately led to the failure of this approach.

1.15.3. PED applied to the deposition of BaF_2 precursors

Precursor deposition for the ex situ processing of YBCO on buffered RABiTS™ remains a continuing challenge. TFA precursors show great promise; however, cracking often occurs for thick (> 2 μm) TFA layers. In contrast, no thickness limit is expected for vapor-deposition processes.

E-beam co-evaporation has been the method of choice for PVD-fabrication of precursors. However, the need for precise composition control (flux feedback) and the poor directionality of the evaporation process motivate the development of alternate approaches.

PED has the potential to overcome these limits: the process is very directional, and our results presented here demonstrate that composition control is possible without complicated feedback mechanisms.

Initial results of ex situ conversion of precursors prepared from a fluoride-based target are indeed promising. Using a target comprised of BaF_2, YF_3, and CuO (type II), a precursor was formed having a composition of Y:Ba:Cu = 1:2.15:2.46 (as determined by inductively coupled plasma mass spectroscopy (ICP-MS).

Table 1.6 shows the results for ex situ conversion of these precursor under two different conditions (low-pressure [200 mTorr O_2] and atmospheric) in the presence of water vapor.

Table 1.6. Conversion of PED precursors on RABiTS™

Thickness (μm)	Conversion	I_c (A)	J_c (MA/cm^2)
0.3	low-pressure	14.0	0.50
0.5	atmospheric	40.6	0.81

Two observations are significant in this context:

- The value of 0.81 MA/cm^2 is the highest number obtained to date on RABiTS™ for a PED-based YBCO process.
- While the J_c of this film is lower that that of an e-beam co-evaporated precursor of similar thickness under similar conditions (at least in part due to the incorrect stoichiometry), the conversion rate of 3.5 Å/s for the PED precursor is about a factor of 2 higher.

Deviation from stoichiometry is obviously a serious difficulty encountered in this work. Three aspects need to be investigated:

1. How much does the stoichiometry vary as function of position on the substrate plate?
2. How much does the stoichiometry vary as function of deposition time?
3. How precisely can the stoichiometry be adjusted to the ideal 1:2:3 ratio?

It is likely that item 3 (getting the accurate composition ratio at a given time and position) can be achieved simply by adjusting the target composition (work currently in progress). However, the most important aspect is to first consider items 2 and 3, as these could be very serious, fundamental hurdles. Fortunately, our results presented here clearly demonstrate that PED yields a very stable deposition process.

First, the composition was analyzed as function of position on the substrate holder. Four positions were measured, as shown in Fig. 1.102. Three measurements were performed along the horizontal direction of the system, each spaced 1 in. apart. An additional data point 1 in. above the center of the plate was also analyzed. All compositional measurements were performed by ICP-MS. Target-to-substrate distance was 8.5 cm, and the growth took place at 15 kV, 12.3 mTorr, at room temperature.

A significant systematic deviation from the ideal 1:2:3 stoichiometry was clearly observed, with all samples being significantly Cu-deficient and Ba-rich. However, the spatial variations within this 2-in.-diam area were only slightly larger than what is measurable with the current ICP-MS apparatus. This shows great promise for larger-area depositions and, in the long term, for reel-to-reel growth.

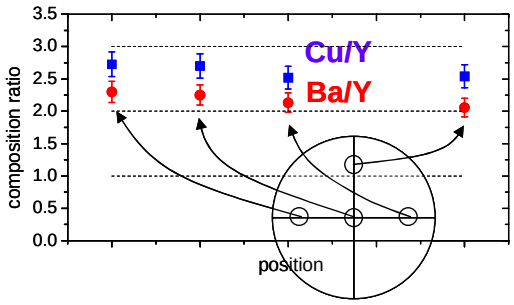

Fig. 1.102 Spatial variation of the composition at various positions on the substrate holder plate. The distance between each data point is 1 in. Composition was determined by ICP-MS, and the point-to-point variations observed are similar to the experimental accuracy.

As a second experiment, a multi-sample holder was mounted, containing six separate substrates that can be moved into the plume (from behind a shield containing a small aperture) manually at separate times during a long run. For this experiment, a 10-min preablation (no sample in the plume) was followed by six consecutive depositions, each lasting 5 h. Thus, the duration of the entire experiment was 30 h. The substrate-to-target distance was 7 cm, and the deposition occurred at room temperature in 12.2 mTorr O_2 and using 15-kV pulses at 5 Hz.

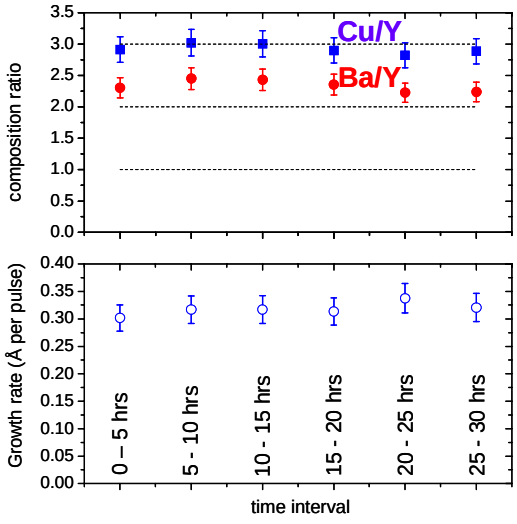

Fig. 1.103. Time evolution of composition (top, determined by ICP-MS) and growth rate (bottom, determined by profilometry) during a 30-h PED deposition at 5 Hz, during which multiple samples were rotated into the plume. Variations of composition and growth rates are comparable to the experimental errors.

As shown in Fig. 1.103, the variations of the composition and of the growth rates (as determined by profilometry from steps at mask edges) are small as compared with the experimental errors of these techniques. All samples were clearly Ba-rich, but there was little change in the degree of off-stoichiometry during the run. Similarly, the growth rate per pulse was 0.3 Å for the entire growth. Therefore, even with the small (1-in.-diam) target, no significant deterioration occurs during the growth, making this approach very promising for deposition onto long lengths.

Obviously, the next step has to be a correction of the film composition via the use of a composition-adjusted target. Additionally, the growth rate can be increased significantly by increasing the tube diameter (from the current 3/16 in. to 3/8 in.).

Even under current conditions, these data allow us to make a determination of reasonably achievable growth rates onto lengths of tape. From the data in Fig. 1.102, it is obvious that a deposition area of 1 × 4 cm is easily achieved. Additional experiments have indicated that the growth rate varies only weakly within a 2-in.-diam area. Therefore, future work may employ a larger area and multiple passes through the deposition zone to utilize the entire width. From the growth rates in Fig. 1.103 we calculate that a 1-μm-thick film would be deposited in 0.93 h and thus that a meter-long tape would be coated in one day.

Multiple passes and multiple sources would increase this rate proportionally. In addition, collection across a longer length (in a single pass) combined with a larger-diameter beam tube is expected to increase this rate by a factor of 2 to 4.

1.15.4. Conclusions

During this fiscal year, the PED process has been perfected via careful adjustment of growth parameters and the installation of an improved triggering mechanism. YBCO films grown on single-crystal substrates routinely exhibit critical current densities exceeding 2 MA/cm^2. However, the combined results of X-ray diffraction, Raman spectroscopy, and cross-sectional TEM clearly show a partial decomposition of the material into $BaCuO_2$ outgrowths and Y_2O_3 inclusions. Lower substrate temperatures did not yield good superconducting films, and we speculate that electron damage occurs and must be annealed out during the growth. Hence, growth onto buffered RABiTS™ tapes was not successful, because the available tapes are not resistant to temperatures exceeding 820ºC.

The highest J_c of YBCO obtained to date by PED onto buffered metallic tapes (here or elsewhere), carrying a current of 0.81 MA/cm^2, was obtained by the ex situ conversion of a precursor deposited at room temperature and containing fluorides. Interestingly, the conversion rate of this precursor was approximately twice that of a comparable layer obtained by e-beam evaporation.

Careful studies of the time and position dependence of the composition during long runs (30 h) showed surprising continuity of the approach, thus offering great promise for the adaptation of the technique to reel-to-reel deposition of precursors.

1.15.5 References

1. Q. D. Jiang et al., *Thin Solid Films* **241**, 100 (1994).

1.16 SELF-ORGANIZED CURRENT TRANSPORT THROUGH LOW ANGLE GRAIN BOUNDARIES IN $YBa_2Cu_3O_{7-\delta}$ THIN FILMS, STUDIED MAGNETOMETRICALLY

J. R. Thompson (University of Tennessee, ORNL); H. J. Kim (University of Tennessee); C. Cantoni, D. K. Christen, R. Feenstra, and D. T. Verebelyi (ORNL)

1.16.1 Introduction

High-temperature superconductors characteristically have highly anisotropic properties and a short scale of the superconducting coherence length (ξ). As a consequence, the critical current density across grain boundaries can be significantly reduced relative to that which flows within grains. For reasons that are not well understood, a large misalignment of adjacent grains suppresses the order parameter along the grain boundary (GB) and as a result, the adjacent grains are weakly linked. The weak-link behavior of a high-angle grain boundary and a near-exponential decrease in the GB critical current density J_c^{GB} with misorientation angle were first studied by Dimos et al. in $YBa_2Cu_3O_{7-\delta}$ materials. Since then, a number of studies have been conducted on this and other high-T_c superconductors, as reviewed recently by Hilgenkamp and Mannhart [1]. This review article provides an excellent overview of grain boundaries in these materials, the controlled synthesis of GBs, current transport, and related topics. Much earlier work focussed on the properties of GBs with relatively large misorientation angles $\theta > 10°$, where intergrain current conduction is severely suppressed. The present work concentrates on materials with lower angle GBs, which are contained in YBCO rings for magnetometric study.

The regime of lower angle grain boundaries is interesting because the mode of current conduction appears to cross over from weak to strong linkage with decreasing tilt angle θ. Technologically this is highly relevant. Recently developed methods for forming highly-textured coated conductors, such as rolling-assisted biaxially textured substrates (RABiTS™) and ion-beam assisted deposition (IBAD), vastly improve the current conduction in multicrystalline coated conductors of high-temperature superconductors by reducing the average misorientation into a regime of low angles ($\theta \leq 7°$). For

sufficiently small angles, the material between dislocation cores on the grain boundary is only mildly perturbed, and this provides a strong conduction channel comparable to or wider than the in-plane coherence length. For further development of coated conductors, an understanding of low-angle GBs is important because it gives guidance as to how highly textured the materials must be. Specifically, whether low-angle GBs are still weakly linked and responsible for large reductions of the GB current density and how the application of an external magnetic field affects the current flow need to be determined.

This magnetometric study of low-angle GBs is based on a simple equation from electrodynamics. A circulating current generates a magnetic dipole moment according to the equation

$$m = (1/2c)\int (r \times J(r))\,\mathrm{d}V \tag{1}$$

where J is the current density at location r. This expression tells us that once the current configuration is established, the current or (spatially uniform) current density can be calculated from the measured magnetic moment of a sample. The current configuration is related to the sample geometry. With the sensitivity of SQUID-based instrumentation and a simple ring geometry that helps define the current path, we obtain the critical current density, J_c, flowing through grain boundaries in the high-temperature superconductor $YBa_2Cu_3O_{7-\delta}$ (YBCO), and for comparison, the J_c of companion rings with no GBs. Furthermore, the magnetic responses *m(H)* of the rings are compared and contrasted. We observe a large peak in the decreasing field branch of the *m(H)* curves for GB rings with θ = 5.1 and 7° and show that its appearance arises largely from a cancellation of the applied magnetic field by self-field effects on weakly linked grain boundaries.

1.16.2 Magnetic Moments in the Critical State

In the critical state model, one assumes that critical currents with density $\pm J_c$ flow throughout the superconductor. In this work, the currents are induced by applying a large magnetic field H_{app} perpendicular to flat, planar samples. It is then straightforward to integrate Eq. (1) and obtain the associated magnetic moment m for several of the sample geometries used here. For example, a flat strip of thickness d, length ℓ, and width w has

$$m_{strip} = J_c d\ell w^2 / 40 \times [1 - w/3\ell] \tag{2}$$

according to the sandpile model. This and following expressions have cgs units with dimensions in cm, J in A/cm^2, and m in erg/G = emu. For the long narrow strips considered here, the factor $[1–w/3\ell] \approx 1$ will be neglected. Equation (2) also gives the moment of an "open circuit" thin ring of the same thickness and width, where $\ell = 2\pi R$ for a ring of radius R.

$$m_{openring} = J_c d(2\pi R) w^2 / 40 \tag{3}$$

Another standard case is that of a disk of outer radius a and thickness d:

$$m_{disk} = J_c \pi d a^3 / 30 \tag{4}$$

From this, it follows that a continuous ring with outer radius a and inner radius a_1 has moment

$$m_{ring} = J_c \pi d (a^3 - a_1^3) / 30 \tag{5}$$

For a thin ring with $a - a_1 = w << a$, Eq. (5) is nearly the same as the simplest expression

$$m_{loop} = I_c \pi a^2 / c \tag{6}$$

where I_c is the critical current and the speed of light c has value 10 in these laboratory units.

Let us now consider the case of a thin ring that crosses a GB. The GB is expected to have a lower critical current density J_c^{GB} and lower critical current I_c^{GB} than the surrounding epitaxial YBCO grain film with critical current density J_c^{Gr}. When applying a magnetic field, we first induce currents that circulate around the outer and inner circumferences of the ring and that screen flux from the central hole [2]; simultaneously, flux penetrates into the grain YBCO and more deeply into the GB. When the current exceeds I_c^{GB}, flux enters the hole along the GB and is trapped there. Application of still higher fields drives flux into all of the grain material where currents with density J_c^{Gr} flow throughout. Thus a portion of the current approaching a GB can cross it and generate the magnetic moment of a loop [Eq. (6)]. The self-organizing, remaining portion of the current makes a "U-turn," giving the magnetic moment of a strip [Eq. (2)]. The resulting Bean-like flux profile is displaced from the center of the strip, just as in the case of a superconducting strip carrying both a transport current and critical state currents. Let us define Δ by $J_c^{GB} = (\Delta/w)\, J_c^{Gr}$ as a measure of the GB current (geometrically $\Delta/2$ corresponds to the displacement of the flux profile from the center line of the "strip"). Then we have

$$m_{GBring} = m_{loop} + m_{strip} \tag{7}$$

$$m_{GBring} = (\Delta/w) J_c^{Gr}\, wd\pi a^2/c + J_c^{Gr} d(2\pi a)(w-\Delta)^2/40 \tag{8}$$

These expressions ignore terms of order $(w/a)^2$. Experimentally, we determine J_c^{Gr} in a separate experiment, then solve Eq. (8) for (Δ/w), from which J_c^{GB} is obtained.

1.16.3 Experimental Aspects

In order to use the above equations effectively for this study, samples were specially designed as rings in the following process. Films of YBCO were prepared on $SrTiO_3$ (STO) [001]-tilt bicrystal substrates by pulsed laser deposition. Three ring samples were made from each YBCO film using standard optical photolithography techniques. One ring was placed across a grain boundary so as to contain two grain boundaries (GB ring); two other rings were patterned on each of the two adjoining single crystals (grain rings). All three rings have the same geometry with an outside diameter $2a$ of 3 mm and an inside diameter $2a_1$ of 2.8 mm, giving a ring width w of 0.10 mm, and a thickness d of 200 nm. The substrate was cut into three pieces, each containing just one ring. Note that all three rings come from a single YBCO film and as a result, the films *per se* should have the same properties, such as current density and pinning force. Bicrystal substrates with 1.8°, 2.8°, 5.1° (two samples), and 7° [001]-tilt boundaries were used to make GB and companion grain ring samples. Sometimes the current density can be diminished by external degrading factors, such as cracks on a sample or by maltreatment. To cross-check the deduced current density values of grain rings, some grain rings were made into an open circuit by etching a line across the 100-μm width (open rings). This changes the geometry of the current path without changing the properties of the superconductor; consistent values of J_c were obtained.

Magnetic measurements were conducted with a SQUID-based Quantum Design MPMS-7 magnetometer. An individual sample was mounted on a Si disk with Duco cement and placed in a Mylar tube for support. For each ring, the magnetic moment was measured as a function of temperature and magnetic field. For temperature sweep experiments, a magnetic field was applied parallel to the *c*-axes of YBCO film at 5 K (500 Oe, 3 kOe, and 3 kOe for grain, GB, and open rings, respectively); the field levels

were chosen to ensure that each sample geometry was fully penetrated by the field. Subsequently, the applied field was reduced to zero ($H_{app} = 0$) to induce circulating currents in the material (and the magnet was "reset" to provide the quietest and most stable magnetic environment). Then we measured the remanent-state magnetic moment as a function of temperature from 5 K to 95 K in 1 K steps. Complementary field-dependent moments *m(H)* (i.e., hysteresis loops) were measured in increasing and decreasing applied magnetic fields in the range from 0 Oe to 30 kOe. The field sweep measurements were conducted at temperatures of 5, 10, 20, 40, 60, 77, and 85 K for each ring. To obtain the critical current density, from the measured magnetic moments, the critical state expressions Eqs. (3–8) were used for each sample configuration.

1.16.4 Results of the Temperature Sweep Experiments

For the temperature sweep measurements, each ring was prepared in the critical state by applying a large magnetic field and then reducing it to zero. Two examples of these results for $J_c(T)$ in zero applied field are shown in Fig. 1.104, for a ring containing a 5.1° GB and its companion grain ring. Both have the same T_c (near 93 K), as did all of the grain, GB, and open rings. For the grain ring in Fig. 1.104, the current density J_c^{Gr} was calculated using Eq. (5). These results are typical of those observed for the companion rings at 5 K in zero applied field, 34–40 MA/cm^2. For the GB ring, the current density J_c^{GB} was calculated using Eq. (8). As evident in the figure, the values are strongly suppressed relative to those in the grain ring. This is particularly so at low temperatures, where J at 5 K in zero applied field lies near 1.6 MA/cm^2. (The higher-J GB data, shown as filled symbols, were obtained in a finite, decreasing magnetic field, as will be discussed below). We reported previously that corresponding studies of 1.8° GB rings yielded current densities almost identical to those for the grain rings [3]. It was argued that the similarity between the 1.8° GB and its companion grain ring is a consequence of the large numbers of twin boundaries in YBCO thin films.

As the misorientation of the grain boundary increases, the GB current density diminishes significantly. While J_c^{GB} is the same as the grain value for a 1.8° boundary, the values at $T = 5$ K fall to ≈ 50% of J_c^{Gr} at θ = 2.8°, to 5% at 5.1°, and to 3% at 7°, respectively. Interestingly (and fortunately for coated conductor applications), the *fractional* transport is larger at $T = 77$ K, rising to ≈ 60% of J_c^{Gr} at θ = 2.8°, to 15–20% at 5.1°, and to 10% of J_c^{Gr} at 7°, respectively. These results show that a small-angle *c*-axis tilt boundary in the range 1.8° < θ ≤ 5.1° clearly impedes the current flowing across it. More precisely, the range 1.8° < θ ≤ 2.8° contains the critical angle where a grain boundary begins to suppress the current flow across it.

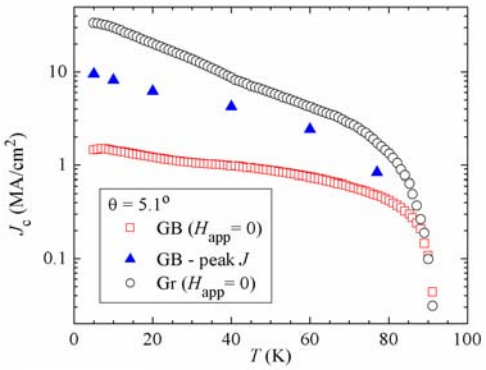

Fig. 1.104. The critical current density, J_c, of $YBa_2Cu_3O_7$ measured magnetically in zero applied magnetic field (open symbols), plotted vs temperature *T*. Results are shown for YBCO rings on $SrTiO_3$ containing a single 5.1° [001] tilt grain boundary (GB) and for comparison, a grain ring (Gr) with no GB. Filled symbols show peak values for J_c in the GB ring measured in-field, as discussed in the text.

1.16.5 Result of the Field Sweep Experiments

The isothermal magnetic response was studied at temperatures $T = 5$–85 K. For the grain and open rings, nicely symmetric curves of magnetic moment vs field were obtained, as illustrated by the inset to Fig. 1.105. The symmetry of the hysteretic *m* about the axis $m = 0$ means that the same absolute magnitude of J flows in the ring for increasing field (lower branch) and decreasing field (upper branch) histories. The critical current density was obtained from Eq. (5) and Eq. (3) for grain and open rings, respectively. Typical values were 34–40 MA/cm^2 in zero applied field at 5 K. Figure 1.105 shows the field and temperature dependence of J_c^{Gr} for one of the grain

rings. The dependence is simple, with a monotonic falloff with both *H* and *T*. As in temperature sweep experiments, the in-field features *m(H,T)* for the 1.8° GB and its companion grain ring were nearly identical in field sweep experiments. The curves of *m* vs *H* for the 1.8° and 2.8° GB rings were as symmetric as those of grain rings.

In contrast, the magnetic response of the rings with 5.1 and 7° grain boundaries is considerably more complex. This is evident in Fig. 1.106, which shows *m(H)* for the 7° ring at several temperatures. Also

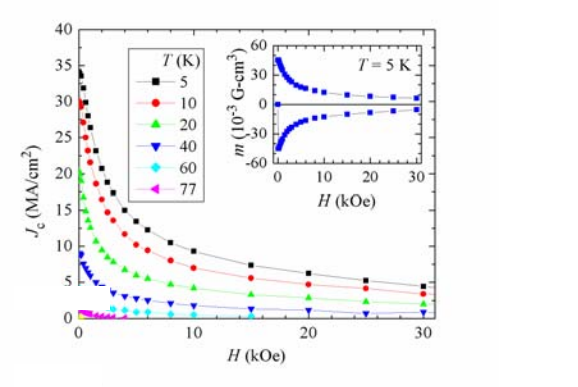

Fig. 1.105. For a YBCO grain ring without grain boundaries, the critical current density, J_c, vs applied field *H* at the temperatures shown. Inset: the magnetic moment *m(H)* at 5 K showing symmetric response in increasing and decreasing field histories.

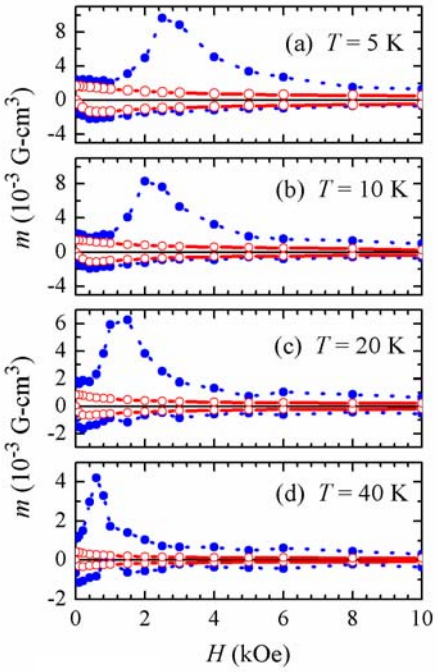

Fig. 1.106. The magnetic moment *m(H)* for a GB ring on $SrTiO_3$ containing a single 5.1° GB. The response is quite asymmetric, with a large peak in *m* and J_c^{GB} in decreasing field. For comparison, the moment of an open ring (open symbols, heavy line) is included to show the approximate magnitude of the signal produced by "U-turn" grain currents.

included for comparison are virgin curves for a representative open ring, which shows the signal produced by a ring with a "grain boundary" of zero conductivity. Qualitatively, the "excess" magnetic moment in the GB ring (larger than the open ring) arises from currents crossing the GB and flowing around the circumference of the ring. The most prominent feature in the *m(H)* curves for the 5.1° and 7° GB rings is the appearance of a large peak in the decreasing field branch; by comparison, the loops for the open ring are symmetric about the $m = 0$ axis, as this signal arises from grain-type currents. Compared with the GB current density in zero applied field, the value at the peak is considerably larger and it occurs at applied fields of several-kOe magnitude. To illustrate the difference, the values of J_c^{GB} at the peak are included in Fig. 1.104 as solid symbols.

The appearance of a peak in the GB current density has been reported many times and has been attributed to the effect of a magnetic field on a Josephson junction, which a grain boundary resembles [4]. The occurrence of a peak in the *m(H)* curves of a GB sample, occurring only in decreasing field, marks the appearance of weak-link behavior in the small-angle grain boundary. It is well known that the maximum tunneling current flows across a Josephson junction when the net magnetic flux, which is perpendicular to the tunneling current flow, become zero on the area of the junction. Applying this idea, one expects that the total magnetic field on a grain boundary H_{local} becomes roughly zero at the peak in J_c. Two major fields acting on the grain boundary are the applied magnetic field H_{app} and the field H_{self} created by induced currents flowing in the vicinity of and parallel to the grain boundary:

$$H_{local} = H_{app} \pm |H_{self}| \tag{9}$$

In increasing field, the directions of those two fields are the same, giving $H_{local} = H_{app} + |H_{self}|$. On the other hand, decreasing the applied field reverses the currents near the grain boundary, giving $H_{local} = H_{app} - |H_{self}|$ and allowing a cancellation of the applied and self fields. At the peak where $H_{local} \approx 0$, one has that $H_{peak} \equiv H_{app,peak} \approx |H_{self}| \propto J$; the last proportionality follows from the fact that H_{self} is created by currents flowing near the GB.

Figure 1.107 tests this scenario by plotting the peak field H_{peak} as a function of grain current density J_c^{Gr}, where both are measured at temperatures from 5 K to 77 K. In Fig. 1.107(a), we consider the simplest approximation that the effective currents have the density J_c^{Gr} of the grains, measured in $H_{app} = 0$. This is the most appropriate choice, since grain currents near the GB (where $H_{local} \approx 0$) contribute most strongly to H_{self}. The YBCO film is fully penetrated by flux, and J_c^{Gr} is determined in separate measurements on companion rings. Indeed, there is a strong correlation between the peak position, H_{peak}, and the grain current density, as shown by the straight line in the figure with correlation coefficient $R^2 = 0.983$. The figure includes data for the weakly linked GBs with $\theta = 5.1$ and 7°. To test
further the conjecture that a null local field produces the peak in J, we reduced the current density in two sets of rings while maintaining the same overall geometry; they were partially deoxygenated by annealing in 0.2 bar of O_2 at 500°C, followed by furnace-cooling. This decreased T_c to ≈ 65 K for the 5.1° GB and 75 K for the 7° GB. Data for those GBs are also included in Fig. 1.107 (labeled "deOx"), and they follow the same trend as the fully oxygenated rings.

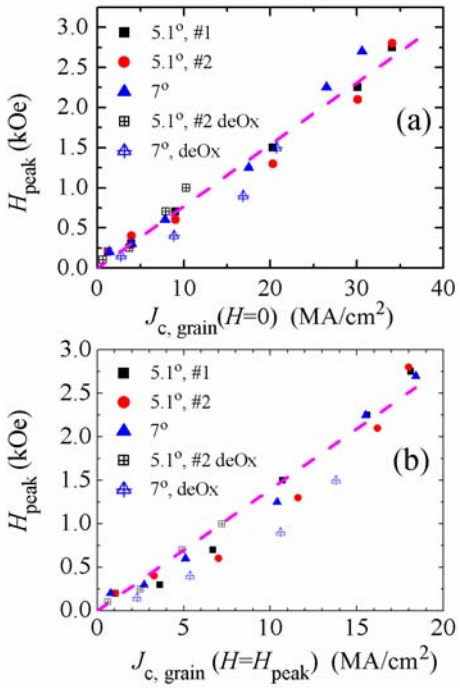

Fig. 1.107. The field H_{peak} where the GB J_c is a maximum in decreasing field, plotted vs grain current density, for the samples shown at temperatures from 5 to 60 K. (a) The current density is J_c^{Gr} measured in zero applied field, $H_{app} = 0$. (b) The current density is the grain value measured at the peak field (i.e., at $H_{app} = H_{peak}$ for each case.

As seen in Fig. 1.107(a), there is a clear correlation between H_{peak} and the grain J_c^{Gr}. One might consider, however, that the appropriate scale of nearby currents is the density J_c^{Gr} measured at $H_{app} = H_{peak}$. Thus Fig. 1.107(b) presents the peak field as a function of this lower, in-field current density. The resulting plot is similar to that in Fig. 1.107(a), with regression coefficient $R^2 = 0.986$. Overall, these analyses show that the position of the peaks in J_c^{GB} tracks the nearby current density quite well. This supports the conjecture that the peaks correspond to a nulling of the local field acting on a weakly linked grain boundary.

Next we ask whether currents in the film can create local fields comparable with the observed H_{peak}. This is a difficult question, as it involves the magnetic field very near the edge of a thin sheet of current-carrying superconductor. For one estimate, let us consider the case at $T = 5$ K with grain current density $J_c^{Gr} \approx 35$ MA/cm^2, where $H_{peak} \approx 2.8$ kOe [Fig. 1.107(a)]. Numerical work of Däumling and Larbalestier [5] has shown that the perpendicular field is $\mu_0 H \approx 1.1\ \mu_0 J_c d$ (in units of tesla) at the edge of a thin disk with radius/thickness = 10^3; this expression gives a field of ~ 1 kOe at the edge of one disk and

$H_{self} \approx 2$ kOe, since current flows on both sides of the grain boundary. An alternative estimate comes from the work of Brandt et al., who consider a very long thin strip of type II superconductor in a perpendicular magnetic field [6]. For the parameters cited, their expression for the normal field near the edge of a single strip gives values of 1.2 kOe at a distance $10 \times \xi_{ab} = 15$ nm from the edge of the strip, and 1.6 kOe at distance ξ_{ab}. Doubling these values as above to account for currents on each side of the grain boundary yields self fields, H_{self}, that are very comparable with the 2.8 kOe observed experimentally. While the geometries (disk, edge of thin strip) differ somewhat from the GB geometry, these estimates give some quantitative support for the "null field-weak link" model for the peak in GB current density.

To probe further the grain boundary system near the peak in J_c^{GB}, we performed minor loop experiments on the 5.1° GB ring at 5 K. The results are shown in Fig. 1.108(a); for comparison, identical measurements on one of the grain rings are shown in Fig. 1.108(b). After making a standard *m(H)* loop to 10 kOe and back to $H = 0$, we began to retrace the loop, increasing H from low field. Then at 2.2 kOe, the applied field was decreased in 2-Oe steps until the magnetic moment reached the decreasing field branch of the *m(H)* curve. (The orientations of the symbols in Fig. 1.108 show the direction of field change.) The changes in m were very gradual and a field change of at least 100 Oe was needed in order to reach the upper branch. This experiment in the increasing field branch was repeated at 4 kOe with similar results. In contrast, the GB system is much more sensitive in the decreasing field branch: when decreasing H from high fields to the peak at 2.6 kOe, an increase of 20 Oe produced a large reduction in the magnetic moment. An increase of only 20 Oe is large enough to switch the magnetic moment almost to the lower branch. At decreasing fields of 1.8 and 4.2 kOe that lie on either side of the peak, the effect is similar although less dramatic at 1.8 kOe where J_c^{GB} is smaller. A smaller feature to note is the "foot" where a minor loop rejoins the main *m(H)* curve; particularly noticeable at the lower branch, this component of m develops as currents with density J_c^{Gr} fully penetrate the "strip-like" portion of the ring.

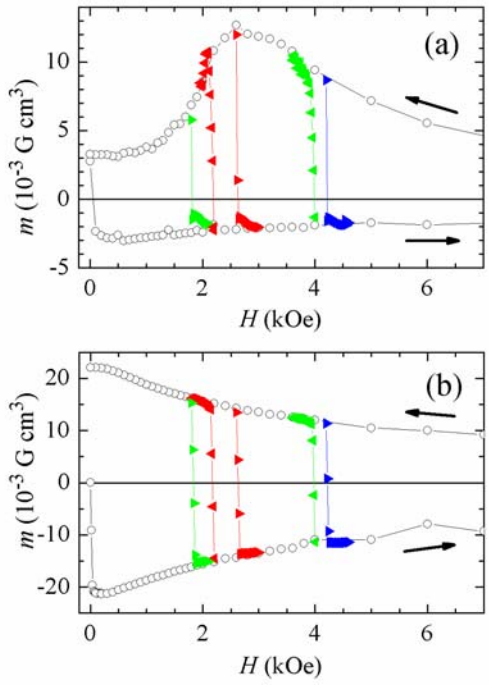

Fig. 1.108. Minor loops *m(H)* at $T = 5$ K for (a) a grain boundary (GB) ring with θ = 5.1° and (b) a grain ring with no GB. In both cases, the open symbols show the envelope signal obtained by monotonically sweeping the field from $H = 0$ up to high field, then down to zero; filled symbols show the effect of 20-Oe steps in H in the reverse direction, where the orientation of the symbols shows the direction of field change. For the grain ring in (b), the response is symmetric, while it is quite asymmetric for the GB ring in (a).

The major conclusion of the minor loop study is that near the peak in decreasing field, the grain boundaries are very sensitive to a reversal in field-sweep direction. Such a reversal induces oppositely directed perimeter currents in the film and switches the sign in Eq. (9) from (–) to (+). Those changes quickly add magnetic flux on the GB, and this degrades the tunneling current across it. In contrast, the same experiments on a grain ring give a symmetric response, as illustrated in Fig. 1.108(b). Steps in H of 20 Oe give uniform changes in m, whether increasing or decreasing; the slope dm/dH is the same as that at $H = 0$, as is evident from the equally spaced points for m. The latter is determined almost entirely by the geometry of the ring through its (effective) demagnetizing factor D. From this perspective, one can consider that the GB ring at its peak has the very large demagnetizing factor of a thin flat ring, but increasing H in a minor loop tends to "open up" the GB and reduce D to the smaller values more

characteristic of a thin strip. This discussion is, of course, only qualitative since some current does flow across the GB. Overall, these minor loop experiments give further support to the picture that the asymmetric, history-dependent J_c^{GB} and its peak in decreasing field all originate in the weak linkage of a grain boundary that is strongly affected by the local field.

Some aspects of the magnetic field dependence remain difficult to understand. In particular, analysis of the magnetic moments in Fig. 1.106 for increasing field history suggests that the values are about a factor-of-2 smaller than one might expect from estimates of H_{local} combined with the observed behavior in the decreasing field branch. This "excess" asymmetry was also observed by Däumling et al. [7] in transport studies on YBCO bicrystals with higher-angle grain boundaries. Other mechanisms, of course, contribute to the transport of critical currents across grain boundaries. These can include pinning of GB vortices by facets on the boundary or pinning of Abrikosov-Josephson vortices on the GB by interactions with (strongly pinned) Abrikosov vortices in the grains. However, none of these other mechanisms readily accounts for a strongly asymmetric response, most notably the pronounced peak in the decreasing field branch only.

1.16.6 Establishing the Critical State

While the results cited so far were obtained with the entire sample fully penetrated with flux, it is informative to examine how the critical state is established. For these experiments, the films were prepared in the virgin state by cooling them to low temperature in zero applied field. Then the magnetic moment was measured as the field was increased in steps of a few Oe. For the grain films patterned into narrow rings, the magnetic response is rather simple: m increases almost linearly with H with a slope $dm/dH \approx a^3$. This is illustrated in Fig. 1.109(a), where the initial slopes lie within 3% of the values calculated using Table I of Brandt [2] with (inner radius a_1)/(outer radius a) = 1.4 mm/1.5 mm = 0.933. This near-linearity is observed from $H = 0$ up to the field of full penetration $H_p \approx 0.1 \times J_c d$ for this geometry [2]. Full penetration, which is marked by a sudden departure from the nominally linear response in Fig. 1.109(a), occurs at progressively lower fields as J_c deteriorates with increasing temperature.

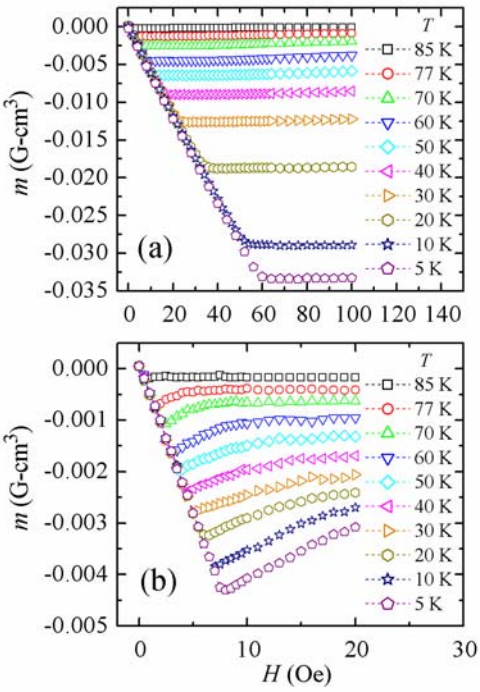

Fig. 1.109. The magnetic moment of virgin YBCO rings produced by applying small magnetic fields, at the temperatures shown. (a) an epitaxial grain ring with no grain boundaries and (b) a ring with grain boundary angle θ = 5.1°.

For rings containing a pair of small-angle grain boundaries, the initial response is similar. To show this, Fig. 1.109(b) presents *m(H)* for a ring with θ = 5.1°. Compared with the grain ring, however, there are two qualitative differences. First, the penetration field is much smaller, due to the lower I_c of the GB; in the range shown, H = 0–20 Oe, the film per se is little penetrated by flux and the moment m is determined almost entirely by circulating currents that cross the GB. Second, further increases in the applied field (above the GB penetration field) immediately reduce the magnitude of m. Again, this can be attributed to the sensitivity of the GB J_c to the local field (i.e., applied plus self-field). Experimentally, the GB ring traps no flux until the applied field exceeds the (negative) peak in m.

Establishing the critical state in an open ring is an interesting contrast. For a thin strip of width w and length ℓ that the open ring resembles, the magnetic moment is given by [2]

$$m(H) = \left(J_c dw^2 \ell / 4c\right) \tanh\left(H / H_c\right) \tag{10}$$

where the scaling field $H_c = J_c d \pi$ and J_c = constant. Figure 1.110 shows the initial magnetization curve, *m(H)*, for an open ring at 5 K where, in comparison to the closed ring, the initial slope is much smaller and the approach to saturation is much more gradual. The solid line shows Eq. (10) drawn with the dimensions *w*, *d*, ℓ of the strip and the current density value J_c = 35 MA/cm^2 obtained from a full hysteresis loop, giving H_c = 22.5 kA/m = 283 Oe. The agreement at low fields is excellent. In larger fields, the theoretical curve lies somewhat below the experimental *m* because J_c is not constant, but rather decreases with *H*.

Also included in Fig. 1.110 are the magnetic responses of GB rings with θ = 5.1 and 7°, all at 5 K. The initial signal (*H* = 0–10 Oe) develops very rapidly; this increase and the subsequent falloff of |*m*| are the same as those shown in Fig. 1.109(b) and discussed above. For larger fields H ≥ 50 Oe, the magnitude of |*m*| again increases. This additional contribution comes from currents induced and flowing entirely within the grain material (not crossing the GB), as evidenced by the fact that the *m(H)* curves for the two GB rings are almost parallel to that for the open ring "strip," but displaced from it. The same phenomenon —generating an additional contribution to *m* by inducing grain currents that are reflected at the GBs— produces the "foot" on the minor loops in Fig. 1.108(a).

1.16.7 Conclusions

Using magntic methods, we have studied current conduction and weak linkage in low-angle grain boundaries. Materials investigated were ring-shaped YBCO films with or without [001]-tilt boundaries. Relating the measured magnetic moments to the current configurations in GB, grain, and open ring samples, we obtained the GB current density, J_c^{GB}, from the ring-like contribution to the magnetic moment. The temperature sweep experiments show that a small misorientation 1.8° < θ ≤ 7° significantly reduces the grain boundary current density J_c^{GB}. However, no difference was observed between the 1.8° GB and its companion grain rings. This study suggests that to obtain the highest current density in YBCO thin films and coated conductors with present grain boundary structures, it will be necessary to reduce the *c*-axis tilt grain boundaries into the range ~ 3–4°. For the 5.1 and 7° GB rings, the *m(H)* (and $J_c(H)$) curves have a large peak in finite field, but only for decreasing field history. In small increasing field, the *m(H)* curve of a GB ring resembles that of an open ring. These two results from the field sweep experiments arise from the weak-linkage in moderately low-angle GBs. The high sensitivity of the current density across a GB to field changes on the GB strongly bolsters the weak-link interpretation of low-angle grain boundaries.

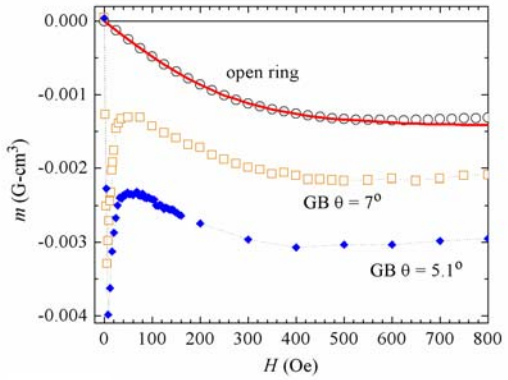

Fig. 1.110. The magnetic response *m(H)* of an open ring; solid line shows a fit to Eq. (10) in the low field region where flux is penetrating the "strip." Also included for comparison is the response of rings with θ = 5.1 and 7°. All data are at *T* = 5 K.

1.16.8 References

1. J. Mannhart and Hilgenkamp, *Rev. Mod. Phys.***74**, 485 (2002).
2. E. H. Brandt, *Phys. Rev. B* **55**, 14513 (1997).
3. D. T. Verebelyi et al., *Appl. Phys. Lett.* **78**, 2031 (2001).
4. J. E. Evetts and B. A. Glowacki, *Cryogenics* **28**, 641 (1988).
5. M. Däumling and D. C. Larbalestier, *Phys. Rev. B* **40**, 9350 (1988).
6. E. H. Brandt, M. V. Indenbom, and A. Forkl, *Europhys. Lett.* **22**, 735 (1993).
7. M. Däumling et al., *Appl. Phys. Lett.* **61**, 1355 (1992).

1.17 HIGH CRITICAL CURRENT MOD EX SITU YBCO FILMS ON RABiTS™ AND MgO-IBAD TEMPLATES

X. Li, M. W. Rupich, W. Zhang, N. Nguyen, T. Kodenkandath, U. Schoop, D. T. Verebelyi, and C. Thieme (American Superconductor); M. Jowett, P. N. Arendt, S. R. Foltyn, and T. G. Holesinger (LANL); T. Aytug, D. K. Christen, and M. P. Paranthaman (ORNL)

1.17.1 Introduction

Ex situ conversion of BaF_2-based precursor films, prepared by metal organic decomposition (MOD) of metal trifluoracetate (TFA) precursors, to YBCO films [1–7] has been recognized as an attractive, low-cost, scaleable process for the epitaxial growth of YBCO films for second-generation coated conductor wires. Although high critical current densities (J_cs) have been reported in thin YBCO films, it has been observed that J_c degrades drastically with increasing film thickness [3–6]. Recently, with the development of an improved single-coating MOD-TFA process, YBCO films with J_cs as high as 4 MA/cm^2 (77 K, self-field) have been demonstrated at a YBCO thickness of 0.9 μm on CeO_2-capped YSZ single crystal [8]. This performance is equivalent to, or better than, that obtained by the pulsed laser deposition (PLD) method [9], confirming that the MOD-YBCO process is capable of achieving high I_c performance. However, in order to apply the solution-based TFA process to grow high-quality YBCO films on flexible metal tapes, a biaxially textured template is required. Rolling Assisted Biaxially Textured Substrates (RABiTS™) [10] and ion-beam-assisted deposition (IBAD) [11, 12] have become two leading techniques for template fabrication. By combining the TFA-MOD process with the RABiTS™ template, uniform YBCO coated conductors with I_c > 100 A/cm-width have been repeatedly demonstrated using a continuous reel-to-reel process over 10-m lengths [13, 14]. Meanwhile, the use of MgO as an IBAD template film has made great progress and has decreased the time to produce the template film by nearly two orders of magnitude compared with the YSZ template [15]. With $LaMnO_3$ as a buffer layer, high-performance YBCO films have been reported on short samples using PLD-YBCO deposition [16, 17]. We have extended this work to what we believe is a scalable manufacturing process by combining MOD-YBCO with both RABiTS™ and MgO-IBAD templates. In this paper, we report our first demonstration of high-I_c, thick YBCO films on both NiW-RABiTS™ and MgO-IBAD substrates using the TFA-MOD ex situ conversion method.

1.17.2 Experiment

The IBAD template has the layer structure of CeO_2/$LaMnO_3$/MgO-IBAD/Hastelloy (referred to as the IBAD sample in this paper). The biaxially textured MgO layer on the Hastelloy substrate was deposited at Los Alamos National Laboratory [15]. The 200-nm-thick $LaMnO_3$ buffer layer was deposited on the MgO-IBAD by rf-magnetron sputtering at Oak Ridge National Laboratory. Details of the MgO-IBAD fabrication and the $LaMnO_3$ deposition process have been published elsewhere [15, 16]. A CeO_2 cap layer with a thickness of about 140 nm was deposited on the $LaMnO_3$ buffered MgO-IBAD templates by rf-magnetron sputtering from an oxide target at 600°C in an Ar and O_2 atmosphere (O_2:Ar ~ 1:3).

The RABiTS™ template used in this study has an architecture of CeO_2/YSZ/Y_2O_3/Ni/NiW (referred to as the RABiTS™ sample). Preparation of the substrate and buffer layers has been described in detail elsewhere [8]. Briefly, it involves the deposition of an epitaxial transient Ni layer on the rolling textured NiW substrate (5 at. % W) followed by the epitaxial growth of Y_2O_3 seed, YSZ barrier and CeO_2 cap layers. The transient Ni layer was deposited by dc-magnetron sputtering. The Y_2O_3 layer (~50 nm) was deposited by electron beam evaporation while the YSZ (~200–300 nm) and CeO_2 layers were deposited by rf-magnetron sputtering. For the purpose of comparison, the CeO_2 layer thickness was also kept at around 140 nm for the RABiTS™ sample in this study unless mentioned otherwise.

The YBCO films on both the RABiTS™ and IBAD templates were deposited by a solution coating process using a TFA-based MOD precursor [8]. The as-deposited films were pyrolyzed at 400ºC in a humid oxygen atmosphere into a green film with a nominal composition of BaF_2, CuO, and Y_2O_3. The

green films were then converted to the epitaxial superconducting phase in a tube furnace with a humidified, low oxygen pressure environment at a temperature of 700 to 800°C.

Phase and crystallinity of the films were characterized by X-ray θ-2θ diffraction. The in-plane texture of the CeO_2 and YBCO layers was measured by the full width at half maximum (FWHM) values of CeO_2 (111) and YBCO (102) X-ray ϕ–scans. Cross-sectional TEM was used to study the film and interface microstructure. The detailed sample preparation has been reported elsewhere [18]. Both cross-sectional SEM and TEM were used for the thickness measurements of the buffers as well as YBCO layers. The transport critical current was measured at 77 K, self-field, using a standard four-point technique over a 1-cm-long sample with a voltage tap distance of 3 mm. A 1- to 2-μm Ag layer was deposited on the samples before the electrical measurements. Critical current values were determined with a 1-μV/cm criterion.

1.17.3 Results and Discussion

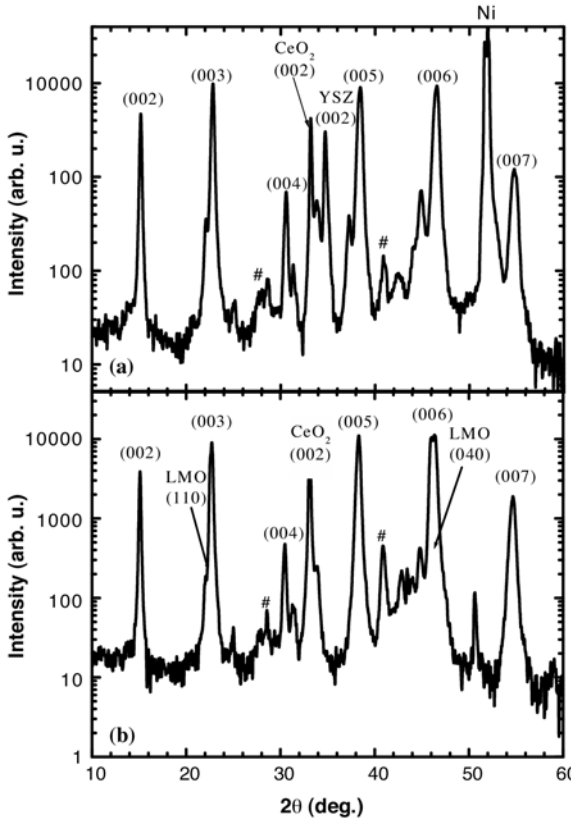

Fig. 1.111. X-ray diffraction spectra of (a) YBCO/CeO_2/YSZ/Y_2O_3/Ni/NiW (RABiTS™ and (b) YBCO/CeO_2/$LaMnO_3$/MgO-IBAD/Hastelloy. The (00*l*) indices on the graph refer to the YBCO (00*l*) diffraction. The "#" indicates the $BaCeO_3$ diffraction.

Figure 1.111 shows the θ-2θ XRD scans of the YBCO films grown on CeO_2 capped RABiTS™ (A) and IBAD (B) samples. In both samples the CeO_2 cap layers present the strong (100)-texture. Meanwhile, as evidenced by the strong (00*l*) diffraction, the *c*-axis-oriented YBCO films were successfully deposited on both the CeO_2-capped RABiTS™ and IBAD samples using ex situ conversion of MOD-TFA YBCO. Minor $BaCeO_3$ formation at the YBCO-CeO_2 interface was observed in both samples.

The high degree of biaxial textured epitaxial CeO_2 caps and the YBCO layers are confirmed by the X-ray ϕ-scans shown in Figure 1.112 for both the RABiTS™ (A) and IBAD (B) samples. The in-plane FWHM values for the 140-nm-thick CeO_2 caps on both the RABiTS™ and IBAD samples are very close (i.e., 5.4° for the RABiTS™ sample, and 5.5° for the IBAD sample). The YBCO in-plane texture has a FWHM of 4.5° for the RABiTS™ sample but a FWHM of 2.5° for the IBAD sample. The in-plane texture of YBCO improves in both films compared with that of the CeO_2 cap layers. The improvement in the in-plane texture is much larger in the IBAD sample, in which the FWHM decreases from 5.5° in the CeO_2 to 2.5° in the YBCO layer.

Figure 1.113 shows the cross-sectional TEM images of YBCO films on both the RABiTS™ and IBAD samples. The YBCO microstructures for the two samples are quite similar even though the thickness of the CeO_2 cap layer for the RABiTS™ sample shown here is 20 nm. The YBCO films consist of a layered structure, in contrast to the columnar structure of the buffer layers. Porosity, inclusions, and secondary

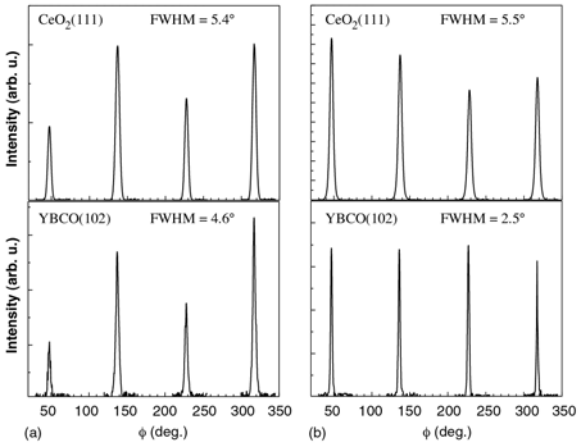

Fig. 1.112. XRD ϕ-scans of CeO_2 and YBCO on (a) YBCO/CeO_2/YSZ/Y_2O_3/Ni/NiW (RABiTS™ and (b) BCO/CeO_2/$LaMnO_3$/ MgO-IBAD/ Hastelloy.

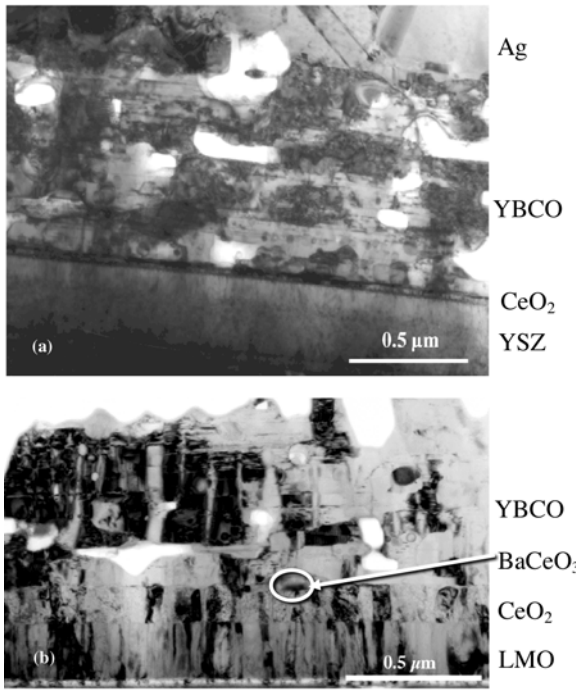

Fig. 1.113. Cross-section TEM of (a) YBCO/CeO_2/YSZ/Y_2O_3/Ni/NiW (RABiTS™) and (b) YBCO/CeO_2/$LaMnO_3$/MgO-IBAD/Hastelloy.

phases are found in the YBCO layer in both samples. Most of the pores appear oriented in the planar direction. The fine horizontal lines observed in the YBCO layers are believed to be stacking faults. In both cases, the interfacial reaction is relatively minor and does not appear to alter the YBCO structure above it. In the IBAD sample the $BaCeO_3$ tends to form in small, discrete areas. The YBCO structure is not altered in areas were $BaCeO_3$ is present compared with areas with a clean CeO_2/YBCO interface. This suggests that most of the $BaCeO_3$ reaction may occur after the initial nucleation and growth of the YBCO. Detailed microstructure analysis of these high-I_c films is under investigation, and the results will be reported in the near future.

The resistance-temperature and I-V curves for a typical MOD-YBCO/RABiTS™ sample are shown in Fig. 1.114. The transition temperature, T_c, is 90.5 K with a ΔT_c of 1 K. The current density of this sample is 2.2 MA/cm^2 (YBCO width of 0.84 cm and thickness of 0.9 μm), which is equivalent to an I_c of 202 A/cm-width. An I_c of 194 A/cm-width or J_c of 2.2 MA/cm^2 (YBCO width of 0.5 cm and thickness of 0.9 μm) was obtained on the IBAD sample. The IBAD sample has a T_c of 92 K and ΔT_c of 0.5 K, as shown in Fig. 1.115. Both J_c and T_c measurement results indicate that the MOD-YBCO films grown on RABiTS™ and IBAD templates have very similar superconducting transport properties.
Although it is generally believed that the transport properties of the YBCO are dictated by its grain boundary microstructure, the similar J_c performance of the two samples reported in this paper does not seem to be correlated with the rather different in-plane texture of the two YBCO films. A possible explanation is that the reduction in J_c due to grain boundary misalignment is small for a misalignment angle less than 4°. Meanwhile, other microstructure characteristics, such as porosity, secondary phases, grain size, and grain structure, may play a dominant role in determining J_c. The similar microstructure observed in both YBCO films is consistent with this hypothesis.

1.17.4 Conclusion

We have demonstrated the successful deposition of high-performance YBCO thick films on both CeO_2-capped RABiTS™ and MgO-IBAD substrates using a low-cost, scalable MOD-TFA ex situ conversion process. Similar YBCO microstructures are obtained in both samples. Critical current levels of

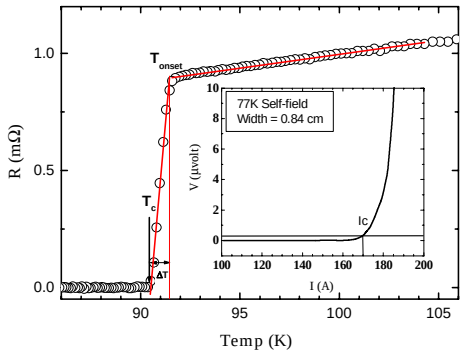

Fig. 1.114. T_c and I_c (inset) plot of Ag/YBCO/ CeO_2/YSZ/Y_2O_3/Ni/NiW (RABiTS™). YBCO thickness is 0.9 μm. I_c is measured with a 1-μV/cm criterion.

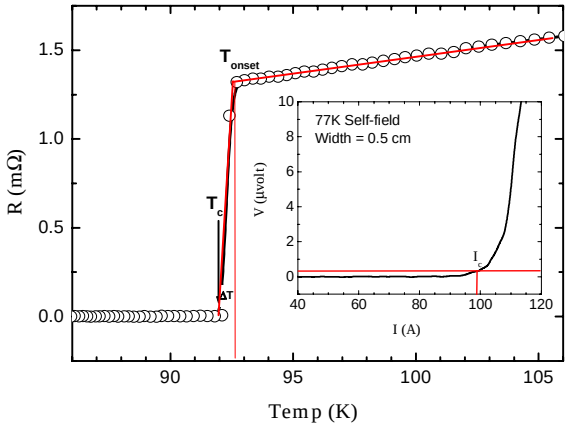

Fig. 1.115. T_c and I_c (inset) plot of Ag/YBCO/CeO_2/$LaMnO_3$/MgO-IBAD/Hastelloy conductor. YBCO thickness is 0.9 μm. I_c is measured with a 1-μV/cm criterion.

202 A/cm-width and 194 A/cm-width were achieved on short RABiTS™ (NiW) substrates and MgO-IBAD/Hastelloy substrates, respectively.

1.17.5 References

1. P. C. McIntyre, M. J. Cima, and A. Roshko, *J. Appl. Phys*. **77** (10), 5263 (1995).
2. P. C. McIntyre, M. J. Cima, and M. F. Ng, *J. Appl. Phys*. **68** (8), 4183 (1990).
3. J. A. Smith, M. J. Cima, and M. N. Sonnenberg, *IEEE Trans. Appl. Supercond*. **9** (2), 1531 (1999).
4. S. Sathyamurthy and K. Salama, *Physica C* **329**, 58 (2000).
5. I. Matsubara et al., *Physica C* **319**, 128 (2000).
6. H. Fuji et al., *Physica C* **378**, 1013 (2002).
7. A. P. Malozemoff et al., *Supercond. Sci. Technol*. **13**, 473 (2000).
8. M. W. Rupich et al., *2002 Appl. Super. Conf. Proc.* (accepted for publication).
9. S. Foltyn et al., *Appl. Phys. Lett*. **63**, 1848 (1993).
10. A. Goyal et al., *Appl. Phys. Lett.* **69**, 1795 (1996).
11. Y. Iijima et al., *Appl.Phys. Lett*. **60**, 769 (1992).
12. X. D. Wu et al., *Appl. Phys. Lett.* **67**, 2397 (1995).
13. L. J. Masur et al., Proceedings of the ISS2002 Conference, Yokohama, Japan, Nov. 11–14, 2002 (submitted).
14. D. T. Verebelyi et al., *IEEE Trans. Appl. Supercond*. (submitted).
15. J. R. Groves et al., *J. Mater. Res.* **16**, 2175 (2001).
16. M. Paranthaman et al., *IEEE Trans. Appl. Supercond*., to be published.
17. T. Aytug et al., *J. Mater. Res.* **17,** 2193 (2002).
18. T. G. Holesinger, et al., *J. Mater. Res*. **15**, 1110 (2000).

1.18 GROWTH OF THICK $YBa_2Cu_3O_{7-\delta}$ FILMS CARRYING AN I_C OF MORE THAN 230 A/cm ON SINGLE $LaMnO_3$ BUFFERED IBAD MgO SUBSTRATES

M. Paranthaman, T. Aytug, and D. K. Christen (ORNL); P. N. Arendt, S. R. Foltyn, J. R. Groves, L. Stan, R. F. DePaula, H. Wang, and T. G. Holesinger (LANL)

A single $LaMnO_3$ buffer layer has been developed for the growth of superconducting thick $YBa_2Cu_3O_{7-\delta}$ (YBCO) films on polycrystalline Ni-alloy substrates where a biaxially textured MgO layer, produced by ion-beam-assisted deposition (IBAD), was used as a template. By using pulsed laser deposition (PLD), a 1.65-μm-thick YBCO film with a critical current density of 1.4×10^6 A/cm^2 in self-field at 75 K has been achieved on sputtered $LaMnO_3$-buffered IBAD-MgO substrates. This corresponds to a critical current (I_c) of 231 A/cm-width. This result demonstrates the possibility of using both an $LaMnO_3$ buffer and an IBAD-MgO template for producing high-current-density YBCO coated conductors.

Major advances have been made in the last 16 years in high-temperature superconductor (HTS) research and development, resulting in increased use of HTS materials in commercial and precommercial electric-power applications. These applications include underground transmission cables, oil-free transformers, superconducting magnetic-energy storage units, fault current limiters, high-efficiency motors, and compact generators. Much progress has already been made, from the near-term commercialization of the first-generation bismuth strontium calcium copper oxide (BSCCO) superconductor tapes to the continuing advancement in second-generation yttrium barium copper oxide (YBCO) coated conductors. Potentially lower cost and improved superconducting properties under magnetic field at liquid nitrogen temperatures are some of the advantages of YBCO-coated conductor composites over BSCCO multifilament composites. The development of second-generation coated conductors continues to show steady improvement toward long-length processing capabilities. Recently, both ion-beam-assisted deposition (IBAD) and rolling-assisted biaxially textured substrate (RABITS™) processes have been used to demonstrate the growth of 10-m-long YBCO superconducting wires carrying an I_c of ~100 A/cm-width. To date, in the IBAD approach, either yttria stabilized zirconia (YSZ) or gadolinium zirconium oxide, $Gd_2Zr_2O_7$ (GZO), has been used as the deposited textured template layers on polycrystalline metal alloy tapes to produce long lengths of YBCO coated conductors. However, the requirement of a thick buffer layer (0.5–1 μm) to obtain the best texture in these templates, may limit the long-length processing efforts. Hence, to overcome this issue, other promising templates such as IBAD magnesium oxide (MgO), have recently been developed.

In the RABiTS™ approach, a four-layer architecture of CeO_2/YSZ/Y_2O_3/Ni/Ni-W is used to fabricate long lengths of buffered tapes by the epitaxial deposition on the thermomechanically textured alloy. In our strategic research, we have developed an alternative, single $LaMnO_3$ (LMO) buffer layer architecture on textured Ni-W substrates and recently demonstrated the growth of 0.2-μm-thick YBCO films with a self-field J_c of more than 1.2 MA/cm^2 at 77 K. From these studies, $LaMnO_3$ has been identified as a good diffusion barrier to nickel contamination.

$LaMnO_3$ is an antiferromagnetic insulator, and orthorhombic perovskite with lattice parameters a = 5.533 Å, b = 5.722 Å, and c = 7.694 Å. The pseudocubic lattice parameter of 3.88 Å is closely matched to YBCO; the lattice mismatch is less than 0.8 %. Following the initial success of our $LaMnO_3$ buffer layer with the RABiTS™ approach, we have extended this strategic research to IBAD-MgO templates as well. Wang et al. showed that IBAD-MgO requires only 10-nm thickness to develop a degree of texture comparable to that of IBAD-YSZ at 1-μm thickness [1]. For equivalent deposition rates, this translates to a process that is ~100 times faster than IBAD-YSZ. In order to determine the compatibility of $LaMnO_3$ with MgO surfaces, $LaMnO_3$ buffers were initially deposited on MgO (100) single-crystal substrates. A self-field J_c of more than 4×10^6 A/cm^2 at 77 K was obtained on 0.2-μm-thick YBCO films grown on $LaMnO_3$-buffered MgO single-crystal substrates using both PLD and ex situ BaF_2 processes, indicating that LMO buffers are highly compatible with MgO surfaces. Very recently, we have demonstrated the growth of 0.2-μm-thick YBCO films with a J_c of 1.8×10^6 A/cm^2 at 77 K and self-field on $LaMnO_3$-

buffered IBAD-MgO substrates. In this paper, we report our first demonstration of the growth of thick YBCO films on $LaMnO_3$-buffered IBAD-MgO templates.

We have grown 200- to 300-nm-thick LMO buffer layers on IBAD-MgO templates on Ni-alloy by rf-magnetron sputtering. The oxide sputter targets were made from single-phase LMO powders, prepared by solid-state reaction and loosely packed in a 4-in. copper tray. Typical sputter conditions consisted of 2 to 5×10^{-5} Torr of H_2O with a total pressure of 3 mTorr forming gas (Ar/H_2 4%). The water pressure is sufficient to oxidize the film to form stoichiometric $LaMnO_3$, when grown at a substrate temperature of ~750°C. The deposition rate was ~0.06 nm/s. The MgO template consists of the following architecture: mechanically polished Hastelloy C-276/amorphous Y_2O_3 nucleation layer/IBAD MgO layer (~10 nm)/ homoepitaxial MgO layer (~25 nm). Briefly, 1-cm-wide Hastelloy C-276 substrates are mechanically polished and spot welded into meter-length loops. These loops are inserted into the deposition system and coated in a continuous mode with approximately 10 nm of IBAD-MgO. The tapes are then coated with another 25 nm of homoepitaxial MgO by using magnetron sputtering. Detailed processing conditions for the preparation of IBAD-MgO templates and the details of the YBCO deposition by PLD were published earlier. The typical YBCO thickness is 1.65 μm. Samples were patterned into microbridges and J_c was measured using a four-point probe configuration at 75 K in self-field. The texture of the samples was quantified by X-ray diffraction (XRD), and sample microstructure was examined by both scanning electron microscopy (SEM) and cross-sectional transmission electron microscopy (TEM).

A typical θ-2θ scan of a 1.65-μm-thick PLD-YBCO film grown on $LaMnO_3$-buffered IBAD-MgO substrate is shown in Fig. 1.116. This scan indicates the presence of a *c*-axis-aligned YBCO film. The presence of NiO impurities was not observed. Figure 1.117 shows the XRD results from out-of-plane (ω) and in-plane (ϕ) scans on YBCO/ $LaMnO_3$/IBAD-MgO/Ni-alloy revealed good biaxial texturing. The full width at half maximum (FWHM) values for ω of MgO (002), $LaMnO_3$ (004), and YBCO (005) are 3.1°, 2.2°, and 1.9°, and those for ϕ of MgO (110), $LaMnO_3$ (110), and YBCO (103) are 8.0°, 8.3°, and 5.3°, respectively. Both in-plane and out-of-plane textures of YBCO improve significantly compared with the IBAD-MgO template layers. This is mainly due to the planarization of the growing surfaces and proves $LaMnO_3$ to be an excellent buffer layer for high-performance superconductor coatings. Figure 1.118 shows the surface

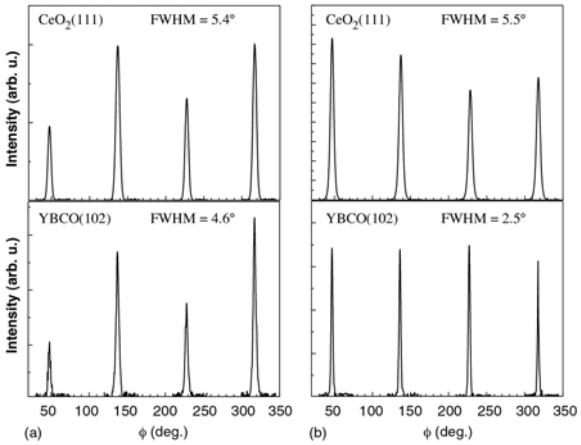

Fig. 1.116. A typical θ-2θ scan for a 1.65-μm-thick YBCO film grown on $LaMnO_3$-buffered IBAD MgO/Ni-alloy substrates using pulsed laser deposition. YBCO film has a preferred *c*-axis orientation.

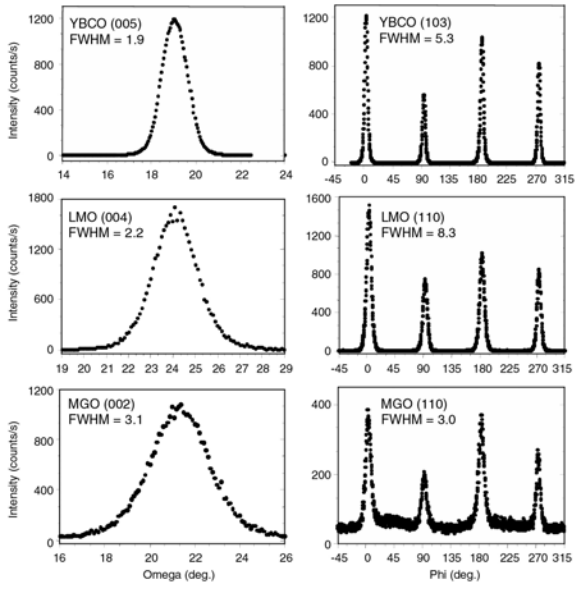

Fig. 1.117. The ω and ϕ scans for a 1.65-μm-thick YBCO film grown on $LaMnO_3$-buffered IBAD MgO/Ni-alloy substrates using pulsed laser deposition. The FWHM values for each scan are shown inside the scans.

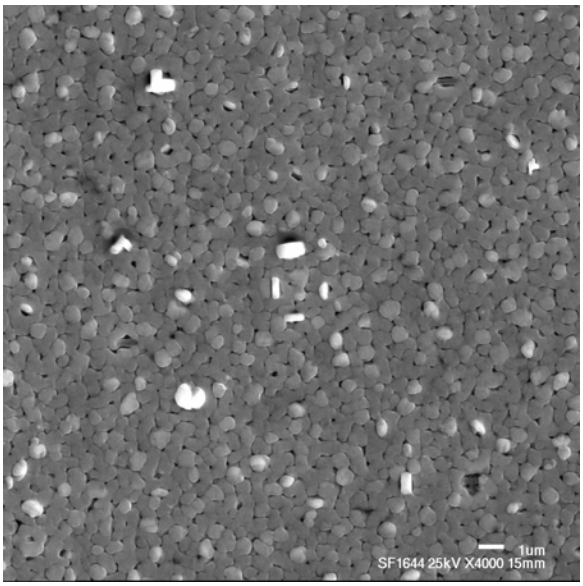

Fig. 1.118. SEM micrograph for a 1.65-μm-thick YBCO film grown on $LaMnO_3$-buffered IBAD MgO/Ni-alloy substrates using pulsed laser deposition.

microstructure of a 1.65-μm-thick YBCO film, grown on $LaMnO_3$-buffered IBAD-MgO/Ni-alloy substrates using PLD, as determined by SEM. The YBCO film appears to have a dense microstructure. The superconducting properties are shown in Fig. 1.119 and Table 1.7. The two microbridges, "x" (approximately 235 μm wide by 5 mm long), and "o" (approximately 225 μm wide by 5 mm long) are patterned on a 1 cm^2 and 50-μm thick C276 alloy substrate. The measured transport I_c for the "x-bridge" is 5.0 A, which translates to a J_c of 1.3×10^6 A/cm^2 at 75 K and self-field, while that of the "o-bridge" is 5.7 A, which translates to a J_c of 1.5×10^6 A/cm^2. The average J_c for the two bridges was 1.4 MA/cm^2, which would give an estimated I_c of 231 A/cm-width.

Recently, $SrRuO_3$ buffer layer has also been shown to be compatible with IBAD-MgO templates, and a J_c of 3.0×10^6 A/cm^2 for a YBCO film thickness of 1.3 μm has been achieved on IBAD-MgO templates with an in-plane mosaic texture of 8°. Because ruthenium is expensive, it remains to be seen whether $SrRuO_3$ is going to be cost-effective relative to our current $LaMnO_3$ layers. Preliminary studies indicate that both $SrRuO_3$ and $LaMnO_3$ layers are not compatible with ex situ BaF_2 and TFA processed YBCO films. However, very recently, Li et al. have demonstrated the growth of TFA-based MOD YBCO films on CeO_2 capped $LaMnO_3$ buffers on IBAD-MgO templates [2]. An I_c of 194 A/cm or J_c of 2.2×10^6 A/cm^2 for a 0.9 μm thick YBCO film was obtained on CeO_2/$LaMnO_3$/IBAD-MgO/Ni-alloy. These results indicate that the $LaMnO_3$ buffer layer provides a very good template for growing high-current-density YBCO films on IBAD-MgO substrates.

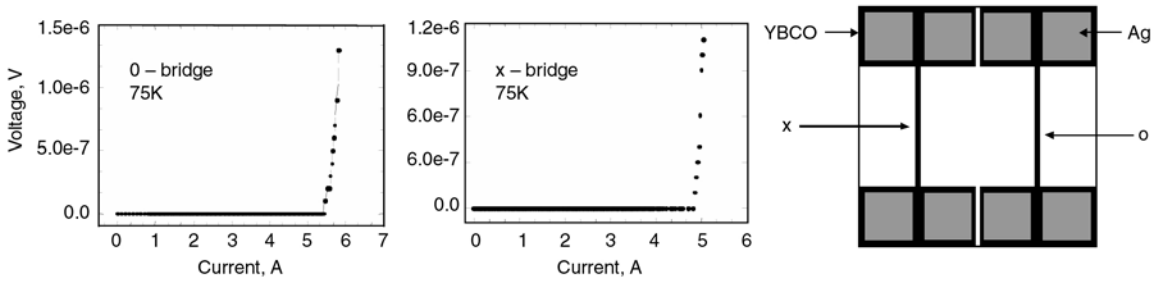

Fig. 1.119. Superconducting properties of a 1.65-μm-thick YBCO film grown on $LaMnO_3$-buffered IBAD MgO/Ni-alloy substrates using pulsed laser deposition. The two microbridges (~225 μm wide by 5 mm long) are patterned on a 1-cm^2 and 50-μm-thick C276 alloy substrate. The average J_c for the two bridges was 1.4 MA/cm^2, which would give an estimated I_c of 231 A/cm width.

Table 1.7. Superconducting properties of a 1.65-μm-thick YBCO film grown on $LaMnO_3$-buffered IBAD MgO/Ni-alloy substrates using pulsed laser deposition

	Width, μm	Length, mm	Thickness, μm	L_c, A	MA/cm^2
x-bridge	235	5	1.65	4.96	1.3
o-bridge	225	5	1.65	5.66	1.5

Cross-sectional TEM bright-field images of a PLD-grown YBCO film on $LaMnO_3$-buffered IBAD-MgO template layers are shown in Fig. 1.120. The sputtered $LaMnO_3$ layer has a dense microstructure. The enlarged cross section in Fig. 1.120(a) shows a clean, planar interface between the $LaMnO_3$ and YBCO layers and no signs of any interfacial reactions between the two layers. Figure 1.120(b) also indicates that a clean and abrupt interface exists between the $LaMnO_3$ and IBAD-MgO layers. In addition, there is no indication of metal diffusion through the buffer layers as indicated by EDS. Selected area diffraction patterns taken at the $LaMnO_3$ and homoepitaxial MgO/IBAD-MgO interface indicate that the alignment between the $LaMnO_3$ and MgO layers is [100] MgO||[110] $LaMnO_3$ and (020) MgO||(1−10) $LaMnO_3$. These results demonstrate that $LaMnO_3$ is compatible with IBAD-MgO templates, and efforts are being made to fabricate long lengths of $LaMnO_3$-buffered IBAD-MgO templates.

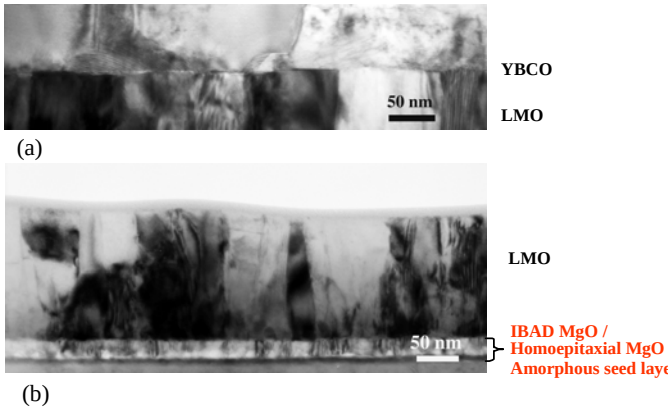

Fig. 1.120. Cross-sectional TEM bright-field image of a PLD grown YBCO film on $LaMnO_3$-buffered IBAD MgO template layers. (a) Enlarged cross section showing (a) the clean interface between the $LaMnO_3$ and the YBCO layers and (b) the dense columnar microstructure of $LaMnO_3$ layers and the clean interface between the $LaMnO_3$ and the homo-epitaxial MgO/IBAD-MgO/amorphous seed layers.

In summary, we have demonstrated the feasibility of $LaMnO_3$ buffer layers with IBAD MgO templates that yields very-high-current-density YBCO films. A transport J_c of over 1.4×10^6 A/cm^2 was obtained on 1.65-μm-thick YBCO films grown on $LaMnO_3$/IBAD-MgO/Ni-alloy substrates. This translates to an I_c of 231 A/cm-width at 75 K and self-field. This performance is comparable to the best results achieved on $LaMnO_3$ buffered IBAD-MgO templates with an in-plane mosaic of 8° and promises a route for producing long lengths of YBCO coated conductors using the combination of an easily scaleable IBAD-MgO template and $LaMnO_3$ buffer layer technology.

1.18.1 References

1. C. P. Wang, K. B. Do, M. R. Beasley, T. H. Geballe, and R. H. Hammond, *Appl. Phys. Lett*. **71**, 2955 (1997).
2. X. Li et al., *Physica C* **390**, 249–53 (2003)

1.19 THICKNESS DEPENDENCE OF THE CRITICAL CURRENT DENSITY IN EX SITU YBCO COATED CONDUCTORS WITH VARIABLE SUBSTRATE TEXTURE

R. Feenstra, D. K. Christen, A. Goyal, A. A. Gapud, P. M. Martin, E. D. Specht, J. D. Budai, M. Paranthaman, D. F. Lee, L. Heatherly, F. A. List, H. Hsu, and D. M. Kroeger (ORNL); D. T. Verebelyi (American Superconductor); B.-W. Kang (Pohang University); T. G. Holesinger, P. N. Arendt, J. R. Groves, and R. F. DePaula (LANL); and D. M. Feldmann and D. C. Larbalestier (University of Wisconsin)

For a coated conductor with a fixed value of the critical current density (J_c), the critical current normalized to conductor width (w), $K_c \equiv I_c/w = t\,J_c$ (units: A/cm), scales proportionally with the HTS later thickness, t. An appealing aspect of coated conductors is that, due to the dominant substrate thickness, relevant variations in t leave the conductor dimensions practically unchanged. On the other hand, the YBCO production rate scales inversely with t. Furthermore, the thickness of a subsequently deposited

stabilizing overlayer, designed to match the critical current, has been estimated to be of similar magnitude as the substrate-YBCO composite, adding a further consideration with respect to conductor geometry.

In practice, J_c is a not a constant but exhibits a negative derivative dJ_c/dt. This behavior appears to depend largely on processing, but it is predicted as well from intrinsic effects related to flux pinning in two-dimensional systems. Thus practical considerations associated with cost of superconductor processing vs substrate preparation, as well as constraints on the engineering critical current density, J_E (K_c divided by total conductor thickness), will likely determine the configuration best suited for meeting I_c targets (for example, using a single HTS coating or a multiple-ply geometry). Irrespectively, it is evident that the most flexible situation for successful technology development lies in the maximization of K_c for a single layer conductor, consuming the least amount of HTS processing (i.e., using as thin a YBCO layer as possible).

A parameter with a profound effect on J_c, but heretofore not systematically considered in $J_c(t)$ studies, is the quality of the substrate's biaxial texture. Through the intrinsic dependence of J_c on grain boundary orientation, by virtue of the epitaxial relationship, J_c and associated transport networks depend strongly on the grain boundary distribution of the substrate being used. Although a complete mapping of such networks is difficult to achieve, an important consequence is that K_c and J_c for coated conductors cannot be meaningfully compared without reference to the substrate texture. A potentially larger issue at hand is whether the benefits of a well-textured substrate, evident in thin YBCO coatings ($t < 0.5$ μm), are maintained in the thick-film regime as well. On the nanometer scale, where grain boundaries affect the local superconducting properties, practically no information exists regarding the interaction between growth-induced defects and dislocation cores of the grain boundary. The possibility could thus arise that growth-induced disorder in thick YBCO coatings would diminish the texture advantage, depriving the technology of an important handle to improve the I_c performance.

The study reported here addresses this issue, expanding on the previous investigations in two significant ways. First, a comparison is made between epitaxial YBCO deposits on multiple coated conductor substrates. As a result of differences in their preparation, buffer layer chemistry, and texture, these substrates enable a range of performance levels, characterized by distinct optimized J_c values in thin (0.33-μm) YBCO coatings. Three varieties of RABiTS™ and a template containing yttria-stabilized zirconia (YSZ) biaxially textured by ion beam assisted deposition (IBAD) were used. Onto these substrates, *c*-axis-oriented YBCO coatings with thicknesses up to 3 μm were successfully grown, enabling a cross-correlation between thickness- and texture-related effects. A recent report by Foltyn et al. compared YBCO coatings of various thicknesses on IBAD-YSZ to epitaxial films on (100) YSZ single crystals [1]. The YBCO was grown by pulsed laser deposition (PLD). Although the current limiting role of substrate-propagated grain boundaries implicitly was in evidence, the observed differences as a function of *t* could not be attributed to texture-related effects because a strong structural deterioration was observed for the coated conductors. This deterioration was identified in the form of so-called "dead layers" (contributing negligibly to I_c) located at either the substrate interface or the film surface. The latter involved essentially all material beyond a 1.5- to 2-μm critical YBCO thickness. No dead layers were identified for the epitaxial films on single-crystal substrates.

Contrasting with that study, the present report involves a two-step precursor approach in which an ex situ anneal was used to bring about the epitaxial growth. Distinguished by the incorporation of BaF_2 as a precursor constituent, this approach is considered advantageous for large-scale coated-conductor production. Indeed, a solution-based variant of this process involving trifluoroacetates is under active pursuit by various research groups around the globe. Although successful formation of 5-μm-thick YBCO films on (100) $SrTiO_3$ single-crystal substrates using the BaF_2 ex situ process has been demonstrated, this is the first reported J_c study in the 0.3- to 3-μm thickness range on coated-conductor substrates. Considering the importance of the growth mechanism for thick epitaxial coatings, a detailed comparison with PLD-deposited YBCO is both scientifically and technologically of interest. Such comparison is made in the second part of this report, following the introduction of an enabling normalization step. While significant parallels are found with respect to $J_c(t)$, important differences are identified as well. A

common mathematical model to fit the $J_c(t)$ dependence is used, and the ways that materials-related effects may be reflected in this dependence and relevant fitting parameters are discussed.

A summary of the coated-conductor substrates used in this study is presented in Table 1.8. Listed are buffer layer architectures and composition of the metallic RABiTS™ template as well as texture information in the form of full-width-at-half-maximum values of substrate and YBCO reflections in X-ray diffraction (XRD) Φ-scans. Although the latter information is insufficient to predict J_c, good qualitative agreement with ΔΦ, was observed. All substrates featured a thin CeO_2 cap layer (< 30 nm) to provide a compatible interface with the YBCO. Identified as the first buffer layer material onto which high-J_c YBCO coatings could be successfully grown by using the ex situ BaF_2 process, this material still provides the most suitable template despite a non-negligible degree of reactivity.

To grow the YBCO coatings, precursors containing controlled mixtures of Y, BaF_2, and Cu were deposited by simultaneous evaporation from three electron-beam sources in a vacuum environment (10^{-6} to 10^{-5} Torr). The precursors were annealed (without intermediate processing) in a furnace in flowing gas mixtures at atmospheric total pressure. Because of limited source supply, multiple deposits were used for precursors thicker than 1 μm. All films, however, independent of *t*, were converted into YBCO during a single heat treatment. Annealing temperatures ranged between 740 and 790°C; the duration was adjusted according to precursor thickness and an average YBCO growth rate of ~1 Å/s. The oxygen partial pressure was set at 200 to 300 mTorr. Added H_2O vapor, needed to initiate YBCO formation, was kept to partial pressures < 5 Torr. Ballast gas was either nitrogen or helium. Flow rates were adjusted to plug-flow velocities of ~4 m/min (measured at room temperature).

While a narrow range of suitable processing conditions has been gradually identified for thin, high-J_c YBCO coatings (on CeO_2), the processing of thicker coatings was found to depend even more strongly on the processing conditions. The combination of H_2O pressure and flow velocity, which control the kinetics of growth, proved to be especially important. As the proper annealing conditions had not been identified, a considerable part of this research involved process optimization. This report reflects a stabilization of this optimization process, providing a baseline for future process improvements. The epitaxy of the YBCO coatings, for all values of *t*, is appropriately described as predominantly or exclusively *c*-axis

Table 1.8. Coated-conductor substrates with representative structural and performance characteristics

Substrate	Architecture[a]	ΔΦ, degrees[b]		J_c(0.33 μm),[c]	Max $K_c(t)$[d]		t_0, μm[e]
		YSZ	YBCO	MA/cm^2	A/cm	μm	
RABiTS™ Ni(1)	Ni/C/Z/C	10.6	10.3	1.0	116	2.5	2.33
Ni(2)	Ni/C/Z/C	8.1	7.3	1.55	164	2.1	2.40
Ni-W	NI(W,Fe)/Ni/Y/Z/C	7.9	6.5	1.5	176 (e)	2.6	2.78
IBAD-YSZ	Ni-alloy/Z(IBAD)/C	12.9	5.4	2.7	239 (e)	2.9	2.24
					270 (p)	2.9	

[a] C = CeO_2, Z = $(Zr,Y)O_2$, Y = Y_2O_3.

[b] Average in-plane texture of the YSZ layer and of 0.33-μm-thick YBCO.

[c] Critical current density of 0.33-μm-thick YBCO.

[d] Highest value of the critical current with corresponding YBCO thickness; values followed by (e) were inferred by extrapolation from the H-field dependence of the critical current density; values followed by (p) were measured on a patterned bridge.

[e] Characteristic "decay" constant t_0 of the critical-current thickness dependence; a simple exponential fit is used in the interval 0.3 to 3 μm: $J_c = J_c(0)\exp(-t/t_0)$.

oriented. The normal-state resistivity ρ is commensurate with this epitaxy. Generally, ρ(300 K) < 300 μΩ.cm for YBCO on RABiTS™, often reaching values as low as ~220 μΩ.cm and exhibiting overall a minor dependence on the thickness. Somewhat higher ρ values resulted on IBAD-YSZ. Critical currents were measured using a standard four-probe geometry. Reported values refer to a 1 μV/cm criterion, self-field, and 77.3 K. Measurements were performed over the full substrate width (3–6 mm). In selected cases

(primarily RABiTS™-NiW), self-field I_c readings could not be directly measured due to instrumental limitations. Extrapolated values from measurements in applied magnetic fields (H||c) were used in those instances. The YBCO thickness was inferred from a calibration of the evaporation rate monitors against readings from Rutherford backscattering spectroscopy and a Tencor profilometer.

The J_c(t) dependence for YBCO coatings on each of the four templates is presented in Fig. 1.121. The intragranular value of J_c for a thin coating on RABiTS™ Ni(1) was measured after micropatterning [2]. Lines represent 120 exponential fits according to $J_c(t) = J_c(0)\exp(-t/t_0)$ with t_0 values as indicated in Table 1.8. Depicted are the best J_c values at the various thickness values for either substrate type. Additionally included in Fig. 1.121 are representative data for 0.33-μm-thick YBCO on (100) $SrTiO_3$ and (CeO_2 buffered) YSZ single-crystal substrates, and a single datum for the intragranular J_c (J_g) for YBCO on RABiTS™-Ni(1) (measured via micropatterning).

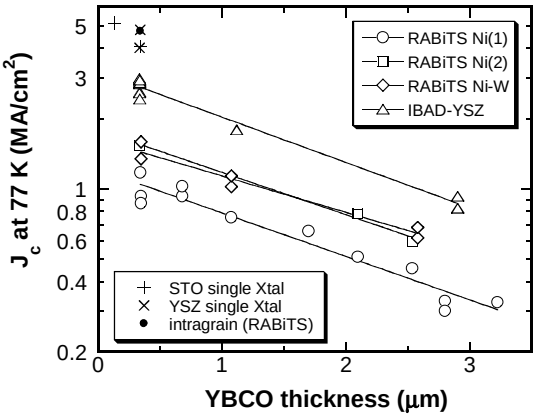

Fig. 1.121. Thickness dependence of the critical current density in ex situ YBCO films on four coated conductor substrates, as well as thin coatings on $SrTiO_3$ (labeled STO) and YSZ single-crystal substrates. (*Source:* D. M. Feldmann et al., *Appl. Phys. Lett.* **79**, 3998 (2001).)

A comparison of these thin-film data clearly highlights the limiting role of substrate-propagated low-angle grain boundaries. Notably, the substrate-related distinction persists with increasing YBCO thickness. In the semi-log plot of Fig. 1.121, the dependences are nearly parallel, indicating a similar fractional reduction in J_c independent of the "starting" value in thin YBCO coatings. It follows that the substrate-propagated grain boundaries limiting J_c in thin YBCO coatings also limit J_c in the thicker coatings. Although the intragranular J_c value is also expected to decrease with t, actual information about this dependence cannot be inferred from the data. This is a significant conclusion because most descriptions favor J_g. The simplest scenario consistent with the observations is that whatever defects cause J_g to decrease with increasing t, there is no interaction with the grain-boundary dislocation cores. In this scenario, J_g would decrease as shown in Fig. 1.121. On the other hand, a stronger $J_g(t)$ dependence could make its influence felt for coatings on better-textured substrates. To rule out this uncertainty and to obtain a consistent understanding, it would be valuable to determine $J_g(t)$ independently, for example, by reexamining epitaxial films on single crystal substrates.

The lines depicted in Fig. 1.121 represent simple exponential fits to the data according to $J_c = J_c(0)\exp(-t / t_0)$. Values of the t_0 "decay" constants, ranging between 2.2 and 2.8 μm for the various substrate materials, are included in Table 1.8. An unsatisfactory aspect of this fit is the prediction that J_c would tend to zero with increasing t. Accordingly, K_c reaches a maximum for $t = t_0$. To examine the $J_c(t)$ dependence in more detail, a combined dataset for the four coated-conductor substrates was created by normalizing $J_c(t)$ by the average measured value at t = 0.33 μm for YBCO coatings on the same substrate. This normalization effectively eliminates texture-related and/or substrate-related effects. The normalized $J_c(t)$ data are plotted in Fig. 1.122 on a linear scale.

Consistent with the near-parallel dependences of Fig. 1.121, the data are seen to collapse onto a "universal" $J_c(t)$ dependence, which we have fitted using a more generalized expression originally proposed by Foltyn et al.[3]:

$$J_c(t) / J_c(0.33\ \mu m) = A + B\exp(-t / t_0) \quad (1)$$

In this expression, the parameter A describes a limiting J_c value in thick YBCO coatings (beyond the present range of investigation), relative to thin-film J_c values on the same substrate. $A = 0$ corresponds to the simple exponential fit described above, providing a technically acceptable fit over the experimental interval. However, small increments in A do not significantly affect the quality of fit. The extra term is accommodated by a decreasing t_0. An upper limit of $A = 0.2$ (with $t_0 = 1.67$ μm) was determined for the available dataset. The calculated dependence is indicated in Fig. 1.122.

The solid line represents a fit according to Eq. (1) in the text with $A = 0.2$, B ≅ 1, and $t_0 = 1.67$ μm. Data for PLD-deposited YBCO on IBAD-YSZ reported by Foltyn et al. [3] are included for comparison, normalized by $J_c(0.33\ \mu m) = 2.79$ MA/cm^2. The dashed line through these data represents a fit according to Eq. (1) with $A = 0.1$, $B = 1.18$, and $t_0 = 1.37$. A preliminary result from subsequent research beyond the 3-μm range [YBCO on RABiTS™-Ni(1)] agrees well with the predicted trend.

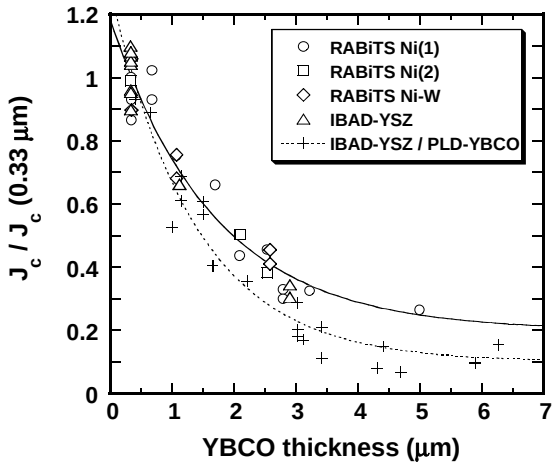

Fig. 1.122. Thickness dependence of the critical current density J_c normalized by its value for a thickness of 0.33 μm for YBCO coatings on the four coated-conductor substrates included in this study. (Source: S. R. Foltyn et al., *Appl. Phys. Lett.* **63**, 1848 (1993).

Using a similar normalization, $J_c(t)$ data from the study of Foltyn et al. [3] for YBCO on IBAD-YSZ are also included in Fig. 1.122. A normalizing value of $J_c(0.33\ \mu m) = 2.79$ MA/cm^2 was inferred from the data in Fig. 1.121 in the corresponding reference, consistent with a high degree of biaxial texture similar to the IBAD-YSZ template used here. A normalized plot of $K_c(t)$ / $J_c(0.33\ \mu m)$ for the two datasets is presented in Fig. 1.123. (The solid and dashed lines were calculated from the fits presented in Fig. 1.122.)

A remarkable consistency in the $J_c(t)$ dependences is observed for $t < 1.5$-2 μm. For either YBCO processing technique, J_c decreases by about 30% when the YBCO thickness is increased from 0.33 to 1 μm. The results diverge, however, for thicker coatings, with the PLD data seemingly tending toward a lower "saturation" value. A fit according to Eq. (1) with $A = 0.1$, indeed, gives a satisfactory representation of the PLD data (optimized towards high J_c values in the range $t > 3.5$ μm). Clearly, the parameter A delineates important tendencies of the material system associated with imperfect growth or film-substrate reactions. For example, $A = 0$, describing a $K_c(t)$ function that tends to zero for large values of t, could depict catastrophic effects such as cracking or a chemical contamination of the YBCO (perhaps leading to a reduced T_c) due to material transport from the metallic substrate. A commonly observed deteriorative mechanism is that of a delayed film-substrate reaction involving only the top (CeO_2) buffer layer. Such reaction may disable a layered region in the YBCO in the substrate

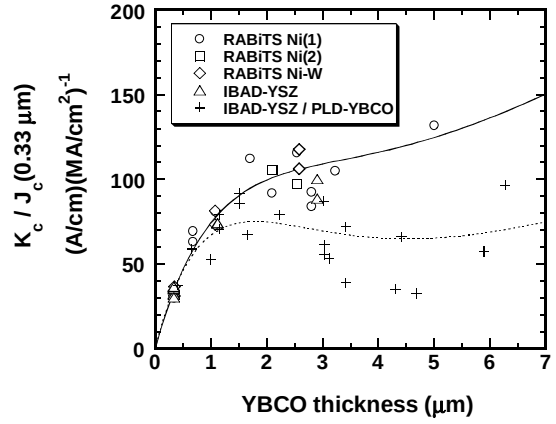

Fig. 1.123. Thickness dependence of the critical current K_c per centimeter of conductor width normalized by the value of J_c for a thickness of 0.33 μm for ex situ YBCO films on four coated conductor substrates and PLD deposited YBCO on IBAD-YSZ. (*Source:* S. R. Foltyn et al., *Appl. Phys. Lett.* **75**, 3692C(1999).

vicinity, leading to local "dead layer." This scenario is potentially well described by a J_c saturation value of $A = 0.1$. At intermediate thickness values, in the course of the deposition process, the loss of well-textured YBCO due to a gradual film-buffer reaction could lead to a net negative derivative dK_c/dt. After the reacting buffer layer material is depleted, however, additional deposits could eventually gain the upper hand, leading to a subsequent K_c increase for very thick YBCO coatings. Structural characterization of the interface region of the PLD YBCO coatings is consistent with this scenario; however, the additional surface dead layer apparently limits K_c to maximum values already reached at the critical thickness of 1.5 to 2 μm.

The ex situ YBCO films, by comparison, appear less influenced by substrate-induced and/or growth-induced "dead layers." This is reflected in the larger A value and the observed monotonic $K_c(t)$ dependence. First indications from electron microscopy and J_c ion-milling studies currently in progress, indeed, confirm the absence of significant dead layers in these YBCO coatings. The YBCO structure is dense at least to a thickness of 2.9 μm. The derivative dK_c/dt, however, is nonmonotonic (predicted to reach a minimum at $t \cong 3.3$ to 3.4 μm according to the fit with $A = 0.2$), suggesting that materials-related effects still dominate. A subtle but significant difference between in situ and ex situ processes with respect to the interpretation of $J_c(t)$ lies in the fact that, in the case of in situ growth, the initial and intermediate stages of growth are independent of the intended final thickness. A time evolution of deteriorative processes thus may be inferred from the comparison of films with different thickness. For ex situ films, similar time-dependent effects could occur, however. Due to material transport inside the precursor layer, facilitating epitaxial YBCO nucleation at the substrate interface, the precursor thickness itself becomes a parameter of the growth process. The observation of $J_c(t)$ behavior described by Eq. (1) with reduced saturation values A, then does not strictly point toward a deteriorative film-substrate reaction but could also reflect an overall less optimized growth process (e.g., a growth process with enhanced secondary phase segregation). The results of improved processing in this scenario should be reflected in a gradually increasing A value.

We conclude this analysis with a discussion of the consequences a reduced J_c in thick YBCO deposits relative to the effect of an improved substrate texture. The representation of Fig. 1.123 allows such comparison. If an arbitrary goal of $K_c = 450$ A/cm for a single YBCO coating were set (exceeding the currently achieved performance of first-generation multifilamentary composites), using a highly textured substrate such as the IBAD-YSZ featured in this study with $J_c(0.33\ \mu m) \cong 3$ MA/cm^2, Fig. 1.123 indicates that ex situ YBCO coatings of about 7 μm thick would be needed to meet the K_c target. (It is assumed that the fit with $A = 0.2$ accurately describes the thick-film regime.) If a better substrate texture quality were available, however, approaching single-crystal limits even further by enabling $J_c(0.33\ \mu m) \cong 4$ MA/cm^2, the corresponding YBCO thickness would shrink to ~3 μm. Such performance may already be achievable with the presently optimized annealing conditions. These predictions are an immediate consequence of the texture-invariant $J_c(t)$ dependence witnessed in this study.

1.19.1 References

1. S. R. Foltyn et al., *Appl. Phys. Lett.* **75**, 3692 (1999).
2. D. M. Feldmann et al., *Appl. Phys. Lett.* **79**, 3998 (2001).
3. S. R. Foltyn et al., *Appl. Phys. Lett.* **63**, 1848 (1993).

2. Technical Progress in Applications Development

2.1 SOUTHWIRE/ORNL HTS CABLE SUPERCONDUCTIVITY PARTNERSHIP INITIATIVE

J. W. Lue, M. J. Cole, J. A. Demko, R. C. Duckworth, A. R. Ellis, P. W. Fisher, M. J. Gouge, D. R. James, P. M. Martin, I. Sauers, and J. P. Stovall

2.1.1 V-I Measurement of 30-m HTS Cables at Southwire

After more than three years of field operation, another direct current (dc) V-I measurement was performed on the Southwire three-phase, 30-m HTS cables on June 6, 2003. Only one of the six HTS conductors in the cables showed some apparent degradation. All three phase conductors still had critical currents no less than 3000 A (the limit of the portable dc power supply used to test the cables). The critical currents of phases 1 and 2 shield conductors remain at about 2100 A. The critical current of the phase-3 shield is now at about 1900 A, about a 10% degradation from the original value.

2.1.2 Triaxial Cable R&D: 5-m Cable Design and Fabrication

In 2001, the ORNL/Southwire cable team designed, built, and tested a 1.5-m-long prototype triaxial cable. Each phase consisted of two layers of BSCCO-2223 HTS tapes. Electrical tests of the cable included the dc V-I curve and alternating current (ac) loss measurements. The three-phase ac loss was close to the sum of the three individual phases. There was no measurable excess ac loss due to the presence of the other concentric phases. A total three-phase ac loss of about 1 W/m was measured at the design operating current of 1250 A rms. Encouraged by the positive test results from this prototype triaxial cable, the Southwire/ORNL team has conceived, designed, and built a 5-m triaxial cable with associated three-phase terminations.

The basic cable configuration used in the 1.5-m and 5-m cables is shown in Fig. 2.1. As shown, there are three concentric phase conductors separated by liquid-nitrogen-impregnated dielectric tape. For the 5-m cable, the design phase current is 1300 A rms at 77 K and the design phase-to-phase voltage is 15 kV. The phase conductors are BSCCO-2223 silver-alloy tapes wound in a helical manner on a 35.6-mm former; each phase has two layers of these HTS tapes. The dielectric material is composed of Cryoflex™ tapes immersed in liquid nitrogen. For equal currents in phases 1, 2, and 3, the current in the copper shield should be about zero. The induced current in the shield for unbalanced three-phase currents was measured in the 1.5-m prototype cable and was found to be small. The liquid nitrogen used for cable cooling flows inside the cryostat. The cryostat has a vacuum space with superinsulation for reducing the heat load from ambient; the design heat in-leak is 2 W/m. The outer diameter of the cryostat is 143 mm.

The 1.5-m prototype cable operated only at low voltage and did not require a termination. The 5-m triaxial cable is a full-scale demonstration of the technology and has a full-scale, three-phase termination. The termination provides for ambient temperature connections to the three phases and the shield. It makes the temperature transition from liquid nitrogen temperature to ambient temperature in the three copper-pipe phase conductors as well as the copper braid shield conductor. For the phase conductors, the design approach of McFee, which assumes that the termination phase conductor is adiabatic except at the cold end, is used to select the cross-sectional area and length of the copper pipes given the 1300-A-rms design current. The design axial conduction loss at full current, assuming no cooling along the conductor, is on the order of 50 W/phase.

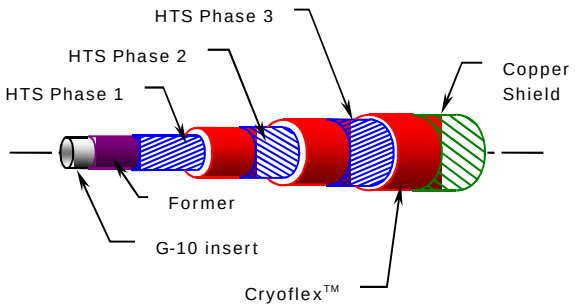

Fig. 2.1. Schematic of the triaxial cable.

Although internal cooling of the termination conductors is possible, it was decided to take the more challenging approach of cooling the termination conductors from the outside only. This approach has the advantage that the cooling circuit is at ground potential, but the disadvantage is that adequate radial heat conduction from the three electrical phases must pass through the termination cross section out to the flowing liquid nitrogen coolant at the wall. In particular, the dielectric material between the phase conductors and between the outer phase and shield conductor has to be a material with adequate thermal conductivity at 77 K and 300 K and must have acceptable electrical insulation and mechanical strength performance over that temperature range. Not only must the 15-kV operating voltage be accommodated, but the termination should be designed for a 50-kV withstand (1 min, dry) and a 110-kV basic impulse level (BIL) voltage per IEEE requirements.

A radial model of the three-phase termination was developed and evaluated using the ANSYS code. Thermal conductivities (at 77 K) of the termination insulation in the range 0.25 to 2 W/m-K were evaluated; the eventual material chosen had a thermal conductivity at 77 K about 75% of the value at 273 K. Since the cable's dielectric system merges with the termination, it is important to keep the temperature at the cold end of the termination low enough to ensure that no nitrogen bubbles will develop in the taped dielectric. If the nitrogen were at 5 atm (a typical lower value), then the temperature would have to be below 94 K. This is possible using the external cooling configuration. The entire termination was modeled using ANSYS; Fig. 2.2 shows the model predictions for temperature distribution for the termination.

The model can then be used to fine-tune the cooling scheme, which does not meet the ideal conditions of the McFee assumptions. The cable is spliced to the termination in the region to the left of zero, where the temperature is low and consistent with cable operation. Large radial temperature gradients do occur in the region cooled by liquid nitrogen, but this is in a part of the termination where liquid nitrogen is not used as a dielectric. The jagged temperature in the liquid-nitrogen-cooled wall is from discrete cooling channels.

Temperature control is provided at the ambient-temperature end of the termination for two reasons: to intercept some of the heat generated by warm parts of the termination during full-power operation and to heat the warm end during conditions of less than full power operation or when the system is idle. The three-phase termination is cooled separately from the 5-m triaxial cable. This was done because one of the objectives of the 5-m cable test program is a thermal measurement of ac losses while running the cable with currents in all three phases. A separate liquid nitrogen cooling path for the cable allows a more sensitive measurement of ac losses in the cable. Shown in Fig. 2.3 is a photograph of the assembled three-phase termination showing the liquid nitrogen connections for termination cooling and the three warm bushings on the right side. The start of the triaxial cable is on the extreme left side.

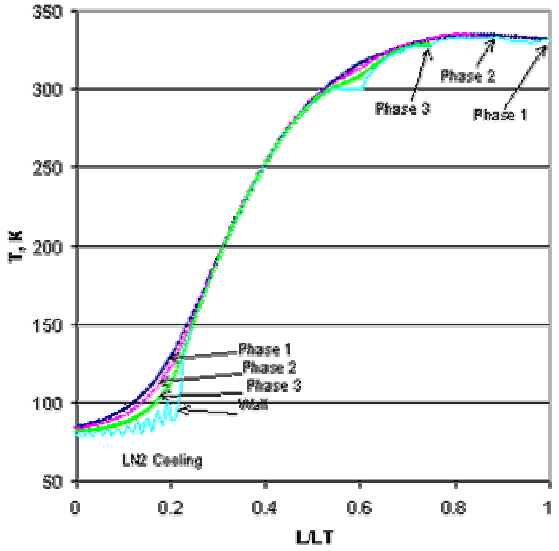

Fig. 2.2. ANSYS-predicted temperature profiles in the termination.

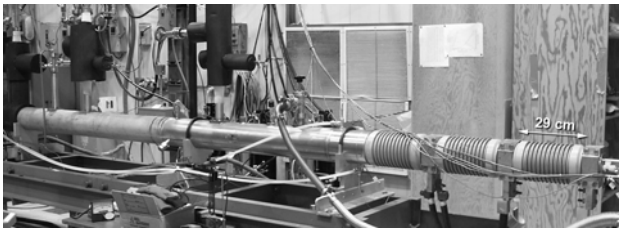

Fig. 2.3. Triaxial cable and termination.

2.1.3 Triaxial Cable R&D: Cable Test Facility Status and Measurements of Thermal Loads

A comprehensive test program was conducted to quantify the potential benefits of this HTS cable. The HTS Cable Test Facility was modified to accommodate the testing of the HTS triaxial cable. The modifications included separating the flow into separate streams to cool the individual terminations at the east and west ends of the facility and the cable. Coriolis flow meters from Micro Motion Incorporated were set up to measure the mass flow through these separate flow paths. A mechanical vacuum pump and connecting line were installed in the system to reduce the bath pressure in the subcooler.

The first tests after gaseous nitrogen filling and purging were a controlled cooldown over about 4.5 h from ambient temperature monitoring temperature gradients and mechanical contractions. Since the start of the test program in early October 2002, the cable has experienced over six cool-downs to operating temperature and warm-up cycles.

The thermal loads for different components of the triaxial HTS cable system have been determined from measurements of the mass flows and the inlet and outlet temperatures of the different cable system components. These components are the east and west end terminations, the triaxial cable with cryostat (cable), and the cryogenic system. A schematic diagram of the separate cooling flow paths is given in Fig 2.4. The individual flows through the separate components were set using throttle valves on the downstream side of each cable component. The heat loads in the terminations and cable are of most interest. The HTS triaxial cable electrical loss is a combination of the ac loss of the main phases and resistive loss in the outer copper shield conductor that carries induced currents from imbalances in the main phases. It can be determined by comparing the thermal load on the cable with no current to the thermal load with current applied. The thermal loads are determined from an energy balance on the liquid nitrogen according to the following equation:

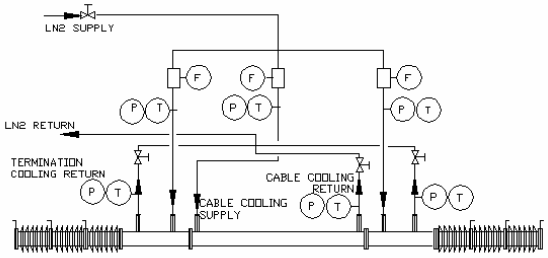

Fig. 2.4. Schematic of the liquid nitrogen flow paths for the separate cooling of the HTS triaxial cable and terminations.

$$Q = \dot{m} C_{\mathrm{p}} \left(T_{\mathrm{out}} - T_{\mathrm{in}} \right)$$

For liquid nitrogen at about 5 bar and 80 K, the specific heat, C_{p}, is 2.06 J/g/K. The actual flow temperatures are measured with calibrated platinum thermometers from Lakeshore mounted in stainless steel sheathed probes. The mass flow was measured with the Coriolis flow meters.

Initial testing was conducted with the subcooler venting straight to atmosphere as had been done on earlier tests of single-phase 5-m HTS cables. A second series of runs was conducted with subatmospheric pressure in the subcooler. The overall system heat load is higher in the triaxial cable system than in the earlier single-phase cable tests because of the addition of four nitrogen lines to the system and the three electrical phases. This resulted in higher operating temperatures for the cable. At these higher temperatures, the cable critical current is reduced and the cable operated stably at 1100 A. It was necessary to pump on the subcooler to achieve the design operating current of 1300 A.

The cable inlet and outlet temperatures are provided in Fig. 2.5 as well as the current applied to phase 1 for a 25-h run. The same current was applied to all three phases, but only phase 1 is shown for clarity. The temperatures show that the cable was approaching steady state. The apparent noise in the temperature signals is actually temperature cycling as the subcooler dewar is automatically filled on about a 15-min cycle based on level switches set at 90% and 95%. The heat loads estimated from the available

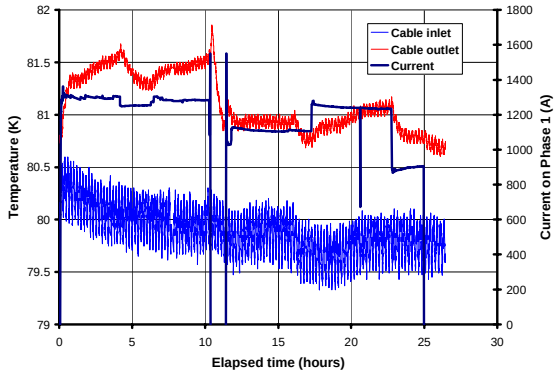

Fig. 2.5. Liquid nitrogen temperatures of cable flow stream and phase 1 current for a subatmospheric subcooler run.

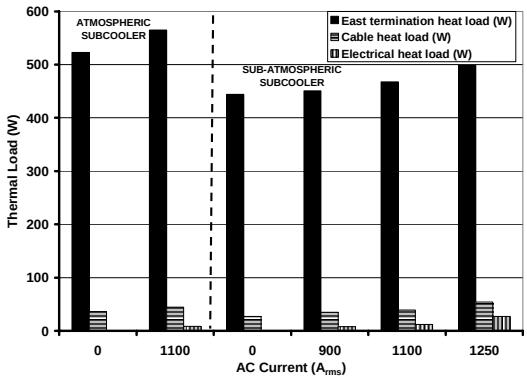

Fig. 2.6. Experimentally determined heat loads from measured temperatures and flows in HTS cable system at different operating currents and subcooler pressures.

measurements are compared in Fig. 2.6 for different currents and with the subcooler at atmospheric pressures (higher temperatures) and subatmospheric pressures (lower temperatures). As expected, there is a noticeable rise in the cable and termination heat load as the current increases. The subatmospheric cable thermal loads appear less than the atmospheric subcooler thermal loads. One reason is thought to be that steady state has not been reached at the different conditions.

The system appeared to reach thermal equilibrium at approximately 5 h after starting a circulating flow through the cable and terminations. DC V-I measurements were made on each of the three phase conductors to determine the critical current of each phase. The critical currents at the measured temperature of 83.6 K and extrapolated to 77 K using the known temperature dependence of critical current were phase-1 (inner phase): 1400/1928 A, phase-2 (middle phase): 1570/2163 A, and phase-3 (outer phase) 1610/2218 A. The V-I curve for phase 1 at 83.6 K is shown in Fig. 2.7. The *n*-value was 12.6 for phase 1, 13.3 for phase 2, and 10.5 for phase 3.

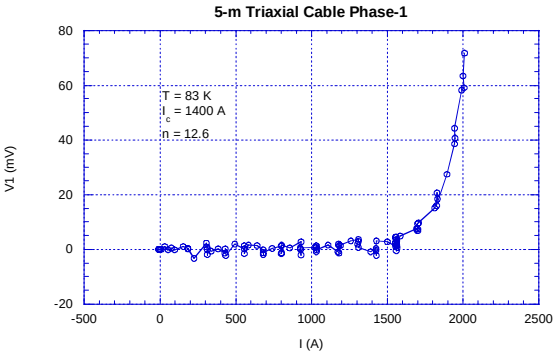

Fig. 2.7. The dc V-I curve of phase 1.

Phase 1 of the triaxial cable was also subjected to an overcurrent hold test to determine its steady-state overcurrent limit. Figure 2.8 shows the voltage drop across the cable as phase-1 current was stepped above its I_c of 1400 A at 83.6 K and held for about 2 min each at currents of 1500 to 1800 A. No appreciable voltage increase was observed at each of the successive current hold points until the last hold at 1800 A. At about 1800 A, there was a controlled thermal runaway after about one minute. There was only a very small voltage rise at 1750 A. At that current limit, the voltage across phase 1 was about 19.5 mV. Therefore, a heat load of about 5.6 W/m on phase 1 appears to be the limit for the present cable configuration and cooling condition.

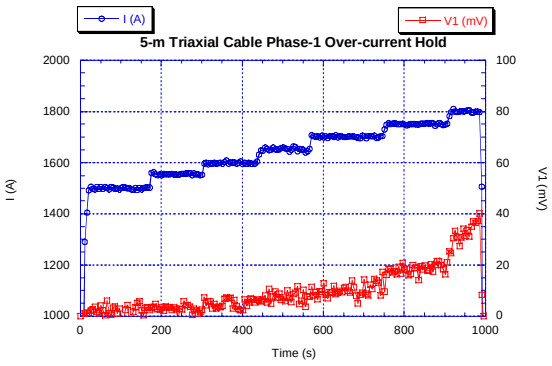

Fig. 2.8. Voltage across phase 1 at successively higher current holds.

The ac losses in the phase conductors were measured. For this purpose a three-phase power supply with a current capability of up to 2000 A per phase was connected to the cable. It was verified with a

Rogowski coil that the three electrical phases were 120 electrical degrees apart. For measurement of ac losses in this configuration, an electrical measurement (using a Rogowski coil with a lock-in amplifier) is not possible due to the coupling between phases. Therefore, a thermal measurement (from the liquid nitrogen flow rate and the temperature rise) was used to measure ac losses in both single-phase and three-phase operation. The measurement was corrected for the heating due to the induced current in the copper shield. The measured ac losses were about 0.45 to 0.50 W/m per phase (1.42 W/m total) at an operating current of ~1100 A rms in all three phases and at a temperature of ~84 K. At this temperature the critical current of phase 1 is about 1400 A.

The monoblock theory, which does not address the interaction between phases, was used to calculate the HTS losses given the operating current, the critical current, and the phase-conductor radial geometry. The simple sum of the losses of the three phases calculated with the monoblock theory was very close to the measured total of 1.42 W/m. Based on the monoblock theory, the total ac loss at the design current of 1300 A would be about 1.7 W/m when the cable is cooled to 77 K. The lowest loss per phase is for balanced three-phase operation; ac losses with an applied current in only a single phase are about twice the loss per phase of three-phase operation. This may be the result of eddy current loss in the cryostat and other metallic structures due to imperfect current shielding in the present short cable configuration. In general, even for drastic imbalances in the phase current, the currents in the shield are typically 10 to 15% or less of the phase current, consistent with previous measurements on the 1.5-m triaxial cable.

2.1.4 Triaxial Cable R&D: Testing of Alternate 5-m Triaxial Cable Cooling Arrangements

The 5-m, 1.3-kA triaxial cable system was run in the alternate cooling arrangements shown in Figs. 2.9 and 2.10. The baseline arrangement is shown in Fig. 2.4; results have been reported previously. The change was made to increase the flow through the cable so that lower temperatures could be reached for reduced ac losses at higher critical current operation. The cable operated at an average temperature of about 83 K in this baseline arrangement. The main restriction is in the center flowmeter, which was used to measure the flow rates in the cable for calorimetric ac loss measurements. The cable flowmeter has a maximum range of around 30 g/s, while the flowmeters used in the terminations have maximum ranges of over 250 g/s. In addition, the heat load is high in the system due to the use of foam-insulated copper tubing in some sections of the liquid nitrogen piping.

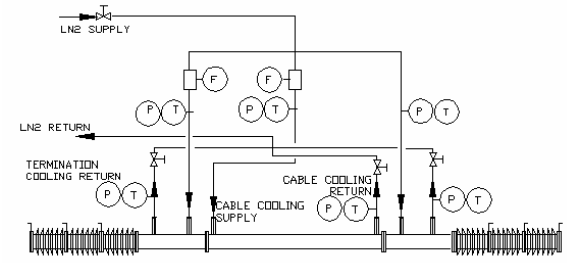

Fig. 2.9. Modified triaxial cable system cooling configuration to use higher-rated flowmeter in cable flow path.

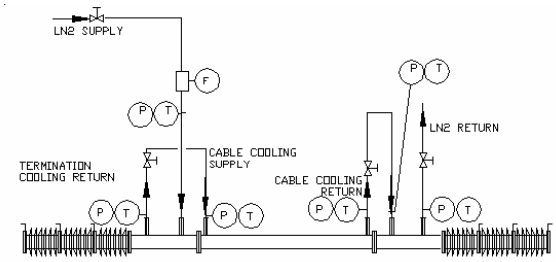

Fig. 2.10. Modified triaxial cable system cooling configuration for single flow path operation.

In the second arrangement, the higher-range flowmeter from the right-side termination was used to measure the flow in the cable, permitting increased liquid nitrogen circulation. In the third arrangement, a single flow path cooling arrangement was used. The temperatures entering and leaving the cable system through the terminations were 77.8 K and 84.5 K, respectively. The average cable temperature at the end of the run was about 80.3 K in the single flow path arrangement. Lower operating temperatures are expected in future tests of the triaxial cable system because of the recent replacement of foam-insulated liquid nitrogen piping with reduced-heat-load vacuum-jacketed lines.

2.1.5 Triaxial Cable R&D: Modifications to the HTS Cable Cryogenic System

From the results of earlier testing of the triaxial cable it was determined that modifications were necessary to the subcooler vacuum pump system in order to reach the desired operating temperatures for the HTS cable. An analysis of the flows in the subcooler piping has been performed to understand the limitations of the existing system and to propose a remedy for the situation. The plumbing is presented in Fig. 2.11. The flow leaves the subcooler and passes through a heater that manifolds the flow into eight flow paths. The flow is warmed up to room temperature and then goes to the vacuum pump.

It was finally decided that to achieve the required vapor flow from the subcooler, that a larger vacuum pump and corresponding heater would be necessary. These items were ordered and will be installed into the system.

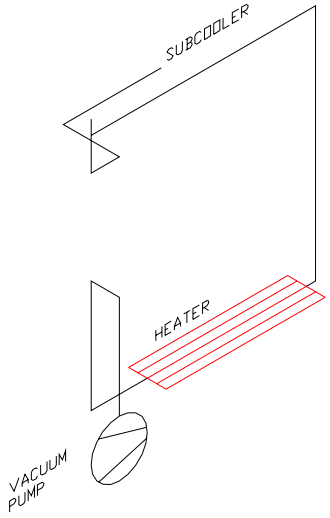

Fig. 2.11. Flow schematic of subcooler vacuum system.

2.1.6 Triaxial Cable R&D: 3-kA, Three-Phase Cable R&D and Design

ORNL and Ultera are building a three-phase termination and a 5-m cable at a higher phase current (3 kA_{rms} per phase) that will be a full-scale prototype of the cable to be installed at the AEP Bixby substation under the Superconductivity Partnerships with Industry (SPI) program. Testing is planned for evaluation of this higher current cable and termination high-voltage dielectric system per the IEEE requirements. Analysis (especially thermal with two different codes: ANSYS and HEATING 7) was completed in March, and by the end of the quarter most of the detailed design work was completed to implement required revisions from the 1.3-kA to the 3-kA phase current termination. Fabrication activity was beginning for the termination long-lead-time components such as copper piping, stainless steel weldments, and the cryostat. In parallel, termination electrical insulation R&D is converging on a material with acceptable electrical properties (partial discharge inception voltage, ac breakdown) and thermal properties (CTE, conductivity), which are being tested in coaxial model termination assemblies.

2.1.7 Triaxial Cable R&D: Analysis of a Liquid Nitrogen Cooled Triaxial HTS Cable System

A triaxial HTS cable design that uses three concentric superconducting layers for the phase conductors separated by a cold dielectric material offers an efficient HTS cable configuration by reducing the amount of superconductor needed and by placing all three phases in a single cryostat. The triaxial cable cooling circuit analyzed includes heat loads at the ends for the cable terminations and cable heat loads due to ac, dielectric, and thermal losses. The HTS cable critical current and ac loss are functions of the local temperature that must be determined by the analysis. The radial heat transfer also has an influence on these parameters due to the relatively low thermal conductivity of the dielectric material separating the HTS phases. A study was conducted to determine whether the triaxial cable must be cooled both inside the former and outside of the cable. One approach to employing a triaxial HTS cable system is shown in Fig. 2.12. In this configuration, cooling is supplied by a refrigeration system at one end of the cable. Liquid nitrogen enters the termination and flows through the cable to the far-

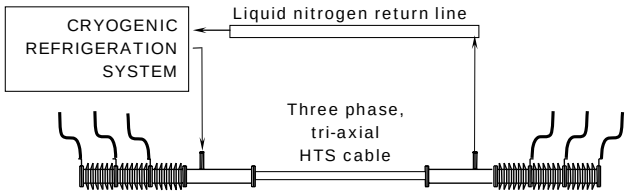

Fig. 2. 12. High-temperature superconducting three-phase triaxial power cable system.

end termination. After cooling the far-end termination, the flow is sent through a separate return line back to the refrigerator. Liquid nitrogen can be circulated through the former and/or the annular space between the outer diameter of the cable and the inner diameter of the cryostat. Baseline dimensions for the cable cryostat and the return cryostat have inner and outer diameters of 0.075 m and 0.125 m, respectively.

This investigation studied cooling options for applications of the triaxial HTS cable. The simplest method is to circulate liquid nitrogen to cool the cable only in the annular space. Another option is to provide cooling in the former as well. Since under normal operation of the cable, there are ac losses in the phases, a radial temperature gradient is developed. The cooling is limited by the conduction through the dielectric material separating the phases. The temperature rise of the HTS causes a decrease in the critical current, which raises the ac loss. The interaction of these three physical mechanisms was numerically modeled for both cooling arrangements. The critical currents for the three phases are given in Table 2.1.

It was first necessary to determine what cooling approach is suitable for the triaxial cable so the radial temperature rise was calculated for several temperatures with cooling on both the inner and outer surface of the cable, and assuming cooling only on the outside of the cable. The temperature rise is measured relative to the coldest surface temperature. The thermal conductivities of the different materials used in the cable construction are given in Table 2.2 along with the composite axial thermal conductivity of the cable and the effective thermal conductivity of the cryostat. To simulate cooling in the former and the annular region, the inner and outer surface temperatures were specified. In order to simplify the analysis, both surfaces have equal temperatures for the cases presented here.

Table 2.1. Critical current at 77 K for each phase

Phase	Critical current (A)
1	5900
2	6500
3	6700

Table 2.2. Thermal conductivities for the cryostat, cable, and materials used to model the cable

Material or component	Thermal conductivity (W/m/K)
Stainless steel	7.1
HTS	415
Bedding and Cryoflex™ tape [4]	0.1
Copper	509
Cryostat vacuum MLI [5]	0.001
Composite cable in axial direction	50

When cooling is only in the annular region between the cable and inner cryostat wall, a zero radial temperature gradient is specified in the former. Solutions for the radial temperature rise profiles for temperatures ranging from 65 K to 85 K are shown in Fig. 2.13. Cooling on both sides of the cable produces a maximum temperature rise of around 0.33 K at the middle phase (phase 2) when the cooled surfaces are at 85 K. When only the outside is cooled, the innermost phase (phase 1) has a temperature rise over 2.7 K for an 85 K outer surface. At 85 K the calculation is optimistic using the monoblock ac loss model, since the ratio of peak to critical current (I_p/I_c) > 1 for phase 1. While the cable operates with lower temperature rises when both sides are cooled, the temperature rise is not too high to prevent using annular cooling only.

To illustrate the feasibility of using a triaxial three-phase HTS cable in a practical long-length situation, a simulation was made of a 2000-m long, 15-kV class cable operating at 3000 A. A summary of the liquid nitrogen inlet parameters, flow rate, and the heat loads from this calculation is provided in Table 2.3. There has been no attempt to optimize the design of the triaxial cable system in these calculations; doing so would require information regarding the specific installation of the HTS cable system. The thermodynamic and transport properties of the liquid nitrogen are functions of pressure and temperature.

At 2000 m, the flow leaves the cable and cools the second termination before entering the return line to come back to the refrigerator. The flow enters the return line after cooling the second termination at 75.8 K and is returned to the refrigerator at 79.35 K.

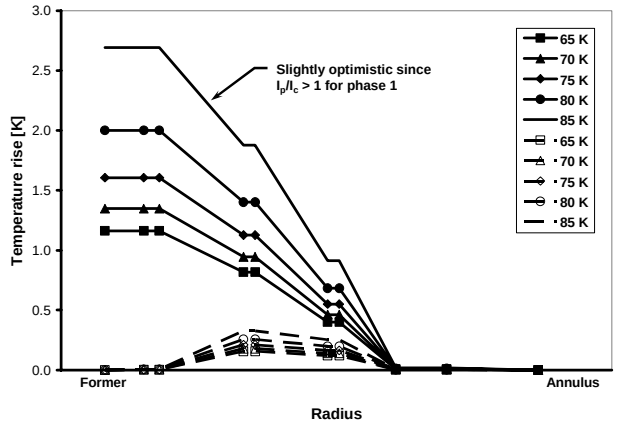

Fig. 2.13. Radial temperature distributions through the triaxial HTS cable for specified boundary temperatures. Cooling in the annulus only (_____). Cooling in the former and annular space (- - - -).

Table 2.3. Summary of the HTS cable heat loads

Parameter	Value
Inlet temperature (K)	65
Inlet pressure (Bar abs)	10
Flow (g/s)	750
Electrical losses (W)	9,159
Cryostat heat load (W)	6,051
Return cryostat heat load (W)	5,526
Termination heat load (W)	1,200
Total HTS cable system thermal load at 65 K (W)	21,936
HTS cable system pressure drop (Bar)	2.51

A summary of the phase conditions at 2000 m is given in Table 2.4. The calculations indicate that the pressure drops for this system are low enough that longer lengths are possible by simply increasing the flow rate of liquid nitrogen through the HTS cable system.

Table 2.4. Summary of the HTS cable phase conditions at 2000 m, where the highest triaxial cable temperature is located

Parameter	Temperature rise (K)	I_p/I_c	AC Loss (W/m)
Phase 1	1.63	0.72	2.51
Phase 2	1.15	0.64	1.45
Phase 3	0.56	0.61	1.24

2.1.8 Triaxial Cable R&D: Cryogenic System for the AEP Demonstration

The cryogenic system specification for use in the American Electric Power (AEP) HTS cable demonstration project with Southwire is being developed. A visit to PHPK, Inc., the vendor for the cryogenic system being used at the Southwire demonstration in Carrollton, Georgia, was made to discuss improvements in a new open-cycle system based on the operating experience gained from the existing system.

2.1.9 Testing of a 1-m Cable with AMSC Tape

A 1-m cable core was built by Southwire to qualify the Cu/Ni-plated BSCCO tapes made by American Superconductor Corporation (AMSC) for use in HTS transmission cables. Electrical testing of the cable was performed in a liquid nitrogen bath. A dc V-I measurement showed an I_c of 4030 A, about the same as expected from the number of tapes used times the listed tape I_c. This is the highest I_c cable ever built by Southwire and tested at ORNL, even though it contains only two layers of HTS tapes. Overcurrent pulses of 1- to 2-s duration were applied to the cable to simulate fault currents due to a short circuit. The cable remained partially superconducting after a 1-s pulse to 8300 A, more than twice the I_c. Next, the ac loss of the cable was measured electrically up to 3 kA rms. The loss data showed about the same current dependence as predicted by the monoblock model but is higher by about 40%. At 2.3 kA rms, the measured ac loss is about 4.5 W/m. A bending test was performed on a piece of the Cu-plated BSCCO tape. It showed no degradation with bending strain up to 0.31%.

2.1.10 Testing of 3-kA Prototype Cable

2.1.10.1 Cable Construction

For the SPI, Ultera plans to install a three-phase HTS cable rated at 3 kA, 13.2 kV (69 MVA) at the AEP Ohio Bixby substation. To prepare for this higher current rating, a 1.5-m-long single-phase prototype cable was fabricated for testing in an open liquid nitrogen bath. The cable was wound with two layers of BSCCO-2223 tapes from AMSC made to Ultera's specification. To simulate this prototype cable as the most demanding inner phase of a triaxial cable, the conductor was covered with the same amount of Cryoflex™ dielectric tapes as would be required for the whole triaxial cable. To achieve cooling on the cable outer diameter only as expected for the triaxial cable, the inside of the former was filled with epoxy to exclude liquid nitrogen from entering the former. A Nichrome heater tape was wrapped on the conductor to simulate the ac heat load. A thin-film resistance temperature detector (RTD) was installed on the HTS tapes in the middle of the cable to measure the conductor temperature rise due to ac losses or overcurrents. Direct current V-I measurements of the cable obtained a cable I_c of 5.8 kA. This is the highest critical current that the Ultera/ORNL team has ever achieved in a cable, regardless of the number of layers used to build it. This shows the progress and the superior current-carrying capability of the AMSC BSCCO tape and the feasibility of making cables rated for 3 kA rms with only two layers of HTS tapes.

2.1.10.2 Heat Load Calibration and Thermal Stability Test

A Nichrome heater was installed to calibrate the ac loss of the cable and to measure its thermal stability. Cooling the cable from the outer diameter may only introduce a heat load limit, beyond which the conductor temperature may get too high and a thermal runaway may develop. The thermal stability of the cable was tested by first applying a heat load of 5-W/m through the heater. After a stable conductor temperature was observed by the RTD, a dc current equal to the rated 3 kA was applied to the cable. The cable current was later raised to 4.2 kA (equal to the peak ac current). Figure 2.14 shows the temperature rise of the conductor as measured by the RTD in response to the heat and cable currents. The 5-W/m heat load is the anticipated total heat load of the 3-kA triaxial cable. With this heat load, the conductor temperature rose by 0.15 K. The addition of up to 4.2 kA of current through the cable only added another 0.04 K. Therefore, a 3-kA triaxial cable should be thermally stable as long as the refrigerator can keep the cable operating temperature within 0.2 K of the allowable maximum.

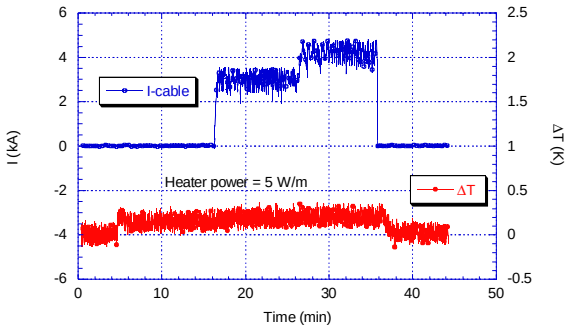

Fig. 2.14. Temperature rise of the conductor with 5 W/m of heat load at different cable currents.

2.1.10.3 AC Losses

The ac loss of the single-phase 3-kA cable was measured both electrically and calorimetrically. For the electrical measurement, the rms voltage and the phase angle, θ, relative to the current were measured with a lock-in amplifier. The per-unit length ac loss was then calculated by $P/L = VI\,\mathrm{Cos}\theta / L$. The calorimetric measurement here is based on the radial temperature gradient generated by the ac loss of the cable relative to the open bath. The loss value for a given temperature rise on the conductor is calibrated by the built-in heater as described before.

The ac loss of this cable was measured up to 3 kA rms. Figure 2.15 shows both the electrically and calorimetrically measured ac loss data as compared with data from the monoblock model calculation. Good

agreement between the two sets of data and the model calculation is obtained. A power fit of the electrical ac loss data for I_{rms} > 900 A gives a power of 2.6; the monoblock model gives an exponent of 3. At the design current of 3 kA rms, the ac loss was measured to be about 1.5 W/m, an acceptably low value for this higher current rating.

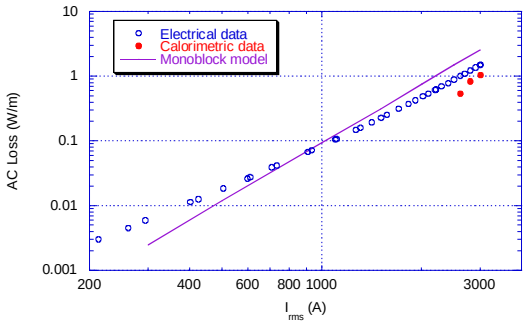

Fig. 2.15. The ac losses of the 3-kA single-phase cable.

2.1.10.4 Fault Overcurrent Test

In addition to having a design operating current of 3 kA rms, the cable must also be designed to sustain fault overcurrents of up to 30 kA (ten times the operating current) for about five cycles at the AEP Bixby station site. To simulate the fault overcurrents, short current pulses were applied to the cable using a 25-kA, 12-V dc power supply. Because of the voltage limitation, the maximum current that can be delivered to the present cable is about 17 kA. To get about the same heating as a 30-kA, 0.1-s pulse, pulse lengths as long as 0.7 s were used in the tests. Figure 2.16 shows the cable voltage in response to a 0.7-s overcurrent pulse. The cable current reached a peak of 16.8 kA and had lowered to 13 kA by the end of the current pulse due to the voltage limitation of the power supply. It is seen that the voltage rise accelerated as the current held on, although the current was decreasing. This indicates an increase of the conductor resistivity due to the overheating of the cable. A peak voltage of 3.4 V was observed at the end of the current pulse. Figure 2.17 shows the conductor temperature as measured by the middle RTD relative to the cable voltage. It is seen that the RTD showed a delay in registering a peak temperature. There was also a substantial broadening of the thermometer curve, indicating heat loss to the coolant and Cryoflex™ insulation in this longer pulse shot.

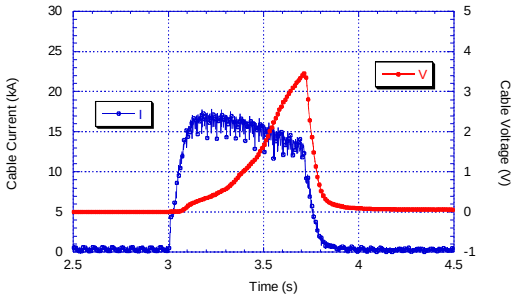

Fig. 2.16. Cable voltage in response to an overcurrent pulse.

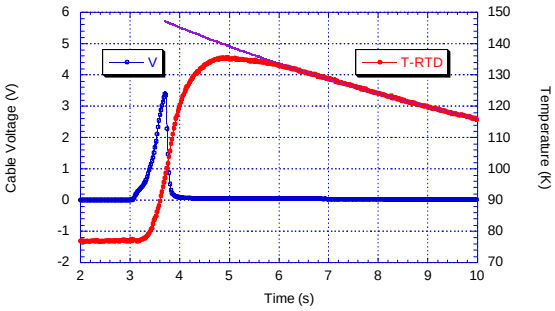

Fig. 2.17. Conductor temperature as measured by the middle RTD relative to the cable voltage.

The temperature curve, however, showed an exponential decay after reaching the peak. An exponential curve fit extrapolated back to the end of current pulse shown in the figure gives a possible peak conductor temperature of 147 K. The resistance of the BSCCO tape used in this cable was measured with a cryocooler to have a linear temperature dependence from room temperature to 115 K. The peak cable voltage of 3.4 V corresponds to a resistivity of 1.4×10^{-8} Ω-m and a temperature of 149 K. Good agreement in estimating the peak temperature reached in the conductor is obtained from these two measurements. Integrating the V-I product of Fig. 2.16 over the current pulse gives a total Joule power generated during the pulse of 217 J/cm^3. On the other hand, the specific heat integral of the conductor from 77 to 148 K gives 129 J/cm^3, so, about 60% of the Joule heating was absorbed by the conductor itself in the longer pulse shot. For the shorter pulse of 0.3 s, about 80% of heat absorption in the conductor was observed.

2.1.11 Testing of a YBCO Prototype Cable

2.1.11.1 Cable Construction

The second-generation YBCO tapes provided by AMSC are coated-conductor composite tapes. The tape has a 75-µm-thick substrate made from Ni5at.%W alloy with a 2-µm nickel overlayer, a 1-µm-thick YBCO layer, 3 µm of Ag, 10 µm of solder, and 50 µm of Cu stabilizer, giving a total thickness of about 150 µm. This tape is called a neutral axis coated conductor by AMSC as the HTS layer is approximately in the center of the tape cross section. The two-layer cable was built by Ultera with the Cu-laminate side facing down in both layers for ease of attachment to the copper end plugs. Each layer had 12 1-cm-wide YBCO tapes wound on a 43-mm-diam former. The inner layer was soldered on the first section of the Cu end plug. The outer layer extends beyond this section and was soldered on the second section of the plug. The Cu plug extended for another 10 cm for making a connection to the high-current power leads. Multiple Cyroflex™ insulation layers covered the cable length to simulate the radial build of an operational cable and as thermal insulation for the purpose of a calorimetric ac loss measurement. The cable has an embedded heater and three flat RTD sensors over the outer conductor layer, one on the centerline and the other two located 31.2 cm from the center of the cable. The AMSC second-generation tape is robust enough to be shipped to Ultera, stored, handled, manufactured into a cable, shipped again to ORNL, and tied into some fairly massive copper cable connections. The complete, instrumented YBCO cable ready for testing is shown in Fig. 2.18.

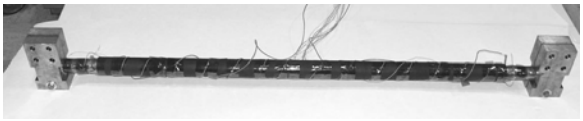

Fig. 2.18. Photograph of the 1.25-m YBCO cable ready for testing. The massive copper end connections for the external copper cables are on each end.

2.1.11.2 Critical Current Tests

All of the dc and ac tests were conducted in an open dewar of liquid nitrogen in Oak Ridge, Tennessee. The liquid nitrogen completely covered the cable and the copper end connections. To measure the dc voltage across the cable, Cu-plated BSCCO tapes were used as voltage taps and were placed around the outer layer of the YBCO cable to equalize the voltage potential. Figure 2.19 shows the experimental voltage-current (V-I) curve data. The inductive and current transfer voltages at lower currents were small compared with the sharp transition of the cable. The cable was measured to have a critical current (I_c) of about 4200 A as compared to a value of 4122 A based on the sum of the average tape I_c of the 24 tapes. Thus, there was little to no degradation resulting from the winding of the YBCO tapes on the cable former. The small flat voltage at about 0.01 to 0.02 mV is believed to be due to nonuniform current distribution in the 24 tapes. The cable *n*-value was measured to be 28, somewhat above the tape average *n*-value of 22 to 24.

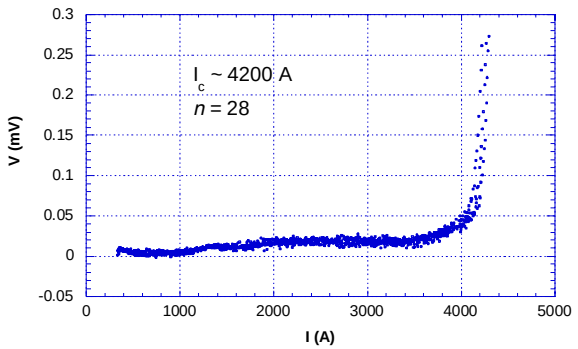

Fig. 2.19. V-I curve of the 1.25-m YBCO cable.

2.1.11.3 AC Tests

The YBCO cable was successfully operated at ac rms currents up to 2500 A, typical of phase currents in the DOE superconducting cable projects (800–3000 A). A null technique was used for the calorimetric ac loss measurement. A heater power of 9 W/m was applied to the cable to cause a temperature rise in the middle RTD of ~0.05 K. When an ac current of 1800 to 2500 A_{rms} was applied, the heater power was

reduced to maintain this temperature. Thus the reduced heater power would equal the ac loss in the cable. For the electric measurements, voltage taps on the cable current clamps and a current reference signal from a Rogowski coil around the input power cable were sent to a standard lock-in amplifier. It was found that the voltage taps beyond the cable gave a larger and consistent straight-line, in-phase voltage at lower currents. This voltage was subtracted out, and the corrected voltage was multiplied by the current to get the ac loss of the cable.

Figure 2.20 shows the measured ac loss as determined calorimetrically and electrically; it can be seen that there is fair agreement between the two measurement techniques. The cable ac loss was measured electrically and thermally to be about 2 W/m at 2000 A_{rms}, corresponding to $I_{peak}/I_c \sim 0.67$. Monoblock model calculations have been added to Fig. 2.20 for the actual cable build with a gap of 600 μm between the two 150-μm-thick YBCO tapes. It can be seen that the measured results are somewhat greater than the monoblock model predictions at higher values of I_{peak}/I_c. These ac losses are somewhat larger than would be expected from a two-layer BSCCO cable with the same I_c and former diameter. Because of the shape and the wide width (1 cm) of the YBCO tape, the radial cable build of 900 μm (nominal two-tape thickness of 300- and 600-μm gap) is believed to be the main contributor to the enhanced ac losses. It is expected that the cable ac loss can be reduced by about a factor of 2 to 3 by using narrow (3- to 5-mm-wide) tapes.

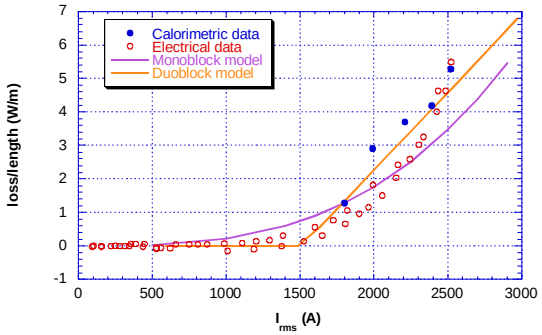

Fig. 2.20. AC loss of the 1.25-m YBCO cable.

2.1.11.4 Overcurrent Tests

Fault overcurrent simulation tests were performed on the YBCO cable. Pulse lengths of 0.1 and 0.2 s were used to simulate 6 and 12 cycles of short-circuit faults in a 60-Hz line. During the first series of 0.1-s pulse tests, the maximum pulse current was limited to 11 kA. In the second series of 0.2-s pulse tests, the maximum pulse current was increased to 12 kA after V-I measurements showed no degradation from the lower pulse currents. Figure 2.21 shows the overcurrent waveform for a peak current of 12 kA for a nominal duration of 0.2 s on the YBCO cable. The cable survived with a temperature rise to about 105 K at the end of the pulse.

This lower-than-expected temperature rise indicated that only about half of the Joule heating generated during the pulse remained in the conductor itself, a result of the loose winding of the wide YBCO tapes. The cable showed no degradation in the critical current after the sequence of overcurrent pulses.

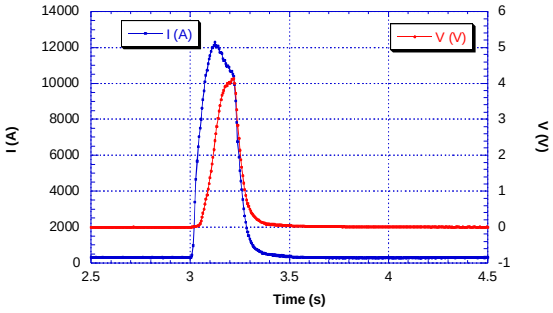

Fig. 2.21. Overcurrent pulse of 12 kA applied to the YBCO cable.

2.1.12 Dielectric Tests: Model Cable Studies

2.1.12.1 Dielectric Tests for 35-kV-Class Cable

Insulation requirements for 35-kV-class cable are dictated by the BIL level, which is 200 kV. Dielectric thickness for Cryoflex™ was determined experimentally by increasing the number of layers of lapped tape insulation on short (2-ft length) model cables. Figure 2.22 shows a plot of impulse breakdown voltage vs thickness (layers), showing that the impulse strength increases linearly with thickness. The highest data point exceeds the 200-kV BIL requirement and provides data required for designing 35-kV-class cables. Because of voltage limitations of the present cryostat and the length required for properly designed stress cones, testing for higher-voltage-class cables will require a larger, higher-voltage cryostat.

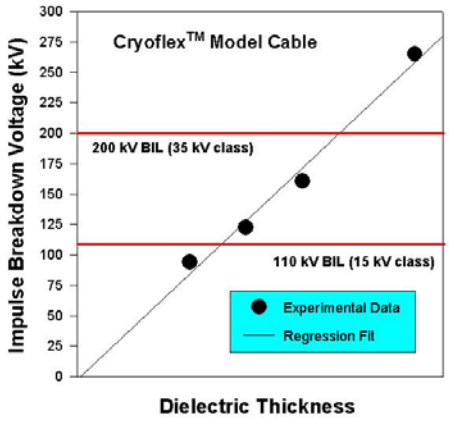

Fig. 2.22. Impulse breakdown voltage vs dielectric thickness for a Cryoflex™ wrapped model cable immersed in liquid nitrogen. Horizontal lines show the 15-kV and 35-kV-class BIL.

2.1.12.2 Dielectric Tapes for Higher-Voltage-Class Cables

New materials are currently under development for higher-voltage-class cables. The higher the strength of the material, the fewer layers will be necessary. Two new materials, Cryoflex™ red and Cryoflex™ blue, have been tested (ac breakdown strength) in model cables and have been found to have improved strength compared with the basic Cryoflex™ tape currently in use. The results are shown in Figure 2.23 and are compared with results for polypropylene laminated paper (PPLP), which is a tape commonly used in oil-impregnated, lapped-tape insulated cables and is currently used in Japan in liquid-nitrogen-filled HTS cables. The data show that all the Cryoflex™ materials exceed the strength of PPLP.

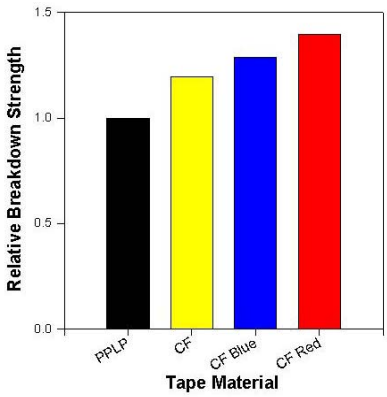

Fig. 2.23. Relative breakdown strengths of PPLP, Cryoflex™, Cryoflex™ blue, and Cryoflex™ red, taking into account the thicknesses of the various tapes.

2.1.12.3 Dielectric Tape Studies

Model cables have been made with tapes of other materials, including improved versions of Cryoflex™ (referred to as supercryoflex) for comparison with Cryoflex™, which is currently used in the 30-m Southwire HTS cable. PPLP has also been studied. AC breakdown, partial discharge (PD) onset, and lightning impulse breakdown have been measured for model cables wrapped with PPLP and immersed in pressurized liquid nitrogen. The breakdown voltages of PPLP were found to be lower (49 kV rms) than those for Cryoflex™ (60 kV rms) for the same number of layers of tape (the PPLP is about 10 to 20% thicker than Cryoflex™). One impulse breakdown test was done on PPLP, yielding 89 kV and giving an impulse-to-breakdown ratio of 1.8.

2.1.13 Partial Discharge in Cryogenic Cables

PD patterns have been used in calculating the energy dissipated in a cryogenic cable as a potential method for assessing aging. For these studies we have used commercially available PPLP tape. Figure 2.24 shows a typical sequence of patterns as the voltage is increased from 22.5 to 45 kV. The pulses are superimposed

on a single cycle of AC, providing the phase relationship between PD and the applied voltage. The patterns are seen to grow in amplitude and in intensity (number of pulses) as the voltage increases. The patterns shift toward the zero crossing, an indication of the increasing space charge in the LN_2-filled butt gaps. At each voltage the total dissipated energy can be calculated. A plot (Fig. 2.25) of the log of the energy dissipated vs the log of the applied voltage gives a slope of 6.4. The slope can be shown to be identical to the *n* value from the aging relationship, $E^n t$ = const. In Fig. 2.26 we plot the PD energy vs voltage for three independent runs, showing a variation from run to run with slopes ranging from 6.4 to 9.8. An average *n* found for these yield 8.1. Actual aging data on PPLP cryogenic cable is needed for comparison with the PD-derived *n* value.

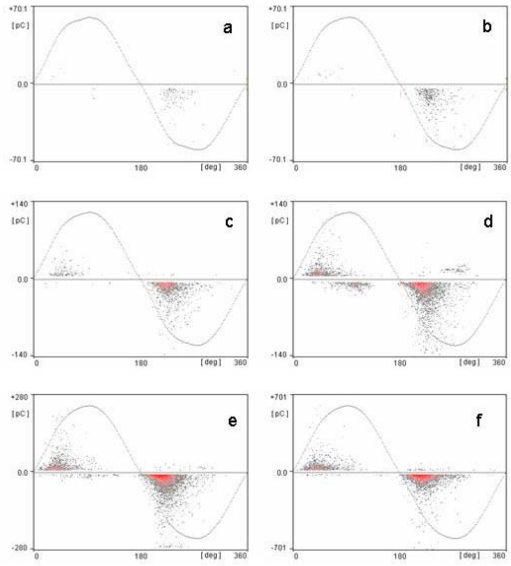

Fig. 2.24. Partial discharge patterns recorded as a function of voltage for PPLP model cables: a, 22.5 kV; b, 25 kV; c, 30 kV; d, 35 kV; e, 40 kV; f, 45 kV.

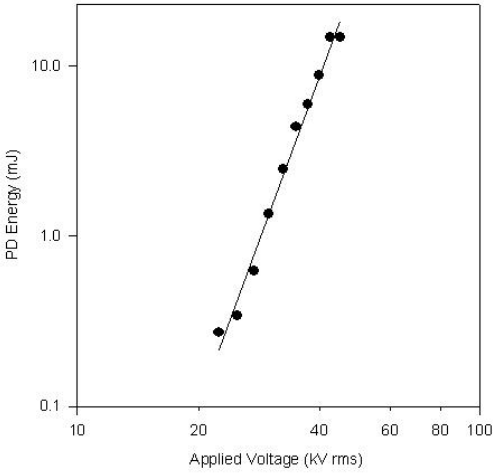

Fig. 2.25. Log-log plot of PD energy dissipation as a function of voltage.

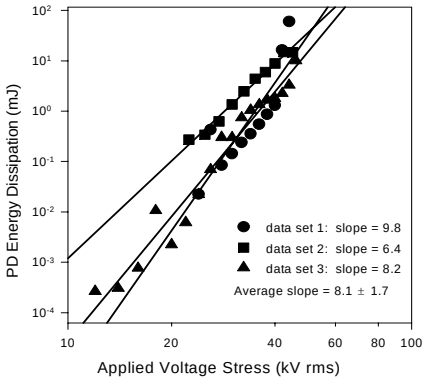

Fig. 2.26. Comparison of three separate data runs of PD energy vs applied voltage stress, giving *n* values ranging from 6.4 to 9.8.

2.1.14 Model Termination Dissection

The high-voltage dielectrics group also supported insulator development and testing for the triaxial cable and termination system. In high-voltage tests, the two large model terminations were broken down and then dissected to determine the cause of failure. Location of the breakdown in each termination sample was determined by cutting the termination into sections and using a high-impedance ohmmeter to determine which section exhibited lower impedance. By using this approach, the failure could be localized to a small segment a few inches in length, after which the outer conductor was removed. This section was then machined in 0.625-mm increments to locate the source of the breakdown. In both model terminations, large voids formed in the casting process were found to be the cause of breakdown.

PD data, obtained for these terminations, have been analyzed, confirming patterns indicative of the presence of voids. Work is continuing in the dissection of the small-model terminations.

2.1.15 3-kA Triaxial Cable Termination R&D

During the last quarter of FY 2003, practically all of the fabricated hardware for the 3-kA, 5-m triaxial cable test was received from the shops. Design, fabrication, and delivery of the hardware was implemented expeditiously because the 3-kA design retained, as much as possible, the basic features of the 1.3-kA design. Work on a dielectric formulation for the terminations was also completed, and the machinery used to produce the dielectric was rebuilt to meet the different needs of the new formulation. The dielectric material is tested in three configurations using flat electrodes, concentric cylindrical electrode samples made in the laboratory and referred to as "baton" samples, and larger concentric cylindrical electrode samples made using the actual machinery and referred to as "barbell" samples. Flat electrode samples of the new dielectric formulation gave good electrical performance that met design goals with ample safety margins. Scaling to baton and barbell samples of the dielectric, however, gave disappointing results. Therefore, aid was enlisted from conventional termination component suppliers that use similar materials in their process to evaluate dielectric production procedures. They identified a potential problem with the procedure and suggested a potential solution that is in the process of being implemented. In some initial tests using their recommendations, baton samples that exceed design specifications for ac breakdown and PD have been made. Repeats of these tests are being made to confirm the procedures in preparation for implementation in barbell samples. After good barbell samples have been produced, the program will proceed to making the full-scale 3-kA terminations.

2.2 WAUKESHA ELECTRIC SYSTEMS/SUPERPOWER/ENERGY EAST HTS UTILITY TRANSFORMER SPI

S. W. Schwenterly, I. Sauers, D. R. James, and A. R. Ellis

2.2.1 5/10-MVA Transformer Fabrication

Design work on the multiple-layer insulation (MLI) blankets for the 5/10-MVA transformer coil assembly was completed, and final drawings were transmitted to SuperPower and Waukesha Electric Systems (WES). SuperPower ordered the blankets from CAD-Cut in Montpelier, Vermont. Procurement activities on the liquid nitrogen tank module for the transformer had been completed by ORNL in the previous fiscal year, and Technifab in Brazil, Indiana, had been selected as the vendor. Technifab completed the liquid nitrogen tank module and shipped it to WES in mid-December. The module had its own subflange, ready for drop-in installation in the transformer tank cover.

The low-temperature cooling module for the transformer coils was completed by ORNL in the previous fiscal year and was successfully tested at WES. Figure 2.27 shows an internal view of the cooling module. Two Cryomech AL-330 cryocoolers are mounted on the top plate (not shown) with bellows couplings, to provide vibration isolation and to allow the coolers to deflect slightly with thermal contraction of the internal transformer components. The bellows assemblies are supported by preloaded springs that resist atmospheric pressure when the tank is evacuated. A liquid-nitrogen-cooled copper shield with MLI hangs below the top flange, surrounding the cryocooler cold heads and heat exchangers. The heat

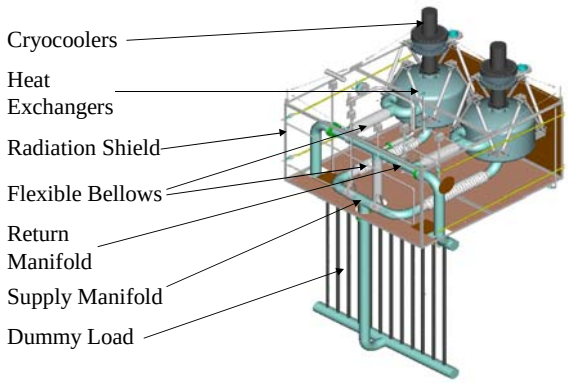

Fig. 2.27. Internal layout of transformer cooling module.

exchangers are basically pressure vessels that contain finned copper arrays connected to the cold heads. Each heat exchanger is supported from the top plate on eight stainless steel struts. Spherical bearings on the strut ends allow the struts to pivot slightly under thermal contraction. Flexible bellows sections in the supply and return piping to the heat exchangers allow for contraction in the piping and the attached transformer cold mass. Temperatures on the cold heads, heat exchangers, and piping are measured by Lakeshore Cryotronics DT-470 diodes calibrated with 0.25 K precision. Radiation shield temperatures are monitored using type T thermocouples. Cooling for the cold head compressors is provided by a water chiller circulating a glycol solution in a closed loop so that the whole system is completely self-contained. An easily removable dummy load that was used for the cooling tests is shown hanging below the cooling module. The heat exchangers, load, and piping form a closed loop that is filled with 10-atm helium gas. The helium circulates in the loop by natural convection, efficiently coupling the load to the cryocoolers.

In the previous fiscal year, PD testing by SuperPower on the first and second phase coil sets for the transformer had indicated relatively low PD inception levels in the range of 1 to 2 kV. In early October, ORNL personnel visited SuperPower to participate in inspection and PD testing on the partly completed third-phase coil set to determine whether its performance could be improved. The ORNL PD detection equipment was shipped to SuperPower for the tests. PD tests were conducted on coil sets and model samples of various practical electrode designs. A few adjustments and modifications were made to help improve high-voltage performance as a result of the inspections. However, after the coil set was completed, it was found to be similar to the other two in PD performance. Since one of the first two sets had been cooled to liquid nitrogen temperature and successfully energized to its full operating voltage for the better part of an hour, it was decided to proceed with installation of all three coil sets.

Final assembly of the 5/10-MVA transformer was carried out at the WES plant. ORNL personnel participated in this process for all ORNL-provided equipment. The HTS coils by SuperPower were installed in the support frame and were mated with the transformer core fabricated by WES. WES completed and leak-tested the vacuum tank. External relief devices and instrumentation for pressure, level control, and temperature were installed in the liquid nitrogen tank assembly, and the liquid nitrogen cryocooler was fitted. The coil cooling module and liquid nitrogen tank assembly were installed into the transformer tank cover. All interconnecting piping was completed and leak checked. Figure 2.28 shows the coil cooling and liquid nitrogen tank modules installed on the cover.

The whole cover assembly was mounted on a lifting fixture and positioned above the phase set assembly in the exact relative location it would have in the vacuum tank. This allowed accurate completion of the interconnections between the cooling system, liquid nitrogen tank, and phase set with good assurance that they would fit properly when installed in the vacuum tank. Figure 2.29 shows a view of the trial assembly. The liquid nitrogen tank and coil cooling module can be seen hanging under the cover at left and center, respectively. All system joints were leak-checked to 10^{-9} atm-cc/s in this preliminary assembly.

Fig. 2.28. LN tank and coil cooling modules on cover.

Fig. 2.29. Trial assembly of transformer coil assembly and top cover.

In March, ORNL personnel visited WES to participate in installation of the MLI blankets on the phase set assembly. The blankets were formed from alternating layers of conductive aluminized Mylar and insulating polyester. They were designed with an electrically insulating inner polyester layer so that they would not be grounded to the underlying liquid nitrogen-cooled heat shields. Great care was applied to prevent electrical shorts between adjacent blankets that could form a shorted turn around any of the three transformer core limbs. This caused a problem in high-voltage testing of the 1-MVA prototype transformer in 1998. All the underlying heat shields and support frame elements are similarly insulated to prevent shorted turns around the core. WES personnel performed ratio tests at several stages in the assembly to verify the absence of shorted turns. Figure 2.30 shows the completed phase coil assembly with the MLI installed as it was lifted into the vacuum tank.

Assembly of the 5/10-MVA transformer was completed early in the third quarter. After the cover assembly was fitted and the tank was evacuated, a global leak check showed that the total leak rate in both the liquid nitrogen and helium systems was in the range of 10^{-6} atm-cc/sec. Pressurizing these internal cooling systems had no effect on tank vacuum with the warm unit. All the cryocooler compressors and other external equipment were installed on the tank. Figure 2.31 shows the completed transformer with the compressors installed.

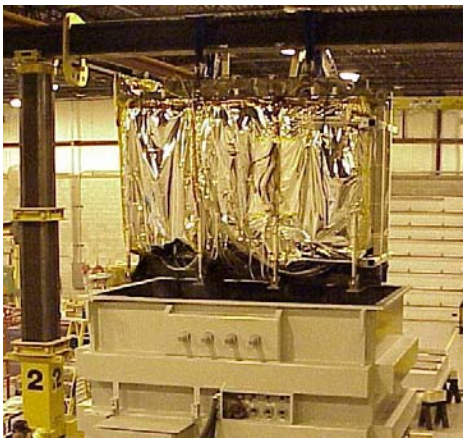

Fig. 2.30. Installation of coil assembly with multiple-layer insulation into vacuum tank.

Fig. 2.31. Completed transformer showing compressor cabinet.

2.2.2 5/10-MVA Transformer Test Results

Preliminary electrical tests at 300 K included ratio, winding resistance, capacitance, and megger to core – all test results were normal. Liquid nitrogen flow was initially under manual control during cooldown. A slow flow was continued over several days to allow the shield and leads to cool uniformly. After the internal nitrogen tank was filled, the liquid nitrogen system ran unattended in closed cycle. The helium loop was pressurized, and the coil cryocoolers were started soon after liquid nitrogen flow began. The coil cooling system cooled the coils to 30 K in about 12 days (see Fig. 2.32). The initial cooldown rate was faster than calculated because the calculations did not consider

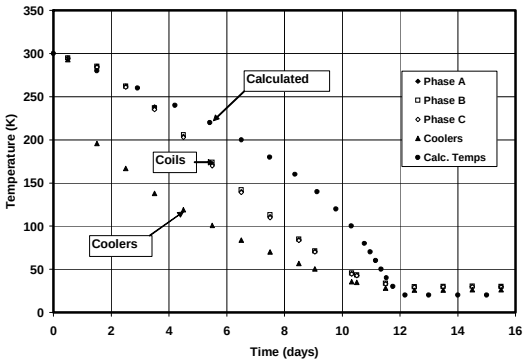

Fig. 2.32. Transformer cooldown curve.

the effect of the liquid nitrogen cooling on the coil shields and support structure. Baseline vacuum was 3×10^{-5} Torr (close to nitrogen vapor pressure at 30 K). During cooldown to 30 K, the winding resistances fell as expected, from 2.8 Ω to 0.01–0.04 mΩ for the high-voltage windings and from 0.03 Ω to 0.01–0.03 mΩ for the low-voltage windings.

Another ratio test after cooldown showed high excitation current on C phase: 1.2 A at 25 V, compared to 0.1 A on other phases. Possible explanations were a ground loop in instrumentation leads or piping or a short from the MLI or liquid nitrogen panels to frame or core. Single-phase tests were carried out with the low-voltage winding shorted. The measured impedance matched the design calculation (all phases ~210 V, 67/705 A, 0.84% impedance). A maximum single-phase current of 94 A (1.4 ×) was reached, limited by available ac power supply voltage. Three-phase tests were carried out with all three low-voltage phases shorted together. Modifications to the variac power supply allowed tests at full line current of 116 A into the high-volume winding. Impedance values matched the single-phase test results. During all the high-current tests, heating that presumably came from the C-phase short caused a slow temperature rise, which limited test times to several hours. After the high-current tests were completed, the transformer was warmed to room temperature, to locate and correct the short around the core on C phase and to fix the small liquid nitrogen and He leaks into the vacuum region to reduce the overall heat load. To investigate these problems, checkout and repair of the transformer began in August at the WES site. A vacuum gauge was connected to each core-cooling circuit to verify that none of them had gone to negative pressure while the tank was evacuated. The core limb and lower yoke panels were still at 1 atm, but the upper yoke panel showed about 25 cm Hg vacuum. This was later traced to a slightly loose feedthrough connection. All the external plumbing connections on the liquid nitrogen tank were checked carefully. No leaks were found, but the bolts holding the cryocooler coldhead into the tank had loosened slightly, probably from the vibration of the unit. A rubber pad was installed under the coldhead to isolate vibrations and reduce noise, and better lock washers were installed. We found later that there were several pinholes in the burst disc on the liquid nitrogen tank vent line. This explains the ice plugs that appeared in this line when the tank pressure went negative, sucking in humid air. This disc has a line of sharp teeth around the outer edge that are supposed to cut it open when it inverts under the set pressure. It appears that some time during cooldown and filling of the tank, a pressure excursion must have partly inverted the burst disc but was not great enough to fail it. The disc contacted the teeth lightly, just enough to cause the pin holes. More instruction will be needed for some of the inexperienced people that participate in the 24-h/day filling operations on the liquid nitrogen tank during the early part of the next cooldown. The whole liquid nitrogen shield system was very wet inside due to the burst disc leak, which prevented proper evacuation of the system for helium leak checks. It was decided to defer these until the unit was untanked.

An excitation current test was performed on the low-voltage (LV) side of all three phases after the tank was vented up to 1 atm with dry air. Results were the same as before, indicating that the phase C short had not changed. At 20 V, the excitation current on phase C was 0.71 A, as compared to 0.078 A on the other two phases.

When the tank was opened, everything appeared in good order—in particular, all the MLI was still properly in place. We disconnected each of the core cooling hoses from the tank wall manifolds and performed the excitation current test. The currents did not change, showing that the core cooling system is not involved in the short. We then disconnected the liquid nitrogen supply and vent hoses between the liquid nitrogen tank and the core/coil unit. We found that with both hoses disconnected, the short current for C-phase dropped to 0.570 A at 20 V. Connecting either hose raised the current back to the original value. Disconnecting the liquid nitrogen tank from the liquid nitrogen shield around the cooling module heat exchangers did not cause any further reduction to the 0.570-A short current. Disconnecting both auxiliary helium circuit hoses from the tank wall fitting similarly did not cause any further reduction.

We pumped out the helium loop and backfilled it with dry nitrogen several times to remove adsorbed helium and to allow connection of the leak detector. After that, the helium background in the system was 3.8×10^{-7} atm-cc/s. We leak-checked all four copper-gasket flanges that couple the cooling module to the 3-in. coil set piping and did not see any indications. A very slight background rise was seen when the

inside of the cooling module LN shield was flooded with helium. After performing the leak checks, we disconnected the four flanges. Disconnecting the C-phase helium return reduced the short current to 0.546 A. Disconnecting the A- and B-phase helium returns respectively reduced the short current to 0.534 A and 0.519 A levels. Disconnecting all the data lines and sensor leads from the tank wall feedthroughs had no effect on the short. At that point, it was clear that the short around phase C was associated with the helium and nitrogen piping. During the rest of August, the tank cover was removed and the unit was taken out of the tank.

During early September, the untanked unit was carefully inspected and leak-checked. Several large leaks were found around the cryogenic breaks that supply liquid nitrogen to the LV coil HTS leads. Some smaller leaks were found in brazed joints between the copper lead heat sinks and stainless liquid nitrogen supply piping. They were repaired by painting them with Stycast epoxy. A leak was also found on a solder joint in the piping on the cooling module radiation shield and was repaired similarly. No leaks were found on any welds. Future designs should eliminate brazed or soldered joints, and fragile ceramic-to-metal seals should be avoided. Leak checks of the helium system, which is all welded construction, showed only a few very small indications that could never be pinpointed. Since most of the leakage in the original tests occurred with high pressure in the system rather than vacuum, it was decided to make an effort to make the bolts on all internal copper-gasket flange joints as tight as possible, to minimize leakage due to bolt stretch under pressure. Under vacuum, all systems in the transformer are now leaktight in the 10^{-9} atm-cc/s range.

The short circuit around phase C was successfully eliminated. A careful analysis of the internal piping geometry of the transformer showed that the short on phase C could only result from contact between the helium and nitrogen systems at two locations: (1) between the inner radiation shield cylinder and the inner bore of the phase C coil set and (2) between the helium supply piping and the bottom radiation shield for phase C. A fiber-optic scope was used to inspect these areas in detail. We eventually discovered that the contact was at location (1), between one of the cooling tubes on the inner bore of the coil and the radiation shield cylinder. A wedge was gently driven into the gap to deflect the shield inward from the coil bore, and insulation was inserted into the space and secured tightly. All three phases then had excitation current near 0.07 A at 20 V. The reason that the contact resulted in a shorted turn around the core on phase C is that the helium and nitrogen piping assemblies come into the coil set from opposite sides of the core. Contact between them on the inner coil bore then resulted in a current path that went through the core window. Since the loop was only completed when the piping assemblies were attached to the tank wall, all the excitation current tests before the unit was tanked were normal. Unfortunately, another excitation current test was not done until the tank was evacuated and cooldown was nearly complete. In future designs, it is advisable that all piping to the coils come in from one side of the core to eliminate this problem.

During the rest of September, the transformer was reassembled. After the unit was reinstalled in the tank and all the piping was reconnected, excitation current tests still continued to be normal. The unit will be cooled down and retested in the first quarter of FY 2004.

2.3 PROPOSED SUPERPOWER MATRIX FAULT CURRENT LIMITER CRADA

S. W. Schwenterly, D. R. James, and I. Sauers

During the past year, SuperPower, Inc., has developed a new concept for a matrix fault current limiter (MFCL). This consists of an array of HTS elements that are arranged to simultaneously go normal in a fault. The fault current is shunted to a parallel array of normal reactive elements that effectively limits the maximum current in the fault and allows downstream breakers to open. After the fault clears and the breakers close, the HTS elements quickly return to the superconducting state and restore normal operation. SuperPower's concept is aimed at transmission-level voltages of 138 kV or more and offers good prospects for successfully achieving these voltages. ORNL participated in a technical review committee meeting in June 2002. The meeting participants determined that the basic concept employed in the MFCL is sound. SuperPower then formed a technical advisory board and held the first meeting in January 2003. The

purpose of the technical advisory board is broader than the technical review committee; it will meet regularly during the project to offer guidance to make sure that the program objectives are met. The first technical advisory board meeting was well attended by representatives from DOE and a mixture of industrial companies, utilities, national laboratories, and universities. The reports of the technical advisory board have been favorable, with no major technical deficiencies identified. SuperPower has requested that ORNL be included as a national laboratory partner on the SPI. A draft statement of work has been developed and agreed to by both parties. Proposed tasks would include the following:

- support the design and fabrication of components for the MFCL cryostat;
- modify an existing, subcooled, pressurized liquid nitrogen cryostat system at ORNL and design and conduct tests to verify the MFCL cooling concept;
- prepare a cryostat system that will be used to design and perform larger-scale cryogenic or combined high-vacuum/cryogenic tests on MFCL components (e.g., high-vacuum current leads, HTS modules), during the course of the MFCL prototype development;
- support development for assembling and testing of MFCL cryogenic subsystems; and
- participate and assist with qualification tests for all prototypes, including beta-prototype final acceptance tests.

ORNL participated (with several other scientists/engineers from national laboratories, utilities, industry and universities) in a 1-day technical advisory committee meeting and a 2-day conceptual design review of the HTS Matrix Fault Current Limiter project at SuperPower, Inc., on June 10, 11, and12. A detailed list of reviewer comments (chits) was assembled by SuperPower that will be tracked through focused development plans and subsequent design reviews.

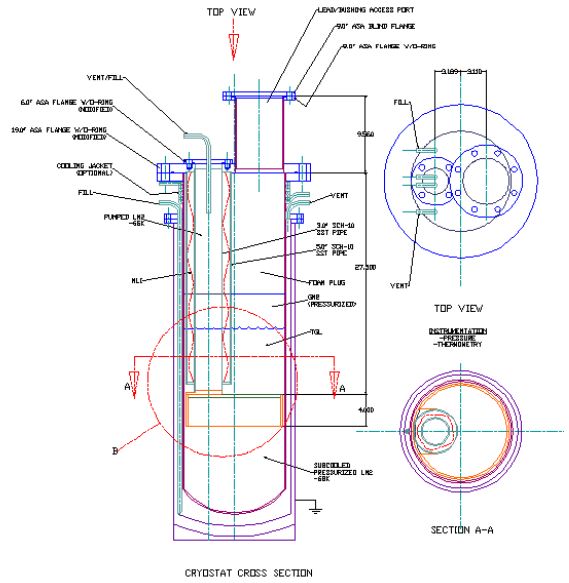

Fig. 2.33. Cross section of pressurized nitrogen cryostat.

A joint statement of work was developed for a draft CRADA that was sent to SuperPower for review and approval. ORNL's tasks include overall engineering design and analysis support, verification tests on the cooling concept, high-voltage and cryogenic tests on prototype MFCL components and assemblies, and testing of high-voltage insulation materials and lead concepts. During the quarter, a conceptual design was completed to modify an existing high-pressure nitrogen cryostat for the cooling concept tests. Figure 2.33 shows a cross section of the modified cryostat.

A vacuum-insulated cold finger projects down into the pressure vessel. A 10-cm-high copper cooling skirt attached to this cold finger simulates the cooling skirt that will be attached to the cryocooler in the actual device. Cooling for the 3- to 5-atm nitrogen in the pressure vessel is provided by liquid nitrogen boiling in the cold finger. A heat source will be energized below the cooling skirt, and temperatures will be measured in several locations in the pressure vessel. Because the surface area available for boiling heat transfer is limited in this design, another version using forced-flow nitrogen in cooling tubes wrapped around the skirt is also being investigated. The cryostat is also provided with another port to allow installation of high-voltage lead bushing assemblies.

2.4 GENERAL ELECTRIC COMPANY HTS GENERATOR SPI

R. C. Duckworth, J. A. Demko, M. J. Gouge, J. W. Lue, and S. W. Schwenterly

2.4.1 Emissivity Experiment

To minimize the heat load for the design of the GE HTS rotor retrofit of a 100-MVA generator, a low-emissivity thermal shield is required. To qualify materials that have low emissivities at cryogenic temperatures, an experimental test apparatus was designed and built. Figure 2.34 shows a schematic of the facility and a picture during its fabrication.

To characterize the emissivity of a given surface, the experimental facility was designed to measure the radiation heat transfer from a room-temperature blackbody to the surface, which was cryogenically anchored to a Cryomech AL330 cryocooler. For a given two-surface radiation exchange, the heat load can be written as

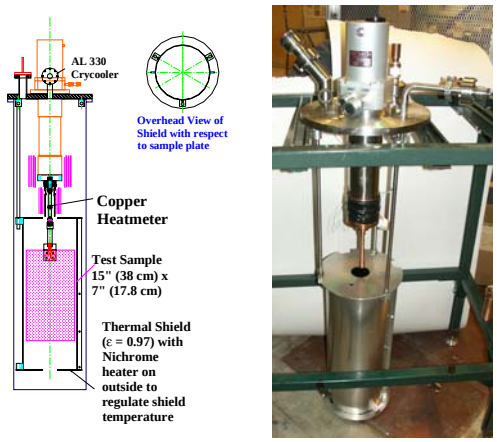

Fig. 2.34. Schematic and picture of emissivity experimental test facility.

$$Q_{sample} = \frac{\sigma\left(T_{shield}{}^{4} - T_{sample}{}^{4}\right)}{\frac{1-\varepsilon_{shield}}{\varepsilon_{shield} A_{shield}} + \frac{1}{A_{shield} F_{shield \rightarrow sample}} + \frac{1-\varepsilon_{sample}}{\varepsilon_{sample} A_{sample}}} \qquad (1)$$

where

σ = Stefan-Boltzmann constant (5.67×10^{-8} W/m^2-K^4)

ε_{shield} = the effective emissivity of the black thermal shield

ε_{sample} = the effective emissivity of the sample

A_{shield} = area of the shield [m^2]

A_{sample} = area of the sample [m^2]

$F_{shield \rightarrow sample}$ = the radiation view factor between the shield and the sample

Once the radiation heat load to the sample is known, the emissivity of the sample can be found. An uncertainty analysis of this equation identified that for the emissivity that changes to the heat load and the shield temperature cause the most significant change in the emissivity (see Table 2.5).

After this calibration was completed, the thermal shield was added to the system. This thermal shield was suspended from the top plate flange and was effectively built as an aluminum can with a diameter of 9 in. and a height of 25 in. On this aluminum surface, a black felt was attached to simulate the blackbody. Black felt was used because of the low outgassing with respect to vacuum, ease of installation, and the increased surface area of the fibers, which enhances the already high emissivity. The position of the

TABLE 2.5. Estimate of uncertainty for a sample with a calculated emissivity of 0.030

Variable	Typical value	Uncertainty	$\delta\varepsilon/\varepsilon \times 100$
T_{shield}	270 K	± 1 K	1.407
ε_{shield}	0.90	±0.05	0.051
T_{sample}	40.0	± 0.2 K	0.004
Q_{sample}	3.0	± 0.2	7.401

heatmeter relative to the copper shield of the heatmeter was examined, and it was determined that having the heatmeter completely out of the thermal shield was the best configuration to minimize the radiant heat transfer into the thermometry (Fig. 2.35). Layers of aluminized MLI were added to the copper shield to minimize the radiant heat transfer from the environment.

Before the sample was inserted into the thermal shield, the amount of background radiation associated with the sample-mounting hardware and the instrumentation leads was determined (Fig. 2.36). After that was done at different shield temperatures, the sample was inserted and the emissivity was measured for a series of copper and silver samples. The emissivity as a function of temperature is shown in Fig. 2.37.

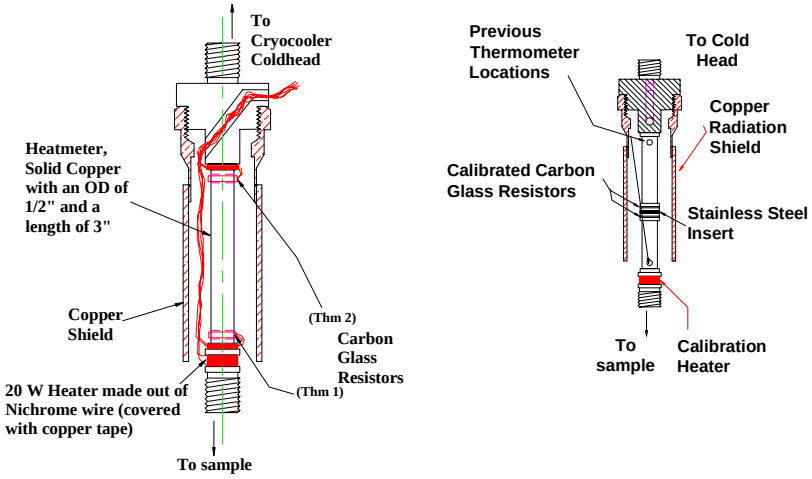

Fig. 2.35. Diagrams of heatmeters: copper (left), modified stainless steel/copper (right).

The values for the copper indicate that the emissivity appears to have some temperature dependence but that the equilibrium points (lowest temperature) appear to be reasonable. Further minimization of the parasitic heat loads is necessary to accurately characterize the radiant heat transfer.

In support of the contamination experiments, an air and water leak was procured from Vacuum Technologies, Inc., to provide a source of contaminants that the thermal shield could see in the operation of the generator. This leak will be installed in the cryostat once the measurement method is proven, and the emissivity will be measured as a function of contaminant mass and material.

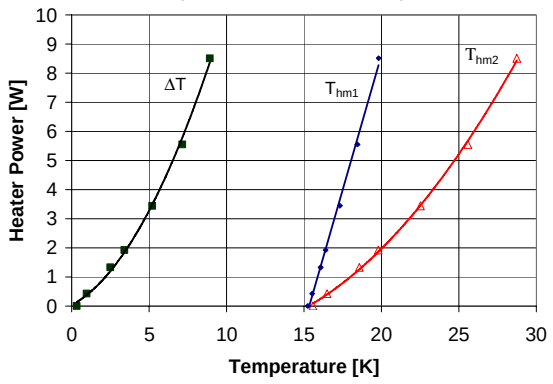

Fig. 2.36. Applied heater power as a function of the heatmeter temperatures and the temperature difference between the two thermometers for the stainless steel heatmeter.

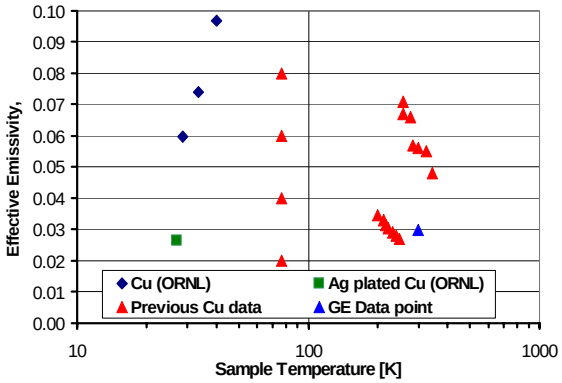

Fig. 2.37. Comparison of previously measured values of copper and silver-plated copper to the measurement of effective emissivity found between 20 K and 40 K.

2.4.2 Partial Discharge Tests

A sample has been prepared for testing turn-to-turn and layer-to-layer insulation for the HTS GE generator coil. PD tests were completed on samples cut from their model coils by GE. The schematic is shown in Fig. 2.38, and a photograph of the sample is shown in Fig. 2.39. PD data will be obtained for adjacent tapes in the interior of the sample as depicted in Fig. 2.38 while the remaining tapes will be at ground potential.

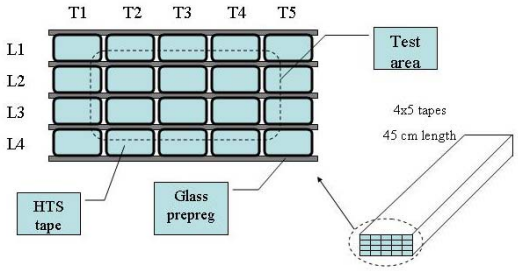

Fig. 2.38. Schematic of tape arrangement for PD testing.

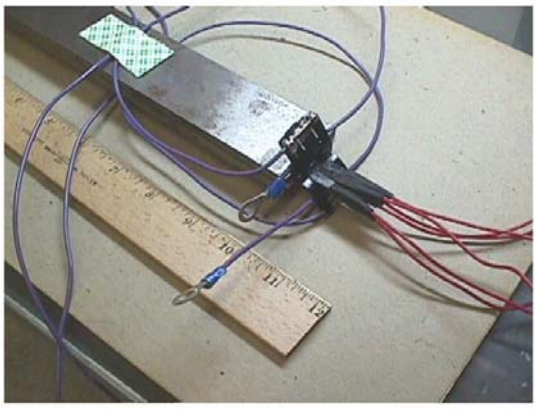

Fig. 2.39. Sample used for PD testing.

2.5 BSCCO AND YBCO BURNOUT EXPERIMENTS IN LIQUID NITROGEN BATH

M. A. Young, J. A. Demko, R. C. Duckworth, J. W. Lue, and M. J. Gouge

Burnout measurements were performed on BSCCO tapes to observe the effect on stability when adding Cryoflex™ layers to the tape surface. The tapes used in this study were manufactured by AMSC and consist of BSCCO-2223 in an Ag/alloy sheath plated with thin layers of Ni and Cu (Table 2.6).

Table 2.6. Properties of the sample tape from AMSC

Cu (%)	4.4
Ni (%)	8.7
Ag/alloy (%)	52.1
BSCCO-2223 (%)	34.7
Length (cm)	24
Width (mm)	4.16
Thickness (mm)	0.24
Critical current (A)	116

2.5.1 Experimental Apparatus and Configuration

A 30 × 7 cm G-10 sample block was constructed with a thickness of 2.5 cm and with a 0.5 cm deep × 1.5 cm wide rectangular groove cut out along its surface. A layer of Kapton™ tape was applied along the groove and covered with Apiezon™ to enhance thermal contact between the sample and block and to provide sealing to the G-10 block to prevent liquid nitrogen from seeping under the tape ash (see Fig. 2.40). The sample was placed flat along the bottom of the groove and into the Apiezon™. Voltage taps were secured to the top surface of the sample with an ostalloy solder at distances approximately 10 cm apart. The ends of the sample were covered with two sheets of indium each and bolted down with 9 × 2.5 cm rectangular copper current lugs with a thickness of more than 1 cm. A desired number of Cryoflex™ layers were then placed over the surface of the tape and were secured by three plastic shims anchored with Kapton™ tape.

Fig. 2.40. Sample holder for burnout current testing of HTS conductors in a liquid nitrogen bath

Burnout measurements were conducted while the sample was completely submerged in a liquid nitrogen bath. The bath level was held constant within a small range of 7.5 cm above the sample surface. After I_c was measured, a constant current at some value above I_c was applied to the sample for up to 60 s. If during this 60-s interval the heat generation in the tape surpassed the amount of heat that could be removed by the liquid nitrogen, an unstable condition was reached. This unstable condition was observed by monitoring the voltage across the tape, which, like temperature, also achieves a runaway situation when stability is lost. The lowest current that resulted in an unstable condition was recorded as the burnout current. If throughout the entire 60 s the sample remained stable, the measurement was taken again at a slightly higher value of current. This process was performed for up to ten layers of Cryoflex™. The last burnout current measured was for the bare-tape case because it usually results in destruction of the sample. Examples of the burnout of the bare and Cryoflex™ cases are shown in Figs 2.41 and 2.42.

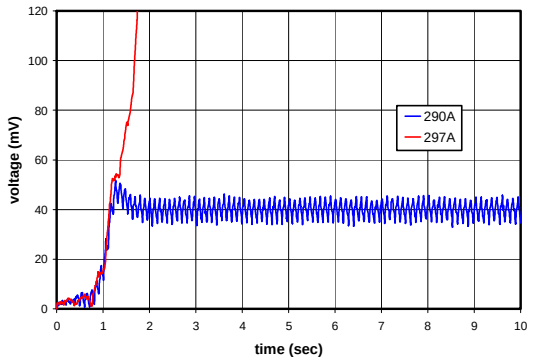

Fig. 2.41. Voltage response to currents above I_c for bare Cu-plated BSCCO tape at 77 K.

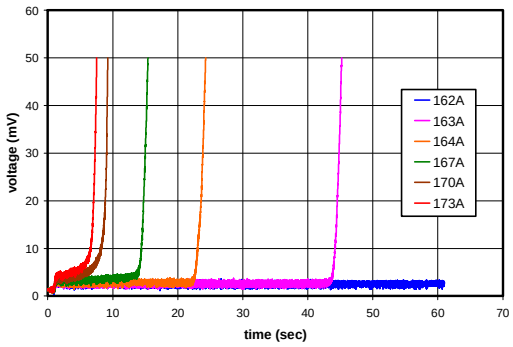

Fig. 2.42. Voltage response to currents above I_c for a tape covered with two layers of Cryoflex™ in a liquid nitrogen bath.

2.5.2 Numerical Model

A numerical model was developed that simulates the burnout behavior of a bare (no Cryoflex™ layers) Cu-plated tape. The model is based on an energy balance of the tape that considers heat conduction across the length of the tape, liquid nitrogen cooling, and Joule heating per unit length of the sample. The Joule heating term is calculated using the critical state model, in which it is assumed that the portion of the transport current carried in the superconductor is the critical current for a given temperature, and the remaining current is carried in the matrix. The matrix resistance was measured down to the critical temperature of the superconductor (104.5 K). Below the critical temperature of the superconductor, a linear extrapolation is used to determine the matrix resistance.

$$\gamma A_{tape} C_P \left(\frac{\partial T}{\partial t} \right) = Q_{conduction} + Q_{joule} - Q_{convection}$$

Where the conduction term is $$Q_{conduction} = \frac{\partial}{\partial x}\left(kA_{tape} \frac{\partial T}{\partial x} \right)$$

the Joule heating term is $Q_{joule} = \dfrac{\rho I_{matrix}^2}{A_{tape}} = R_{tape} I_{matrix}^2$ where $I_{matrix} = I_{transport} - I_c$

the convection cooling term is $Q_{convection} = hP(T_{tape} - T_{LN2})$

The convection heat transfer assumes pool boiling when the temperature difference is below 10 K. At this point the critical heat flux is reached and film boiling occurs. In order to reduce the complexity of the model, the ends of the sample were held constant at T_{LN2}, which is a logical assumption because the sample

ends are anchored by large masses of copper. The model also considers heat conduction between the sample and the G-10 mounting block, which may act as a heat sink. Critical current values are approximated according to temperature based on data from earlier measurements on similar tape.

2.5.3 Comparison Between Numerical Model and Results

The model was simulated for various values of transport current. In Fig. 2.43, the analytical results are compared to an experimental burnout case. The results show that a large degree of correlation exists between the voltages generated by the model and the voltage measured in the laboratory. The burnout times and currents calculated by the model are within an acceptable range; experimental values can change from one measurement to the next. Currently, the capabilities of the model are in the process of being expanded to consider the effect of Cryoflex™ layers on the surface of the sample. In addition to the first-generation BSSCO conductor, a series of copper-laminated second-generation YBCO-coated conductors were measured to determine whether the burnout limit is affected by the conductor. Figure 2.44 shows the comparison between the BSCCO and YBCO in addition to the results of BSCCO found with the numerical model. The success of the model with the Cryoflex™ for the BSCCO will be applied to the copper-laminated YBCO once the voltage and current transfer characteristics are added.

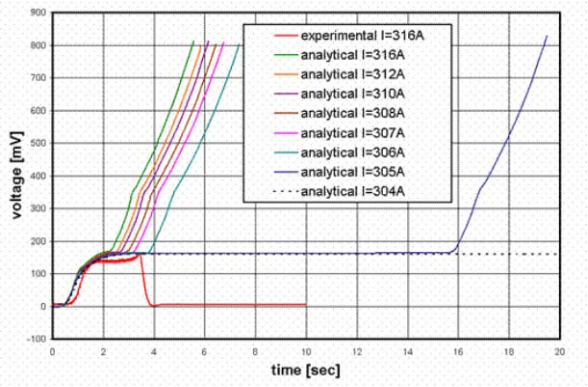

Fig. 2.43. Comparison of experimental and modeling results.

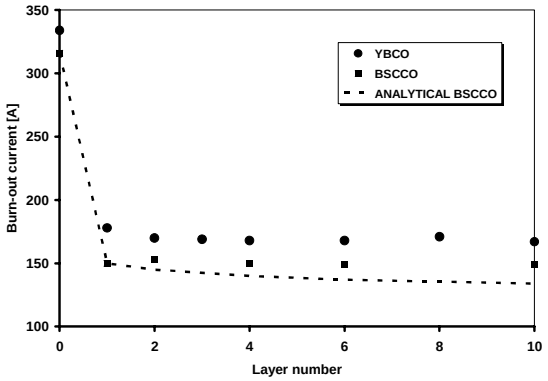

Fig. 2.44. Measured burnout current of BSCCO and YBCO HTS tapes and the calculated burnout current for BSCCO with different numbers of Cryoflex™ layers.

2.6 AC LOSSES IN SILVER COATED YBCO RABiTS™ TAPES

R. C. Duckworth, J. R. Thompson, M. J. Gouge, and J. W. Lue

Transport ac loss measurements were conducted on a RABiTS™-processed YBCO tape provided by AMSC. The sample that was tested had an overall width of 1 cm, a YBCO thickness of 1 μm, a 3-μm silver cap layer, and a nickel alloy substrate that was composed of 75 μm of Ni-5at%W and a 2–μm nickel overlayer. To measure the ac losses, two techniques have been utilized. First, a single, liquid nitrogen referenced thermocouple was attached to the sample, and the losses that were generated over an insulated region were measured when both ac and dc currents are applied. This was accomplished by calibrating the thermocouple response against a known heat generation produced by a short-duration dc current ($I > I_c$) and then comparing this response to those produced when ac currents are applied over the same time interval. The second method is a common electrical technique, where sample voltage taps are wound cylindrically at a constant pitch around the sample. This voltage signal is sent into a lock-in amplifier, where its magnitude and phase with respect to the reference current were found. A simple schematic of each technique is shown in Fig. 2.45.

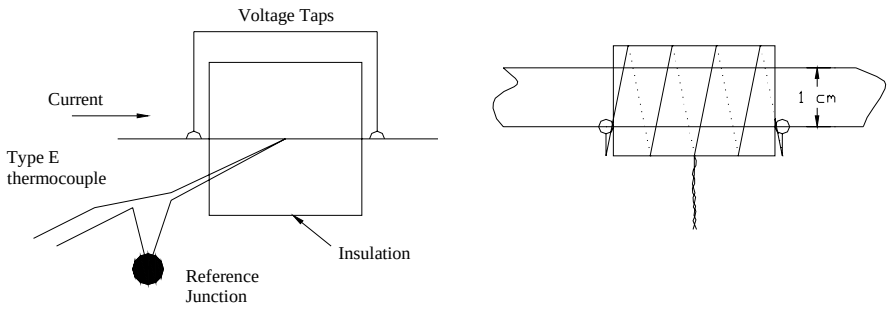

Fig. 2.45. Setup of thermal and electrical measurement of ac losses.

Figure 2.46 shows the thermal and electrical measurements of the ac losses for a YBCO sample with a critical current of 140 A. These results were compared to the Norris elliptical and thin-strip models to better understand the dependence of the losses on peak current. Since the measurements were slightly higher than either Norris model, an additional loss mechanism other than the hysteretic loss of the YBCO was suspected. To determine the additional loss mechanism, the role of the substrate in the presence of ac current was studied. Previous work on other nickel alloys such as Ni-Cr has shown that the ferromagnetic contribution to the ac losses from the substrate can be significant at low currents. Using a SQUID-based magnetometer, the magnetization loop for the Ni-5at.%W substrate was measured in the presence of an applied magnetic field parallel to the tape, which simulates the field that the substrate would see when ac currents are applied to the sample. By integrating this magnetization over the entire applied magnetic field cycle, the loss per cycle is obtained. Figure 2.47 shows the ferromagnetic loss for a Ni-5at.%W substrate with a nickel overlayer and without a nickel overlayer as a function of peak current, which was obtained by converting the applied field to the equivalent ac sample current.

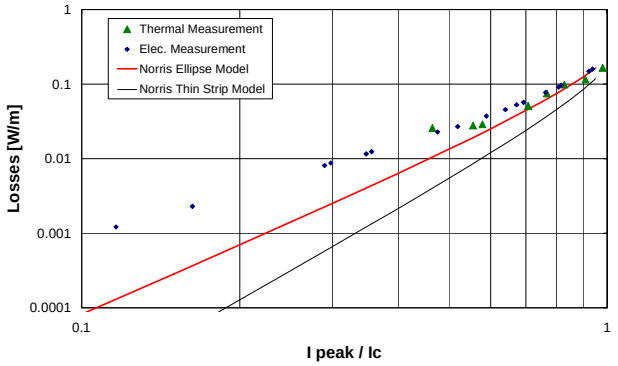

Fig. 2.46. Comparison of electrical/thermal measurements of ac losses for a YBCO RABiTS™ sample with an I_c of 140 A with Norris elliptical and thin strip model for hysteretic losses.

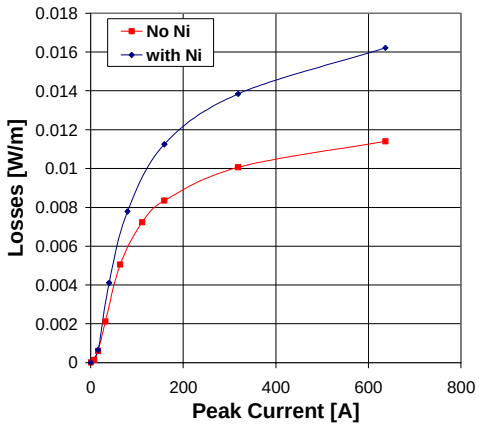

Fig. 2.47. Comparison of the ferromagnetic loss that was measured at 95 K between samples with and without nickel overlayers on a Ni-5 at.%W substrate.

When the ferromagnetic loss is added to the hysteretic loss associated with the Norris elliptical model, both the thermal and electrical measurements agree well with theory (Fig. 2.48). These results demonstrate the importance of the substrate in the ac losses as well as the uniformity of the critical current density of the conductor. This uniformity is an issue since the Norris elliptical model was a better fit to the experimental data than the Norris thin strip model despite the sample having a clear thin strip geometry with an width-to-thickness aspect ratio of 1000. Additional YBCO samples with different substrates will

be examined to observe the effect of substrates on the uniformity of the critical current density as well as the ferromagnetic losses.

When the ac losses for the sample without the nickel overlayer were measured, it was found that the Norris thin strip model plus the ferromagnetic losses of the substrate accounted for the measured ac loss, as shown in Fig. 2.49.

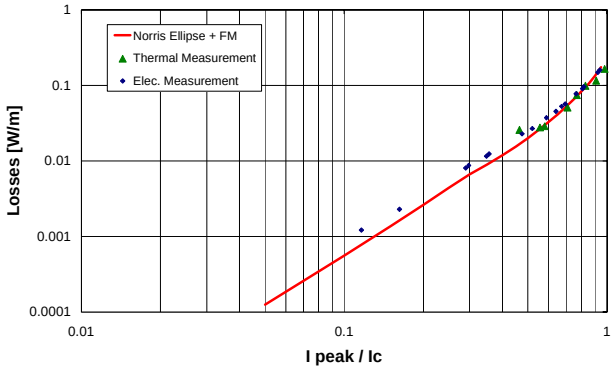

Fig. 2.48. Comparison of the measured ac losses to the modified Norris elliptical model where the ferromagnetic losses from the substrate have been added to the hysteretic losses.

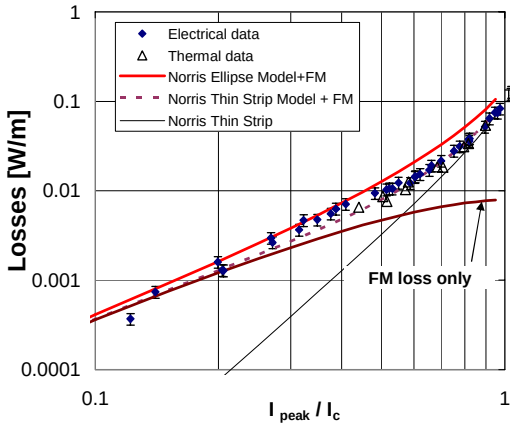

Fig. 2.49. Comparison of the electrical and thermal measurements of ac losses for a YBCO RABiTS™ sample with a critical current of 110 A with Norris elliptical and thin strip model for hysteretic losses.

While the switch from the Norris elliptical representation of the loss (Ni5at.%W with Ni) to the Norris thin strip representation (Ni5at.%W without Ni) coincided with the removal of the nickel overlayer, there is not enough evidence to suggest that a relationship between the two exists. Previous measurements of different YBCO conductor geometries by other groups have observed similar disagreement between data and the Norris models of the hysteretic superconducting loss. The difference was attributed to and proved to be the result of nonuniform critical current density across the sample width in some cases. Methods of characterizing the critical current density as a function of width are being pursued.

2.7 STRATEGIC RESEARCH—HIGH VOLTAGE AND DIELECTRICS STUDIES

I. Sauers, A. R. Ellis, D. R. James, A. Muller, and M. O. Pace

2.7.1. Conference on Electrical Insulation and Dielectric Phenomena (CEIDP)

D. R. James and I. Sauers attended the 2002 Conference on Electrical Insulation and Dielectric Phenomena (CEIDP) held October 2002. They presented three papers reporting their results on cable aging of HTS cables, high-voltage breakdown of epoxies and epoxy composites in liquid nitrogen, and vacuum surface flashover at cryogenic temperature. They also participated in several meetings, including the CEIDP board meeting, CEIDP technical program committee, Dielectrics and Electrical Insulation Society (DEIS) Adcom, and IEEE S-32-11 Gas Dielectrics Committee. They also met with several experts in the field of high voltage, dielectrics, and PD and discussed issues relevant to ongoing projects in HTS applications. I. Sauers also proposed hosting the 2005 CEIDP, which was accepted by the CEIDP Board. A number of papers at the conference were of particular interest and relevance to the ORNL high-voltage and dielectrics research. Specific technical areas of interest included dielectric materials, aging, PD, high-voltage breakdown, space charge effects, vacuum breakdown, liquids, and electric field and discharge modeling. One paper of note discussed the effect of filler size on breakdown strength of solid epoxy.

Nanometer particle fillers do not appear to reduce the breakdown strength as found for micron-sized filler particles while preserving mechanical strength. This finding could be important toward the development of solid materials for high-voltage cryogenic applications where fillers are required for thermal conduction as well as for mechanical strength but tend to lower dielectric strength.

A paper from the Swiss Federal Institute of Technology, Zurich, discussed simulation of small microcracks parallel to the electrical field in polymeric materials such as those due to mechanical stress in fiber-reinforced epoxy. The PD inception voltage decreases significantly as the diameter of the crack increases. Hence these type cracks are much less of a problem than spherical or elliptical voids often occurring. A paper discussed changes in dielectric response in glass-fiber reinforced epoxy due to debonding at the interface. Differential thermal expansion under local heating was proposed as the cause. Hence thermal contraction could also cause such effects, which are significant for cryogenic insulation. Prof. Naoki Hayakawa (Nagoya University, Japan) discussed the effects of bubbles in liquid nitrogen. He also performed experiments on the simultaneous application of thermal shock and high-voltage breakdown. Prof. Peter Morshuis (Delft University of Technology, The Netherlands) in a paper discussed the time delay for onset of PD in a void. This work is highly relevant to ORNL studies on voids in epoxy. James and Sauers also met with Dr. Toshikatsu Tanaka (Waseda University), who has organized a special issue of the *IEEE Transactions on Electrical Insulation* devoted to applications of cryogenic dielectrics to superconductivity.

2.7.2 Solid Dielectrics for HTS Applications

2.7.2.1 Flat Samples of Stycast 2850 KT

Breakdown strengths and PD onset and extinction voltages were measured for 1- and 5-mm flat samples of Stycast 2850 KT at room temperature. For comparison, Stycast 2850 FT was also studied. The FT and KT have the same resin and filler particles but differ mainly in size of the filler particle, the KT having much larger filler particles than the FT. Electrically, the KT has a much lower breakdown strength and PD onset than the FT. Table 2.7 shows the results for 1- and 5-mm-thick samples of KT and 5-mm samples of FT. The FT is greater than a factor of two higher in strength than the KT. Decreases in dielectric strength and PD onset were found for increasing epoxy thickness, an important consideration in the design of larger-scale devices.

Table 2.7. Partial discharge (PD) onset and breakdown (BD) for Stycast 2850[a]

Sample	PD onset (kV)	Charge (pC)	BD (kV ac, rms)
FT: 5-mm samples, PD onset > 11 kV/mm			
1	> 57.1		> 140.3
2	39.8	45	> 140.5
3	> 54.8		> 140.2
4	> 54.7		> 135.0
5	51.2	~1	
6	> 55.4		> 135.0
KT: 5-mm samples, PD onset = 5.7 kV/mm			
1	28.4	7	74.4
2	35	6	79
3	27	5	75.9
4	27	7	83.4
5	30–38	3–7	71.3
6	23	10	*b*
Ave	28.4		76.8
KT: 1-mm samples, PD onset > 8.85 kV/mm			
1	8.8		9.3
2	10	8–9	5.5
3	9.4	170–180	20.3
4	6.9		15.9
	8	16	
5	10	10–12	23.8
6	8	100–120	17
Ave	8.85		17.3[c]

[a]">" indicates flashover (i.e., the limit of the power-supply current or setup).
[b]Did not try to BD (PD pattern also shows arches).
[c]Excluded BD 5.5.

2.7.2.2 Simulated Defects in Solid Epoxy

Two types of defects were investigated: (1) defects due to poor mixing of the catalyst with the resin and (2) holes drilled into solid epoxy to simulate large voids. Table 2.8 shows the results of high-voltage tests performed on these simulated defective samples. The lowest PD onset and highest PD charge amplitudes were found for the case of a hole drilled at an angle representative of a randomly occurring irregular void in solid epoxy.

Table 2.8. Effect of defect type on partial discharge onset for 5-mm-thick samples

Sample #	Sample Description	PD onset (kV)	PD magnitude (pC) ICM	PD magnitude (pC) PD3	PD Ext. (kV)	Comments
12-11-02#KT1	Not deaired	13.7	14-16	14-16		near end of scan PD went off scale
		13.7	900-1000	700-800		repeat with gain change
		15.2	900-1200	750-1000	9.0	
12-11-02#KT2	Not deaired	10.0	1200-1300	1000-1100	8.0	
12-11-02#KT3	Not deaired	15.0	10-15	10-15		PD on after 30 seconds of scan intermittant
		18.0	8-10	8-10	1.0	PD constant
12-11-02#KT4	1/16" hole	5.2	650-900	750-900	3.0	PD came on at end of first scan
12-11-02#KT5	1/8" hole straight	9.3	2400-2500	1800	4.4	
12-11-02#KT6	1/8" hole at 60^{o} angle	5.2	1800-2400	1200-1500	3.2	PD on after 20 seconds

2.7.3 Effect of Particle Filler Size on Breakdown Strength

Studies were initiated on the effect of particle filler size on the breakdown strength of epoxy resin. Aluminum oxide particles of various sizes were mixed with the optically transparent resin Araldite 5808 (without catalyst) and subjected to ac ramp-to-failure voltages.

2.7.3.1 Partial discharge and breakdown in epoxy mixtures

Various epoxy/filler combinations have been tested for PD and ac breakdown in small (1- and 2-mm gap length) cast electrode samples. Generally, the two electrode gap lengths were tested for each mixture type. Samples were tested at room temperature in an oil bath to prevent external flashover. For PD measurements both PD inception and extinction voltage were determined for each sample, and the PD magnitude and phase-resolved patterns were recorded. In some cases the PD patterns observed were representative of internal voids. Following PD testing, each sample was subjected to a ramp-to-breakdown ac test. Dissections of some of the samples are planned in order to determine the presence of voids. A few of the mixtures have been tested over a wider range of gap lengths, ranging from 1 to 5 mm, to examine scaling issues in longer gap samples. Generally, the dielectric strength per millimeter decreases with increasing gap length. In addition, some of the samples showing higher room-temperature breakdown strengths will be tested at cryogenic temperatures.

2.7.3.2 Pressure effect of PD in voids in epoxy

The dielectric strength of solid epoxy samples seriously degrades when internal voids, present in the solid, are exposed to a high electric field. The voids occur as a result of bubbles formed during the pouring, mixing, and curing of the epoxy, leaving a pocket of gas in the solid. The voids have a lower dielectric strength than the surrounding solid and the electric field is generally intensified in the void due to the difference in permittivities between the gas in the void and surrounding solid dielectric. It is generally not known what the composition or the pressure of the gas is in the void. Since PD is a gas discharge phenomenon, that is, a discharge streamer propagating in the gas, it is important to establish when PD is likely to occur and if the observed PD patterns can be used as a diagnostic for the presence and nature of internal voids. To further examine this effect, a specially made sample was prepared containing an artificial 3.2-mm void with access to outside the sample to a gas-handling manifold (Fig. 2.50), permitting evacuation of the void and filling with a gas to a given pressure. Preliminary experiments on voids injected

with nitrogen or SF_6 have shown partial agreement with Paschen curves (for each gas), which govern the breakdown behavior of gases in uniform electric fields (Fig. 2.51). These studies are ongoing and should provide important data that can be used in diagnosing PD on HTS electrical equipment which use solid dielectric insulation.

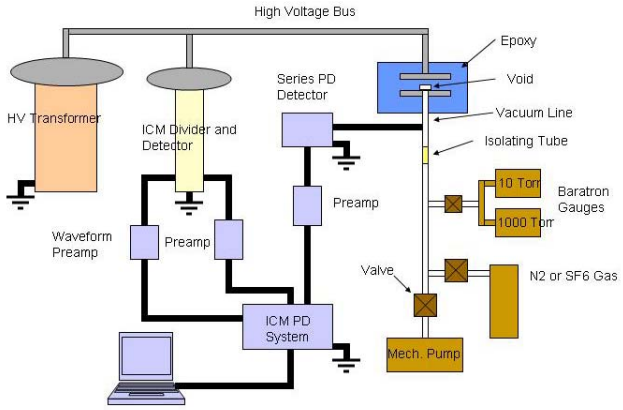

Fig. 2.50. Schematic layout of experiment to study the pressure effect of PD in artificial voids.

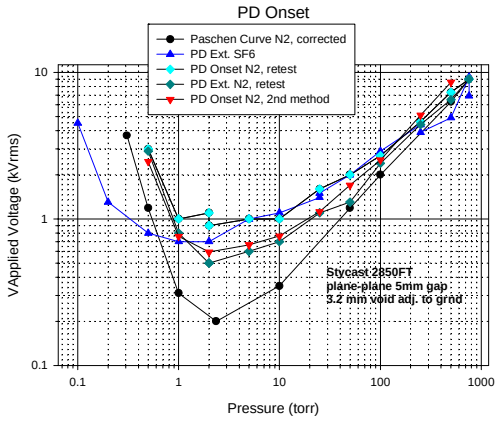

Fig. 2.51. Plot of onset and extinction voltages for nitrogen and SF_6 in a 3.2-mm void in epoxy adjacent to the ground electrode as a function of pressure. Also plotted is the nitrogen Paschen curve corrected for the particular void/electrode geometry used in the experiment.

2.7.4 Stycast 2850 KT Studies

Previous experiments on Stycast 2850 KT using catalyst 11 indicate that the epoxy is quite viscous, having a propensity for forming and retaining bubbles. Removal of bubbles is difficult, leading to a solid that contains voids, substantially reducing the breakdown strength of the material. Two approaches have been taken to potentially obviate this problem. The first was to use a de-airing agent, which reduces the surface tension to prevent bubbles from forming. The second approach was to use a different catalyst, 24LV, which appears to reduce the viscosity sufficiently to facilitate bubble removal during the pouring and casting process. Based on X-ray imaging and dissection of the samples, both approaches were found to be effective.

2.8 CRYOGENICS INITIATIVE

M. J. Gouge and J. A. Demko

The objective of this cryogenic industry partnership procurement is to accelerate the enabling technology for development of cryogenic cooling to obtain improved performance at or near the DOE Cryogenic Roadmap goals. The assessment report that the statement of work is based on is available at this website: http://www.ornl.gov/HTSC/pdf/CryoAssessRpt.pdf. This focused R&D effort will enhance the cryogenic system, enabling technology required for HTS electric applications, which can make a real impact on the reliability, security, and stability of America's electric transmission and distribution infrastructure.

The request for proposal for this HTS program cryogenics initiative was concurred with by DOE and was issued in late August 2002 with proposals due in November 2002. Technical evaluation of the multiple cryogenic initiative proposals was completed by a multi-laboratory team (ORNL, ANL, and LANL) in February 2003. The UT-Battelle procurement group used this to document the evaluation

results. UT-Battelle (ORNL), acting for DOE, selected three proposals for negotiation of an award to develop advanced cryogenic refrigeration systems for HTS power applications:

- Praxair, Inc., Danbury, Connecticut, will lead a team that includes CFIC, Inc., Troy, N.Y., and consultants from LANL and the National Institute of Standards and Technology. The team will develop pulse tube cryocoolers operating at 60 to 80 K over a power range of 300 to 1500 W. The award will be for a three-year period with 50% cost-sharing by the Praxair-led team.

- Cryomech, Inc., Syracuse, N.Y., will develop a GM cryocooler operating at 25 to 40 K and having a capacity of up to 200 W and a pulse tube cryocooler operating at 60 to 80 K and having a capacity of up to 300 W. The award will be for a three-year period with 50% cost-sharing by Cryomech.

- Stirling Technology Company (STC), Kennewick, Washington, will lead a team that includes Atlas Scientific, Inc., San José, California, the University of Wisconsin-Madison, and the National Institute of Standards and Technology. The team will develop pulse tube cryocoolers operating at 50 to 80 K at a power level of up to of 300 W. The award will be for a three-year period with 50% cost-sharing by the STC-led team.

The total effort is estimated at about $10 M over a three-year period with an equal cost sharing between DOE and the industrial teams. Contracts were negotiated with Praxair and Cryomech in the late summer of 2003, and a contract is planned with the STC team to commence work in 2004. A visit was made to CFIC, Inc. (part of the Praxair-led team) in June 2003 to review their pressure wave generator technology and Qdrive line of research cryocoolers. CFIC's TwinSTAR™ pressure wave generators are valveless electroacoustic devices, like extremely powerful audio speakers, that produce high-intensity acoustic power (alternating pressure and volume flow). Pressure amplitudes up to 25% of mean pressure and volume amplitudes of 300 L/s are possible with matched, pressurized loads. TwinSTARs are balanced, high-efficiency resonant drivers offering nonwearing, oil-free, low-noise and low-vibration operation at frequencies of 30 to 60Hz.

A short status report of the DOE Cryogenics Initiative was given at the start of the HTS systems session at the DOE Annual Peer Review in July 2003. In late September, meetings were conducted with Praxair and Cryomech technical staff at the Cryogenic Engineering Conference to discuss the status of their recently initiated R&D. Kick-off visits are scheduled by ORNL staff (Gouge and Demko) to Praxair and Cryomech (both in New York) in early November.

2.9 SPI OVERSIGHT/READINESS REVIEWS

ORNL has been asked to coordinate a DOE initiative to support the SPI program to help ensure that SPI demonstration projects go as planned via a series of phased readiness reviews. The focus is on collaboration with the SPI team to identify potential failure modes; issues involving cryogenic temperatures and high voltage are major concerns. Expertise will be provided as needed from national laboratories, universities, and consultants. M. J. Gouge and Jim Daley (DOE) provided an overview of the proposed SPI oversight program at the January 2003 DOE Wire Development Workshop to a subset of the meeting participants involved with SPI projects. M. J. Gouge and Don Gubser (Naval Research Laboratory) participated in a 1-day review of the HTS coil and associated support structure for the 500-mm-bore, reciprocating magnetic separator project at DuPont Superconductivity on March 10, 2003. M. J. Gouge and Russ Eaton visited Waukesha Electric Systems in June 2003 to review the progress on assembly and cooldown of the 5/10 MVA transformer and to go over the plans for high-current and high-voltage electrical testing given the known issue of low PD inception voltage in the HTS phase sets. M. J. Gouge and several other scientists from LANL, ANL, and CAPS participated in a 1-day technical advisory committee meeting and a 2-day conceptual design review of the HTS Matrix Fault Current Limiter project at SuperPower, Inc., on June 10 through 12 (this project was subsequently initiated as an SPI project in

July). A detailed list of reviewer comments (chits) was assembled by SuperPower that will be tracked through focused development plans and subsequent design reviews. A short status report of the SPI oversight program was given at the start of the HTS systems session at the DOE Annual Peer Review in July 2003. M. J. Gouge (ORNL) and Paul Bakke (DOE) participated in the Conceptual Design Review of the General Electric 7A6 HTS Generator on July 30 and 31 and provided technical feedback to GE program management.

2.10 ENHANCEMENTS TO THE MULHOLLAND MODEL IN 2003

B. McConnell and T. Sheahen

During this fiscal year, a number of improvements have been made to the Mulholland Model and to the documentation that accompanies it, known as the "Mulholland Report." The revised model and write-up are found at the "Reports and Roadmaps" section of the ORNL web page (http://www.ornl.gov/HTSC). As indicated on the revised contents page, the model differences are described in Appendices 2, 16, 17, 18, 19, and the new Appendix 20 on macros. The revised model is found at the following link: (http://www.ornl.gov/HTSC/pdf/HTSMarketBetaRev1). The principal direction of all these changes has been to make the model easier for the analyst to use while carrying out his or her own study of issues related to HTS devices.

The Mulholland Model has been designed to be a tool to aid in market analysis. However, when first publicized in draft form in early 2000, many people got the impression the model was a mystic oracle of absolute and definite answers. By the Applied Superconductivity Conference of summer 2000, we tried to emphasize the "tool" aspect and disparage the "oracle" image but many prospective users were still reticent to dive in and carry out all the necessary steps to utilize it properly. Thus there was an inertia associated with this set of numbers that came from a preliminary calculation whose intent had been to illustrate the general idea.

Starting in 2001, the Mulholland Model has been revised with the user in mind. Bob Lawrence & Associates is now the principal contractor working on this model along with ORNL. As of summer 2003, there are now a number of exercises that can be carried out by the model (using "Macros" in Microsoft Excel). These exercises vary certain parameters of the model, such as

- the escalation rate for growth of electricity demand in future years,
- the rate of replacing aging equipment with HTS devices,
- the improvement of wire performance,
- the improvement of cryogenic efficiency, and
- the market penetration model:
  - the saturation level of ultimate market share captured and
  - the year in which the sales of each device first becomes profitable.

Note that the variation of timing in the market penetration model is a very important parameter (if a realistic scenario is to be calculated), and this variation has now been automated. For example, if an analyst changes the cryogenic load associated with some HTS device, a few mouse-clicks will yield a plausible and self-consistent estimate of that device's market-penetration trajectory.

Analysts can download and use this model to aid their own efforts, with almost none of the difficulties they faced with the initial model. Since some things can be "obvious" to the developer of a program but obscure to a new user, we stand ready to guide analysts through any points of confusion that may occur. It is emphatically our intent that many different users try out the Mulholland Model, adapt it for their own purposes, and discover what a useful tool it can be. For example, with other inputs fixed, the impact of growth in electricity demand can be run iteratively to generate a graph (see Fig. 2.52).

Other Excel macros also facilitate analytic studies. Ultimately, a more extensive and probably quite different model that somehow includes non-energy savings benefits needs to be developed. Fault-current

limiters and magnetic separation units have markets that are not driven by energy savings. Other needed improvements include the conductor-cost-projection models. Specifically, the Mulholland model could be adapted to take advantage of more realistic numbers that provide an accurate link between production quantity and conductor $/kA-m.

Also, the base engineering models for each major device (motors, generators, ac cables, and transformers) need to be updated. Here is one example: The model supposes that ac HTS cables could someday supplant 115–250 kV of overhead for new growth; cost data is based on 1998 knowledge. By now we know enough about the cost of inductive compensation and capital so that the economics are unfavorable here; yet the model still includes it as though the market is realistic. A more realistic alternative for cables would be to include the very low impedance and dc applications. Similarly, revisions for the other devices are constantly evolving as experience by SPI partners produces more accurate data. Indeed, given the complete ignorance about high current ac-dc inverter/rectifier costs, the DC HTS cable is only marginally capable of modeling at this level.

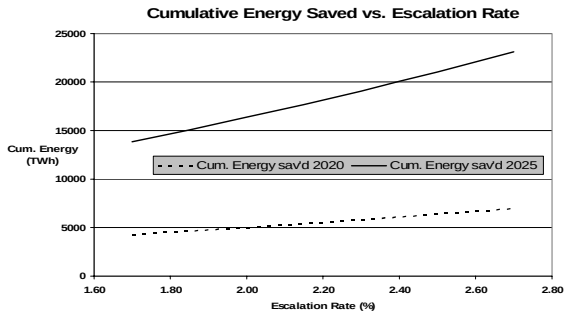

Fig. 2.52. Sample graph showing the impact of the growth in the demand for electricity.

Feedback on the model from users would be greatly appreciated. If funding is available, we would be glad to help users run the model for their particular inputs. Please provide feedback or questions via e-mail to either Ben McConnell, (865) 576-2733, mcconnellbw@ornl.gov or Tom Sheahen, (301) 387-2522, tsheahen@alum.mit.edu.

3. Summary of Technology Partnership Activities

3.1 BACKGROUND

Oak Ridge National Laboratory (ORNL) is a key participant in the U.S. Department of Energy's (DOE's) national effort on electric power applications of high-temperature superconductivity (HTS). ORNL has formed effective teams that combine the resources of the Laboratory with the entrepreneurial drive of private companies. New technology partnership mechanisms, a feature of the ORNL Superconducting Technology Program for Electric Power Systems since its inception in 1988, have resulted in 42 superconductivity "pilot center" cooperative agreements and 10 cooperative research and development agreements (CRADAs). Eight cooperative agreements and two interagency agreements were active during FY 2003. In addition, licensing agreements, joint inventions, and joint publications with the private industry partners have ensured that there *is* technology transfer throughout the program.

Technology partnering on Laboratory-industry teams can occur in several ways. In the ORNL program, the cooperative development level of technology partnering is emphasized: joint Laboratory-industry teams work on problems that (1) require combined resources and expertise and (2) have a clear objective of precompetitive research and technology development. For the project to succeed, each partner depends on the success of the other. Most of the cooperative projects with private industry and the Laboratory precompetitive research and development (R&D) projects involve developing key technology in which commercialization of the results is expected to occur after a minimum of 3 to 5 years.

3.2 RELATIONSHIP TO THE DOE MISSION

The ORNL program mission is that of its program sponsor, DOE's Office of Electric Transmission and Distribution Superconductivity Program: to develop the technology base necessary for industry to proceed to commercialization of electric energy applications of HTS. HTS will enable new energy-efficient motors, transformers, and transmission lines and will also provide electric power equipment manufacturers with strategic technology for global competitiveness. Electric utilities can defer acquisition of new transmission rights-of-way with successful introduction of superconducting cables. System stability and protection will be enhanced with the introduction of fault-current limiters. Distributed utility systems in the future, which will include distributed generation systems, will benefit from the small size and light weight of the next generation of electric power equipment. In addition, oil-free power transformers and cables will provide a cost-effective, more environmentally friendly option for the utility sector.

3.3 FUNDING

DOE funding for the ORNL program and a summary of funds-out cooperative agreements in 2003 are shown in Tables 3.1 and 3.2. Funds-out to industry, universities, and other federal agencies (e.g., the National Institute of Standards and Technology) was more than $4 million in FY 2003.

3.4 TECHNOLOGY PARTNERSHIP APPROACH

An interdisciplinary approach uses many of the resources available at ORNL to meet the program goals for joint Laboratory-industry development of HTS technology for electric power applications. The superconductivity agreement mechanism interlinks R&D projects with industry and universities that optimize utilization of facilities, expertise, and program resources for the benefit of all participants. This program also coordinates the ORNL activities with the other national laboratories, government agencies, university centers, and industry groups.

Cooperative agreements ensure that technology development is industry-driven. The ORNL Office of Technology Transfer and Economic Development and patent counsel work together to place these agreements. Where appropriate, these efforts are coordinated with projects within ORNL that are funded by the DOE Office of Science as well as Work for Others and ORNL Laboratory Director's R&D Fund projects.

Effective funds-out to industry is used to supplement industry cost share. In FY 2003, $4 million in funds-out to industry and universities was provided through cooperative agreements and subcontracts. To keep industry involved from the start of the program and to ensure commercialization potential, all of these technology-partnering mechanisms are augmented by CRADAs, user agreements, and licensing activities.

Responsiveness to American industry has high priority in this program. An ORNL ad hoc technical review committee, consisting of a project manager, a scientific coordinator, a manager for conductor development, and a manager for applications development, reviews all inquiries from industry and recommends projects for possible funding. This review ensures that (1) the proposed work fits the program mission, (2) the work is collaborative, (3) there is legitimate commercial interest, and (4) the work is feasible. Substantial private-sector cost share is required on cooperative agreements.

ORNL provides support to the DOE Headquarters (DOE-HQ) Superconductivity Program for Electric Power Systems by identifying, guiding, and monitoring R&D at ORNL and ORNL subcontractor sites and by performing coordination, analysis, and planning of activities related to the national program.

ORNL works with the other program laboratories to address such issues as communication among program participants, workshop and meeting implementation, planned competitive solicitations and superconductivity agreements, and coordination of technical and economic assessments. ORNL leads the Superconductivity Partnerships with Industry Technical Review Committee and manages the Cryogenics Initiative subcontracts on behalf of all the program stakeholders.

Table 3.1. Superconducting Technology Program funding: authorization and outlay by fiscal year

Funding type	New budget authorization/outlay ($K)				
	1999	**2000**	**2001**	**2002**	**2003**
Direct scientific and technical[a]	5,416	5,616	8,989	6,494	7,653
Management and outreach	400	400	400	420	467
Subtotal—ORNL	**5,816**	**6,016**	**9,389**	**6,914**	**8,120**
Subcontracts	3,244	4,099	4,680	3,330	4,045
Funds-out cooperative agreements[b]	795	585	945	370	485
Total program	9,855	10,700	15,014	10,614	12,650

[a]Includes ORNL capital equipment ($1.4 M in FY 2001 for Accelerated Coated Conductor Laboratory).
[b]Includes interagency agreements (National Institute of Standards and Technology, National Aeronautics and Space Administration, and the National Science Foundation).

3.5 PROGRAM INVENTIONS

A summary of the new invention disclosures for FY 2003 is shown in Table 3.3. Patents issued in FY 2003 are shown in Table 3.4, and all patents issued since 1994 are shown in Table 3.5.

Table 3.2. Superconductivity Program summary of cooperative agreements as of September 30, 2003

Participant	Approved term	Type[a]	Total agreement cost share ($K)			Technology area
			By DOE		By industry	
			To ORNL	To industry		
American Superconductor	4/5/01–4/4/05	C	2,400	0	2,400	HTS conductors for electric power applications, BSCCO-2223 Wire Development Group, and YBCO wires
General Electric Company	8/2/02–7/31/05	C	650	0	650	Design and development of a 100-MVA HTS generator
MicroCoating Technologies	5/15/03–5/14/05	C	200	0	100	Demonstration of high current density YBCO films on CCVD buffers
National Institute of Science and Technology						
Gaithersburg	12/1/00–12/31/03	IAG	0	610	610	YBCO phase diagram support
Boulder	3/98–2/29/04	IAG	0	1,102	1,102	Electromechanical properties for superconductor applications
Neocera	8/1/2001–9/30/03	FO	250	205	260	Pulsed e-beam deposition as a viable method for HTS coated conductor development
Oxford Instruments	1/94–1/31/04	C	1,450	0	1,675	Develop technology for dip-coated BSCCO-2212 wire and RABiTS™
Southwire Company	2/1/97–9/30/05	FO	12,066	500	12,631	Develop HTS cable technology
SuperPower, Inc.	10/8/02–10/7/04	C	100	0	100	Produce high current density YBCO coated conductors
Waukesha Electric Systems	6/15/97–9/30/04	FO	3,197	250	2,556.4	HTS transformer
Total active			20,213	2,667	22,084.4	
Total completed			17,124	6,330.6	22,236.7	
TOTALS			37,337	8,997.6	44,321.1	

[a]C = CRADA, IAG = interagency agreement, FO = funds-out

Table 3.3. Invention disclosures during FY 2003

ID No.	Subject	Submitted by
1155C	New Precursor Route to Produce Epitaxial Oxide Buffers on Biaxially Textured Metal and Alloy Substrates (CRADA)	M. Paranthaman, S. Sathyamurthy, T. Aytug, and M. W. Rupich (American Superconductor)
1204	Copper-Based Textured Substrates for Application with a Biaxially Textured Buffer Layer	A. Goyal
1205	Textured Substrates for a Range of Applications	A. Goyal
1206	Biaxially Textured Copper-Based Substrates	A. Goyal
1218	Method of Fabricating Copper-Based, Textured, Ternary Alloy Substrates for a Range of Applications	A. Goyal
1287	Biaxially Textured Overlayers for Conducting Buffer Layer Architectures	M. Paranthaman and T. Aytug
1323	Overlayers for Ni-Alloy Based YBCO Coated Conductors	M. Paranthaman and T. Aytug

Table 3.4. Patents issued in FY 2003

Patent No.	Date issued	Title
6,468,591	October 22, 2002	Method for Making MgO Buffer Layers on Rolled Nickel or Copper as Superconductor Substrates
6,486,100 B1	November 26, 2002	Method for Preparing Preferentially Oriented, High Temperature Superconductors Using Solution Reagents
6,555,256, B1	April 29, 2003	Method of Depositing an Electrically Conductive Oxide Film on a Textured Metallic Substrate and Articles Formed Therefrom
6,599,346 B2	July 29, 2003	Biaxially Textured Articles Formed by Powder Metallurgy
6,602,313 B2	August 5, 2003	Biaxially Textured Articles Formed by Powder Metallurgy
6,607,839 B2	August 19, 2003	Biaxially Textured Articles Formed by Powder Metallurgy
6,610,413	August 26, 2003	Biaxially Textured Articles Formed by Powder Metallurgy
6,610,414	August 26, 2003	Biaxially Textured Articles Formed by Powder Metallurgy
6,617,283 B2	September 9, 2003	Method of Depositing an Electrically Conductive Oxide Buffer Layer on a Textured Substrate and Articles Formed Therefrom

Table 3.5. Cumulative listing of patents

Patent No./ID No.	Date issued	Title
5,357,756 (1185-X)	October 25, 1994	Bipolar Pulse Field for Magnetic Refrigeration
5,395,821 (1039-X)	March 7, 1995	Method of Producing Pb-Stabilized Superconductor Precursors and Method of Producing Superconductor Articles Therefrom
5,525,583 (1471-X) (with AMSC)	June 11, 1996	Superconducting Magnetic Coil
5,546,261	August 13, 1996	Hermetically Sealed Superconducting Magnet Motor
5,646,097	July 8, 1997	Method of Fabricating a (1223) Tl-Ba-Ca-Cu-O Superconductor
5,739,086 (1640-X)	April 14, 1998	Structures Having Enhanced Biaxial Texture and Method of Fabricating Same
5,741,377 (1640-X)	April 21, 1998	Structures Having Enhanced Biaxial Texture and Method of Fabricating Same
5,830,828 (1193-X)	November 3, 1998	Process for Fabricating Continuous Lengths of Superconductor
5,846,912 (1512-X)	December 8, 1998	Method for Preparation of Textured $YBa_2Cu_3O_x$ Superconductor
5,898,020 (1640-X)	April 27, 1999	Structures Having Enhanced Biaxial Texture and Method of Fabricating Same
5,958,599 (1640-X)	September 28, 1999	Structures Having Enhanced Biaxial Texture
5,964,966	October 12, 1999	Method of Forming Biaxially Textured Alloy Substrates and Devices Thereon
5,968,877 (18-19)	October 19, 1999	High-T_c YBCO Superconductor Deposited on Biaxially Textured Ni Substrate
5,972,847 (458)	October 26, 1999	Method for Making High-Critical-Current-Density $YBa_2Cu_3O_7$ Superconducting Layers on Metallic Substrates.
6,055,446 (1193)	April 25, 2000	Continuous Lengths of Oxide Superconductors
6,077,344 (223)	June 20, 2000	Sol-Gel Deposition of Buffer Layers on Biaxially Textured Metal Substances
6,106,615 (368)	August 22, 2000	Method of Forming Biaxially Textured Alloy Substrates and Devices Thereon
6,114,287 (534) (HTSPC-023)	September 5, 2000	Method of Deforming a Biaxially Textured Buffer Layer on a Textured Metallic Substrate and Articles Therefrom
6,150,034 (467)	November 21, 2000	Buffer Layers on Rolled Nickel, or Copper as Superconductor Substrates
6,156,376 (467)	December 5, 2000	Buffer Layers on Metal Surfaces having Biaxial Texture as Superconductor Substrates
6,159,610 (467)	December 12, 2000	Buffer Layers on Metal Surfaces having Biaxial Texture as Superconductor Substrates
6,180,570 B1 (312)	January 30, 2001	Biaxially Textured Articles Formed by Plastic Deformation
6,256,521 B1 (1784, new 148)	July 3, 2001	Preferentially Oriented, High Temperature Superconductors by Seeding and a Method for Their Preparation
6,261,704 B1 (218)	July 17, 2001	MgO Buffer Layers on Rolled Nickel or Copper as Superconductor Substrates

Table 3.5. Cumulative listing of patents (continued)

Patent No./ID No.	Date issued	Title
6,70,908 B1 (734)	August 7, 2001	Rare Earth Zirconium Oxide Buffer Layers on Metal Substrates
6,286,194 B (1193)	September 11, 2001	Apparatus for Fabricating Continuous Lengths of Superconductor
6,296,701 B1 (296)	October 2, 2001	Method of Depositing An Electrically Conductive Oxide Film on a Textured Metallic Substrate and Articles Formed Therefrom
6,331,199 B1 (316.1)	December 18, 2001	Biaxially Textured Articles Formed by Powder Metallurgy
6,375,768 B1 (312)	April 23, 2002	Method for Making Biaxially Textured Articles by Plastic Deformation
6,385,835 B1 (Div of 5830828)	May 14, 2002	Apparatus for Fabricating Continuous Lengths of Superconductor
6,399,154 B1 (734)	June 4, 2002	Laminate Article
6,440,211 B1 (649)	August 27, 2002	Method of Depositing Buffer Layers on Biaxially Textured Metal Substrates
6,447,714 B1 (316.0)	September 10, 2002	Method for Forming Biaxially Textured Articles by Powder Metallurgy
6,451,450 B1 (749)	September 17, 2002	Method of Depositing a Protective Layer over a Biaxially Textured Alloy Substrate and Composition Therefrom
6,468,591 (218)	October 22, 2002	Method for Making MgO Buffer Layers on Rolled Nickel or Copper as Superconductor Substrates
6,486,100 B1 (1784, new 148)?	November 26, 2002	Method for Preparing Preferentially Oriented, High Temperature Superconductors Using Solution Reagents
6,555,256, B1	April 29, 2003	Method of Depositing an Electrically Conductive Oxide Film on a Textured Metallic Substrate and Articles Formed Therefrom
6,599,346 B2 (316.3)	July 29, 2003	Biaxially Textured Articles Formed by Powder Metallurgy
6,602,313 B2 (316.2)	August 5, 2003	Biaxially Textured Articles Formed by Powder Metallurgy
6,607,839 B2 (316.9)	August 19, 2003	Biaxially Textured Articles Formed by Powder Metallurgy
6,610,413 (316.5)	August 26, 2003	Biaxially Textured Articles Formed by Powder Metallurgy
6,610,414 (316.11)	August 26, 2003	Biaxially Textured Articles Formed by Powder Metallurgy
6,617,283 B2 (889)	September 9, 2003	Method of Depositing an Electrically Conductive Oxide Buffer Layer on a Textured Substrate and Articles Formed Therefrom

4. Events, Honors, and Awards

4.1 TWO ORNL SUPERCONDUCTIVITY PAPERS AMONG "MOST HIGHLY CITED" SINCE 1995

Two ORNL papers are among the "most highly cited" since 1995 in the scientific journal *Physica C: Superconductivity*, according to the citation index "Essential Science Indicators":

M. Paranthaman, A. Goyal, F. A. List, E. D. Specht, D. F. Lee, P. M. Martin, D. M. Kroeger, Q. He, D. K. Christen, D. P. Norton, and J. D. Budai, "Growth of Biaxially Textured Buffer Layers on Rolled-Ni Substrates by Electron Beam Evaporation," *Physica C: Superconductivity* **275** (3–4), 266–72 (20 February 1997).

H. M. Christen, H. Y. Zhai, C. Cantoni, M. Paranthaman, B. C. Sales, C. Rouleau, D. P. Norton, D. K. Christen, and D. H. Lowndes, "Superconducting Magnesium Diboride Films with $T_c \approx 24$ K Grown by Pulsed Laser Deposition with In Situ Anneal," *Physica C: Superconductivity* **353** (3–4), 157–61 (15 May 2001).

These are the only papers among the group of 14 that represent the work of researchers at a U.S. national laboratory that is funded by the DOE Office of Energy Efficiency and Renewable Energy. A listing of the most highly cited papers published in *Physica C: Superconductivity* since 1995 may be found at: http://www.physicsconnect.com/condensed/mostcited_physc.htm.

4.2 SUPERPOWER, INC., AND ORNL EXECUTE A NEW CRADA

SuperPower, Inc., of Schenectady, N.Y., and ORNL executed a CRADA to develop second-generation HTS technologies. They signed the CRADA on October 10, 2002 (Fig. 4.1). In the first phase of the project, ORNL will provide the Oak Ridge RABiTS™ textured template to SuperPower so that SuperPower can demonstrate the feasibility of using its proprietary techniques to grow high-current superconductor coatings on RABiTS™. With the execution of this CRADA, SuperPower's second-generation HTS program is now strongly supported by collaborations with all three major national laboratories that are spearheading the DOE HTS development projects. The CRADA takes advantage of SuperPower's unique capability to grow the superconductor on textured templates using two different reel-to-reel processes: pulsed laser deposition and metal-organic chemical vapor deposition. Through this new partnership the two groups will work to help achieve the DOE program vision of a low-cost, high-performance YBCO coated conductor that would offer significant reductions in electrical losses and operating costs as well as increased power transfer capacity.

Fig. 4.1. Pictured at the SuperPower, Inc., CRADA-signing ceremony are (left to right) "Selva" Selvamanickam and Phil Pellegrino (SuperPower, Inc.), Bill Madia (ORNL), and George Malosh (DOE-ORO).

4.3 SOUTHWIRE MANAGEMENT TEAM VISITS ORNL

ORNL's key partner in superconducting cable research visited ORNL for tours and discussions on November 19 (Fig. 4.2). The Southwire Company CEO and president, Stuart Thorn, and the president of Southwire's business development division, Lee Richards, visited ORNL for the first time. In addition to visiting the cable research facilities in the Fusion Energy Division, the Southwire team toured a broad spectrum of materials processing and characterization labs in the Metals and Ceramics Division.

Fig. 4.2. Vinod Sikka of ORNL's Metals and Ceramics Division (with sample) speaking with (left to right) Steen Christensen (NKT Cable Company, Denmark), and R. L. Huey, Jr., Stuart Thorn, and Lee Richards (Southwire).

4.4 SUMMER 2003 UNDERGRADUATE INTERNS

The ORNL Superconductivity Program again participated in the summer intern programs conducted by Oak Ridge Institute for Science and Education. Following are the names of our summer interns and their mentors:

Name	College	ORNL Mentor
Emily Diane Miller	Juniata College	David Christen/Rich Kerchner
Daniel Deschenes	California State University, Fresno	Isidor Sauers
Carl Hippner	Embry-Riddle Aeronautical University, Daytona	Patrick Martin
Richard Kinch	University of Puerto Rico	Amit Goyal
Steven Scruggs	University of Houston	M. Parans Paranthaman

4.5 ORNL RESEARCHER AWARDED PRIZE

Claudia Cantoni of ORNL's Condensed Matter Sciences Division won the European Society for Applied Superconductivity's Oral Contribution Prize at the 6th European Conference on Applied Superconductivity, held September 14–18, 2003, in Sorrento, Napoli, Italy (Fig. 4.3).

Fig. 4.3. Claudia Cantoni, of ORNL's Condensed Matter Sciences Division.

5. Presentations/Publications

PUBLISHED

Agassi, D., D. K. Christen, and S. J. Pennycook, "Flux Pinning and Critical Currents at Low-Angle Grain Boundaries in High-Temperature Superconductors," *Appl. Phys. Lett.* **81** (15), 2803–2805 (2002).

Andreone, A., E. Di Gennaro, G. Lamura, M. Salluzzo, A. Purnell, L. F. Cohen, L. Hao, J. Gallop, C. Cantoni, and M. Paranthaman, "A Study on the Nonlinear Microwave Electrodynamic Response of e-Beam Evaporated MgB_2 Superconducting Thin Films," *Supercond. Sci. Technol.* **16**, 260–63 (2003).

Aytug, T., A. Goyal, N. Rutter, M. Paranthaman, J. R. Thompson, H. Y. Zhai, and D. K. Christen, "High Critical Current Density $YBa_2Cu_3O_{7-}$ Coatings on $LaMnO_3$-Buffered Biaxially Textured Cu Tapes for Coated Conductor Applications," *J. Mater. Res.* **18** (4), 872–77 (2003).

Aytug, T., M. P. Paranthaman, B. W. Kang, D. B. Beach, S. Sathyamurthy, E. D. Specht, D. F. Lee, R. Feenstra, A. Goyal, D. M. Kroeger, K. J. Leonard, P. M. Martin, and D. K. Christen, "Reel-to-Reel Continuous Chemical Solution Deposition of Epitaxial Gd_2O_3 Buffer Layers on Biaxially Textured Metal Tapes for the Fabrication of $YBa_2Cu_3O_{7-\delta}$ Coated Conductors," *J. Am. Ceram. Soc.* **86** (2), 257–65 (2003).

Aytug, T., M. Paranthaman, S. Kang, H. Y. Zhai, H. M. Christen, C. E. Vallet, S. Sathyamurthy, A. Goyal, and D. K. Christen, "$LaMnO_3$: A Single Oxide Buffer Layer for High-J_c $YBa_2Cu_3O_{7-\delta}$ Coated Conductors," *IEEE Transactions on Applied Superconductivity* **13** (2), 2661–64 (2003).

Bhuiyan, M. S., M. Paranthaman, S. Sathyamurthy, T. Aytug, S. Kang, D. F. Lee, A. Goyal, E. A. Payzant, and K. Salama, "MOD Approach for the Growth of Epitaxial CeO_2 Buffer Layers on Biaxially Textured Ni-W Substrates for YBCO Coated Conductors," *Supercond. Sci. Technol.* **16**, 1305–1309 (2003).

Cantoni, C., D. K. Christen, A. Goyal, L. Heatherly, F. A. List, G. W. Ownby, D. M. Zehner, H. M. Christen, and C. M. Rouleau, "Growth of Oxide Seed Layers on Ni and Other Technological Interesting Metal Substrates: Issues Related to Formation and Control of Sulfur Superstructures for Texture Optimization," *IEEE Transactions on Applied Superconductivity* **(13)** 2, 2646–50 (2003).

Cantoni, C., D. K. Christen, M. Varela, J. R. Thompson, S. J. Pennycook, E. D. Specht, and A. Goyal, "Deposition and Characterization of $YBa_2Cu_3O_{7-\delta}/LaMnO_3/MgO/TiN$ Heterostructures on Cu Metal Substrates for Development of Coated Conductors," *J. Mater. Res.* **18** (10), 2387–2400 (2003).

Cantoni, C., D. K. Christen, L. Heatherly, F. A. List, A. Goyal, G. W. Ownby, and D. M. Zehner, "Control of the Sulfur C (2 × 2) Superstructure on {100}<100>Textured Metals for RABiTS Applications," book chapter, pp. 17–32 in *Processing of High Temperature Superconductors*, CT140, American Ceramic Society (2003).

Cheggour, N., J. W. Ekin, C. C. Clickner, D. T. Verebelyi, C. L. H. Thieme, A. P. Malozemoff, R. Feenstra, A. Goyal, and M. Paranthaman, "Transverse Compressive Stress Effect in Y-Ba-Cu-O Coatings on Biaxially Textured Ni and Ni-W Substrates," *IEEE Transactions on Applied Superconductivity* **13** (2), 3530–33 (2003).

Cheggour, N., J. W. Ekin, C. C. Clickner, R. Feenstra, A. Goyal, M. Paranthaman, and N. Rutter, "Effect of Transverse Compressive Stress on Transport Critical Current Density of Y-Ba-Cu-O Coated Ni and Ni-W RABiTS Tapes," book chapter, pp. 157–70 in *Processing of High Temperature Superconductors*, CT140, American Ceramic Society (2003).

Demko, J. A., J. W. Lue, M. J. Gouge, D. Lindsay, M. Roden, D. Willen, M. Daumling, J. E. Fesmire, and S. D. Augustynowicz, "Cryostat Vacuum Thermal Considerations for HTS Power Transmission Cable Systems," *IEEE Transactions on Applied Superconductivity* **13** (2), 1930–33 (2003) .

Duckworth, R. C., J. R. Thompson, M. J. Gouge, J. W. Lue, A. O. Ijaduola, D. Yu, and D. T. Verebelyi, "Transport ac Loss Studies of YBCO Coated Conductors with Nickel Alloy Substrates," *Supercond. Sci. Technol.* **16**, 1294–98 (2003).

Duckworth, R. C., J. W. Lue, D. F. Lee, R. Grabovickic, and M. J. Gouge, "The Role of Nickel Substrates in the Quench Dynamics of Silver Coated YBCO Tapes," *IEEE Transactions on Applied Superconductivity* **13** (2), 1768–71 (2003).

Fisher, P. W., M. J. Cole, J. A. Demko, C. A. Foster, M. J. Gouge, R. W. Grabovickic, J. W. Lue, and J. P. Stovall, "Design, Analysis, and Fabrication of a Tri-Axial Cable System," *IEEE Transactions on Applied Superconductivity* **13** (2), 1938–41 (2003).

Gapud, A. A., D. K. Christen, J. R. Thompson, and M. Yethiraj, "Electrical Transport, Magnetic, and Structural Properties of the Vortex Lattice of V_3Si in the Vicinity of the Peak Effect," *Phys. Rev. B* **67** (10), 104516-1–104516-7 (2003).

Gapud, A. A., D. K. Christen, J. R. Thompson, and M. Yethiraj, "Electrical Transport, Magnetic, and Structural Properties of the Vortex Lattice in Superconducting V_3Si," *Physica B* **329–333**, 1363–64 (2003).

Gouge, M. J., M. J. Cole, J. A. Demko, P. W. Fisher, C. A. Foster, R. Grabovickic, D. T. Lindsay, J. W. Lue, M. L. Roden, and J. C. Tolbert, "High-Temperature Superconducting Tri-Axial Power Cable," *Physica C* **392–396**, 1180–85 (2003).

Goyal, A., W. Wong-Ng, M. Murakami, and J. Driscoll, editors, *Processing of High Temperature Superconductors*, (Ceramic Transactions, Volume 140), proceedings of the Processing of High Temperature Superconductors Symposium held during the Annual Meeting of The American Ceramic Society, April 28–May 1, 2002, American Ceramic Society (2003).

Goyal, A., R. Feenstra, M. Paranthaman, J. R. Thompson, B. Y. Kang, C. Cantoni, D. F. Lee, F. A. List, P. M. Martin, E. Lara-Curzio, C. Stevens, D. M. Kroeger, M. Kowalewski, E. D. Specht, T. Aytug, S. Sathyamurthy, R. K. Williams, and R. E. Ericson, "Strengthened, Biaxially Textured Ni Substrate with Small Alloying Additions for Coated Conductor Applications," *Physica C* **382**, 251–62 (2002).

Grabovickic, R., J. W. Lue, M. J. Gouge, J. A. Demko, and R. C. Duckworth, "Measurements of Temperature Dependence of the Stability and Quench Propagation of a 20-cm-long RABiTS Y-Ba-Cu-O Tape," *IEEE Transactions on Applied Superconductivity*, **13** (2), 1726–30 (2003).

Gupta, Anurag, H. Narayan, D. Astill, D. Kanjilal, C. Ferdeghini, M. Paranthaman, and A. V. Narlikar, "Study of Magnetization and Pinning Mechanisms in MgB_2 Thin Film Superconductors: Effect of Heavy Ion Irradiation," *Supercond. Sci. Technol.* **16** , 951–55 (2003).

James, D. R., I. Sauers, M. O. Pace, and A. R. Ellis, "High Voltage Breakdown of Solid Epoxies at Room Temperature and in Liquid Nitrogen," ,pp. 542–45 in *2002 Annual Report Conference on Electrical Insulation and Dielectric Phenomena*, IEEE Pub. No. 02CH37372 (2002).

King, A. C., S. S. Shoup, M. K. White, S. L. Krebs, D. M. Mattox, T. Polley, N. Darnell, K. R. Marken, S. Hong, and B. Czabaj (MicroCoating Technologies and Oxford Superconducting Technology), "The Progress Made Using the Combustion Chemical Vapor Deposition (CCVD) Technique to Fabricate $YBa_2Cu_3O_{7-\chi}$ Coated Conductors," *IEEE Transactions on Applied Superconductivity*, **13** (2), 2643–45 (2003).

Leonard, K. J., A. Goyal, D. M. Kroeger, J. W. Jones, S. Kang, N. Rutter, M. Paranthaman, D. F. Lee, and B. W. Kang, "Thickness Dependence of Microstructure and Critical Current Density of $YBa_2Cu_3O_{7-\delta}$ on Rolling-Assisted Biaxially Textured Substrates," *J. Mater. Res.* **18** (5), 1109–22 (2003).

Leonard, K. J., S. Kang, A. Goyal, K. A. Yarborough, and D. M. Kroeger, "Microstructural Characterization of Thick $YBa_2Cu_3O_{7-\delta}$ Films on Improved Rolling-Assisted Biaxially Textured Substrates," *J. Mater. Res*, **18** (7), 1723–32 (2003).

Li, X, M. W. Rupich, W. Zhang, N. Nguyen, T. Kodenkandath, U. Schoop, D. T. Verebelyi, C. Thieme, M. Jowett, P. N. Arendt, S. R. Foltyn, T. G. Holesinger, T. Aytug, D. K. Christen, and M. P. Paranthaman, "High Critical Current MOD ex situ YBCO \Films on RABiTS™ and MgO-IBAD Templates," *Physica C* **390**, 249–53 (2003).

List, F. A., E. D. Specht, L. Heatherly, K. J. Leonard, S. Sathyamurthy, and D. M. Kroeger, "Crystalline Phase Development during Vacuum Conversion of Thin Barium Fluoride Precursor Films on Metallic Substrates," *Physica C* **391**, 350–62 (2003).

Maroni, V. A., N. N. Murphy, M. Mika, Z. P. Luo, Y. Tang, H. Claus, D. J. Miller, J.-H. Park, S. E. Dorris, G. N. Riley, Jr., S. Fleshler, and R. K. Williams, "Search for a Silver-Sheathed 1212-Type Superconductor with a Grain Colony Microstructure: $M_1Sr_2Y_{1-\chi}Ca_\chi Cu_2O_z$ with M=(Bi,Pb), (Cd,Pb), and (Fe,Pb)," *IEEE Transactions on Applied Superconductivity* **13** (1), 7–16 (2003).

Paranthaman, M. P., S. Sathyamurthy, Z. Y. Zhai, H. M. Christen, S. Kang, and A. Goyal, "Demonstration of High Current Density YBCO Films on all Solution Buffers," book chapter, pp. 249–56 in *Processing of High Temperature Superconductors*, CT140, American Ceramic Society (2003).

Paranthaman, M. P., A. Goyal, R. Feenstra, T. Izumi, and V. Selvamanickam, "MRS Superconductivity Workshop Explored Issues Related to Second-Generation YBCO-Coated Conductors," *MRS Bulletin*, 812–14 (October 2002).

Paranthaman, M. P., D. K. Christen, H. M. Christen, J. R. Thompson, H. R. Kerchner, C. Cantoni, and H. Y. Zhai, "Growth of High Current Density MgB_2 Films using ex-situ Precursor Approach," *Physica C* **378–381** (2), 1252–1255 (2002).

Paranthaman, M. P., T. Aytug, S. Sathyamurthy, D. B. Beach, A. Goyal, D. F. Lee, B. W. Kang, L. Heatherly, E. D. Specht, K. J. Leonard, D. K. Christen, and D. M. Kroeger, "Bulk Solution Techniques to Fabricate High-J_c YBCO Coated Conductors," *Physica C* **378-381** (2), 1009–12 (2002).

Paranthaman, M. P., D. K. Christen, H. M. Christen, J. R. Thompson, C. Cantoni, H. Y. Zhai, and R. Jin, "Superconducting MgB_2 Films with Enhanced Critical Current Densities and Irreversibility Fields," book chapter, pp. 475–84 in *Studies of High Temperature Superconductors (Advances in Research and Applications)*, Vol. 38, ed. Anant Narlikar, Nova Science Publishers, Inc.

Paranthaman, M. P., T. Aytug, D. K. Christen, P. N. Arendt, S. R. Foltyn, J. R. Groves, L. Stan, R. F. DePaula, H. Wang, and T. G. Holesinger, "Growth of Thick $YBa_2Cu_3O_{7-\delta}$ Films Carrying a Critical Current of over 230A/cm on Single $LaMnO_3$-Buffered Ion-Beam Assisted Deposition MgO Substrates," *J. Mater. Res*. **18 (**9), 2055–59 (2003).

Paranthaman, M. P., T. Aytug, S. Kang, R. Feenstra, J. D. Budai, D. K. Christen, P. N. Arendt, J. R. Groves, R. F. DePaula, S. R. Foltyn, and T. G. Holesinger, "Fabrication of High J_c YBCO Tapes using the Newly Developed Lanthanum Manganate Single Buffer Layers," *IEEE Transactions on Applied Superconductivity* **13** (2), 2481–83 (2003).

Purnell, A. J., A. A. Zhukov, T. Nurgaliev, G. Lamura, Y. Bugoslavsky, Z. Lockman, J. L. MacManus-Driscoll, H. Y. Zhai, H. M. Christen, M. P. Paranthaman, D. H. Lowndes, M. H. Jo, M. G. Blamire, L. Hao, J. C. Gallop, and L. F. Cohen, "The Microwave Surface Impedance of MgB_2 Thin Films," *Supercond. Sci. Technol.* **16**, 1–6 (2003).

Rupich, M. W., U. Schoop, D. T. Verebelyi, C. Thieme, W. Zhang, X. Li, T. Kodenkandath, N. Nguyen, E. Siegal, D. Buczek, J. Lynch, M. Jowett, E. Thompson, J.-S. Wang, J. Scudiere, A. P. Malozemoff, Q. Li, S. Annavarapu, S. Cui, L. Fritzemeier, B. Aldrich, C. Craven, F. Neu, A. Goyal, and M. Paranthaman, "YBCO Coated Conductors," *IEEE Transactions on Applied Superconductivity* **13** (2), 2458–61 (2003).

Sambasivan, S., I. Kim, S. Barnett, M. A. Zurbuchen, J. Ji, B. W. Kang, A. Goyal, P. N. Barnes, C. E. Oberly, "New Approach to Depositing Yttria-Stabilized Zirconia Buffer Layers for Coated Conductors," *J. Mater. Res.* **18** (4), 919–28 (2003).

Sathyamurthy, S., M. P. Paranthaman, H.-Y. Zhai, H. M. Christen, C. Cantoni, A. Goyal, and P. M. Martin, "Solution Processing of Lanthanum Zirconate Films as Single Buffer Layers for High I_c YBCO Coated Conductors," *IEEE Transactions on Applied Superconductivity* **13** (2), 2658–60 (2003).

Sauers, I., D. R. James, M. O. Pace, and A. R. Ellis, "Surface Flashover of Fiberglass Reinforced Plastic in Vacuum at Cryogenic Temperature," pp. 818–21 in *2002 Annual Report Conference on Electrical Insulation and Dielectric Phenomena*, IEEE Pub. No. 02CH37372 (2002).

Sauers, I, D. R. James, A. R. Ellis, and M. O. Pace, "High Voltage Studies of Dielectric Materials for HTS Power Equipment," *IEEE Trans. Dielectrics EI*, **9** (6), 922–31 (2002) (Special Issue).

Pace, M. O., I. Sauers, D. R. James, and A. R. Ellis, "Aging of Lapped Tape Insulated Model Cables at Cryogenic Temperature," pp. 27–30 in *2002 Annual Report Conference on Electrical Insulation and Dielectric Phenomena*, IEEE Pub. No. 02CH37372 (2002).

Specht, E. D., F. A. List, D. F. Lee, K. L. More, A. Goyal, W. B. Robbins, and D. O'Neill, "Uniform Texture in Meter-Long $YBa_2Cu_3O_7$ Tape," *Physica C* **382**, 342–48 (2002).

Verebelyi, D. T., U. Schoop, C. Thieme, X. Li, W. Zhang, T. Kodenkandath, A. P. Malozemoff, N. Nguyen, E. Siegal, D. Buczek, J . Lynch, J. Scudiere, M. Rupich, A. Goyal, E. D. Specht, P. Martin, and M. Paranthaman, "Uniform Performance of Continuously Processed MOD-YBCO-Coated Conductors using a Textured Ni-W Substrate," *Supercond. Sci. Technol.* **16** , L19–L22 (2003).

Xie, Y. Y., J. Z. Wu, T. Aytug, D. K. Christen, and A. H. Cardona, "Diffusion Mechanism of Cation-Exchange Process for Fabrication of $HgBa_2CaCu_2O_{6+}$ Superconducting Films," *Appl. Phys. Lett.* **81** (21), 4002–4004 (2002).

Xu, Y, A. Goyal, N. A. Rutter, D. Shi, M. Paranthaman, S. Sathyamurthy, P. M. Martin, and D. M. Kroeger, "Fabrication of High-Critical Current Density $YBa_2Cu_3O_{7-\delta}$ Films using a Fluorine-Free Sol Gel Approach," *J. Mater. Res.* **18 (**3), 677–81 (2003).

Xu, Y., D. Shi, A. Goyal, M. Paranthaman, N. A. Rutter, P. Martin, and D. Kroeger, "$YBa_2Cu_3O_{7-\delta}$ Films through a Fluorine-Free TMAP MOD Approach," book chapter, pp. 129–36 in *Processing of High Temperature Superconductors*, CT140, American Ceramic Society (2003).

Young, M. A., J. A. Demko, M. J. Gouge, M. O. Pace, J. W. Lue, and R. Grabovickic, "Measurements of the Performance of BSCCO HTS Tape under Magnetic Fields with a Cryocooled Test Rig," *IEEE Transactions on Applied Superconductivity*, **13** (2), 2964–67 (2003).

Zhai, H. Y., H. M. Christen, P. M. Martin, L. Zhang, and D. H. Lowndes, "Direct Electrical Heating of Metal Tape Substrates for Coated Conductor Deposition," *IEEE Transactions on Applied Superconductivity* **13** (2), 2622–24 (2003).

Zurbuchen, M. A., S. Sambasivan, I. Kim, J. Rechner, J. Wessling, J. Ji, S. Barnett, B. F. Kang, A. Goyal, P. A. Barnes, and C. E. Oberly, "An Economical Route for Production of High-Quality YSZ Buffer Layers using the ECONO™ Process," book chapter, pp. 77–90 in *Processing of High Temperature Superconductors*, CT140, American Ceramic Society (2003).

SUBMITTED

Aytug, T., A. Goyal, N. Rutter, M. Paranthaman, J. R. Thompson, H. Y. Zhai, and D. K. Christen, "High-J_c $YBa_2Cu_3O_{7-}$ Coatings on $LaMnO_3$ Buffered Biaxially-Textured Cu Tapes for Coated Conductor Applications," accepted for publication in *J. Mater. Res., Rapid Communications.*

Aytug, T., M. P. Paranthaman, A. Goyal, A. Gapud, N. Rutter, H.-Y. Zhai, and D. K. Christen, "Development of Conductive $La_{0.7}Sr_{0.3}MnO_3$ Buffer Layers for Cu-Based RABiTS," paper submitted to proceedings of Annual Meeting and Expo. of American Ceramics Society, Nashville, TN, April 27–30, 2003.

Aytug, T., M. Paranthaman, J. R. Thompson, A. Goyal, N. Rutter, H. Y. Zhai, A. A. Gapud, A. O. Ijaduola, and D. K. Christen, "Electrical and Magnetic Properties of Conductive Cu-Based Coated Conductor," paper submitted to *Appl. Phys. Lett.*

Aytug, T., M. Paranthaman, J. R. Thompson, A. Goyal, N. Rutter, N. Y. Zhai, A. A. Gapud, A. O. Ijaduola, and D. K. Christen, "Development of Conductive Buffer Layers for Cu-Based RABiTS Coated Conductors," submitted to *Appl. Phys. Lett.*

Bugoslavsky, Y., Y. Miyoshi, G. K. Perkins, A. D. Caplin, L. F. Cohen, H. Y. Zhai, H. M. Christen, A. V. Pogrebnyakov, and O. V. Dolgov, "Superconducting Gap Structure and Pinning in Disordered MgB_2 Films," paper submitted to proceedings of Sixth European Conference on Applied Superconductivity (EUCAS 2003), Sorrento, Napoli, Italy, 14–18 September.

Cantoni, C., D. K. Christen, E. D. Specht, M. Varela, J. R. Thompson, A. Goyal, and S. J. Pennycook, "Buffer Layers for Development of High-J_c Cu-Based Coated Conductors," paper submitted to proceedings of Sixth European Conference on Applied Superconductivity (EUCAS 2003), Sorrento Napoli, Italy, 14–18 September. (Proceedings will be published by the Institute of Physics as a CD ROM and partial proceedings in a special issue of *Supercond. Sci. Technol.*)

Cantoni, C., D. K. Christen, M. Varela, J. R. Thompson, S. J. Pennycook, E. D. Specht, and A. Goyal., "Deposition and Characterization of $YBa_2Cu_3O_{7-}$/$LaMnO_3$/MgO/TiN Heterostructures on Cu Metal Substrates for Development of Coated Conductors," submitted to Journal of Materials Research.

Cheggour, N., J. W. Ekin, C. C. Clickner, D. T. Verebelyi, C. L. H. Thieme, R. Feenstra, and A. Goyal, "Reversible Axial-Strain Effect and Extended Strain Limits in Y-Ba-Cu-O Coatings on Deformation-Textured Substrates," paper submitted to *Appl. Phys. Lett.*

Duckworth, R. C., J. R. Thompson, M. J. Gouge, J. W. Lui, A. O. Ijaduola, D. Yu, and D. T. Verebelyi, "Transport AC Loss Studies of YBCO Coated Conductors with Nickel Alloy Substrates," submitted to *Superconductor Science and Technology*.

Feenstra, R., A. A. Gapud, D. K. Christen, T. Aytug, E. D. Specht, L. Heatherly, N. Rutter, A. Goyal, T. G. Holesinger, P. N. Arendt, D. M. Feldmann, and D. C. Larbalestier, "Uniform Dependence of the Critical Current Density on YBCO Layer Thickness in RABiTS and IBAD-Type Coated Conductors," European Conference on Applied Superconductivity (EUCAS), Sorrento, Italy, September 14–18, 2003.

Feldmann, D. M., D. C. Larbalestier, R. Feenstra, A. A. Gapud, J. D. Budai, T. G. Holesinger, and P. N. Arendt, "Through-Thickness Superconducting and Normal-State Transport Properties Revealed by Thinning of Thick Film ex situ $YBa_2Cu_3O_{7-x}$ Coated Conductors, paper submitted to *Appl. Phys. Lett*.

Gapud, A. A., D. K. Christen, J. R. Thompson, and M. Yethiraj, "Electrical Transport, Magnetic, and Structural Properties of the Vortex Lattice of V_3Si in the Vicinity of the Peak Effect," submitted to *Physical Review B.*

Gouge, M. J., M. J. Cole, J. A. Demko, P. W. Fisher, C. A. Foster, R. Grabovickic, D. T. Lindsay, J. W. Lue, M. L. Roden and J. C. Tolbert, "High Temperature Superconducting Tri-Axial Power Cable," presented at 15th International Symposium on Superconductivity, Yokohama, Japan, November 11–13, 2002, and accepted for publication in *Physica C*.

Hawsey, R. A., "Overview of U.S. Developments in Coated Conductors," invited abstract submitted to the Sixteenth International Symposium on Superconductivity (ISS2003) to be held October 27–29, Tsukuba, Japan.

James, D. R., I. Sauers, A. R. Ellis, M. O. Pace, and D. J. Beschenes, "Effect of Gas Pressure on Partial Discharge in Voids in Epoxy," paper submitted to proceedings of the 2003 IEEE Conference on Electrical Insulation and Dielectric Phenomena, Albuquerque NM, Oct. 18–23, 2003.

Kang, S., A. Goyal, K. J. Leonard, N. A. Rutter, D. F. Lee, D. M. Kroeger, M. Paranthaman, "High Critical Current $YBa_2Cu_3O_{7-\delta}$ Thick Films on Rolling-Assisted Biaxially Textured Substrates (RABiTS)," paper submitted to *J. Mater. Res.*

Lee, D. F., K. J. Leonard, L. Heatherly, Jr., J. Yoo, F. A. List, N. Rutter, S. W. Cook, S. Sathyamurthy, M. Paranthaman, P. M. Martin, A. Goyal, and D. M. Kroeger, "Reel-to-Reel ex situ Conversation of High Critical Current Density Electron Beam Co-Evaporated BaF_2 Precursor on RABiTS," paper submitted to *Supercond. Sci.Technol.*

Leonard, K. J., B. W. Kang, A. Goyal, D. M. Kroeger, J. W. Jones, S. Kang, N. Rutter, M. Paranthaman, and D. F. Lee, "Microstructure Characterization of the Thickness Dependence of Critical Current Density of $YBa_2Cu_3O_{7-\delta}$ on Rolling-Assisted Biaxially Textured Substrates," submitted to *J. Mater. Res*.

Leonard, K. J., S. Kang, A. Goyal, D. M. Kroeger, and B. Kang, "Analytical Transmission Electron Microscopy of Thick $YBa_2Cu_3O_{7-\delta}$ Films on RABiTS," paper submitted to proceedings of Annual Meeting and Expo. of American Ceramics Society, Nashville, TN, April 27–30, 2003.

Leonard, K. J., S. Kang, A. Goyal, K. A. Yarborough, and D. M. Kroeger, "Microstructural Characterization of Thick $YBa_2Cu_3O_{7-\delta}$ Films on Improved Rolling-Assisted Biaxially Textured Substrates," submitted to *J. Mater. Res*.

Li, X., M. W. Rupich, W. Zhang, N. Nguyen, T. Kodenkandath, U. Schoop, D. T. Verebelyi, C. Thieme, M. Teplitsky, P. N. Arendt, S. R. Foltyn, T. G. Holesinger, T. Aytug, D. K. Christen, and M. P. Paranthaman, "High Critical Current MOD ex situ YBCO Films on RABiTS™ and MgO-IBAD Templates," submitted to *Physica C.*

List, F. A., E. D. Specht, L. Heatherly, K. J. Leonard, S. Sathyamurthy, and D. M. Kroeger, "Crystalline Phase Development during Vacuum Conversion of Thin Barium Fluoride Precursor Films on Metallic Substrates," submitted to *Physica C.*

Maroni, V. A., N. N. Murphy, M. Mika, Z. P. Luo, Y. Tang, H. Claus, D. J. Miller, J. H. Parks, S. E. Dorris, G. N. Riley, Jr., S. Fleshler, and R. K. Williams, "Search for a Silver-Sheathed 1212-Type Superconductor with a Grain Colony Microstructure: $M_1Sr_2Y_{1-x}Ca_xCu_2O_z$ with M = (Bi,Pb), (Cd,Pb), and (Fe,Pb)," accepted for publication in IEEE Trans. Appl. Supercond.

Palau, A., T. Puig, X. Obradors, E. Pardo, C. Navau, A. Sanchez, Ch. Jooss, A. Usoskin, H. C. Freyhardt, L. Fernandez, B. Holzapfel, and R. Feenstra, "Inductive Determination of Inter- and Intra-Grain Critical Current Densities of $YBa_2Cu_3O_{7-x}$ IBAD and RABiT Coated Conductors," European Conference on Applied Superconductivity (EUCAS), Sorrento, Italy, September 14–18, 2003.

Palau, A., T. Puig, X. Obradors, A. Usoskin, H. Freyhardt, L. Fernandez, B. Holzapfel, R. Feenstra, A. Sanchez, and E. Pardo, "Magnetic Granularity Analysis of YBCO Coated Conductors," to be published in Physica C as part of proceedings for 7th International Conference on Materials and Mechanisms of Superconductivity and High Temperature Superconductors, Rio de Janeiro, Brazil, May 25–30, 2003.

Paranthaman, M. P., "Non-Fluorine Based Bulk Solution Techniques to Grow Superconducting $YBa_2Cu_3O_{7-\delta}$ Films—A Review," submitted book chapter for *Next Generation HTS Conductors*, edited by A. Goyal, Plenum Publishing Corporation.

Paranthaman, M. P., S. Sathyamurthy, H. Y. Zhai, H. M. Christen, S. Kang, and A. Goyal, "Demonstration of High Current Density YBCO Films on All Solution Buffers," submitted to proceedings of the American Ceramic Society 104th Annual Meeting and Exposition, April 28–May 1, 2002, St. Louis, Mo.

Paranthaman, M. P., T. Aytug, H. Y. Zhai, H. M. Christen, D. K. Christen, A. Goyal, L. Heatherly, and D. M. Kroeger, "Development of Low-Cost Alternative Buffer Layer Architectures for YBCO Coated Conductors," paper submitted to proceedings of American Ceramic Society's 105th Annual Meeting, Nashville TN, April 27–30, 2003.

Paranthaman, M., T. Aytug, D. K. Christen, P. N. Arendt, S. R. Foltyn, J. R. Groves, L. Stan, R. F. DePaula, H. Wang, and T. G. Holesinger, "Growth of Thick $YBa_2Cu_3O_{7-\delta}$ Films Carrying an I_c of over 230 A/cm on Single $LaMnO_3$ Buffered IBAD MgO Substrates," submitted to *J. Mater. Res.*

Puig, T., A. Palau, X. Obradors, A. Usoskin, Ch. Jooss, H. Freyhardt, L. Fernandez, B. Holzapfel, R. Feenstra, A. Sanchez, and E. Pardo, "Inductive Evaluation of the Electromagnetic Granularity of YBCO Coated Conductors," European Conference on Applied Superconductivity (EUCAS), Sorrento, Italy, September 14–18, 2003.

Puig, T., A. Palau, X. Obradors, A. Usoskin, H. Freyhardt, L. Fernandez, B. Holzapfel, R. Feenstra, A. Sanchez, and E. Pardo, "Magnetic Granularity Analysis of YBCO Coated Conductors," Seventh International Conference on Materials and Mechanisms of Superconductivity and High Temperature Superconductors, Rio de Janeiro, Brazil, May 25–30, 2003.

Puig, T., A. Palau, X. Obradors, E. Pardo, A. Sanchez, A. Usoskin, C. H. Jooss, H. Freyhardt, R. Feenstra, L. Fernandez, and B. Holzapfel, "Non-Conventional Inductive Behavior of $YBa_2Cu_3O_7$ Coated Conductors: A New Physical Re-Understanding," CEC/ICMC Conference, Anchorage, Alaska, September 22–26, 2003.

Sathyamurthy, S., M. Paranthaman, H.-Y. Zhai, S. Kang, C. Cantoni, S. Cook, L. Heatherly, A. Goyal, H. M. Christen, M. S. Bhuiyan, and K. Salama, "Solution Buffer Layers for YBCO Coated Conductors," paper submitted to proceedings of Annual Meeting and Expo. of American Ceramics Society, Nashville, TN, April 27–30, 2003.

Sauers, I., M. O. Pace, D. R. James, and A. R. Ellis, "Energy Dissipation by Partial Discharge in Cryogenic Cables," paper submitted to proceedings of the 2003 IEEE Conference on Electrical Insulation and Dielectric Phenomena, Albuquerque NM, Oct. 18–23, 2003.

Structures on Cu Metal Substrates for Development of Coated Conductors," submitted to *Journal of Materials Research*.

Thompson, J. R., H. J. Kim, C. Cantoni, D. K. Christen, R. Feenstra, and D. T. Verebelyi, "Self-Organized Current Transport through Low-Angle Grain Boundaries in $YBa_2Cu_3O_{7-\delta}$ Thin Films, Studied Magnetometrically," paper (joint with BES) submitted to *Phys. Review B.*

W. Wong-Ng, L. P. Cook, J. Suh, R. Feenstra, T. Haugan, and P. Barnes, "Phase Equilibria of Ba-R-Cu-O for Coated-Conductor Applications (R = Lanthanides and Yttrium)," 7th International Conference on Materials and Mechanisms of Superconductivity and High Temperature Superconductors, Rio de Janeiro, Brazil, May 25–30, 2003.

Wong-Ng, W., I. Levin, L. P. Cook, J. P. Cline, and R. Feenstra, "High Temperature X-Ray Study of Phases Evolution and Texture of $Ba_2YCu_3O_{6+x}$ Films Using the BaF_2 Process," Fall Electronics Division Symposium "Epitaxial Growth of Functional Oxides," Orlando, Florida, October 12–17, 2003.

Xu, Y., A. Goyal, J. Lian, N. A. Rutter, D. Shi, S. Sathyamurthy, M. Paranthaman, P. M. Martin, and D. M. Kroeger, "Preparation of YBCO Films on CeO_2-Buffered (001) YSZ Substrates by a Non-Fluorine MOD Method," submitted to *Supercond. Sci. and Technol*.

Yoo, J., K. J. Leonard, D. F. Lee, H. S. Hsu, L. Heatherly, F. A. List, N. A. Rutter, A. Goyal, M. Paranthaman, and D. M. Kroeger, "Effects of Conversion Parameters on the Transport Properties of YBCO Films in the BaF_2 ex-situ Process," paper submitted to *J. Mater. Res.*

The following papers were submitted to the proceedings of the 2003 Cryogenic Engineering Conference /International Cryogenic Materials Conference (CEC/ICMC), Anchorage, Alaska, Sept. 22–26.

Demko, J. A., J. W. Lue, M. J. Gouge, P. W. Fisher, D. Lindsay, and M. Roden, "Analysis of a Liquid Nitrogen Cooled Tri-Axial High-Temperature Superconducting Cable System."

Fisher, P. W., M. J. Cole, J. A. Demko, M. J. Gouge, D. T. Lindsay, J. W. Lue, A. L. Qualls, M. L. Roden, and J. C. Tolbert, "Tri-Axial Cable Terminations for 1.3- and 3-kA HTS Cables."

Gouge, M. J., J. W. Lue, J. A. Demko, R. C. Duckworth, P. W. Fisher, M. Daumling, D. T. Lindsay, M. L. Roden, and J. C. Tolbert, "Testing of a 1.25-m HTS Cable Made from YBCO Tapes."

Lue, J. W., J. A. Demko, P. W. Fisher, R. C. Duckworth, M. J. Gouge, J. C. Tolbert, M. L. Roden, and D. T. Lindsay, "Tests of 5-m-Long Tri-Axial HTS Cables."

Paranthaman, M. P., S. Sathyamurthy, T. Aytug, K. Leonard, A. Goyal, H. Y. Zhai, D. M. Kroeger, D. K. Christen, X. Li, D. T. Verebelyi, U. Schoop, C. Thieme, T. Kodenkandath, W. Zhang, and M. W. Rupich, "Buffer Layer R&D for YBCO Coated Conductor Composite Wires."

Sauers, I., D. R. James, M. O. Pace, A. R. Ellis, and A. C. Muller, "High-Voltage Breakdown, Partial Discharge, and Aging in Lapped Tape Insulated Cold Dielectric Model Cables."

Schwenterly, S. W., M. J. Cole, J. A. Demko, E. F. Pleva, and D. W. Hazelton, "Design and Operating Performance of Cryocooled Helium Thermosiphon Loops for HTS Transformers."

Young, M. A., J. A. Demko, R. C. Duckworth, J. W. Lue, M. J. Gouge, and M. O. Pace, "Burnout Test of First- and Second-Generation HTS Tapes in Liquid Nitrogen Bath Cooling."

ABSTRACTS

Cantoni, C., D. K. Christen, A. Goyal, L. Heatherly, F. A. List, E. D. Specht, M. Varela, and S. J. Pennycook, "Metal-Oxide Interfaces in 2nd Generation HTS Wires: Mechanism of Epitaxial Growth of Oxide Films Mediated by a Sulfur Superstructure," invited abstract submitted to the 204th Electrochemical Society's Fall Meeting, Orlando, Florida, October 12–17, 2003.

Cantoni, C., D. K. Christen, E. D. Specht, M. Varela, J. R. Thompson, A. Goyal, and S. J. Pennycook, "Buffer Layers for Development of High-J_c Cu-Based Coated Conductors," invited abstract submitted to European Conference on Applied Superconductivity (EUCAS), Sorrento, Italy, September 14–18, 2003.

Cantoni, C., D. K. Christen, E. D. Specht, M. Varela, K. Kim, A. A. Gapud, T. Aytug, A. Goyal, S. J. Pennycook, and J. R. Thompson, "Buffer Layers for Development of High-J_c Cu-Based Coated Conductors," abstract submitted to International Workshop on Coated Conductors for Applications, Orta (MI), Italy, September 11–13, 2003.

Christen, D. K., "Vortices and Flux Pinning Coated Conductors," invited abstract submitted to MURI-CC-03 Workshop, Madison, Wisconsin, June 11–13, 2003.

Feenstra, R., A. A. Gapud, D. K. Christen, T. Aytug, E. D. Specht, L. Heatherly, N. Rutter, A. Goyal, T. G. Holesinger, P. N. Arendt, D. M. Feldmann, and D. C. Larbalestier, "Uniform Dependence of the Critical Current Density on YBCO Layer Thickness in RABiTS and IBAD-type Coated Conductors, abstract submitted to European Conference on Applied Superconductivity (EUCAS), Sorrento, Italy, September 14–18, 2003.

Heatherly, L., A. Goyal, N. Rutter, F. A. List, K. J. Leonard, D. F. Lee, P. M. Martin, D. M. Kroeger, and S. W. Cook, "Procedure for Developing Robust RABiTS for the Reliable Production of High Current Carrying YBCO Superconductors," abstract submitted to the Annual Meeting and Expo of American Ceramics Society, Nashville, TN, April 27–30, 2003.

List, F. A., E. D. Specht, L. Heatherly, K. J. Leonard, S. Sathyamurthy, D. M. Kroeger, P. G. Clem, J. T. Dawley, "Vacuum Conversion of Fluorine Based Precursor Films on Metallic Substrates Studied by X-ray Diffraction," abstract submitted to the Annual Meeting and Expo of American Ceramics Society, Nashville, TN, April 27–30, 2003.

Paranthaman, M. P., T. Aytug, R. Feenstra, D. K. Christen, A. Goyal, D. M. Kroeger, P. N. Arendt, L. Stan, J. R. Groves, R. F. DePaula, S. R. Foltyn, "Development of Low-Cost Alternative Buffer Layer Architectures for YBCO Coated Conductors," abstract submitted to the Annual Meeting and Expo of American Ceramics Society, Nashville, TN, April 27–30, 2003.

Xu, Y., A. Goyal, L. Heatherly, D. F. Lee, P. M. Martin, M. Paranthaman, D. M. Kroeger, D. Shi, "High J_c $YBa_2Cu_3O_{7-\delta}$," abstract submitted to the Annual Meeting and Expo. of American Ceramics Society, Nashville, TN, April 27–30, 2003.

INTERNAL DISTRIBUTION

1. D. B. Beach
2. E. E. Bloom
3. M. A. Brown
4. M. V. Buchanan
5. D. K. Christen
6. J. F. Cooke
7. L. M. Dickens
8. M. J. Gouge
9. A. Goyal
10-19. R. A. Hawsey
20. D. J. Hill
21. W. Koncinski
22. S. L. Milora
23. C. Narula
24. M. Paranthaman
25. R. D. Quinn
26. J. Johnson, OTIC

EXTERNAL DISTRIBUTION

27. N. Aversa, Consultant, Waukesha Electric Systems, 400 S. Prairie Ave., Waukesha, WI 53186-5937
28. U. Balachandran, Argonne National Laboratory, ET/212, 9700 South Cass Ave., Argonne, IL 60439-4838
29. P. N. Barnes, Air Force Research Laboratory, AFRL/PRPG, 2645 Fifth Street, WPAFB, OH 45433-7919
30. R. Bhattacharya, National Renewable Energy Laboratory, 1617 Cole Blvd., Golden, CO 80401
31. J. W. Bray, Physicist/Program Manager, General Electric Corporate Research and Development, P.O. Box 8, Schenectady, NY 12301
32. L. Castelloni, Metal Oxide Technologies Inc., 8807 Emmott Rd., Suite 100, Houston, TX 77040
33. H. S. Chhabra,TD-2, U.S. Department of Energy, 6H-034/FORS, 1000 Independence Ave., S.W., Washington, DC 20585
34. P. G. Clem, Sandia National Laboratories, MS 1411, P.O. Box 5800, Albuquerque, NM 87185-1405
35. J. G. Daley, TD-2, U.S. Department of Energy, 6H-034/FORS, 1000 Independence Ave., S.W., Washington, DC 20585
36. D. Driscoll, Rockwell Automation, 6040 Ponders Ct., Greenville, SC 29615
37. J. Ekin, National Institute of Standards and Technology, 325 Broadway, Boulder, CO 80303
38. R. E. George,TD-2, U.S. Department of Energy, 6H-034/FORS, 1000 Independence Ave., S.W., Washington, DC 20585
39. J. W. Glotfelty, TD-1, U.S. Department of Energy, 1000 Independence Avenue, S.W., Washington, DC 20585
40. H. Harshavardhan, Neocera, 10000 Virginia Manor Rd., Beltsville, MD 20705
41. P. A. Hoffman, EE-2D, U.S. Department of Energy, 1000 Independence Ave., S.W., Washington, DC 20585
42. X. Huang, General Electric Corporate Research and Development, EP-113, P. O. Box 8, Schenectady, NY 12301
43. L. Kovalsky, SuperPower, Inc., 450 Duane Avenue, Schenectady, NY 12305
44. V. Kruse, Southwire Company, P. O. Box 1000, Carrollton, GA 30119
45. D. C. Larbalestier, University of Wisconsin–Madison, Applied Superconductivity Center, 1500 Engineering Drive, Madison, WI 53706-1687
46. W. C. Lin, U.S. Department of Energy, Office of Assistant Manager for Energy Research and Development, Oak Ridge Field Office, P.O. Box 2008, Oak Ridge, TN 37831-6269
47. D. Lindsay, Southwire Company, P. O. Box 1000, Carrollton, GA 30119
48. A. P. Malozemoff, American Superconductor Corporation, Two Technology Dr., Westborough, MA 01581

49. K. R. Marken, Jr., Oxford Superconducting Technology, P.O. Box 429, Carteret, NJ 07008-0429
50. S. P. Mehta, Waukesha Electric Systems, 400 S. Prairie Ave., Waukesha, WI 53186-5937
51. C. E. Oberly, WL/POOX-2, Aerospace Power Div., Wright Laboratory, 2645 Fifth St., WPAFB OH 45433-6563
52. P. N. Overholt, TD-2, U.S. Department of Energy, 1000 Independence Avenue, S.W., Washington, DC 20585
53. S. M. Parker, Oxford Superconducting Technology, P.O. Box 429, Carteret, NJ 07008-0429
54. W. P. Parks, Jr., TD-2, U.S. Department of Energy, 1000 Independence Avenue, S.W., Washington, DC 20585
55. P. Pellegrino, SuperPower, Inc., 450 Duane Avenue, Schenectady, NY 12305
56. D. E. Peterson, Los Alamos National Laboratory, Superconductivity Technology Center, P.O. Box 1663, MS K763, Los Alamos, NM 87545
57. E. Pleva, Waukesha Electric Systems, 400 S. Prairie Ave., Waukesha, WI 53186-5937
58. M. J. Reed, TD-2, U.S. Department of Energy, 1000 Independence Avenue, S.W., Washington, DC 20585
59. C. Reis, SuperPower, Inc., 450 Duane Avenue, Schenectady, NY 12305
60. L. Richards, Southwire Company, P. O. Box 1000, Carrollton, GA 30119
61. J. Scudiere, American Superconductor Corporation, Two Technology Drive, Westborough, MA 01581
62. V. Selvamanickam, SuperPower, Inc., 450 Duane Avenue, Schenectady, NY 12305
63. M. Suenaga, Brookhaven National Laboratory, Bldg. 480, P. O. Box 5000, Upton, NY 11973-5000
64. S. Thorn, Southwire Company, P.O. Box 1000, Carrollton, GA 30119
65. D. T. Verebelyi, American Superconductor Corporation, Two Technology Drive, Westborough, MA 01581
66. K. Weeber, GE Electronic and Photonic Systems Technologies, 1 Research Circle, Bldg EP, Rm 111c, Niskayuna, NY 12309
67. D. O. Welch, Brookhaven National Laboratory, Materials Science Division, Upton, Long Island, NY 11973
68. W. Wong-Ng, National Institute of Standards and Technology, Ceramics Division, Building 223, A-256 Materials, Gaithersburg, MD 20899
69. G. Yurek, American Superconductor Corporation, Two Technology Drive, Westborough, MA 01581